UNIVERSITY OF CALIFORNIA SAN DIEGO

Development of micro-spectroscopic tools for analysis of environmental interfaces

A Dissertation submitted in partial satisfaction of the requirements
for the degree Doctor of Philosophy

in

Chemistry

by

Deborah Kim

Committee in charge:

Professor Vicki H. Grassian, Chair
Professor Jon Pokorski
Professor Jonathan Slade
Professor Wei Xiong

2023

The Dissertation of Deborah Kim is approved, and it is acceptable in quality and form for publication on microfilm and electronically

University of California San Diego

2023

DEDICATION

This dissertation is dedicated to my family, who are my biggest cheerleaders, and my friends, who have walked this 5- year journey with me and helped make it one of the most special times of my life.

TABLE OF CONTENTS

LIST OF FIGURES

LIST OF TABLES

ACKNOWLEDGEMENTS

First and foremost, I would like to acknowledge all of my advisors and mentors who have played a role in this Ph.D. journey. I would like to thank Dr. Vicki H. Grassian, who has provided me with the guidance and direction needed for me to complete this dissertation. Thank you for always making time to meet and advise me through all parts of my research for the past 5 years. In addition, I would like to specially thank her for allowing me to take on opportunities that helped me grow as a leader. Thank you for your support and all the time you have spent helping me move forward in this journey! Next, I would like to thank my undergraduate advisor, Dr. Juan G. Navea, for sparking my initial interest in research. Juan, thank you for being the most supportive mentor I could have asked for during my time at Skidmore as well as UCSD. By allowing me to join your lab when I knew nothing about atmospheric chemistry, you encouraged me to pursue a Ph.D. in chemistry, which is something I never knew was possible. Lastly, I would like to thank my mentor from my summer internship at Ionis, Parita. Parita, thank you for being so supportive and believing that I can do anything. I appreciate you working so hard to connect me with so many different people at Ionis to help me propel myself forward in my career.

Next, I would like to thank everyone I met during my time in the Grassian Group. Victor, thank you for teaching me everything I know about AFM-IR today and for being a great mentor in the group. Thank you for being patient with me and sitting through all of my presentations – I couldn't have gotten to where I am now without you! Steph and Kyle, thank you for sticking through all of this with me since Day 1! It's crazy to think that we all started out summer rotation together and now we are finishing up this program together. Mike and Izaac, thanks for always making the office a fun place to hang out in when we all needed a break from research. Mike, thanks for enabling my pottery and always finding the most random pottery things to spend my

money on. Izaac, thanks for always bringing in Pancha and all the dinner parties at your house! Ellen, thanks for always being so welcoming to me and for that period of grad school where we worked out together at the most insane times.

When I first moved to California 5 years ago, I stepped into this state not knowing a single person. During my Ph.D. journey, I have been blessed with meeting the most incredible, lifelong friends who truly have helped me grow into the person I am today. To start, I would like to acknowledge Steph, who is someone that has been with me through all of the thick and thin parts of grad school. Thank you for first my labmate, then workout buddy, co-outreach leader for SWIGS, co-dogsitter, roommate, and sister. You are such an inspiration, and I am looking forward to seeing all of the amazing things you will accomplish in your future. I am so lucky to have met you and grown with you over these past 5 years and can't wait to see what things come our way for the rest of our lives! I also want to thank Eric for sharing Steph with me and for unintentionally being our personal trainer! More importantly, however, thank you for always making me feel like you have my back in anything I do. Lastly, I would like to thank my partner, who has been a stable and unwavering support system for me. Thank you for always looking out for me, especially during the times when I can't do so myself and for always making me feel secure. Also, thank you for always feeding me with home-cooked meals.

I would also like to thank my friends Liana, Tay, and Haeun, who I met at the beginning of this program and have made countless memories with since. Liana, thank you for always being down to going on random, spontaneous food trips whether they're in San Diego or LA. Also, thank you for being my east-coast buddy and appreciating NY/NJ bagels with me. Tay, you are my raccoon buddy! We had such a fun time the first few years of grad school, and I'm so glad to have had those moments with you that really bonded us for the rest of our lives! Thank you for all of

our Sidecar doughnut runs – I'm really going to miss them! Haeun, you have been one of my biggest supporters since Day 1 and thank you for always being down to grab spicy Korean food and talking about family with me. I'm going to miss our food runs and conversation so much! Next, I would like to thank Sarah, who I initially met as Victor's undergrad in the Grassian Group but quickly developed into "the other loud person in the AFM room". Sarah, I'm so happy that we met and instantly bonded. I'm going to miss you and your welcoming family but most of all, Cletus and Cooder. Thank you for always letting me play with them when I'm in need of puppy therapy. I'm so excited to see what you'll be doing in this next chapter of your life! Outside of my Ph.D. program, I was blessed to have met, Raksha, who was my roommate for the first 4 years of my time in San Diego. Raksha, you are truly one of the best things that UCSD has done and I'm so happy to have made a lifelong friend from what was initially a random assignment. I'm so proud of you and honored to have seen you grow as a person and as a doctor during our 4 years together.

Lastly, I would like to thank my family for staying safe and healthy and, providing me the space to complete this degree. Adding on another 5 years of school after 4 years of undergrad is a lot of time, and I appreciate each and every one of you for never forgetting to remind me how proud you are of me. Thank you to my dad and my mom for always reminding me of my accomplishments and helping me out whenever I need. Thank you to my umma and stepdad in Korea for always sending my massive care packages filled with snacks every once in a while. Thank you to my brother for taking on a lot more responsibilities on the East Coast for the past 5 years. Most importantly, thank you to my halmoni for sticking through these 5 years and never losing the smile on her face. I can't wait to come back home and make up for some of that lost time with you! I would also like to thank my cousins, who never know what I am doing but are always so happy to cheer me on. And lastly, I would like to thank my partner's family – Cat, Uppa,

Andy, Sarah, Jamy, Wilson, Calvin, Gloria, and Ava for always making me so welcome and creating another home away from home for me in California.

Chapter 3, in full, is a reprint of the material as it appears in ACS Earth and Space Chemistry, 2021. Kim, D.; Grassian, V. H. The dissertation author was the primary investigator and author of this paper.

Chapter 4, in full, is a reprint of the material as it appears in Environmental Science: Processes and Impacts, 2023. Kim, D.; Grassian, V. H. The dissertation author was the primary investigator and author of this paper.

Chapter 5, contains unpublished material coauthored with Townsley, S. and Grassian, V. H. The dissertation author was the primary investigator and author of this paper.

Chapter 6 contains a compilation of published and unpublished material co-authored with Kaluarachchi, C., Goodman, A., Kutchko, B, Townsley, S., and Grassian, V. H. The dissertation author was one of the co-authors for some of the studies presented in this chapter.

VITA

2018 Bachelor of Arts in Chemistry, Skidmore College

2020 Master of Science in Chemistry, University of California San Diego

2023 Doctor of Philosophy in Chemistry, University of California San Diego

PUBLICATIONS

Farmer, D. K., Vance, M. E., Poppendieck, D., Mayer, K., Li, J., Link, M., Ditto, J., Webb, M., Morrison, G., Turpin, B., **Kim, D.**, Grassian, V. H., O'Brien, R., Collins, D. Pandit, S., Kroll, J., Mael, L., Alves, M., Goldstein, A. The Chemical Assessment of Surfaces and Air (CASA) Study: Using chemical perturbations in a test house to investigate indoor processes. 2023. In preparation.

Kim, D., Townsley, S., Kutchko, B., Goodman, A., Grassian V. H. Interaction of Hydrogen with Shale: Potential Implications for Subsurface Hydrogen Storage. 2023. In preparation.

Madawala, C. K., Molina, C., **Kim, D.**, Leibensperger III, R., Mehndiratta, L., Lee, J., Dinasquet, J., Malfatti, F., Prather, K. A., Deane, G., Stokes, D., Lee, C., Grassian, V. H., Tivanki, A. V. The Effects of Wind Speed on Size-Dependent Morphology and Composition of Nascent Sea Spray Aerosols. 2023. In preparation.

Molina, C., **Kim, D.**, Grassian, V. H. A Comparison of Different Vibrational Spectroscopic Probes (ATR-FTIR, O-PTIR, Raman, and AFM-IR) of Lipids and Other Compounds Found in Environmental Samples: Case Study – Sea Spray Aerosols. 2023. In preparation.

Kim, D., Townsley, S., Grassian, V.H. Vibrational Spectroscopy as a Probe of Geochemical Thin Films and Single Particle on Macro, Micro, and Nanoscales. 2023. Submitted.

Kim, D., Grassian, V.H. Analysis of Micro- and Nanoscale Heterogeneities within Environmentally Relevant Thin Films Containing Biological Components, Oxyanions and Minerals Using AFM-PTIR Spectroscopy. *Environmental Science: Processes and Impacts.* 2023.

Kaluarachchi, C. P.; Or, V. W.; Lan, Y.; Hasenecz, E. S.; **Kim, D.**; Madawala, C. K.; Dorcé,

G. P.; Mayer, K. J.; Sauer, J. S.; Lee, C.; Cappa, C. D.; Bertram, T. H.; Stone, E. A.; Prather, K. A.; Grassian, V. H.; Tivanski, A. V. Effects of Atmospheric Aging Processes on Nascent Sea Spray Aerosol Physicochemical Properties. *ACS Earth & Space Chemistry.* 2022.

Kim, D., Grassian, V.H. ATR-FTIR and AFM-IR Spectroscopic Investigation of Suwannee River Fulvic Acid and Its Interactions with α– FeOOH. *ACS Earth and Space Chemistry.* 2021.

Or, V. W., Wade, M., Patel, S., Alves, M. R., **Kim, D.**, Schwab, S., Przelomski, H., O'Brien, R., Rim, D., Corsi, R. L., Vance, M. E., Farmer, D. K., Grassian, V. H. Glass surface evolution following gas adsorption and particle deposition from indoor cooking events as probed by microspectroscopic analysis. *Environmental Science: Processes & Impacts.* 2020.

ABSTRACT OF THE DISSERTATION

Development of micro-spectroscopic tools for analysis of environmental interfaces

by

Deborah Kim

Doctor of Philosophy in Chemistry

University of California San Diego, 2023

Professor Vicki H. Grassian, Chair

Interfacial chemistry is important in many key molecular processes that are critical to water quality and treatment and can also drive the fate and transport of chemical contaminants in the environment. There are three key constituents of these environmentally-relevant water systems that are well-known to interact with geochemical interfaces: organic matter, oxyanions, and biological components. Mineral surfaces in particular are extremely diverse in composition and structure; they can include iron oxides, clay minerals, and carbonates. Therefore, these different

geochemical interfaces present a complex array of surface compositions and structures whereby surface catalyzed reactions can occur and potential byproducts can lead to chemical contaminants in the environment.

Traditional IR spectroscopy has offered valuable information in understanding how environmental adsorbates interact with mineral surfaces. The reason for this is due to the inherent molecular-level information that can be obtained due to changes in the vibrational mode frequencies for adsorbed versus solution phase species. To date, there still remains a bit of uncertainty with how individual components interact both as isolated components and when co-adsorbed with other species and the degree to which there is heterogeneity within these systems. In this dissertation, micro-spectroscopic probes such as Atomic Force Microscopy-Infrared (AFM-IR) spectroscopy and Optical Photothermal Infrared (O-PTIR) spectroscopy are compared to more traditional infrared methods in order to provide insights and a different perspective on these interactions as they probe both morphology and spectral signals with submicron spatial resolution. Overall, these novel studies have shown that micro-spectroscopic probes offer new insights into the chemistry occurring on solid mineral surfaces in the environment and provide examples of how these techniques can be used in future work.

CHAPTER 1
INTRODUCTION

1.1 Geochemical Interfaces Are Complex and Are Composed of a Large Diversity of Compounds

According to a 2019 WHO/UNICEF report, 2.2 billion people in this world lack access to clean water, and recently, it was suggested that we are entering an "invisible" water pollution crisis.[1–3] At the core of human survival and socio-economic growth, water quality has grown to become a universal topic of interest. Over the past few decades, this issue has significantly grown all across the world, whether it means some having too much water due to flooding or too little water from droughts.[4] While scientists and engineers have worked to combat this growing issue in efforts to make clean water accessible, most of these efforts have been concentrated in large-scale projects. For example, membrane technology has been developed to utilize membrane filters for treating large volumes of water from various aquatic sources.[5,6] However, to date, there still lacks an understanding of much of the chemistry that occurs in these types of water systems, and, as chemists, one approach that can be taken is looking into the surface chemistry.[7]

Surface chemistry plays an important and key role as molecular processes drive the fate and transport of chemicals present in water systems and is related to the interaction with natural and engineered surfaces.[8] Due to the complex nature of reactions at interfaces, this chemistry can be difficult to understand and model. As such, understanding the many different types of molecular-level interactions occurring on complex geochemical interfaces is daunting yet important as these interactions control and influence many environmental processes. The chemical interactions between adsorbed water and environmental interfaces have been widely explored;

however, there still lacks an understanding regarding the adsorption of other environmentally-relevant compounds onto these geochemical interfaces.[9] There are three key components that have been known to interact with geochemical interfaces: organic matter, oxyanions, and biological components.[10,11]

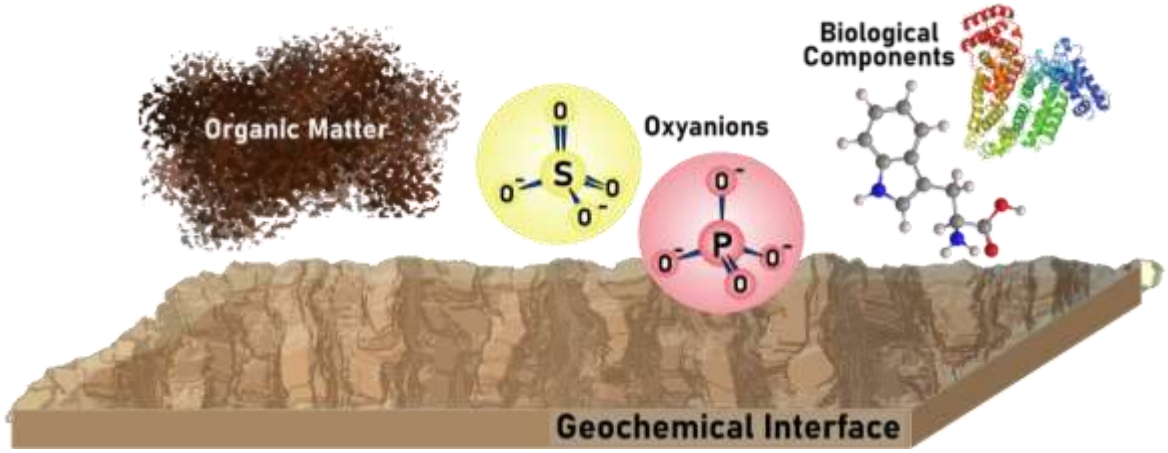

Figure 1.1 A cartoon diagram depicting the different types of environmentally relevant adsorbates available to interact with geochemical interfaces.

To start, a "geochemical interface" can be defined broadly as a mineral surface present in complex aqueous systems that can be found in various environments, such as groundwater or soil. A broad, general term such as "geochemical interfaces" allows for the encompassing of a wide range of minerals, chemical compounds and environmental conditions. Geochemical interfaces are extremely diverse in not only composition but also structure. To name a few examples, they can include mineral oxides such as iron, aluminum, titanium, and silicon oxides, as well as clay minerals and carbonates. While it is important to understand the type of interactions occurring along geochemical interfaces, it is important that we understand the properties and relevance of such materials.

Mineral oxides are often found naturally, but also as a result of being leached from anthropogenic sources such as landfills or consumer products.[12,13] Hematite and goethite are examples of iron oxides and oxyhydroxides, respectively, are the most commonly found naturally occurring mineral oxide, namely due to its large abundance of Earth's composition.[14–20] Iron's prevalence on Earth allows for it to play an important role in a wide range of atmospheric systems. Mineral dust aerosols, which can be transported in the atmosphere thousands of miles from the source region, can be dry or wet deposited onto different ecosystems, where they can provide important nutrients and drive biogeochemical cycles.[17,18,21–23] Mineral dust aerosols are a complex mixture of minerals and secondary species due to reactions in the atmosphere with trace atmospheric gases including sulfur and nitrogen oxides. Some common mineral oxides found in mineral dust aerosols are TiO_2, SiO_2, and Al_2O_3.[24,25] TiO_2 is an active interface for environmental reactions, as it contains surface hydroxyl groups that are readily available for surface interactions and is a semiconductor photocatalyst. In addition, TiO_2 has great industrial importance since it is found in building structures but often in human personal care products such as sunscreen.[13,17,26] Like titanium dioxide and some carbonates, the various polymorphs and forms of silicon dioxide are present in industrial materials such as window glass or buildings but also naturally occurring in minerals, in the form of quartz.[17,18,26] The acidic and basic properties of mineral oxides allow them to participate in a wider variety of chemical reactions, e.g. aluminum and magnesium oxides.[25,27] In some cases, as already noted for TiO_2, mineral oxides have also been found to act as photocatalysts, making them sensitive to environmental variables such as light.[28] All of these types of geochemical interfaces have been found to interact with various components present in water systems including organic matter, oxyanions, and biological components.[12,29,30] In addition,

they react with chemical contaminants that can cause surface catalyzed reactions, forming undesired byproducts.[31]

Natural organic matter (NOM) represents a large class of compounds that originate from plants, animals, and microbial debris commonly found in both aquatic and terrestrial systems. These complex molecules contain a variety of functional groups that are active in interfacial chemistry.[32] Suwannee River Fulvic Acid (SRFA) is a type of fulvic acid collected from the Suwannee River in Georgia. It has a smaller molar mass and is more soluble than its equally abundant counterpart, humic acid. This species is commonly used as a model fraction of natural organic matter.[33,34] Like most natural organic matter compounds, SRFA contains a myriad of aliphatic carbon chains, as well as carboxylic and phenolic functional groups and is thus, known to be highly complex and heterogenous by nature.[35] Previous studies have focused on the surface adsorption of this species on both oxide and oxyhydroxide iron surfaces. For example, the adsorption of fulvic acid, a type of natural organic matter (NOM), onto iron-containing mineral surfaces has been reported to form metal-bonded surface complexes in acidic environments over basic environments[36–38]. While studies involving single-component systems have thus far provided great insight into some of the chemical interactions occurring on the molecular level, the environment is a complex, multi-component system and it is important to investigate the complex mixtures as well as described in this thesis.

In addition to natural organic matter, minerals interact with various components such as biological macromolecules and oxyanions in groundwater.[7,8,10,39] For biological components, Bovine Serum Albumin (BSA) has been chosen as a model protein to represent this class of adsorbates due to its stability in the environment as well as its natural state in a circumneutral pH.[40–42] In addition, BSA is low in cost, accessible, and similar to human protein.[40–42] It is also

water-soluble and available at high purity, allowing for laboratory experiments to be conducted easily and efficiently. While there have been a great number of studies involving BSA and its pH dependency for adsorption on nanoparticle and geochemical interfaces, there is still remain questions regarding this protein's chemical interactions on the molecular level with these geochemical surfaces.[40,41,43–45] Other classes of biological components known to interact with minerals are biofilms, which have been found to grow on various metal-containing solid surfaces.[46,47] It should be noted that the class of biological components encompasses many different forms, starting from amino acids and protein to macromolecular structures like biofilms.

For oxyanions, sulfates have been chosen as they are highly abundant in groundwater and soil-containing environments.[48] Common environmentally-relevant oxyanions include sulfates such as sodium sulfate and ammonium sulfate, and nitrates, such as sodium nitrate.[49–51] These species can also affect radiative processes by making up cloud condensation nuclei, which can scatter light, or reflect sunlight, resulting in a cooling effect.[52,53] In addition, these species can also act as common adsorbates and can compete for sites on mineral surfaces.[54,55] Lastly, oxyanion derivatives such as sulfates and nitrates are also present in mineral dust aerosols. These particles can undergo heterogenous reactions in the atmosphere that can result in the formation of sulfate or nitrate coatings that drive different atmospheric processes.[27,49,50]

To date, there still remains a bit uncertainty with how individual components behave in more complex media and the degree to which there is heterogeneity within these complex systems, especially on the nano and microscale level and this thesis probes these different length scales as described in the next section.

1.2 The Development and Need for Microspectroscopic Probes

Vibrational spectroscopy is a tool that has been used for decades to study and understand the complex chemical reactions present in environmental systems. This technique can probe unique chemical signatures that can accurately and easily characterize a wide variety of chemical species. A more comprehensive mechanistic understanding of the processes the chemical species undergo is achieved by monitoring peak shape, position, and relative intensity of chemical spectra. This is extremely important, as these molecular mechanisms are at the forefront of chemical reactions occurring along geochemical interfaces. Over the past few decades, a great deal of the current literature has made valuable observations with traditional macroscopic spectroscopic studies.[29,30,56] However, limiting some of the current understanding we have on the chemistry occurring in these environmental systems is more specialized tools needed to probe complex interfaces. Most recently, the emerging technology and development of microspectroscopic probes have been found to be able to shed light and provide a different but equally useful perspective on these reactions.[57–61]

Traditional IR spectroscopy has offered valuable information in understanding how these environmental adsorbates interact with mineral species. The reason for this is due to the molecular nature of the chemistry occurring on these environmental surfaces. One particular method that is commonly used in this field of work is Attenuated Total Reflection - Fourier Transform Infrared (ATR-FTIR) spectroscopy. In short, ATR-FTIR spectroscopy is a vibrational spectroscopic technique based on the total internal reflection of an IR beam at the boundary between two media. This total internal reflection allows for high-resolution chemical spectra to be achieved for chemical characterization of both known and unknown samples.[29,30,56] Specifically, ATR-FTIR spectroscopy has been a useful tool for probing mineral surfaces and their interactions with

different compounds found in groundwater providing insights on surface speciation, surface conformation and surface chemistry.[29,56,62,63]

ATR-FTIR spectroscopy provides spectral characterization of thin films and surface adsorption onto these films. This information can be used to deduce specific molecular mechanisms of different processes.[29,62] However, further insights into the nano and microscale measurements can provide information about phase segregation, degree of interactions, and the overall nano and microscale heterogeneities observed in these systems. In efforts to achieve this type of information, there have been complementary studies utilizing both IR or Raman spectroscopy and microscopy to gather both physical and chemical information on the single particle level.[64–66] Microspectroscopic tools have proven to be crucial in understanding and defining the distribution of components within complex environmental samples. They provide both chemical and spatial information that could give some insights into the chemistry that occurs at the molecular level on these interfaces, in a single instrument. In this dissertation, a total of two different microspectroscopic probes, AFM-IR and O-PTIR spectroscopy, are utilized and compared with a traditional IR spectroscopic technique, ATR-FTIR spectroscopy. A summary of the three spectroscopic techniques as well as their respective instruments is shown in Figure 1.2.

Atomic Force Microscopy –Infrared (AFM-IR) spectroscopy is a hybrid technique that combines the nanoscale spatial resolution of AFM with the chemical analysis capability of IR spectroscopy by using the cantilever tip as the detector for IR absorbance. Current work utilizing this technique has been mainly applied to systems in polymers, materials as well as life sciences.[58,67] However, to date, AFM-IR spectroscopy has yet to be applied to geochemical substrates despite their diversity in size, composition, and structure. The majority of environmental applications of AFM-IR spectroscopy has been focused in microplastics research.[58,67–69] While

microplastics are a growing concern in aquatic systems, much of the chemistry occurring in the environments in which they are found such as geochemical interfaces, are crucial to understand since they contribute to the fate of such contaminants over time. With proper development for analysis of environmental systems, this technique can provide valuable information on phase segregation, degree of interactions and the overall nanoscale heterogeneities present in complex systems.[58,67,70] Data collected from the nanoIR2 system can include high-resolution nanoscale images, nanoscale point spectra, functional group maps, as well as hyperspectral maps.

Optical Photothermal Infrared (O-PTIR) spectroscopy is one of the newest microspectroscopic tools based upon the phenomenon of photothermal expansion of a sample upon illumination of light, that has been developed to probe these complex samples and is. Unlike AFM-IR spectroscopy, which converts the deflection of the cantilever from this expansion to IR absorbance signal, O-PTIR spectroscopy translates this expansion as a change in the refractive index of the sample.[71] By using a visible light source that is collinear to the IR laser beam as the probe, an O-PTIR signal is generated when this modulated probe beam is reflected back to the detector. In addition, Raman spectra can also be collected simultaneously, which significantly broadens the number of samples that can be analyzed with this single instrument.[72–75]

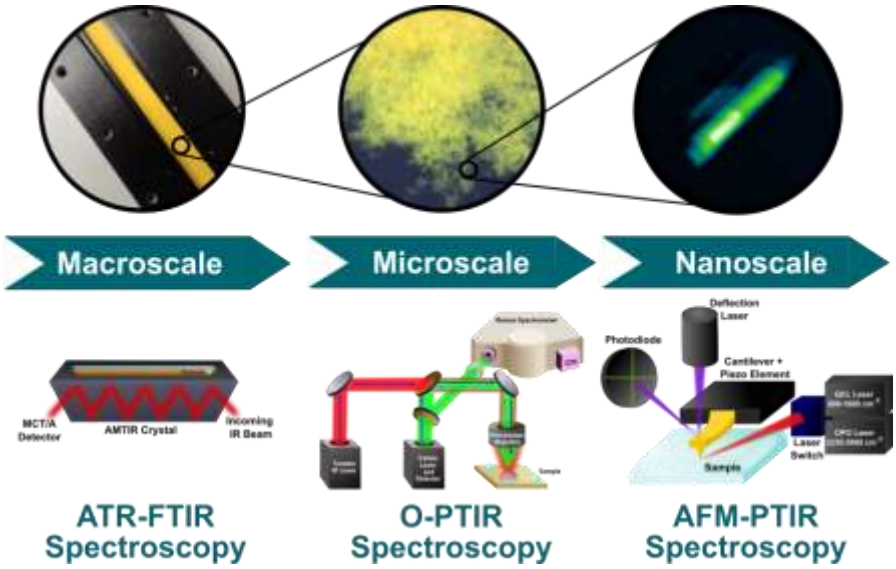

Figure 1.2 Three different techniques – ATR-FTIR, O-PTIR, and AFM-IR spectroscopy - provide valuable chemical and physical information on three different length scales – macroscale, microscale, and nanoscale.

Another big advantage of the mIRage-Raman is its ability to operate as a non-contact technique, meaning that sample preparation is minimal. This allows for thick, rough, and poorly adhered samples to be analyzed, which are some of the limitations encountered using AFM-IR spectroscopy on these complex samples. It is important to note that while the resolution of the mIRage-Raman is sub-micron, if nanoscale spatial resolution is necessary, the AFM-IR spectrometer can be used complementarily. Furthermore, chemical spectral characterization can be confirmed with the ATR-FTIR spectrometer. Due to these capabilities, the potential for these instruments is limitless. Researchers can analyze highly complex field samples on various substrates that cover a wide range of substrate thickness and roughness such as silica wafers, glass, and gypsum. By using microspectroscopic probes the physicochemical properties of these films, on both the nano and microscale, and how these properties change in the presence of different environmental factors can be successfully probed.

The focus of this dissertation research is on developing microspectroscopic tools for the analysis of environmental interfaces on both nanometer and micrometer length scales. These interfaces include mineral surfaces and their interactions with different chemical and biological species found in groundwater including dissolved organic matter, biological macromolecules, and oxyanions.

1.3 Thesis Objective

The research presented in this dissertation provides insight into the potential of microspectroscopic techniques for analysis of complex environmental systems. Two different microspectroscopic techniques are discussed extensively in this work: Atomic Force Microscopy-Infrared (AFM-IR) spectroscopy and Optical-Photothermal Infrared (O-PTIR) spectroscopy.

Chapter 2 describes, in detail, the various instrumentation and experimental methods used for studies presented in this dissertation. In addition, there are theoretical descriptions of Attenuated Total Reflection-Fourier Transform Infrared (ATR-FTIR), O-PTIR, AFM-IR, and Raman spectroscopy of the instrumentation and experimental methods used in this study. A materials table is also provided listing the sources and descriptions of materials used for experimental studies.

Chapter 3 compares the interaction of Suwannee River Fulvic Acid (SRFA), a representative class of organic matter, and geochemical interfaces, such as goethite, probed by ATR-FTIR and AFM-IR spectroscopy. SRFA interactions with goethite has been an interaction studied for decades using traditional IR spectroscopic techniques. By directly comparing information we can obtain from utilizing ATR-FTIR spectroscopy with that from AFM-IR

spectroscopy, we see that this widely known interaction is much more heterogenous than thought to be. With AFM-IR spectroscopy, we have elucidated these interactions on a single particle scale and show how at the nanoscale level, SRFA does not coat goethite nanoparticles evenly, as it also is seen to interact with itself.

Chapter 4 explores the use of AFM-IR spectroscopy in multi-component environment. In all environmental systems, there exists a myriad number of compounds and components that contribute to the chemistry that occurs along the geochemical interface. These compounds can include biological components, oxyanions, and organic matter. Chapter 3 discusses the interaction of organic matter with goethite, so in this chapter, the interactions of a model protein, BSA, with sodium sulfate, a representative oxyanion, with goethite, is investigated. From analysis with AFM-IR spectroscopy, phase segregation as well as both physical and chemical microscale and nanoscale heterogeneities have been detected.

Chapter 5 extends the potential of microspectroscopic probes *via* introduction of a new technique called O-PTIR spectroscopy. Here, a comprehensive analysis of ATR-FTIR, O-PTIR, AFM-IR, and Raman spectroscopy is completed for different compounds and representative of minerals including oxides, carbonates, sulfates and nitrates, aluminosilicates, and complex, heterogenous samples. Overall, these analyses depict the clear benefits and downsides of analyzing compounds on the macro, micro, and nanoscale level.

Chapter 6 summarizes a collaborative study using these novel techniques. This includes investigating the impact of injecting hydrogen gas into shale rock samples. While the heterogeneity of shale is widely known, the chemical and physical properties have not been studied extensively with microspectroscopic probes. Utilizing a combination of these methodologies can result in potential implications of subsurface hydrogen storage for shale samples that can help in uncovering

some of its complexities. Upon reaction with hydrogen gas, Eagle Ford, a type of shale, has been observed to reduce the naturally abundant carbonates present in the sample as well as form pyrite, a mineral containing iron sulfides.

Chapter 7 compiles three other studies that utilized these different microspectroscopic probes as a complementary technique. This includes the application of AFM-IR spectroscopy is seen to be extremely useful for three major field campaigns. Two campaigns focused on outdoor chemistry and the chemistry of substrate deposited sea spray aerosols, and one campaign focused on indoor chemistry from wildfire smoke. The three campaigns are named Sea Spray Chemistry and Particle Evolution (SeaSCAPE), Characterizing Atmospheric-Oceanic parameters of SOARS (CHAOS), and Chemical Assessment of Surfaces and Air (CASA). The ability to look at single particles onto various substrates can provide a more complete understanding of the composition and complex chemistry occurring within these systems.

1.4 Bibliography

(1) *Drinking Water*. https://www.who.int/news-room/fact-sheets/detail/drinking-water (accessed 2023-06-06).

(2) *Progress on Drinking Water, Sanitation and Hygiene Update and SDG Baselines*; 2017.

(3) *'Invisible' crisis of water quality threatens human and environmental well-being*. https://news.un.org/en/story/2019/08/1044551 (accessed 2023-06-06).

(4) Myers, D. N. *Why Monitor Water Quality?* https://www.epa.gov/assessing (accessed 2023-06-05).

(5) Ezugbe, E. O.; Rathilal, S. Membrane Technologies in Wastewater Treatment: A Review. *Membr.* **2020**, *10 (89)*, 1-28.

(6) Tang, M.; Cziczo, D. J.; Grassian, V. H. Interactions of Water with Mineral Dust Aerosol: Water Adsorption, Hygroscopicity, Cloud Condensation, and Ice Nucleation. *Chem. Rev*. **2016**, *116* (7), 4205–4259.

(7) Jury, W. A.; Vaux, H. The Role of Science in Solving the World's Emerging Water Problems. *PNAS* **2005**. 102 (44), 15715-15720.

(8) Somorjai, G. A.; Li, Y. Impact of Surface Chemistry. PNAS, **2010**, *108* (3) 917-924.

(9) Rubasinghege, G.; Grassian, V. H. Role(s) of Adsorbed Water in the Surface Chemistry of Environmental Interfaces. *Chem. Commun.* **2013**, *49*, 3071-3094.

(10) Bertsch, P. M.; Seaman, J. C. Characterization of Complex Mineral Assemblages: Implications for Contaminant Transport and Environmental Remediation. *PNAS* **1999**, *96* (7), 3350–3357.

(11) Kim, D.; Grassian, V. H. Analysis of Micro- and Nanoscale Heterogeneities within Environmentally Relevant Thin Films Containing Biological Components, Oxyanions and Minerals Using AFM-PTIR Spectroscopy. *Environ. Sci. Process Impacts* **2023**, *25* (3), 484-495.

(12) Sit, I.; Wu, H.; Grassian, V. H. Environmental Aspects of Oxide Nanoparticles: Probing Oxide Nanoparticle Surface Processes Under Different Environmental Conditions. *Ann. Rev. Anal. Chem.* **2021**, *14*, 489-514.

(13) Song, W.; Li, G.; Grassian, V. H.; Larsen, S. C. Development of Improved Materials for Environmental Applications: Nanocrystalline NaY Zeolites. *Environ. Sci. Technol.* **2005**, *39* (5), 1214–1220.

(14) Kok, J. F.; Storelvemo, T.; Kaydis, V. A.; Adebiyi, A. A.; Mahowald, N. M.; Evan, A. T.; He, C.; Leung, D. M. Mineral Dust Aerosol Impacts on Global Climate and Climate Change. *Nat. Rev. Earth Environ.* **2023**, *4*, 71–86.

(15) Brown, G. E.; Henrich, V. E.; Casey, W. H.; Clark, D. L.; Eggleston, C.; Felmy, A.; Goodman, D. W.; Grätzel, M.; Maciel, G.; McCarthy, M. I.; Nealson, K. H.; Sverjensky, A.; Toney, M. F.; Zachara, J. M. Metal Oxide Surfaces and Their Interactions with Aqueous Solutions and Microbial Organisms. *Chem. Rev.* **1999**, *99*, 77-174.

(16) Gao, J.; Mikutta, R.; Jansen, B.; Guggenberger, G.; Vogel, C.; Kalbitz, K. The Multilayer Model of Soil Mineral–Organic Interfaces—a Review. *J. Plant Nutr. Soil Sci*. **2020**, *183* (1), 27–41.

(17) Cwiertny, D. M.; Hunter, G. J.; Pettibone, J. M.; Scherer, M. M.; Grassian, V. H. Surface Chemistry and Dissolution of α-FeOOH Nanorods and Microrods: Environmental Implications of Size-Dependent Interactions with Oxalate. *J. Phys. Chem. C* **2009**, *113* (6), 2175–2186.

(18) Cwiertny, D. M.; Handler, R. M.; Schaefer, M. V.; Grassian, V. H.; Scherer, M. M. Interpreting Nanoscale Size-Effects in Aggregated Fe-Oxide Suspensions: Reaction of Fe (II) with Goethite. *Geochim. Cosmochim. Acta* **2008**, *72* (5), 1365–1380.

(19) Song, X.; Boily, J. F. Structural Controls on OH Site Availability and Reactivity at Iron Oxyhydroxide Particle Surfaces. *Phys. Chemis. Chem. Physics* **2012**, *14* (8), 2579–2586.

(20) Song, X.; Boily, J. F. Water Vapor Adsorption on Goethite. *Environ. Sci. Technol.* **2013**, *47* (13), 7171–7177.

(21) Waychunas, G. A.; Kim, C. S.; Banfield, J. F. Nanoparticulate Iron Oxide Minerals in Soils and Sediments: Unique Properties and Contaminant Scavenging Mechanisms. In *J. Nanopart. Res*. **2005**, *7*, 409–433.

(22) Bhattacharyya, A.; Schmidt, M. P.; Stavitski, E.; Martínez, C. E. Iron Speciation in Peats: Chemical and Spectroscopic Evidence for the Co-Occurrence of Ferric and Ferrous Iron in Organic Complexes and Mineral Precipitates. *Org. Geochem.* **2018**, *115*, 124–137.

(23) Hwang, H. J.; Ro, C. U. Direct Observation of Nitrate and Sulfate Formations from Mineral Dust and Sea-Salts Using Low-Z Particle Electron Probe X-Ray Microanalysis. *Atmos. Environ.* **2006**, *40* (21), 3869–3880.

(24) Usher, C. R.; Michel, A. E.; Grassian, V. H. Reactions on Mineral Dust. *Chem. Rev.* **2003**, *103* (12), 4883–4939.

(25) Goodman, A. L.; Underwood, G. M.; Grassian, V. H. Heterogeneous Reaction of NO_2: Characterization of Gas-Phase and Adsorbed Products from the Reaction, $2NO_2(g) + H_2O(a) \rightarrow HONO(g) + HNO_3$ (a) on Hydrated Silica Particles. *J. Phys. Chem. A* **1999**, *103* (36), 7217–7223.

(26) Sobanska, S.; Hwang, H.; Choël, M.; Jung, H. J.; Eom, H. J.; Kim, H.; Barbillat, J.; Ro, C. U. Investigation of the Chemical Mixing State of Individual Asian Dust Particles by the Combined Use of Electron Probe X-Ray Microanalysis and Raman Microspectrometry. *Anal. Chem.* **2012**, *84* (7), 3145–3154

(27) Goodman, A. L.; Li, P.; Usher, C. R.; Grassian, V. H. Heterogeneous Uptake of Sulfur Dioxide on Aluminum and Magnesium Oxide Particles. *J. Phys. Chem. A* **2001**, *105* (25), 6109–6120.

(28) Yu, Z.; Jang, M.; Park, J. Modeling Atmospheric Mineral Aerosol Chemistry to Predict Heterogeneous Photooxidation of SO_2. *Atmos. Chem. Phys.* **2017**, *17* (16), 10001–10017.

(29) Mudunkotuwa, I. A.; Grassian, V. H. Biological and Environmental Media Control Oxide Nanoparticle Surface Composition: The Roles of Biological Components (Proteins and Amino Acids), Inorganic Oxyanions and Humic Acid. *Environ. Sci. Nano.* **2015**, *2* (5), 429–439.

(30) Mudunkotuwa, I. A.; Minshid, A. Al; Grassian, V. H. ATR-FTIR Spectroscopy as a Tool to Probe Surface Adsorption on Nanoparticles at the Liquid-Solid Interface in Environmentally and Biologically Relevant Media. *Analyst* **2014**, *139* (5), 870–881.

(31) O'Day, P. A. Molecular Environmental Geochemistry. *Rev. of Geophys.* **1999**, *37* (2), 249–274.

(32) Islam, M. A.; Morton, D. W.; Johnson, B. B.; Angove, M. J. Adsorption of Humic and Fulvic Acids onto a Range of Adsorbents in Aqueous Systems, and Their Effect on the Adsorption of Other Species: A Review. *Sep. Purif. Technol.* **2020**, *247* (116949), 1-19.

(33) Weng, L.; Van Riemsdijk, W. H.; Koopal, L. K.; Hiemstra, T. Adsorption of Humic Substances on Goethite: Comparison between Humic Acids and Fulvic Acids. *Environ. Sci. Technol.* **2006**, *40* (24), 7494–7500.

(34) Jayalath, S.; Larsen, S. C.; Grassian, V. H. Surface Adsorption of Nordic Aquatic Fulvic Acid on Amine-Functionalized and Non-Functionalized Mesoporous Silica Nanoparticles. *Environ. Sci. Nano.* **2018**, *5* (9), 2162–2172.

(35) Ritchie, J. D.; Michael Perdue, E. Proton-Binding Study of Standard and Reference Fulvic Acids, Humic Acids, and Natural Organic Matter. *Geochim. Cosmochim. Acta* **2003**, *67* (1), 85–96.

(36) Filius, J. D.; Lumsdon, D. G.; Meeussen, J. C. L.; Hiemstra, T.; Van Riemsdijk, W. H. Adsorption of Fulvic Acid on Goethite. *Geochim. Cosmochim. Acta* **2000**, *64* (1), 51–60.

(37) Yoon, T. H.; Johnson, S. B.; Gordon, E. B. Adsorption of Suwannee River Fulvic Acid on Aluminum Oxyhydroxide Surfaces: An in Situ ATR-FTIR Study. *Lang.* **2004**, *20* (14), 5655–5658.

(38) Yang, K.; Xing, B. Interactions of Humic Acid with Nanosized Inorganic Oxides. *Env. Poll.* **2009**, *157* (4), 1095–1100.

(39) Hazen, R. M.; Sverjensky, D. A. Mineral Surfaces, Geochemical Complexities, and the Origins of Life. *Cold Spring Harb. Perspect. Biol.* **2010**, *2* (5), 1-21.

(40) Schmidt, M. P.; Martínez, C. E. Supramolecular Association Impacts Biomolecule Adsorption onto Goethite. *Environ. Sci. Technol.* **2018**, *52* (7), 4079–4089.

(41) Xu, Z.; Grassian, V. H. Bovine Serum Albumin Adsorption on TiO_2 Nanoparticle Surfaces: Effects of pH and Coadsorption of Phosphate on Protein-Surface Interactions and Protein Structure. *J. Phys. Chem. C* **2017**, *121* (39), 21763–21771.

(42) Phan, H. T. M.; Bartelt-Hunt, S.; Rodenhausen, K. B.; Schubert, M.; Bartz, J. C. Investigation of Bovine Serum Albumin (BSA) Attachment onto Self-Assembled Monolayers (SAMs) Using Combinatorial Quartz Crystal Microbalance with Dissipation (QCM-D) and Spectroscopic Ellipsometry (SE). *PLoS One* **2015**, *10* (10), 1-20.

(43) Servagent-Noinville, S.; Revault, M.; Quiquampoix, H.; Baron, M. H. Conformational Changes of Bovine Serum Albumin Induced by Adsorption on Different Clay Surfaces: FTIR Analysis. *J. Coll. Int. Sci.* **2000**, *221* (2), 273–283.

(44) Givens, B. E.; Diklich, N. D.; Fiegel, J.; Grassian, V. H. Adsorption of Bovine Serum Albumin on Silicon Dioxide Nanoparticles: Impact of p H on Nanoparticle–Protein Interactions. *Biointerph.* **2017**, *12* (2), 1-9.

(45) Givens, B. E.; Xu, Z.; Fiegel, J.; Grassian, V. H. Bovine Serum Albumin Adsorption on SiO_2 and TiO_2 Nanoparticle Surfaces at Circumneutral and Acidic pH: A Tale of Two Nano-Bio Surface Interactions. *J. Coll. Int. Sci.* **2017**, *493*, 334–341.

(46) Tuck, B.; Watkin, E.; Somers, A.; Machuca, L. L. A Critical Review of Marine Biofilms on Metallic Materials. *NPJ Mat. Degrad*. **2022**, *6* (25), 1-12.

(47) Procópio, L. The Role of Biofilms in the Corrosion of Steel in Marine Environments. *World J.Microbio.Biotech*. **2019**, *35* (73), 1-8.

(48) Hug, S. J. In Situ Fourier Transform Infrared Measurements of Sulfate Adsorption on Hematite in Aqueous Solutions. *J. Coll. Int. Sci.* **1997**, *188* (2), 415–422.

(49) Xu, C.; Deng, K.; Li, J.; Xu, R. Impact of Environmental Conditions on Aggregation Kinetics of Hematite and Goethite Nanoparticles. *J. Nanoparticle Res.* **2015**, *17* (10).

(50) Hoffman, R. C.; Laskin, A.; Finlayson-Pitts, B. J. Sodium Nitrate Particles: Physical and Chemical Properties during Hydration and Dehydration, and Implications for Aged Sea Salt Aerosols. *J. Aerosol Sci.* **2004**, *35* (7), 869–887.

(51) Maria, S. F.; Russell, L. M.; Turpin, B. J.; Porcja, R. J.; Campos, T. L.; Weber, R. J.; Huebert, B. J. Source Signatures of Carbon Monoxide and Organic Functional Groups in Asian Pacific Regional Aerosol Characterization Experiment (ACE-Asia) Submicron Aerosol Types. *J. Geophys. Res.: Atmos.* **2003**, *108* (23), 1-14.

(52) Hatch, C. D.; Gierlus, K. M.; Schuttlefield, J. D.; Grassian, V. H. Water Adsorption and Cloud Condensation Nuclei Activity of Calcite and Calcite Coated with Model Humic and Fulvic Acids. *Atmos. Environ.* **2008**, *42* (22), 5672–5684.

(53) Gibson, E. R.; Gierlus, K. M.; Hudson, P. K.; Grassian, V. H. Generation of Internally Mixed Insoluble and Soluble Aerosol Particles to Investigate the Impact of Atmospheric Aging and Heterogeneous Processing on the CCN Activity of Mineral Dust Aerosol. *Aerosol Sci. Tech.* **2007**, *41* (10), 914–924.

(54) Kim, D.; Grassian, V. H. Attenuated Total Reflection-Fourier Transform Infrared and Atomic Force Microscopy-Infrared Spectroscopic Investigation of Suwannee River Fulvic Acid and Its Interactions with α-FeOOH. *ACS Earth Sp. Chem.* **2022**, *6* (1), 81–89.

(55) Violante, A. Elucidating Mechanisms of Competitive Sorption at the Mineral/Water Interface. *Adv. in Agro.* **2013**, *118*, 111–176.

(56) Sit, I.; Wu, H.; Grassian, V. H. Environmental Aspects of Oxide Nanoparticles: Probing Oxide Nanoparticle Surface Processes Under Different Environmental Conditions. *Ann. Rev. Anal. Chem.* **2021**, *14*, 489-514.

(57) Dazzi, A.; Prater, C. B. AFM-IR: Technology and Applications in Nanoscale Infrared Spectroscopy and Chemical Imaging. *Chem. Rev.* **2016**, *117* (7), 5146–5173.

(58) Dazzi, A.; Prater, C. B.; Hu, Q.; Bruce, D.; Rabolt, J. F.; Marcott, C. Focal Point Review AFM-IR: Combining Atomic Force Microscopy and Infrared Spectroscopy for Nanoscale Chemical Characterization. *Appl. Spectrosc.* **2012**, *66* (12), 1365–1384.

(59) Kansiz, M.; Prater, C.; Dillon, E.; Lo, M.; Anderson, J.; Marcott, C.; Demissie, A.; Chen, Y.; Kunkel, G. Optical Photothermal Infrared Microspectroscopy with Simultaneous Raman – A New Non-Contact Failure Analysis Technique for Identification of <10 μm Organic Contamination in the Hard Drive and Other Electronics Industries. *Micros. Today* **2020**, *28* (3), 26–36.

(60) Klementieva, O.; Sandt, C.; Martinsson, I.; Kansiz, M.; Gouras, G. K.; Borondics, F. Super-Resolution Infrared Imaging of Polymorphic Amyloid Aggregates Directly in Neurons. *Adv. Sci.* **2020**, *7* (1903004), 1-9.

(61) Bondy, A. L.; Kirpes, R. M.; Merzel, R. L.; Pratt, K. A.; Banaszak Holl, M. M.; Ault, A. P. Atomic Force Microscopy-Infrared Spectroscopy of Individual Atmospheric Aerosol Particles: Subdiffraction Limit Vibrational Spectroscopy and Morphological Analysis. *Anal. Chem.* **2017**, *89* (17), 8594–8598.

(62) Mudunkotuwa, I. A.; Minshid, A. Al; Grassian, V. H. ATR-FTIR Spectroscopy as a Tool to Probe Surface Adsorption on Nanoparticles at the Liquid-Solid Interface in Environmentally and Biologically Relevant Media. *Analyst* **2014**, *139* (5), 870–881.

(63) Kim, D.; Grassian, V. H. Attenuated Total Reflection-Fourier Transform Infrared and Atomic Force Microscopy-Infrared Spectroscopic Investigation of Suwannee River Fulvic Acid and Its Interactions with α-FeOOH. *ACS Earth Sp. Chem.* **2022**, *6* (1), 81–89.

(64) Ro, C.-U.; Oh, K.-Y.; Kim, H.; Chun, Y.; Osán, J.; de Hoog, J.; Grieken, V. Chemical Speciation of Individual Atmospheric Particles Using Low-Z Electron Probe X-Ray Microanalysis: Characterizing "Asian Dust" Deposited with Rainwater in Seoul, Korea. *Atmos. Environ.* **2001**, *35* (29), 4995-5005.

(65) Li, W.; Shao, L.; Zhang, D.; Ro, C. U.; Hu, M.; Bi, X.; Geng, H.; Matsuki, A.; Niu, H.; Chen, J. A Review of Single Aerosol Particle Studies in the Atmosphere of East Asia: Morphology, Mixing State, Source, and Heterogeneous Reactions. *J. Cleaner Prod.*, **2016**, *112*, 1330–1349.

(66) Ro, C. U.; Hwang, H.; Kim, H.; Chun, Y.; Van Grieken, R. Single-Particle Characterization of Four "Asian Dust" Samples Collected in Korea, Using Low-Z Particle Electron Probe X-Ray Microanalysis. *Environ. Sci. Technol.* **2005**, *39* (6), 1409–1419.

(67) Dazzi, A.; Prater, C. B. AFM-IR: Technology and Applications in Nanoscale Infrared Spectroscopy and Chemical Imaging. *Chem. Rev.* **2016**, *117* (7), 5146–5173.

(68) Luo, H.; Xiang, Y.; Zhao, Y.; Li, Y.; Pan, X. Nanoscale Infrared, Thermal and Mechanical Properties of Aged Microplastics Revealed by an Atomic Force Microscopy Coupled with Infrared Spectroscopy (AFM-IR) Technique. *Sci. Tot. Env.* **2020**, *744*, 1-9.

(69) Weckhuysen, B.; Meirer, F.; Oord, R.; Zettler, E.; Van Sebille, E. Nanoscale Infrared Spectroscopy Reveals Nanoplastics at 5000 m Depth in the South Atlantic Ocean. *Phys. Sci.* **2021**, 1-14.

(70) Mathurin, J.; Pancani, E.; Deniset-Besseau, A. How to Unravel the Chemical Structure and Component Localization of Individual Drug-Loaded Polymeric Nanoparticles by Using Tapping AFM-IR. *Analyst* **2018**, *143*, 5940–5949.

(71) Zhang, D.; Li, C.; Zhang, C.; Slipchenko, M. N.; Eakins, G.; Cheng, J. X. Depth-Resolved Mid-Infrared Photothermal Imaging of Living Cells and Organisms with Submicrometer Spatial Resolution. *Sci. Adv.* **2016**, *2* (9), 1-7.

(72) Li, C.; Zhang, D.; Slipchenko, M. N.; Cheng, J. X. Mid-Infrared Photothermal Imaging of Active Pharmaceutical Ingredients at Submicrometer Spatial Resolution. *Anal. Chem.* **2017**. *89*, (9), 4863–4867.

(73) Bai, Y.; Zhang, D.; Lan, L.; Huang, Y.; Maize, K.; Shakouri, A.; Cheng, J. X. Ultrafast Chemical Imaging by Widefield Photothermal Sensing of Infrared Absorption. *Sci. Adv.* **2019**, *5* (7), 1-8.

(74) Li, X.; Zhang, D.; Bai, Y.; Wang, W.; Liang, J.; Cheng, J. X. Fingerprinting a Living Cell by Raman Integrated Mid-Infrared Photothermal Microscopy. *Anal. Chem.* **2019**, *91* (16), 10750-10756.

(75) Rindelaub, J. D.; Craig, R. L.; Nandy, L.; Bondy, A. L.; Dutcher, C. S.; Shepson, P. B.; Ault, A. P. Direct Measurement of PH in Individual Particles via Raman Microspectroscopy and Variation in Acidity with Relative Humidity. *J. Phys. Chem. A* **2016**, *120* (6), 911–917.

CHAPTER 2
EXPERIMENTAL METHODS

In this chapter, information about sources of chemicals and materials, sample preparation, and instrumentation is introduced and described in detail. In particular, the theory, method of operation, and components of Attenuated Total Reflectance-Fourier Transform Infrared (ATR-FTIR), Atomic Force Microscopy- Infrared (AFM-IR), Optical Photothermal Infrared (O-PTIR), and Raman spectroscopy are discussed. These have been the primary techniques used for the experiments presented in this dissertation.

2.1 Sources of Chemicals and Materials

Many of the experiments described in this thesis involve the formation of thin films of different minerals and varying environmentally relevant adsorbates. These substances range from humic substances to biological components as well as oxyanions. A comprehensive list of these materials and their respective sources, as well as the substrates they were deposited on, are summarized in Table 2.1 below.

Table 2.1 Summary of sources and information on chemicals and materials used for experiments presented in this dissertation.

Category	Minerals	CAS #	Source
Substrates	AMTIR Crystal	N/A	Pike Technologies
	CaF_2	N/A	Crystran Limited
	Silica Wafer	N/A	Ted Pella
Oxides	α-FeOOH	20344-49-4	Alfa Aesar
	α-Al_2O_3	1344-28-1	Alfa Aesar
	TiO_2 Anatase	13463-67-7	Nanostructured % Amorphous Materials Inc.
	Amorphous SiO_2	7631-86-9	Aldrich Chemistry
Carbonates, Sulfates, and Nitrates	$NaNO_3$	7631-99-4	Sigma-Aldrich
	Calcite	471-34-1	Alfa Aesar
	Na_2SO_4	7757-82-6	Fisher Chemical
	$(NH_4)_2SO_4$	7783-20-2	Fisher Scientific
Clays and Aluminosilicates	Kaolinite	1318-74-7	Sigma-Aldrich
	Montmorillonite	SWy-2 *	The Clay Minerals Society
	Zeolite	1318-02-1	Sigma
Complex Multi-component Samples	Arizona Test Dust	ISO 12103-1*	Powder Technology Inc.
Organic Matter	Suwannee River Fulvic Acid	Standard III - 3S101F*	International Humic Substances Society
	Suwannee River Humic Acid	Standard III - 3S101H*	International Humic Substances Society
Biological Components	Bovine Serum Albumin	9048-46-8	Sigma-Aldrich

*CAS # is not provided, so specific type of sample is provided as an alternative

2.2 Sample Preparation

As discussed previously, many of these thin films that were prepared for the experiments presented in this dissertation have been deposited on a variety of different substrates. It should be noted that these substrates were chosen for each respective technique due to the absence of spectral interference.

For ATR-FTIR measurements, the ATR crystal, an Amorphous Material Transmitting Infrared Radiation (AMTIR) was used. Before deposition of a thin film, these crystals were

thoroughly cleaned with a Q-Tip and Kimwipe with both an aqueous and an organic solvent. Often, Milli-Q water was used for the aqueous solvent and either ethanol or methanol were used as the organic solvent. For O-PTIR-Raman and AFM-IR spectroscopic studies, calcium fluoride (CaF_2) and silica wafer substrates, respectively, were used. CaF_2 substrates were purchased from Crystran Limited and silica wafers were purchased from Ted Pella. Before depositing a thin film, these substrates were cleaned by soaking and sonicating in Milli-Q water for 30 minutes, then soaking in ethanol/methanol for 30 minutes and then finally rinsed with Milli-Q water. Finally, these substrates were allowed to air-dry before being in contact with the sample material.

Once the substrates have been cleaned, thin films were prepared using the steps depicted in Figure 2.1. First, a solution containing the dissolved or suspended sample of interest is prepared in a glass vial. Contents and concentration of these solutions differ depending on the study. Specific details about the solution preparation can be found in the Materials and Methods sections for each of the chapters. Dried, thin films of each compound were prepared by drop-casting a fixed volume of each solution onto a designated substrate. For example, a 1 mL aliquot of tock solution was deposited onto the ATR crystal, whereas for CaF_2 and silica wafer substrates, a 5 µL aliquot was casted. Due to the differences in the volume of sample material, a thin film on an ATR crystal was dried for at least 5 hours and the CaF_2 and silica wafer substrates were dried for 3 hours.

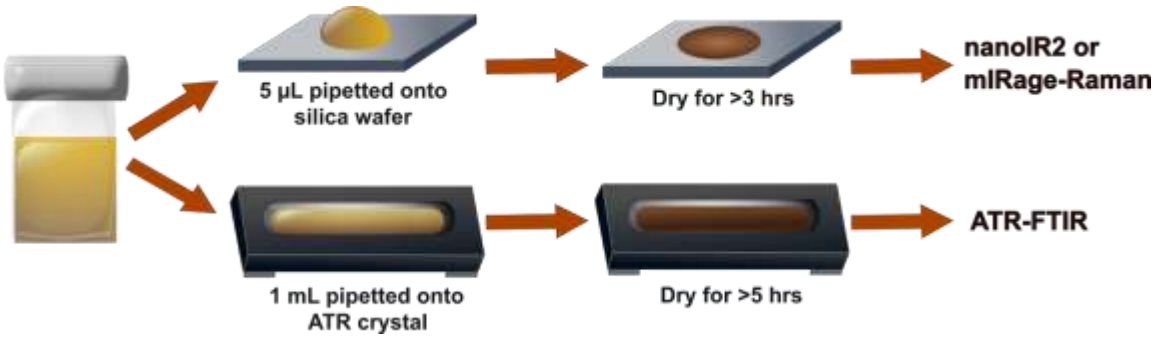

Figure 2.1 Schematic of substrate sample preparation.

2.3 Attenuated Total Reflection – Fourier Transform Infrared (ATR-FTIR) Spectroscopy

ATR-FTIR spectroscopy is a macroscopic bulk measurement technique that provides infrared peaks in the mid-infrared spectral range. ATR-FTIR spectroscopy is based upon the principles of vibrational IR spectroscopy; when IR radiation is illuminated onto a sample, the energy of the electromagnetic waves is absorbed by the molecule and results in a change in the dipole moment. More specifically, this technique operates when an incoming infrared light source is reflected internally at the interface between an optically dense medium, the ATR crystal, and an optically rare medium, the sample, where the angle of incidence exceeds the critical angle. When the evanescent wave created by this reflection is absorbed by the molecules in the sample, it results in a change in the dipole moment, which generates an IR spectrum.[1–3] This process is depicted in Figure 2.2.

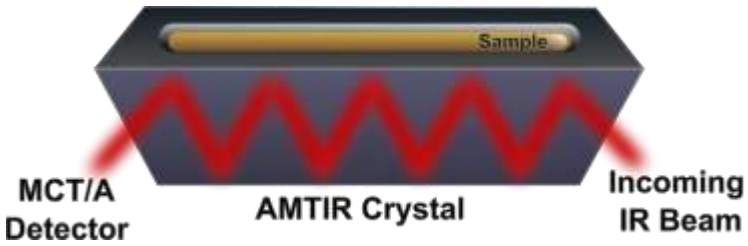

Figure 2.2 Schematic of total internal reflection occurring along the interface between an optically dense ATR crystal (AMTIR crystal) and an optically rare sample.

Theoretically, the principles of IR absorption, A, can be converted from the ratio of the transmitted and incident intensity, T, as a function of the wavelength, represented by Beer's Law below[4]:

$$A = \varepsilon bc$$

(Eq. 2.1)

Here, ε represents the molar absorptivity of the sample, b is the path length, and c is the concentration of the sample.[4] Thus, the selection rule for AFM-IR spectroscopy is similar to transmission IR spectroscopy. For infrared active modes, the transition from a ground to excited vibrational state can only occur when the change is in the dipole moment is nonzero, according to Equation 2.2[5].

$$\left(\frac{d\mu}{dr}\right)_{r_{eq}} \neq 0$$

(Eq. 2.2)

The $\frac{d\mu}{dr}$ term indicates the change in induced dipole, μ, with distance r, where r_{eq} represents the equilibrium bond length. For ATR-FTIR spectroscopy, the penetration depth, d_p, of the IR beam into the sample. This is expressed by Equation 2.3[1].

$$d_p = \frac{\lambda_1}{2\pi\sqrt{sin^2\theta - {n_{21}}^2}}$$

(Eq. 2.3)

Here, λ_1 refers to the wavelength of light divided by the refractive index of the ATR crystal and θ represents the angle of incidence of the IR beam. n_{21} is representative of the ratio of the refractive indices of an optically dense medium (ATR crystal) to the optically rare medium (sample).[1,6] The

concentration, c, of these absorbed species measured by ATR-FTIR spectroscopy, A, can be rewritten as the modified Beer's Law as shown in Equation 2.4.[6]

$$A = \varepsilon n d_e c$$

(Eq. 2.4)

In this equation, ε refers to the molar absorption coefficient, which is a function of wavenumber, and n refers to the number of internal reflections at the interface of the ATR crystal and sample. For AMTIR crystals, n is 10. Lastly, d_e refers to the effective penetration, which is used for inhomogeneous samples.[1,7]

For ATR-FTIR spectroscopic measurements, the instrument, a Nicolet iS10 FTIR spectrometer, equipped with an MCT-A detector, with a spectral range of 725 to 4000 cm^{-1} was used. A 500 µL Teflon-coated horizontal flow cell that housed an AMTIR crystal (Pike Technologies) held the sample. While the capped flow cell can hold 500 µL in liquid volume, when open, the trough of the cell can hold up to 1 mL in liquid volume. Once the thin films were prepared and dried, infrared (IR) spectra at a resolution of 4 cm^{-1} were averaged over 100 scans. For this dissertation, all spectra obtained from the instrument were processed using the OMNIC software and plotted *via* Origin.

2.4 Atomic Force Microscopy –Infrared (AFM-IR) Spectroscopy

AFM-IR spectroscopy is a hybrid technique that combines the nanoscale spatial resolution of AFM with the chemical analysis capability of IR spectroscopy by using the cantilever tip as the

detector for IR absorbance. This technique was developed to overcome the limitations of AFM and IR spectroscopy. While AFM has no intrinsic ability to chemically discriminate materials, IR spectroscopy is greatly limited by its spatial resolution, which ranges from 2.5-20 μm. By taking advantage of both techniques, a high spatial resolution on the scale of 10-30 nm can be achieved.[8]

As shown in Figure 2.3, the AFM-IR spectrometer operates using two different types of lasers. The instrument consists of a deflection laser which is in direct contact and motion with the cantilever and can be used to generate a 3-dimensional topographical height image based on the position that is bounced onto the photodiode.[9,10] In addition, it consists of a tunable IR laser, which is in contact with the sample and used for chemical characterization of the material based on localized thermal expansion from IR absorption.[11] The current nanoIR2 microscopy system (Bruker, Anasys – Santa Barbara, CA) is equipped with a QCL laser, with a spectral range from 800 to 1800 cm^{-1} as well as an optical parametric oscillator (OPO) laser that has a spectral range of 850 to 2000 cm^{-1} and 2235 to 3600 cm^{-1}. The majority of the data collected and presented in this dissertation has utilized the QCL laser over the OPO laser. While the OPO laser offers a range that can provide chemical information regarding the C-H, N-H, and O-H stretching regions, the spectra are only compatible for contact mode imaging, which makes it extremely difficult to sample softer or poorly-adhered samples. In addition, the QCL laser is about 10 times faster in operation time than the OPO laser, and also provides higher quality spectra, making it even more favorable. However, the OPO laser is still a crucial component to the capabilities of this system that can be utilized when necessary for future studies and collaborations.

There are two main methods of height imaging that is most commonly used: contact mode and tapping mode.[9,10] In contact mode, the cantilever is in direct contact with the sample as it moves laterally across the surface. With a longer, more flexible cantilever, this mode of imaging

is suited for harder sample surfaces, as the motion may be abrasive due to the larger force induced between the tip and the sample. Conversely, in tapping mode, the cantilever is in oscillating contact with the sample, with minimal frictional force. For this mode, a shorter and stiffer cantilever can be used to image softer sample surfaces. In both modes of AFM imaging, a feedback loop is employed, as the height of the cantilever changes in response to the changes in height of the sample. For contact mode, the feedback parameter is the cantilever deflection while for tapping mode, it is the cantilever oscillation amplitude.[9,10] Lastly, a key feature of AFM-IR spectroscopy that allows it to be a powerful tool, is its ability to image a particular sample area and map that same region with a particular wavelength of light at a spatial resolution that cannot be attained with conventional infrared spectroscopy. The mapped image will thus be able to give information about the spatial distribution of functional groups in addition to information about the heterogeneity of the sample.[11]

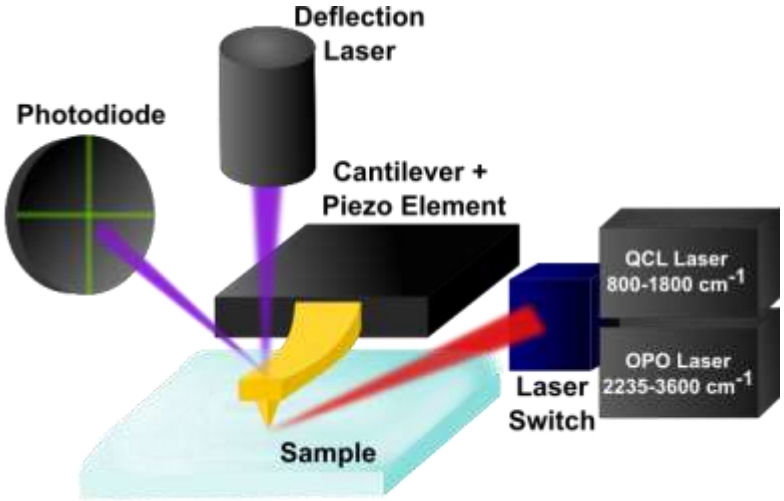

Figure 2.3 Simplified schematic of AFM-IR systems deploying three lasers- one for mapping out topographical features and the other two for infrared excitation, for two different wavenumber regions.

Following excitation of the ground vibrational state from the absorption of IR laser irradiation, heat is released into the sample matrix as it goes back down into its ground state. The maximum temperature is dependent on basic properties of the sample, such as sample volume (*V*), density (ρ), and heat capacity (*C*) as well as properties of the laser pulse such as the power, P_{abs}, and duration, t_p. This is represented in Equation 2.5[8]:

$$T_{max} = \frac{P_{abs} t_p}{V \rho C}$$

(Eq. 2.5)

The increase in temperature of the sample matrix is physically translated into a local thermal expansion resulting from an increase in internal stress. As the sample expands, there is a change in the radius of the sample; therefore, this expansion is denoted by the change in radius over time. This can be seen in Equation 2.6[8].

$$\frac{dr(t)}{r} = B \alpha_{th} T(t)$$

(Eq. 2.6)

B is a constant representative of the sample geometry, α_{th} is the thermal expansion coefficient, and $T(t)$ is the temperature decay as the sample cools in the absence of the laser pulses. This temperature decay is dependent on the duration of the laser pulse, and sample relaxation time, which indicates a time dependent change in the temperature. These contribute to the illumination conditions of the measurement, which is also dependent on the type of laser that is used. Together, these components are combined to describe the thermal contribution, H_{th}, of the overall signal.

By taking advantage of this localized thermal expansion, the photothermal induced resonance (PTIR) in which this sample expansion is detected mechanically through a device that is sensitive to changes in force and displacement, such as an AFM cantilever tip can be used to measure infrared resonances on the nanoscale. Utilizing this phenomenon allows AFM-IR spectroscopy to be used for chemical characterization of samples as it directly relates the thermal expansion with the cantilever deflection.

Assuming that the tip of the cantilever is rigid, the force received by the tip is given by Equation 2.7[8],

$$F(t) = k_z dr(t) = k_z r B \alpha_{th} T(t)$$

(Eq. 2.7)

where k_z is the spring constant of contact, which is partially dependent on the stiffness of both the tip and the sample. This describes the mechanical contribution, which can be denoted, H_m. The bending of the cantilever from this applied force is measured by using optical lever detection instead of cantilever deflection because of the feedback system that is utilized by the instrument. This contribution is denoted as the cantilever contribution, H_{AFM}.

By accounting for the optical contribution, H_{opt}, the signal transduction of PTIR, S_n, is represented by Equation 2.8, below[8]:

$$S_n(\omega_n, \sigma) = H_m H_{AFM} H_{opt} H_{th} \sigma \kappa(\sigma)$$

(Eq. 2.8)

This equation represents the PTIR response as a function of frequency, ω_n, and wavelength, σ and is simplified as an expression composed with its mechanical, cantilever, optical, and thermal contributions. The n^{th} subscript represents various modes of frequency after a Fourier Transform (FT) is applied to the temporal signal. Generally, it is most traditional to record the signal obtained from the fundamental frequency, as it possesses the most energy, denoted by S_0. Although Equation 6 appears to be complex, the four contributions remain constant within the same sample, probe, and laser, used for measurement. These changes in the detected signal are largely dependent on the wavelength of light illuminated onto the sample. Thus, the PTIR signal is proportional to the changes in cantilever motion induced by the thermal expansion, ultimately, from the sample absorbance of the IR irradiation.

For AFM-IR analysis, a wide variety of substrates and types of cantilevers can be used to extract different types of information from a sample. While cantilevers can vary in size, shape, and material, substrates can vary in material and flatness.[12–14] For the course of the studies presented in this text, two main types of cantilevers are used: one for tapping mode and contact mode. All probes are purchased directly from Bruker. Both cantilevers are gold-coated silicon nitride probes, with tip radii of ~30 nm. The cantilever used for tapping mode has a resonant frequency of 75 ± 15 kHz and a spring constant of 1 to 7 N/m, while that for contact mode has a resonant frequency of 13 kHz and a spring constant of 0.06 to 0.4 N/m. The importance of gold-coated cantilevers should be highlighted because they specifically have been chosen for signal enhancement.[15] With the additional coating of gold on the cantilever tip, some spatial resolution is lost; however, gold-coated cantilevers allow for an enhancement effect as the electric field is localized at the AFM tip. Furthermore, the gold coating can help protect the AFM from being damaged and directly interacting with light.[15,16]

So far, the capabilities of the nanoIR2 have proven to be extremely useful in providing high spatial resolution for both image and point spectra. In addition, our current nanoIR2 system is also equipped with an environmental cell (Bruker) which allows for the facilitation of *in situ* studies of physical particle transformation under variable humidity conditions.[17,18] A liquid flow line attached to the environmental cell sources the increase in humidity of the cell, that is manually sealed onto the AFM head with tape. If the cell is sealed properly, the humidity remains stable, and this stability is monitored by a relative humidity sensor (SHT3x, Sensirion) that is attached to the system. The humidity levels are controlled by adjusting the mixing ratio of dry air to humid air until the desired percentage is achieved. In order for the environmental cell to operate optimally, all of these variables must be checked before inserting a sample inside the system.

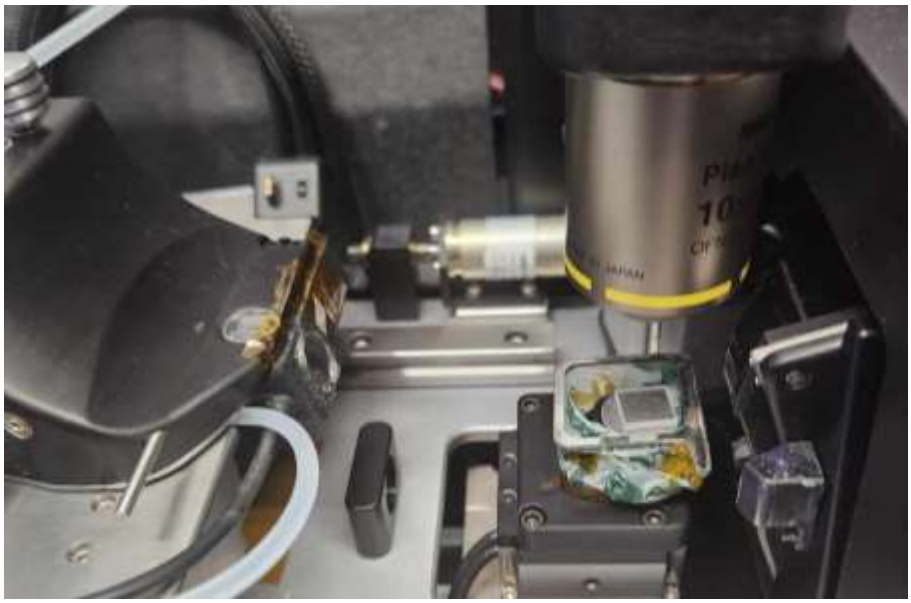

Figure 2.4 Images of current nanoIR2 system when equipped with the environmental cell accessory.

Sodium chloride (NaCl) particles are used for this environmental cell calibration since their deliquescence point is at 75% relative humidity. This is a well-known and well-studied system,

making it a great preliminary experiment to check the viability of the environmental chamber. Figure 2.5 shows the difference in height and shape of an NaCl particle as it undergoes deliquescence at 75%.

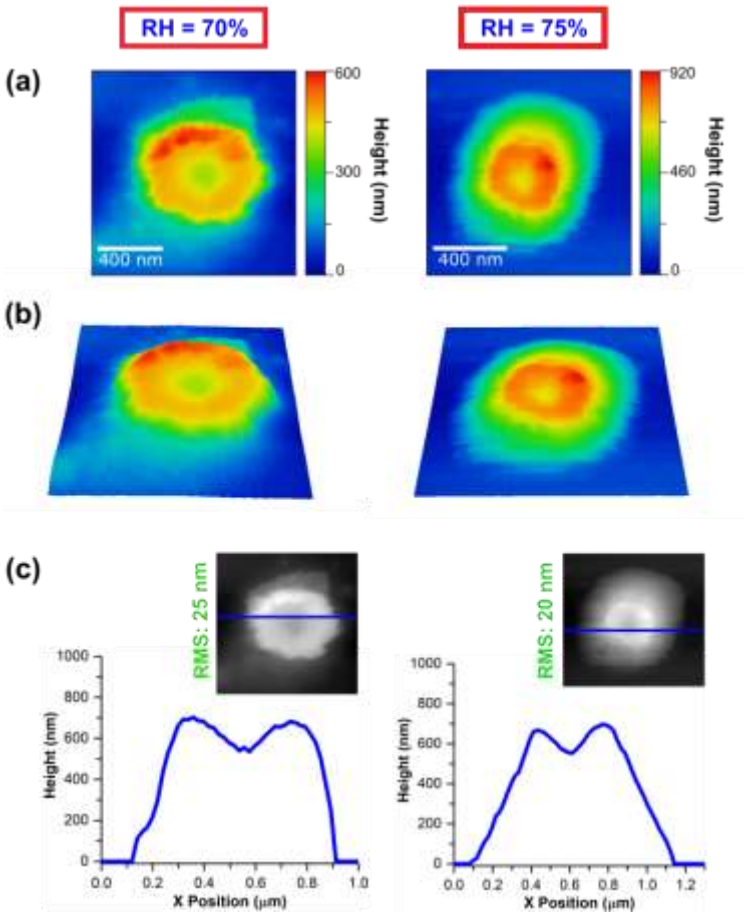

Figure 2.5 (a) AFM 2D-height images of a NaCl particle at (a) 70% and (b) 75%. (a) AFM 2D height image of NaCl particle at 70% (left) and 75% (right) relative humidity. (b) AFM 3D height image of NaCl particles at 70% and 75% relative humidity. (c) Height profiles of NaCl at 70% and 75% on the left and right, respectively. The location of the height profile is shown in the horizontal blue line shown on the upper right corner. Root mean square, RMS, roughness values are also indicated in green.

Figure 2.5a depicts an AFM 2D-height image of an irregular-shaped NaCl particle, at 70% relative humidity. The particle is 600 nm tall. On the other hand, Figure 2.5b shows a deliquesced NaCl particle at 75% relative humidity. The particle is larger as it uptakes water, and has grown in height

to 700 nm and in width from about 700 nm to 950 nm. The volume-equivalent diameter of the dry and wet NaCl particle were calculated to be 0.87 and 1.6 µm, respectively, which results in a growth factor of 1.8. Figure 2.5c shows the height profiles of the particles.

Calibration for the nanoIR2 system is broken down into 2 types: an image calibration using a test grating and a spectral calibration using a test sample. An image calibration tests the movement of the AFM stage. This calibration is done periodically to ensure proper mechanical operation of the instrument, but especially after major changes such as installation of a new AFM head or an environmental cell. The test grating used for this calibration are rectangular gratings (TGQ1, NT-MDT), which have small, squares that are 1.3 µm in width and length on each side and about 40 nm in height. Proper imaging of this sample with accurate measurements that have been listed above indicates optimal imaging operation of the instrument. An example calibration of this test grating is shown below, in Figure 2.6:

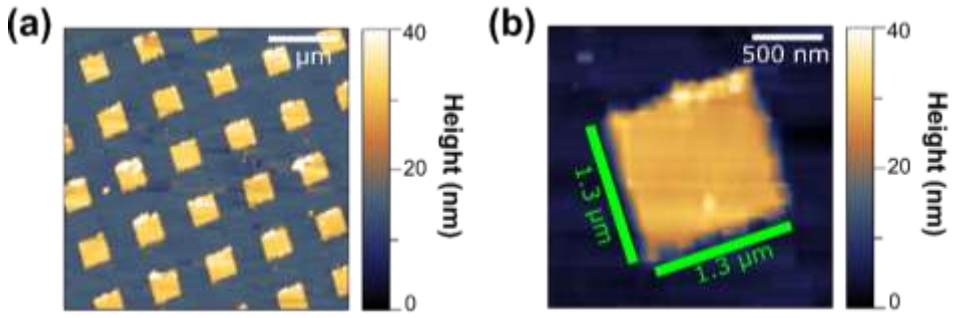

Figure 2.6 AFM 2D-height images of test grating for image calibration are shown. (a) shows a 20x20 µm image of the test grating. (b) shows a single square with a width and length of 1.3 µm and a height of 40 nm, confirming proper calibration of the nanoIR2 imaging system.

The spectral calibration utilizes a 10x10 mm ZnSe substrate that consists of microtomed films of polystyrene (PS) and polymethyl methacrylate (PMMA) beads embedded into thick films of epoxy. The QCL laser consists of a total of 4 chips that cover short wavenumber ranges that

overlap to make up the full, 800 to 1800 cm^{-1} region. Both the PMMA and epoxy have distinct spectral features that cover this range for calibration. The PMMA beads have a distinct 1728 cm^{-1} peak, representing C=O and a 1260 cm^{-1} peak, representing C-O bands. The ratio of these two bands should be roughly 2 to 1. In addition, epoxy has distinct peaks at 1508 cm^{-1} and 1608 cm^{-1}, representing C-C and C=C stretching modes, respectively.[19,20] An example of the spectral calibration run with the test sample can be seen in Figure 2.7.

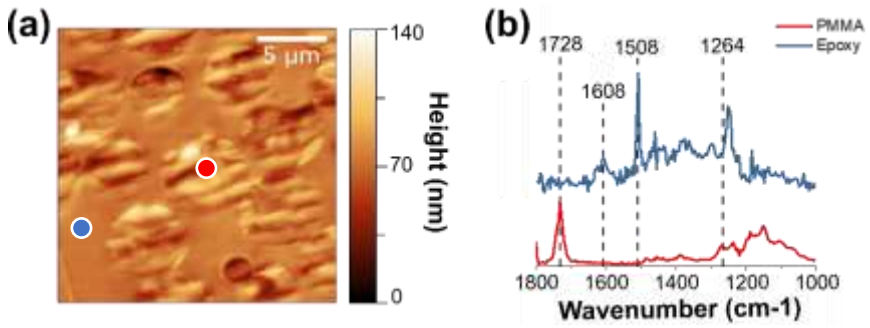

Figure 2.7 Spectral calibration of nanoIR2 system with ZnSe test sample. (a) shows the AFM-2D height image of the test sample. Circular features are PMMA beads embedded on a thick film of epoxy. (b) shows two point spectra taken on the surface – one on the epoxy surface (blue) and the other on a PMMA bead (red).

In addition to spectral calibration, the laser systems are also calibrated with a background spectrum at the start of every experiment. This spectrum is taken in order to account for any variability in the laser power across the four chips and accounted for automatically in the PTIR spectra.

Data collection with the nanoIR2 systems includes AFM images, AFM-IR spectra, as well as AFM-IR chemical maps. Some of the factors for this data collection that should be considered are image and spectral resolution, scan rate, and IR power. Details for each of these factors, including information about the substrate, are specific to every experiment and project, and can be found in the Materials and Methods section of each thesis chapter. After data collection, AFM

images and PTIR maps are processed using the Gwyddion software. All AFM-IR spectra presented in this manuscript are plotted *via* Origin.

2.5 Optical – Photothermal Infrared (O-PTIR) Spectroscopy

Microspectroscopic tools have proven to be crucial in understanding and defining the distribution of components within complex environmental samples.[21–24] O-PTIR spectroscopy is another microspectroscopic tool that will be used to probe samples and is based upon the phenomenon of photothermal expansion of a sample upon illumination of light. Unlike AFM-IR spectroscopy, which converts the deflection of the cantilever from this expansion to IR absorbance signal, O-PTIR spectroscopy translates this expansion as a change in the refractive index of the sample.[25] By using a visible light source that is collinear to the IR laser beam as the probe, an O-PTIR signal is generated when this modulated probe beam is reflected back to the detector. In addition, by attaching a monochromator and 532 nm CCD detector, Raman spectra can also be collected simultaneously, which significantly broadens the number of samples that can be analyzed with this single instrument.[25–27] A collinear pulsed IR laser and continuous visible light laser are incident on the sample of interest through a Cassegrain objective lens. The IR light when absorbed by the sample causes a local warming in that region. This warming leads to a thermal lensing effect with a change in the local refractive index that impacts the propagation of the probe, visible light beam. Most importantly for this instrument is that the spatial resolution is determined by the visible light on the order of 0.6 μm for the O-PTIR signal. A schematic of this instrument is shown in Figure 2.8.

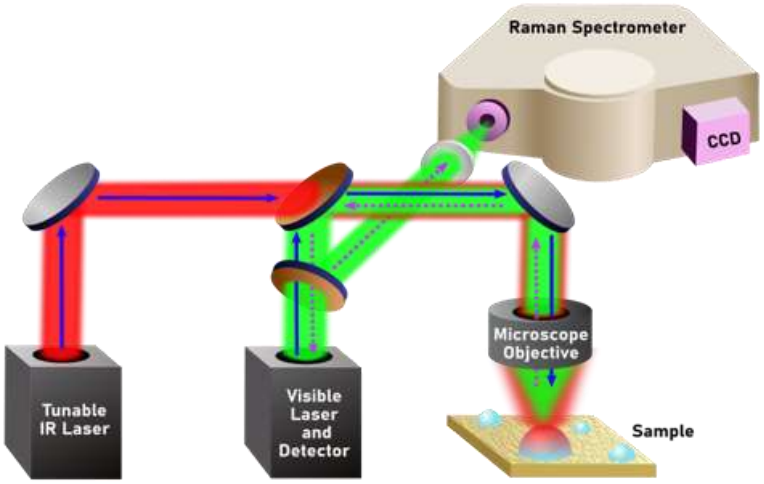

Figure 2.8 Schematic of the mIRage-Raman system that operates on the basis of optical photothermal infrared (O-PTIR) spectroscopy.

In addition to the O-PTIR signal, the green laser also can be used for Raman spectroscopy by the analysis of the visible laser beam scattered off of the sample – using a monochromator and CCD detector. Thus, the instrument is capable of collecting infrared and Raman spectra simultaneously. This now provides unique capabilities for the interrogation of complex environmental samples as well as other complex materials of interest to these studies.

The spectroscopic component of the mIRage-Raman is not only based upon the principles of IR spectroscopy but also Raman spectroscopy. Therefore, like the AFM-IR, the absorption of IR radiation in the mIRage-Raman is represented by Beer's Law and follows the same selection rule, as previously shown in Equation 2.1 and 2.2, respectively. However, the addition of the Raman spectrometer introduces the principle of Raman spectroscopy, which measures the amount of scattered light from a sample. While IR spectra can be obtained when the changes in the molecular vibrations result in a change in the molecule's dipole moment, Raman spectra can be obtained when these vibrations result in a change in the molecule's polarizability.

As the IR pulse illuminates the sample, there results in a local temperature increase in the sample as well as a thermal expansion. This localized heating is represented by Equation 2.7[28]:

$$\Delta T = \frac{Q}{C_p m}$$

(Eq. 2.5)

Here, Q represents the amount of heat generated, C_p is the specific heat of the sample, and m is the mass.

Simultaneously, a visible light source is positioned and made collinear to this IR laser beam. The visible light acts as the probe that detects the IR absorption, as this local temperature results in a local change in the refractive index shown in Equation 2.8[28].

$$\Delta n = \alpha \Delta T$$

(Eq. 2.6)

Here, α is the thermo-optic coefficient, which is a function of wavenumber. This change in the refractive index consequently affects the propagation of the probe beam by creating a refractive index gradient that acts as a lens. This effect is called the thermal lensing effect, which is based upon the phenomenon of optical photothermal induced resonance (O-PTIR).[29,30] Here, a pulsed tunable IR laser illuminates a sample, converting this energy into heat and thus a local temperature increase. This is then translated to an expansion, resulting in a change in the refractive index of the sample.[25] At the same time, an unmodulated visible light source is used as a probe and made collinear to this IR laser beam. As IR absorbance occurs, there exists a change in the probe intensity,

which is reflected back to the detector.[26,27] This modulated probe beam, which is expressed as ΔP_{pr}, is what generates the O-PTIR signal, which is linearly proportional to the IR absorbance of the sample, as shown in Equation 2.7[25]:

$$\Delta P_{pr} \propto \frac{\sigma N \alpha}{\kappa C_p} P_{pr} P_{IR} \quad \text{(Eq. 2.7)}$$

The first few terms describe the physical property of the sample, where σ is the absorption cross-section, N is the number density, κ is the heat conductivity, C_p is the heat capacity and α is the thermo-optic coefficient. The probe and infrared laser powers are represented by P_{pr} and P_{IR}, respectively.[25,26,31] In addition, the Raman scattering signal is generated simultaneously, as the scattered photons are optically separated from this modulated signal and sent to the Raman spectrometer.[26]

Like the data obtained from the nanoIR2 system, the mIRage-Raman provides both physical and chemical characterization data. First, the optical images of the sample in interest are collected with two objectives: a 10X, low magnification, visible objective lens and a 40X, high magnification reflective Cassegrain objective lens. While both optical images depict the physical features to these samples, the 40X reflective Cassegrain objective is specifically used for O-PTIR spectral data collection. The 10X visible objective can provide a lower resolution optical image of the sample to find which regions to target. The mIRage infrared + Raman microscope system (Photothermal Spectroscopy Corp., Santa Barbara, CA) consists of a continuous wave, 532 nm laser. It is also equipped with two mid-IR tunable lasers: a quantum cascade laser (QCL) and an optical parametric oscillator (OPO) laser, that are used for O-PTIR spectroscopic measurements.

The spectral range for the QCL laser is 755 to 1850 cm^{-1} and the spectral range for the OPO laser is 2600 to 3600 cm^{-1}. In addition to the IR lasers, a Raman laser with a CCD detector and a spectral range of 400 to 4000 cm^{-1} is also coupled to the system.

Different settings for data collection are tailored to each sample for optimal results. The IR laser and probe power are two important factors that contribute to the O-PTIR spectra. For Raman spectral measurements, the most optimal probe power and integration time are also determined by the settings that give the highest signal-to-noise ratio. These power settings vary heavily for each sample and more details regarding these settings can be found in the Materials and Methods section of each chapter. After data collection, all O-PTIR Raman spectra are baseline corrected using the Photothermal PTIR Studio software. All O-PTIR Raman spectra presented in this manuscript were plotted *via* Origin.

2.6 Raman Spectroscopy

Raman spectroscopy is the measure of light that is scattered by a molecule. It is often complemented with IR spectroscopic studies in order to provide a more comprehensive perspective of the vibrational modes of a molecule. While IR spectroscopy is dependent on a compound's change in dipole moment upon infrared absorption, Raman spectroscopy refers to a compound's change in polarizability, α, as it scatters the incoming photon coming from the initial light source. Specifically, the polarizability of a molecule refers to the tendency of a molecule to generate induced electric dipole moments when they are in the presence of an electric field. This relationship is depicted by Equation 2.8[32].

$$\mu_{ind} = \alpha\varepsilon$$

(Eq. 2.8)

When an electric field, ε, is applied to a Raman-active molecule, the change in the molecule's polarizability results in an induced dipole moment, μ_{ind}. This scattered light is what is detected by the Raman spectrometer.

Upon subjected to an electric field, polarization of the molecular electron cloud is induced, which results in a molecule being temporarily left in a higher energy state, called a virtual state. This virtual state is not only short-lived but also not stable, as the photon is quickly re-emitted in the form of scattered light. Figure 2.9 depicts the three different types of scattering that occur in Raman spectroscopy: Rayleigh scattering, Anti-Stokes Raman scattering, and Stokes Raman scattering.[5,32]

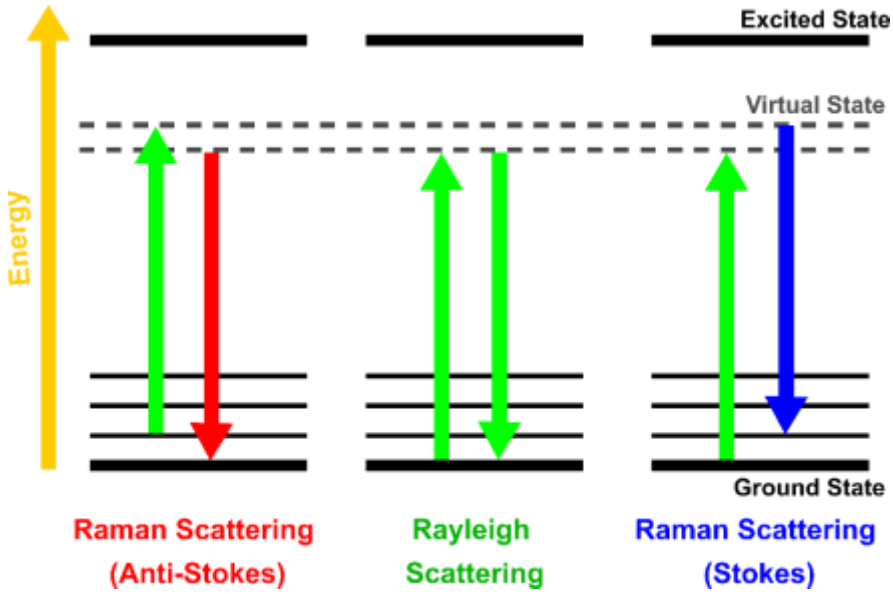

Figure 2.9 There are three different types of scattering patterns that are observed in Raman spectroscopy. From left to right, Anti-Stokes Raman scattering, Rayleigh scattering, and Stokes Raman scattering is depicted.

Rayleigh scattering occurs when the energy of the scattered photon is equal to that of the incoming light, resulting in an elastic scattering process. This type of scattering is the most common. As seen by Figure 2.9, the molecule is excited to a virtual state and then relaxes back down to where it started. Most molecules undergo Rayleigh scattering, making it the most common and intense process compared to the other types. Raman scattering, on the other hand, describes the process of inelastic scattering, where the energy of the initial photon is different from that of the scattered, re-emitted photon. There are two different types of Raman scattering: Anti-Stokes and Stokes. Stokes scattering refers to the process in which molecule gains energy from the incident photon, exciting it to a higher virtual state. Re-emission of this photon will bring the system to a higher vibrational state than it started off with. Anti-Stokes scattering can occur when molecules contain thermal energy which allows for them to start off in an excited state as opposed to ground state, reaching a higher virtual state. As it is remitted down to the ground state, there is a transfer of energy from the initial molecule to the scattered photon. Of the two types of scattering, Stokes scattering is more common than Anti-Stokes scattering.[5,32]

2.7 Spectroscopic Probes of Environmental Thin Films and Interfaces

This chapter describes the theoretical as well as the operational framework for three different vibrational spectroscopic probes used in this thesis. These probes have been applied to different environmental samples and geochemical interfaces as discussed in detail Chapters 3, 4, 5 and 6. Additionally, these techniques have been used in combination so as to probe multiple

length scales from macro to micro to nano. These different scales provide insights into the complexity and heterogeneities within environmental thin films and their interfaces.

2.8 Bibliography

(1) Mudunkotuwa, I. A.; Minshid, A. Al; Grassian, V. H. ATR-FTIR Spectroscopy as a Tool to Probe Surface Adsorption on Nanoparticles at the Liquid-Solid Interface in Environmentally and Biologically Relevant Media. *Analyst* **2014**, *139* (5), 870–881.

(2) Hase, M.; Scheffelmaier, R.; Hayden, S.; Rivera, D. Quantitative *in situ* Attenuated Total Internal Reflection Fourier Transform Infrared Study of the Isotherms of Poly(sodium 4-styrene sulfonate) Adsorption to a TiO_2 Surface over a Range of Cetylpyridinium Bromide Monohydrate Concentration. *Langmuir* **2010**, *26* (8), 5534–5543.

(3) Sit, I.; Quirk, E.; Hettiarachchi, E.; Grassian, V. H. Differential Surface Interactions and Surface Templating of Nucleotides (dGMP, dCMP, dAMP, and dTMP) on Oxide Particle Surfaces. *Langmuir* **2022**, *38* (49), 15038–15049.

(4) Cannon, C. G.; C Butterworth, I. S.; Photocell, A.; Photocell, B. Beer's Law, and Spectrophotometer Linearity Figure 2. Absorbance vs. Wavelength for Naphthalene Scarlet. **2023**, *25* (1), 168-170.

(5) Skoog, D. A.; Holler, F. J.; Crouch, S. R. *Principles of Instrumental Analysis*, Sixth.; Brooks Cole: Belmont, **2007**.

(6) Mudunkotuwa, I. A.; Grassian, V. H. Biological and Environmental Media Control Oxide Nanoparticle Surface Composition: The Roles of Biological Components (Proteins and Amino Acids), Inorganic Oxyanions and Humic Acid. *Environ. Sci. Nano* **2015**, *2* (5), 429–439.

(7) Grdadolnik, J. ATR-FTIR Spectroscopy: Its Advantages and Limitations. *Acta. Chim. Slov.* **2002**, *49* (3), 631–642.

(8) Dazzi, A.; Prater, C. B.; Hu, Q.; Bruce, D.; Rabolt, J. F.; Marcott, C. Focal Point Review AFM-IR: Combining Atomic Force Microscopy and Infrared Spectroscopy for Nanoscale Chemical Characterization. *Appl. Spectrosc.* **2012**, *66* (12), 1365–1384.

(9) Voigtländer, B. *Atomic Force Microscopy*, 2nd ed.; Springer International Publishing, **2019**.

(10) Braga, P. C.; Ricci, D. *Atomic Force Microscopy: Biomedical Methods and Applications*; Humana Press, **2004**.

(11) Dazzi, A.; Prater, C. B. AFM-IR: Technology and Applications in Nanoscale Infrared Spectroscopy and Chemical Imaging. *Chem. Rev.* **2016**, *117* (7), 5146–5173.

(12) Shute, M. A.; Farchone, R.; Linder, A. P., K. P.; Gavin, R.; Goss, C.; Lieberman, V. Preparation of Mica and Doerfler Silicon Substrates for DNA Origami Analysis and Experimentation. *J. Vis. Exp.* **2015**, *101*, (52972) 1-8.

(13) Chada, N.; Sigdel, K. P.; Reddy, R.; Gari, S.; Matin, T. R.; Randall, L. L.; King, G. M. Glass Is a Viable Substrate for Precision Force Microscopy of Membrane Proteins. *Sci. Rep.* **2015**, *5* (12550), 1-8.

(14) Schumacher, Z.; Miyahara, Y.; Aeschimann, L.; Grütter, P. Improved Atomic Force Microscopy Cantilever Performance by Partial Reflective Coating. *Beilstein J. Nanotechnol.* **2015**, *6*, 1450–1456.

(15) Bruker Nano Surfaces. *Using AFM-IR for the Nanoscale Chemical Characterization of Polymeric and Thin Film Samples*. AZO Materials. https://www.azom.com/article.aspx?ArticleID=18109.

(16) Centrone, A. Infrared Imaging and Spectroscopy Beyond the Diffraction Limit. *Annu. Rev. Anal. Chem.* **2015**, *8*, 101–126.

(17) Or, V. W. Ph.D. Dissertation, University of California San Diego (2021).

(18) Or V. W.; Estillore, A. D.; Tivanski, A. V.; Grassian, V. H. Lab on a Tip: Atomic Force Microscopy-Photothermal Infrared Spectroscopy of Atmospherically Relevant Organic/Inorganic Aerosol Particles in the Nanometer to Micrometer Size Range. *Analyst* **2018**, *143* (12), 2765–2774.

(19) González, M.; Cabanelas, J. C.; Baselga, J. 3 Applications of FTIR on Epoxy Resins-Identification, Monitoring the Curing Process, Phase Separation and Water Uptake. *InTech* **2012**, 261-284.

(20) Infrared Spectroscopy of Polyacrylates Estimating Kinetics Data of Fluorescence Band Parameters Using a Streak Camera 3D Printing and the Art of Making Small Working Prototype Spectrometers. *Spec*. **2023**, *38* (1), 10-14.

(21) Jubb, A. M.; Rebecca Stokes, M.; McAleer, R. J.; Hackley, P. C.; Dillon, E.; Qu, J. Mapping Ancient Sedimentary Organic Matter Molecular Structure at Nanoscales Using Optical Photothermal Infrared Spectroscopy. *Org. Geochem.* **2023**, *177*, 104569-104578.

(22) Gieroba, B.; Kalisz, G.; Krysa, M.; Khalavka, M.; Przekora, A. Application of Vibrational Spectroscopic Techniques in the Study of the Natural Polysaccharides and Their Cross-Linking Process. *Int. Journal of Molecular Sci*. **2023**, *24* (3), 2630-2658.

(23) Mirrielees, J. A.; Kirpes, R. M.; Haas, S. M.; Rauschenberg, C. D.; Matrai, P. A.; Remenapp, A.; Boschi, V. L.; Grannas, A. M.; Pratt, K. A.; Ault, A. P. Probing Individual Particles Generated at the Freshwater-Seawater Interface through Combined Raman, Photothermal Infrared, and X-Ray Spectroscopic Characterization. *ACS Measurement Science Au* **2022**, *2* (6), 605–619.

(24) Olson, N. E.; Xiao, Y.; Lei, Z.; Ault, A. P. Simultaneous Optical Photothermal Infrared (O-PTIR) and Raman Spectroscopy of Submicrometer Atmospheric Particles. *Anal. Chem.* **2020**, *92* (14), 9932–9939.

(25) Zhang, D.; Li, C.; Zhang, C.; Slipchenko, M. N.; Eakins, G.; Cheng, J. X. Depth-Resolved Mid-Infrared Photothermal Imaging of Living Cells and Organisms with Submicrometer Spatial Resolution. *Sci. Adv.* **2016**, *2* (9), 1-7.

(26) Li, X.; Zhang, D.; Bai, Y.; Wang, W.; Liang, J.; Cheng, J. X. Fingerprinting a Living Cell by Raman Integrated Mid-Infrared Photothermal Microscopy. *Anal. Chem.* **2019**, *91* (16), 10750-10756.

(27) Li, Z.; Aleshire, K.; Kuno, M.; Hartland, G. V. Super-Resolution Far-Field Infrared Imaging by Photothermal Heterodyne Imaging. *J. Phys. Chem. B* **2017**, *91*(16), 10750-10756.

(28) Zhang, D.; Lan, L.; Bai, Y.; Majeed, H.; Kandel, M. E.; Popescu, G.; Cheng, J. X. Bond-Selective Transient Phase Imaging *via* Sensing of the Infrared Photothermal Effect. *Light Sci. Appl.* **2019**, *8* (116), 1-12.

(29) Klementieva, O.; Sandt, C.; Martinsson, I.; Kansiz, M.; Gouras, G. K.; Borondics, F. Super-Resolution Infrared Imaging of Polymorphic Amyloid Aggregates Directly in Neurons. *Advanced Science* **2020**, *7*, 1-9.

(30) Marcott, C.; Kansiz, M.; Dillon, E.; Cook, D.; Mang, M. N.; Noda, I. Two-Dimensional Correlation Analysis of Highly Spatially Resolved Simultaneous IR and Raman Spectral Imaging of Bioplastics Composite Using Optical Photothermal Infrared and Raman Spectroscopy. *J. Mol. Struct.* **2020**, *1210*, 1-6.

(31) Bai, Y.; Zhang, D.; Lan, L.; Huang, Y.; Maize, K.; Shakouri, A.; Cheng, J. X. Ultrafast Chemical Imaging by Widefield Photothermal Sensing of Infrared Absorption. *Sci. Adv.* **2019**, *5* (7), 1-8.

(32) Smith, Ewen.; Dent, Geoffrey. *Modern Raman Spectroscopy: A Practical Approach*; J. Wiley, **2005**.

CHAPTER 3
ATTENTUATED TOTAL REFLECTION-FOURIER TRANSFORM INFRARED AND ATOMIC FORCE MICROSCOPY-INFRARED SPECTROSCOPIC INVESTIGATION OF SUWANNEE RIVER FULVIC ACID AND ITS INTERACTIONS WITH α–FeOOH

3.1 Abstract

Suwannee River Fulvic Acid (SRFA) and its interaction with α–FeOOH have been investigated using two different spectroscopic techniques – ATR-FTIR spectroscopy and AFM-IR spectroscopy. ATR-FTIR spectroscopy of SRFA thin films yields information on functional groups present within these films prepared from solutions of three different pH values (3, 6 and 8). This technique can also be used to probe the interaction of SRFA with α–FeOOH particle surfaces and the impact that pH has on these surface interactions. AFM-IR spectroscopy offers a different perspective as it probes both film morphology and spectral signals with nanoscale spatial resolution. Herein, we apply AFM-IR spectroscopy to investigate SRFA thin films and the interactions with α–FeOOH. Results from this study show that pH impacts the speciation of SRFA and its interaction with α-FeOOH. Furthermore, there are nanoscale and microscale heterogeneities in these thin films as shown in height images, point spectra and spectral maps. Overall, these measurements using two different vibrational spectroscopic techniques provide insights into the heterogeneity of natural organic matter and its interactions with mineral surfaces.

3.2 Introduction

Natural organic matter (NOM) represents a large class of compounds that originate from plants, animals, and microbial debris commonly found in both aquatic and terrestrial systems. These complex molecules contain a variety of functional groups that are active in interfacial chemistry.[1] Both humic and fulvic acids are commonly used as model fractions of NOM. Compared to its equally abundant counterpart humic acid, fulvic acid is known to have a smaller molar mass and is relatively more soluble with a higher molar ratio of phenolic and carboxylic functional groups.[2,3] These different functional groups can interact with mineral surfaces through hydrogen bonding as well as electrostatic interactions.[4–6]

The adsorption of NOM onto mineral surfaces has the ability to alter the properties of mineral particle surfaces and the chemistry that occurs on these surfaces. This includes not only the rate or extent of mineral dissolution but also the mechanism and transport of other naturally occurring species, both organic and inorganic, present in the environment. Moreover, NOM can impact the transport of contaminants.[7] Among various mineral surfaces, oxyhydroxides are abundant, naturally occurring minerals. Goethite, α-FeOOH, has been chosen for this study due to its importance in iron cycling and its prevalence as a coating to other soil minerals found in the natural environment.[8,9] While a small percentage in soil composition, goethite surfaces can actually account for up to 50-80% of the total surface area of soil, allowing them to be readily available for interaction with NOM.[10,11] Fulvic and humic acids are capable of coordinating with iron to form stable complexes.[5] Additionally, these interactions are dependent on important environmental variables such as pH. A previous computational study by Filius *et al*. reported that in more acidic environments, carboxylic and phenolic functional groups are more susceptible to undergo inner sphere coordination with α-FeOOH surfaces, while in higher pH environments, they are likely to undergo outer sphere coordination.[12] Moreover, the detailed nature of NOM

adsorption is complex because of the intrinsic heterogeneity of these samples which contain many different compounds.[1,13]

The goal of this study is to gain further insights into the heterogenous nature and behavior of SRFA and its interactions with α-FeOOH in thin films as well as the interaction of SRFA with individual particles and small particle aggregates by combining two spectroscopic techniques – attenuated total reflection-Fourier transform infrared (ATR-FTIR) and atomic force microscopy-infrared (AFM-IR) spectroscopy. ATR-FTIR spectroscopy can provide an *in situ* probe of the functional groups present in complex samples and can give high quality spectra that can be used to better understand binding mechanisms of organic and inorganic species with various geochemical interfaces.[14] AFM-IR spectroscopy is a hybrid microspectroscopic technique that provides nanoscale spatial resolution. With this spatial resolution, spectral mapping reveals heterogeneities on the nanoscale within a sample.[15] Herein, we are able to gain direct insight into SRFA thin films and SRFA interactions with α-FeOOH using AFM-IR spectroscopy in order to better understand intrinsic heterogeneities that may have an impact on the fate and transport of pollutants in the environment.

3.3 Experimental Methods

Sample preparation and source of materials. In these studies, samples were prepared using several different protocols. For studies of thin films of SRFA (purchased from International Humic Substances Society), 5 mg was dissolved in 5 mL of Milli-Q water and the pH was adjusted to pH 3, 6, or 8 with either 1 M HCl or NaOH. Approximately 5 µL of these solutions was drop-cast onto a silica wafer that had been cleaned with isopropanol and DI water. The solutions were then used

to dry for a few hours as described in more details below. Thin films of SRFA and α-FeOOH particles (Alfa Aesar, Lot #H05M26), with an average length and width of 320 ± 140 nm and 21 ± 9 nm, respectively (Figure 3.1) and a BET surface area of 24 m^2/g, were prepared by making a 1 mg/mL solution of α-FeOOH particles in 3 mL of a 100 ppm solution of pH adjusted SRFA.

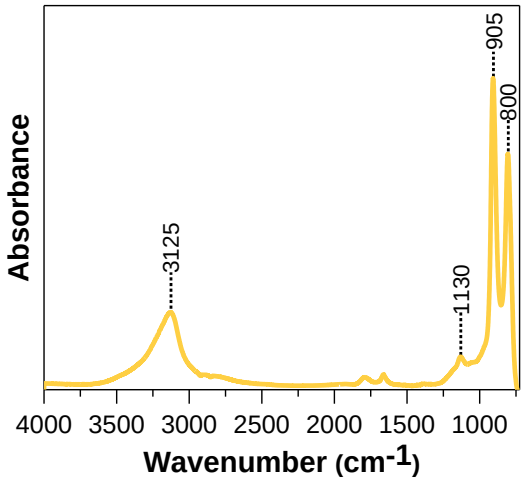

Figure 3.1 ATR-FTIR spectra of a dried, α-FeOOH thin film. The most intense peaks are seen for the in/out-of-plane O-H bending modes are indicated by 800 and 905 cm^{-1} and the 3125 cm^{-1} is indicative of the O-H stretching modes.

In order to facilitate mixing of the α-FeOOH particles in solution, the suspension was probe-sonicated for 30 seconds, inverted, and repeated once more. After sonication, the initial translucent solution with suspended α-FeOOH particles transformed into a homogenous, opaque, yellow suspension. For AFM-IR analysis, 5 µL of this solution was deposited onto a cleaned silica wafer and allowed to dry for >3 hours. For ATR-FTIR analysis, 1 mL of this suspension was deposited onto an AMTIR crystal for 5 hours. These different drying times allowed for water to evaporate from the film were dependent on the amount of solution deposited as can be seen in the collected preliminary spectra due to the absence of the bending and stretching modes of water at ca. 1640 and 3400 cm^{-1}, respectively.

Attenuated Total Reflectance Fourier Transform Infrared (ATR-FTIR) spectroscopy. ATR-FTIR spectroscopy is based upon the principle of total internal reflection. The ATR accessory consists of a 500 µL horizontal, Teflon-coated flow cell that houses an ATR internal reflecting element, an AMTIR crystal (Pike Technologies). When fully capped, the flow cell can hold a solution volume of 500 µL, but when open, the trough can hold a solution volume of approximately 1 mL. The AMTIR crystal was chosen specifically for its high effective path length and its wide operational pH range from 1 to 9. Upon total internal reflection between the optically dense ATR crystal and the optically rare sample, an evanescent wave is created and is used to probe both solutions and thin films of SRFA and α-FeOOH.[16] For measurements of thin films, a 1 mL solution of just SRFA or of α-FeOOH was deposited onto the ATR crystal. After drying of the film, infrared spectra were collected. All collected spectra were averaged over 100 scans at a resolution of 4 cm^{-1} over a spectral range from 725 to 4000 cm^{-1}. This was done for pH values of 3, 6 and 8. For solution phase spectra, a water background at each pH was collected and subtracted from each of the spectra, this results in a difference spectrum, which shows only new absorptions due to SRFA.

In-situ ATR-FTIR spectroscopy of surface adsorption of 100 ppm SRFA in solution onto an α-FeOOH thin film. For surface adsorption studies from solution, a thin film of α-FeOOH nanoparticles was prepared by drop-casting a 5 mg/mL solution of α-FeOOH in Milli-Q water onto a cleaned AMTIR crystal and the solution was allowed to dry on the AMTIR crystal. Before SRFA adsorption was initiated, the thin film was flushed with MilliQ water containing 30 mM KCl for ionic strength, adjusted to the pH of interest with 1 M HCl/NaOH, for 30 min at a flow rate of ~1 mL/min. This step dislodged any loosely adhered particles. Following the flow of MilliQ water, a

background spectrum was collected of the thin film at the pH and ionic strength adjusted aqueous solution. A solution of 100 ppm of SRFA was prepared at the appropriately adjusted pH and the SRFA solution was flowed over the α-FeOOH film at ~1 mL/min over the course of 90 minutes. The 90-minute time period was determined in preliminary experiments as the length of time needed for the absorption bands due to adsorbed SRFA to reach maximum intensity. During this time, spectra were collected every 5 minutes and desorption spectra were collected with the same optima water solution the film was initially treated with. This procedure was repeated for pH 6 and pH 8 SRFA solutions with the respective optima water. In addition, solution-phase spectra of 1 mL SRFA solution prepared at pH values of 3, 6 and 8 were also collected as a basis of comparison.

Atomic Force Microscopy-Infrared (AFM-IR) spectroscopy. AFM-IR spectroscopy is a hybrid technique that combines the nanoscale spatial resolution of AFM with the chemical analysis capability of IR spectroscopy by using the cantilever tip as the detector. This technique implements the phenomenon of Photothermal Induced Resonance (PTIR), which describes the photothermal expansion induced by the infrared absorption of the sample from the illuminated light at a given frequency. The expansion of the sample is detected by the deflection of the flexible cantilever, resulting in a change of the position of the deflection laser on the photodiode. This change is transduced into the IR signal, and a resulting PTIR spectrum.[17,18]

Samples were analyzed with a nanoIR2 microscopy system (Bruker, Anasys – Santa Barbara, CA) equipped with a mid-IR tunable quantum cascade laser (QCL). AFM images were collected at a scan rate of 0.2 Hz. Both images and PTIR spectra were collected using gold-coated silicon nitride probes, with tip radii of ~30 nm. Both contact and tapping mode probes were used, with the former having a spring constant of 0.06 to 0.4 N/m and a resonant frequency of 13 kHz

and the latter having a spring constant of 1 to 7 N/m, and a resonant frequency of 75 kHz. PTIR spectra were collected with a resolution of 5 cm^{-1} at various locations across the surface. Chemical maps were obtained by tuning the laser at a fixed wavelength over the selected region, with a scan rate of 0.2 Hz. Hyperspectral maps shown were obtained by collecting spectra over an array of selected regions over the full range of 800-1800 cm^{-1}. Collected spectra at various points within the image were then used to generate a heat map at different wavenumbers. For these experiments, 5 μL of the SRFA and α-FeOOH solution at the three different pH values were deposited onto a cleaned silica wafer and dried for at least 3 hours. Once dried, the films were ready for AFM-IR analysis. Analysis of single particles were also obtained from the nanoIR2 system.

3.4 Results and Discussion

ATR-FTIR spectroscopy of SRFA thin films. Figure 3.2 shows ATR-FTIR spectra of SRFA at three pH values: both in solution and as a condensed thin film, respectively, are shown. As SRFA undergoes a transition from the solution phase to a condensed thin film, the relative intensity of the functional groups increases as they become more dried from the evaporation of water. This is consistent with the observed physical change from a light-yellow colored solution to a dark brown film. Using the geometrical dimensions of the horizontal ATR cell and assuming a density of 1.5 g/mL, the film thickness is determined to be ca. 1 μm, on the order of the penetration depth of the evanescent wave.[16,19] In order to clearly identify functional groups present in the solution phase measurements, a higher SRFA concentration of 1000 ppm is shown in Figure 3.2.

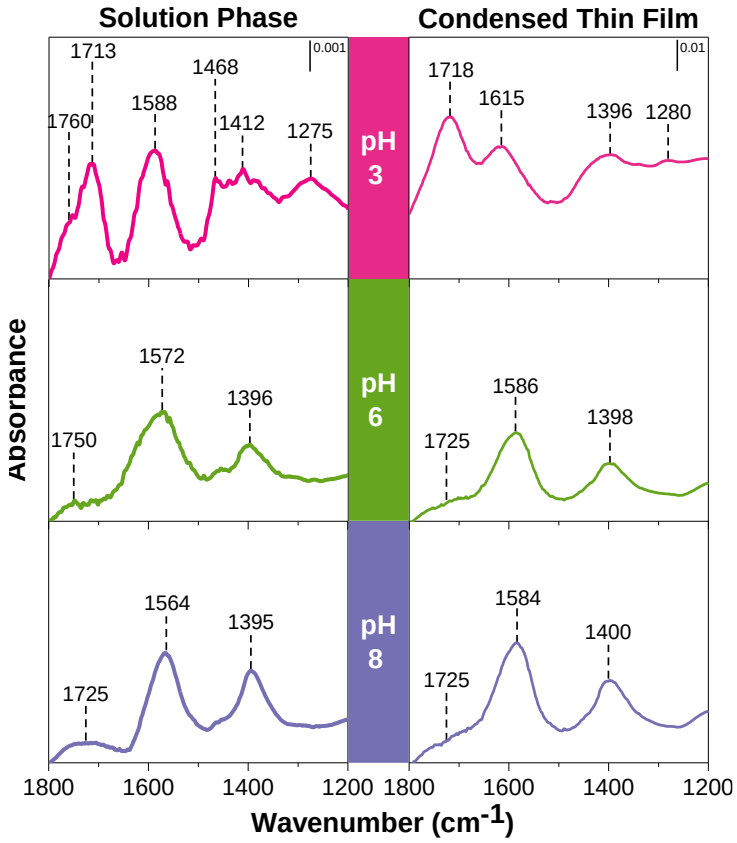

Figure 3.2. ATR-FTIR spectra of SRFA at three different pH values 3, 6 and 8. The left panel shows spectra of 1000 ppm SRFA in solution phase. The right panel shows spectra for a dried ca. 1 µm condensed thin film of 100ppm SRFA prepared from solutions at the three different pH values.

For the solution and condensed phases, infrared absorption bands at 1713 cm^{-1} and 1718 cm^{-1} respectively can be assigned to the C=O stretching vibrational mode of the protonated carboxylic acid groups. These peaks are primarily present in highly acidic environments, whereas at a higher pH, the deprotonated carboxylate group shows the presence of the symmetric and asymmetric carboxylate stretching modes. These two vibrational modes are seen over a range of wavenumbers, from 1560 to 1615 cm^{-1} and 1395 to 1415 cm^{-1}, respectively. The broadness of each of the bands suggests the presence of additional contributions from vibrational modes of other functional groups. Assignments for these different vibrational modes are provided in Table 3.1. The absorption band at 1275 to 1280 cm^{-1} is attributed to the C-O-H stretching mode present in

phenolic-type molecular structures. In addition, the solution phase measurement for pH 8 shows a less intense 1725 cm^{-1} band, which is assigned to the vibrational mode of esters and ketones present within these organic macromolecules, rather than that of carboxylic acid at the higher pH value. Although not all spectra show distinct peaks at both 1275 cm^{-1} and 1725 cm^{-1} regions, it is again important to note that the ATR-FTIR spectra are very broad and, in these regions, there is some intensity, indicating the presence of these functional groups although their peak positions may be poorly resolved in this complex multi-component sample.

Table 3.1 Vibrational assignments for different functional groups within SRFA and α-FeOOH.[3–5,20–23]

Wavenumber Range (cm^{-1})	Vibrational Assignment
1725	C=O stretching of aldehydes, esters, ketones, saturated ethers
1710-1720	C=O stretching of carboxylic acid
1640	C=O stretching of quinones, conjugated ketones
1580-1620	Aromatic C=C
1600	Asymmetric COO- stretching of carboxylate with partial protonation from neighboring carboxyl groups
1560-1615	Symmetric stretching of COO-
1590-1680	Asymmetric ring breathing modes of aromatic groups
1500-1680	C=O stretching of quinones and amide I, C=N of imines, C=C of alkenes, C=C of aromatics
1350-1500	Symmetric ring breathing of aromatics, C-H and O-H bending modes, C-H deformation of CH_3 and CH_2
1445-1450	Symmetric COO-stretching of carboxylate with partial protonation from neighboring carboxyl groups
1385-1415	Asymmetric stretching of COO-
1408	Aromaticity from aromatic rings and deformation of aliphatic C-H and O-H in phenols and alcohols
1400-1450	Iron-fulvate complex
1255-1275	C-O-H phenolic, C-O stretching of phenol, C-O stretching of alcohols, bending of phenol OH and alcohol OH,
895-905	In and out of plane bending of the bulk O-H groups for iron oxyhydroxide

AFM-IR spectroscopy of SRFA thin films. To provide additional information, AFM-IR spectroscopy was employed. AFM images and PTIR spectra were collected at specific points within these images. In Figure 3.3, 5x5 μm AFM deflection images of condensed thin films prepared at pH 3, 6, and 8 are shown. The images provide insights into the surface morphology of these SRFA thin films. They show that these films consist of smooth areas of aggregated particles that are randomly dispersed throughout the film, consistent with what has been reported in previous AFM studies of NOM thin films.[24,25] Point spectra are collected at the colored dots marked on these images. Aggregates possessing fractal geometries within the film are highly visible, and these are the regions in which point spectra were taken, as these are the regions with high organic content.[26]

The presence of protonated carboxylic acid functional groups is indicated by peaks near 1715 cm^{-1}. There is also variation in the range of peak frequencies observed for the symmetric and asymmetric carboxylate vibrational modes as shown by the bands present between 1550 to 1655 cm^{-1} and 1385 to 1395 cm^{-1}. Peaks present at 1445 to 1450 cm^{-1} are considered to be contributions from partially protonated symmetric carboxylate stretching *via* neighboring carboxyl groups, specifically as they are present primarily in acidic environments.[20] The C-O stretching and C-O-H vibrational frequencies from phenol groups that are present within SRFA are observed at frequencies between 1255 and 1280 cm^{-1} and C=O carbonyl groups from ketones and esters are seen at the 1725 cm^{-1} peak. The heterogeneity in the spectra recorded at pH 3 is important to note, as the major absorption peaks vary from region to region. For example, while the first region is rich in carboxylic acid, the second region is highly abundant in esters and ketones, as indicated by the 1715 cm^{-1} and 1725 cm^{-1} peak, respectively. The third region, on the other hand, appears to contain high levels of carboxylate functional groups. This spectral variability is a clear indication

of heterogeneity within the same pH 3 film, confirming the presence of different functional groups, as supported by other micro-spectroscopic probes such as X-ray spectromicroscopy.[13] Overall, the spectra show similar features as seen in the ATR-FTIR spectra presented in Figure 3.2.

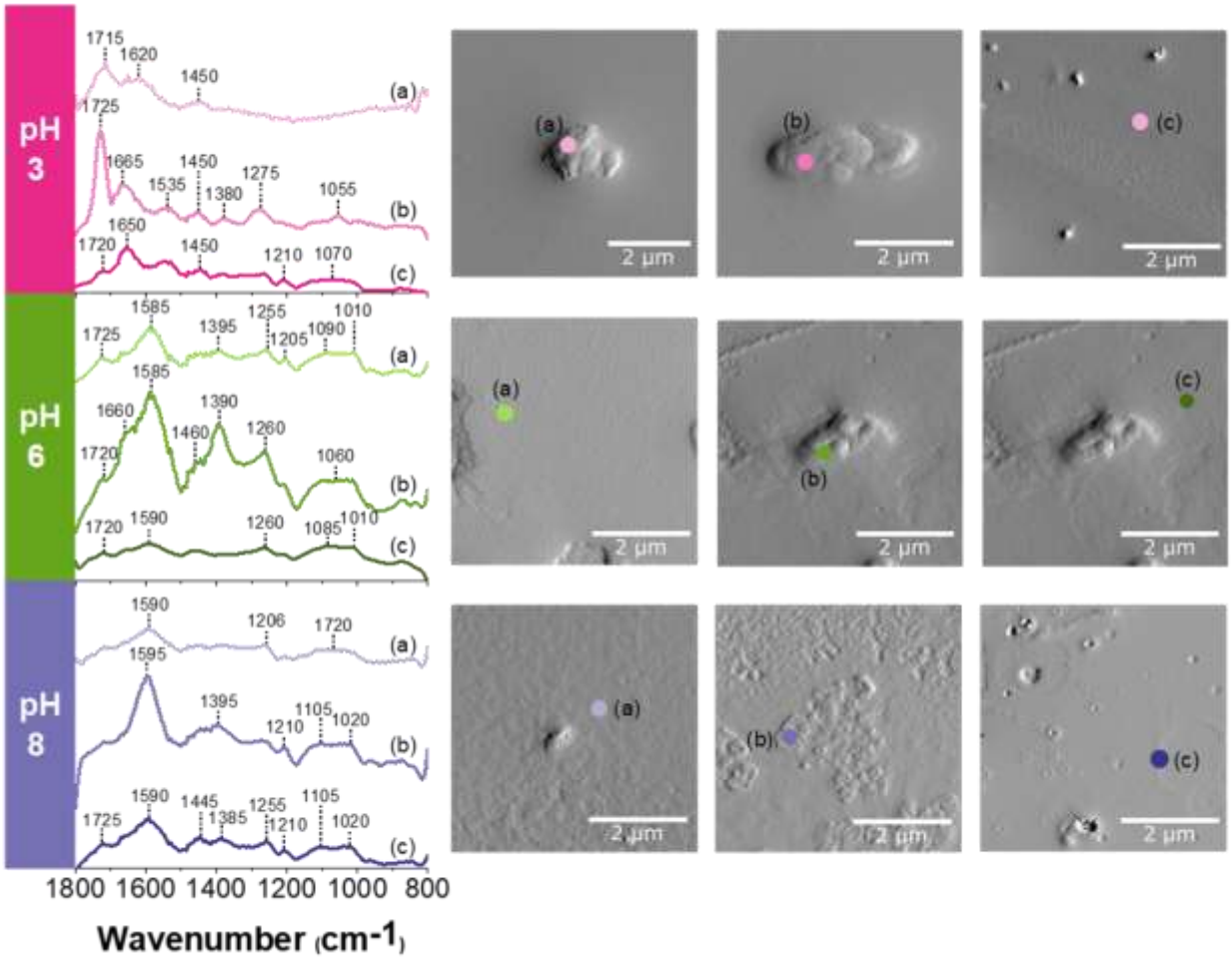

Figure 3.3 AFM-IR images and spectra of dried thin films prepared from solutions of pH 3,6, and 8 on different regions of the same sample. The variation in intensity and peak shape in these spectra indicate heterogeneity of the SRFA thin film in terms of the amount of SRFA present and potentially different compounds within different regions. Images on the right are deflection images of the 5x5 µm thin films of SRFA, in which point spectra were taken. Film thickness of the films shown varies from region to region but are on the order of ca. 400 nm.

It is important to note that a collection of PTIR spectra were chosen to represent the spectra from AFM-IR spectroscopy, rather than an average spectrum over a macroscopic large ensemble

across the film, as is the case for ATR-FTIR spectroscopy. This was specifically chosen to highlight the variation in spectra at these various locations, which is more representative of the heterogenous nature of SRFA. With AFM-IR spectroscopy, specific nanoscale regions of the film can be achieved on the order of 30 nanometers, which is the diameter of the AFM tip. This nanoscale interrogation allows for highly selective analyses *via* specific point spectra and thus provides information on the heterogeneity on this length scale.

Thin films of SRFA and α-FeOOH. The adsorption of NOM, specifically fulvic and humic acid, has been examined by a number of studies over the past few decades, where both inner and outer-sphere complexation has been proposed to be important in the interaction of SRFA with different minerals.[4–6,12,20,22,27] We can examine the spectra in Figure 3.4 obtained from *in-situ* ATR-FTIR spectra of α-FeOOH thin films upon adsorption of SRFA from solutions, measured as a function of time, to gain more insight into the interactions present in these samples.

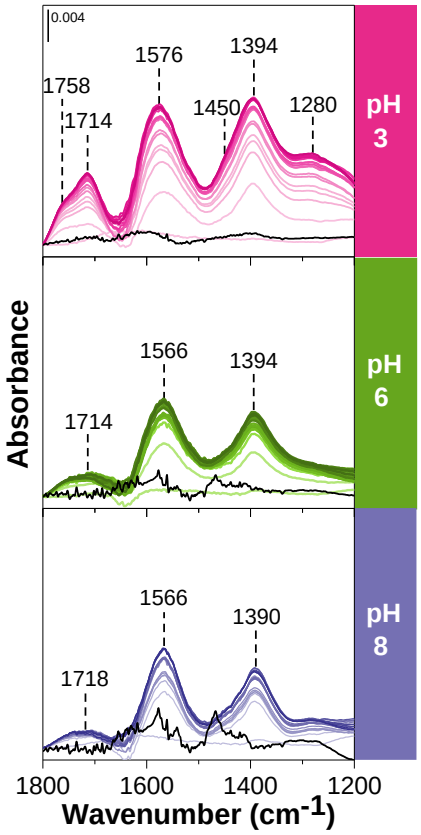

Figure 3.4 ATR-FTIR spectra of 100 ppm SRFA in solution adsorbed onto a thin film of α-FeOOH, over a time period of 90 min, at three different pH values. The black dotted spectrum is that of the 100 ppm SRFA solution at the corresponding pH.

It can be seen that the intensities of the major bands are observed at 1394 cm^{-1}, 1576 cm^{-1}, and 1714 cm^{-1} for pH 3, increase over a time period of 90 minutes, at which the surface is fully saturated with SRFA. Upon adsorption from the solution, there is a clear difference between the intensities of these bands before and after interaction with the iron oxyhydroxide. As seen in Figure 3.4, the intensities of the major peaks present in the SRFA spectrum when α-FeOOH is present is approximately four times greater than those seen in only the SRFA spectrum. This increase in intensity suggests the presence of various states of SRFA, which can include hydrogen bonding to surface hydroxyl groups; this is a similar phenomenon observed by Persson and Axe in their study regarding oxalate adsorption onto α-FeOOH.[28] In addition, in the pH 3 spectra, a slight shoulder

at 1450 cm^{-1} can potentially be resolved as absorption time increases. However, as stated previously, it is important to note that the broad nature of these bands can make this resolution difficult.

In pH 6 and 8 environments, there is little difference in frequencies of the peaks in the ATR-FTIR spectra. For example, when comparing the spectra with and without α-FeOOH, the symmetric and asymmetric carboxylate stretching modes are present from 1572 cm^{-1} and 1396 cm^{-1} without α-FeOOH and 1566 cm^{-1} and 1394 cm^{-1}, with α-FeOOH at pH 6 are all within 6 cm^{-1}. These peak positions are in close agreement with each other, which was also observed in the pH 8 environment, where the symmetric and asymmetric carboxylate stretching modes are present from 1566 cm^{-1} and 1394 cm^{-1} without α-FeOOH, and 1566 cm^{-1} and 1390 cm^{-1}, with α-FeOOH, respectively. The significant increase in the intensities, specifically in the presence of α-FeOOH, indicate that any interaction is a variation of hydrogen-bonding along the surface. This behavior has been observed in similar, higher pH environments, as reported previously by Yoon *et al*., who stated outer-sphere coordination as a potential dominating mechanism in the adsorption of SRFA onto a boehmite/water interface.[20] In these environmental conditions, such low-molecular weight organic acids like SRFA, are preferred to form hydrogen-bonded surface complexes, rather than inner-sphere coordination, or metal-bonded surface complexes.[28,29]

Figure 3.5 shows a clear comparison of ATR-FTIR spectra obtained from dried, thin films of SRFA, both with and without α-FeOOH. It is important to highlight that in both of these thin films, there is the same mass of SRFA present, indicating that any differences in the spectral shifts and intensity are due to interactions with α-FeOOH nanoparticles. Two absorption bands, located at 790 and 895 ± 5 cm^{-1}, can be seen in Figure 3.5a. These represent the in/out-of-plane

bending modes of O-H, as shown in the ATR-FTIR spectrum of a dried, α-FeOOH thin film in Figure 3.1.

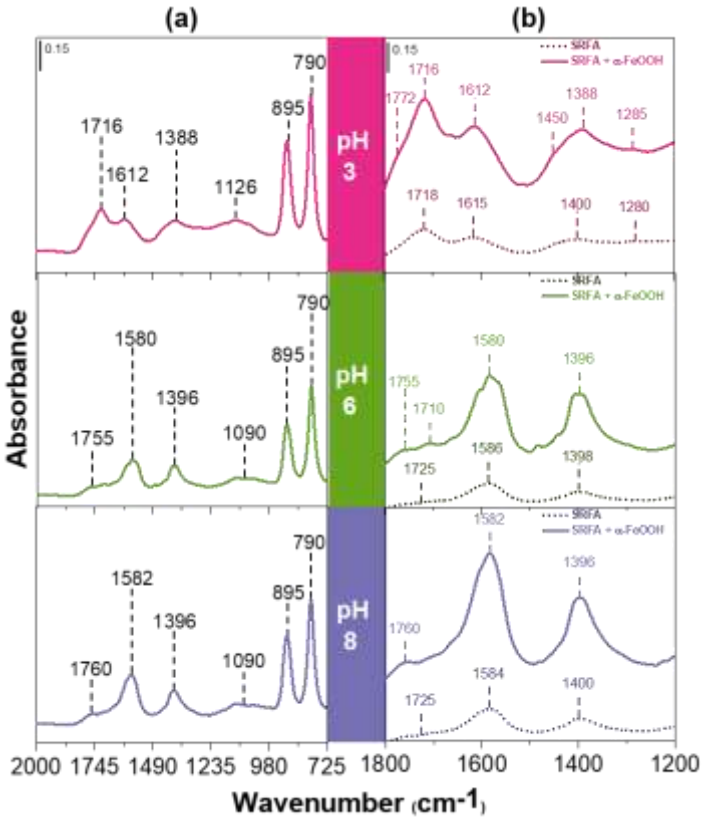

Figure 3.5 ATR-FTIR spectra of SRFA- α-FeOOH thin films prepared from drying solutions at pH 3, 6, and 8. The left panel (a) indicates the range from 725 to 2000 cm^{-1}. The right panel (b) is a comparison between SRFA with and without α-FeOOH in the 1200 to 1800 cm^{-1} spectral region.

Previous studies have identified the ca. 1400 cm^{-1} peak as a result of complexation between the carboxylate anion from SRFA and Fe^{3+}, to form iron fulvate as discussed in Section 3.2.[5,6,21] The bands present in this region in the SRFA thin film have been assigned to the symmetric stretching mode from carboxylate groups, but due to the broad nature of these peaks, it is difficult to determine whether or not a specific vibrational mode is in fact representative of the iron-fulvate complex. The most prominent difference between SRFA films with and without α-FeOOH present

is a shift from a broad, 1396 cm^{-1} peak to a broader, red-shifted 1388 cm^{-1} peak with a more defined shoulder at 1450 cm^{-1}. This broadening can be attributed to the presence of the higher frequency shoulder which is representative of the iron-fulvate complex. This can be seen clearly in Figure 3.5C. Filius *et al.* have suggested that inner-sphere coordination is more likely at low pH, due to the more positively charged mineral surface. Thus, this explains the broader nature of the 1388 cm^{-1} peak in pH 3, compared to pH 6 and 8, due to the formation of cation-fulvic bonds.[12]

When compared with the pH 3 condensed thin film spectrum of SRFA presented in Figure 3.2, there is an observed broadening of this region of ~40 cm^{-1} in the presence of α-FeOOH. This comparison for the pH 3 spectra can be seen in Figure 3.5b. These effects, as suggested by Boily *et al.* could be attributed to inhomogeneous peak broadening, which results from the lack of an evenly distributed monolayer on the surface, suggesting outer-sphere binding modes.[29,30] While the inner-sphere complexation is more likely to be found in highly acidic environments, outer-sphere complexation could also exist simultaneously, and potentially be more dominant in less acidic environments like pH 6 and 8, which is supported by several studies.[4,12,28,29]

While complexation has been successfully detected in pH 3, it is important to note that the α-FeOOH nanoparticles were not washed prior to deposition, resulting in ATR-FTIR spectra that is reflective of potential contributions from SRFA not complexed to the surface. However, the significant increase in spectral intensity remains consistent with what has been observed in the *in situ* measurements, indicating surface interactions between the two components. Most notably, across all pH values, there exist lower intensity shifts in the band positions at the symmetric and asymmetric carboxylate functional groups, which is attributed to complexation to either the surface Fe, surface hydroxyl groups, or aggregation of SRFA. Moreover, it should be highlighted that the collected ATR-FTIR spectra are averages of multiple spectra taken across a large surface. It is

highly likely that the resulting broad spectra obscure any shifts in prominent bands that could provide direct evidence for new binding mechanisms or even phase segregation. Therefore, it is important to probe this interaction using a more spatially resolved technique, such as AFM-IR spectroscopy, to further understand these interactions and understand this complexity.

AFM-IR spectroscopy of SRFA and α-FeOOH *thin films.* The infrared absorption spectra shown in Figure 3.6 differs from that of SRFA thin films alone. Compared to the AFM-IR spectra of SRFA thin films (Figure 3.3), the spectra shown in Figure 3.6 show peaks in the 1400 to 1440 cm^{-1} across all pH values, suggesting the presence of SRFA complexation with the surface *via* inner-sphere coordination.

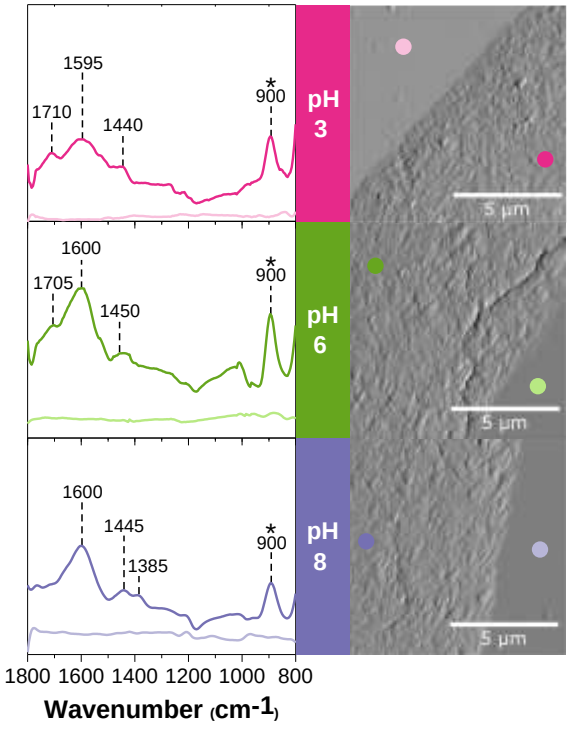

Figure 3.6 AFM-IR height image and corresponding point spectra of SRFA/ α-FeOOH thin films at (a) pH 3, (b) pH 6 and (c) pH 8. The presence of α-FeOOH is confirmed by the peak at 900 cm^{-1}, as indicated by an asterisk (*) in these spectra. These films with both SRFA and α-FeOOH are thicker (on the order of 1.5 µm) compared to those of just SRFA.

While the symmetric carboxylate stretching vibration is not as evident in these spectra, it is important to note the non-zero absorption in this region may suggest a weaker, albeit poorly resolved, spectral contribution is present. There is a prominent shift from 1655 cm^{-1} to 1595 cm^{-1} in the films prepared under acidic conditions at pH 3 as well as a shift from 1590 cm^{-1} to 1600 cm^{-1} in the pH 6 prepared films. These frequency shifts suggest complexation of COO^- functional groups of SRFA to either surface hydroxyls or iron, indicating inner-sphere SRFA adsorption onto α-FeOOH. Based on the spectroscopic evidence from AFM-IR analysis, it can be concluded that the adsorption of SRFA onto α-FeOOH is most likely a combination of both inner and outer-sphere complexation, that is, pH dependent. In addition, it is important to note that these spectra are taken *via* AFM-IR spectroscopy, that allows for highly selective spectral analysis of particular regions of interest compared to an ensemble average that is probed by ATR-FTIR spectroscopy.

In Figure 3.7, a 25x25 point hyperspectral image was collected across a 15x15 μm region. The hyperspectral imaging irradiates each point of the selected region across the full range of the laser, from 800-1800 cm^{-1}. By gathering the relative intensities of absorption of each wavenumber at each point, a heat map can be generated, providing insight into the spatial distribution of select functional groups that are present in different spatial regions.

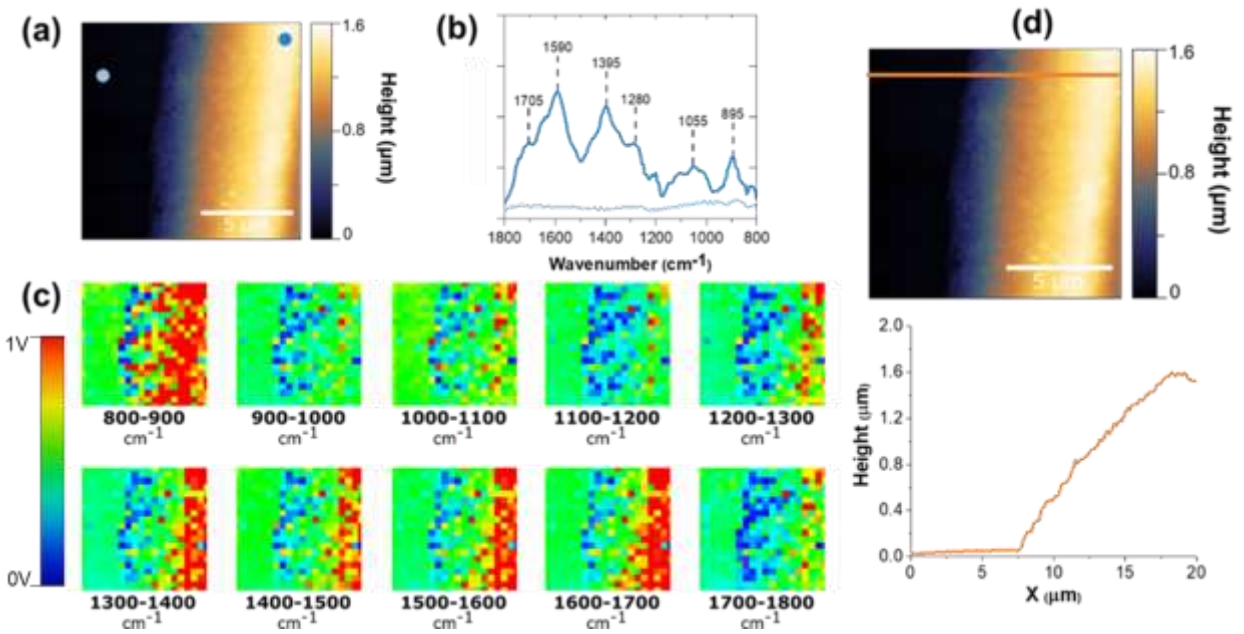

Figure 3.7 AFM-IR hyperspectral imaging of SRFA/α-FeOOH thin film at pH 3. The height image of this 15x15 µm image is shown in (a) where point spectra were collected as shown in (b) both on and off the edge of the thin film; (c) is a 25x25 point hyperspectral map of this region and (d) a line scan and associated height profile across the film is shown.

In Figure 3.7, the heat map in the 800 to 900 cm^{-1} region suggests an abundance of α-FeOOH particles that are within the thin film. Additionally, the functional groups present in SRFA can be found predominantly in the 1300-1400 cm^{-1} and 1500-1700 cm^{-1} range, which is consistent with the highest intensities in the heat maps. The heat map of the 1400-1500 cm^{-1} region, which consists of the range in which metal bonded surface complexation of SRFA is present, contains fewer hot spots than the maps representative of SRFA functional groups. While the presence of hot spots is sufficient evidence for Fe-SRFA complexation, it also shows the presence of α-FeOOH and SRFA – co-located or not in the different regions. The maps indicate that while α-FeOOH is present starting at the edge of the film, SRFA becomes more strongly present towards the inner center of the film. This suggests that when these films are made, through drop-casting and drying, some separation occurs between α-FeOOH and SRFA. The separation of α-FeOOH and SRFA

suggests that even in a thin film, SRFA does not fully coat all of the α-FeOOH particles. Only a small percentage of SRFA may be reacting with the surface, leaving the majority of the macromolecules not interacting with α–FeOOH in the film. The presence of separated α-FeOOH and SRFA aggregates suggests that while SRFA favorably binds to these α-FeOOH interfaces present in these films, they are also prone to form multilayer films, resulting in nanoscale regions of enrichment of SRFA in some regions and enrichment of α–FeOOH. Studies such as Kleber *et al.* have discussed various mechanisms in which organic matter covers mineral surfaces, reporting how NOM often self-organizes onto these surfaces in at least two or more layers, due to its amphiphilic properties.[31] The formation of these multilayer aggregates, therefore, would thus result in decreasing the adsorption onto the mineral surface.[20]

AFM-IR imaging and spectroscopy of SRFA and α-FeOOH *single particles and small aggregates.* AFM images of unreacted α-FeOOH, seen in Figure 3.8, show that α-FeOOH possesses a distinctive long, rod-like shape, which has been resolved as single rods in lower concentrations. These images also indicate that α-FeOOH nanoparticles are susceptible to aggregation as can be seen from the formation of small aggregates in a slightly more concentrated region.

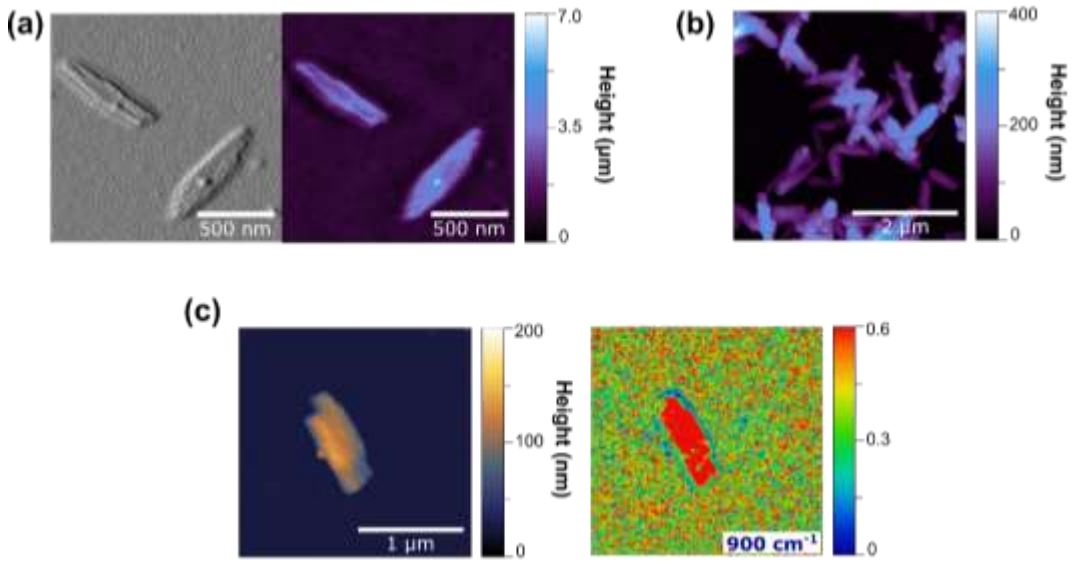

Figure 3.8 AFM-IR images of α-FeOOH on the (a) individual particle level and (b) as clusters. As the α-FeOOH nanoparticles aggregate into clusters, there is also an increase in the overall height. A map at 900 cm^{-1} an α-FeOOH cluster is shown in (c), which is representative of the in/out-of-plane bending modes of O-H of the iron oxyhydroxide (see Figure 3.1). These collection of images and maps are representative of α-FeOOH nanoparticles prior to SRFA exposure.

The spectral map taken at 900 cm^{-1} confirms the presence of α-FeOOH and its corresponding rod-like shape. By using AFM-IR spectroscopy, we are able to identify individual nanoparticles and clusters, using both the physical and chemical information provided by highly resolved images and mapping. The nanoscale spatial resolution offered by this technique can also provide important insights into single particles and small aggregates of a-FeOOH interacting with SRFA.

Figure 3.9 shows images of individual particles and small aggregates of α-FeOOH coated with SRFA. In these single particle maps, there are regions of low-signal, indicating bare α–FeOOH or low coverages of SRFA as well as regions that are indicative of high coverages of SRFA-coated α–FeOOH particles, confirming the inherent heterogenous nature of the surface adsorption process.[32,33] This is in agreement with a recent study by Possinger *et al*. which showed evidence of the spatial separation of organic matter composition in OM-rich regions in the

presence of mineral surfaces.[32] The heterogenous distribution of SRFA along α-FeOOH nanoparticles contributes to this development of a more complex model that more accurately captures the complexities of mineral surfaces and their interaction with NOM.

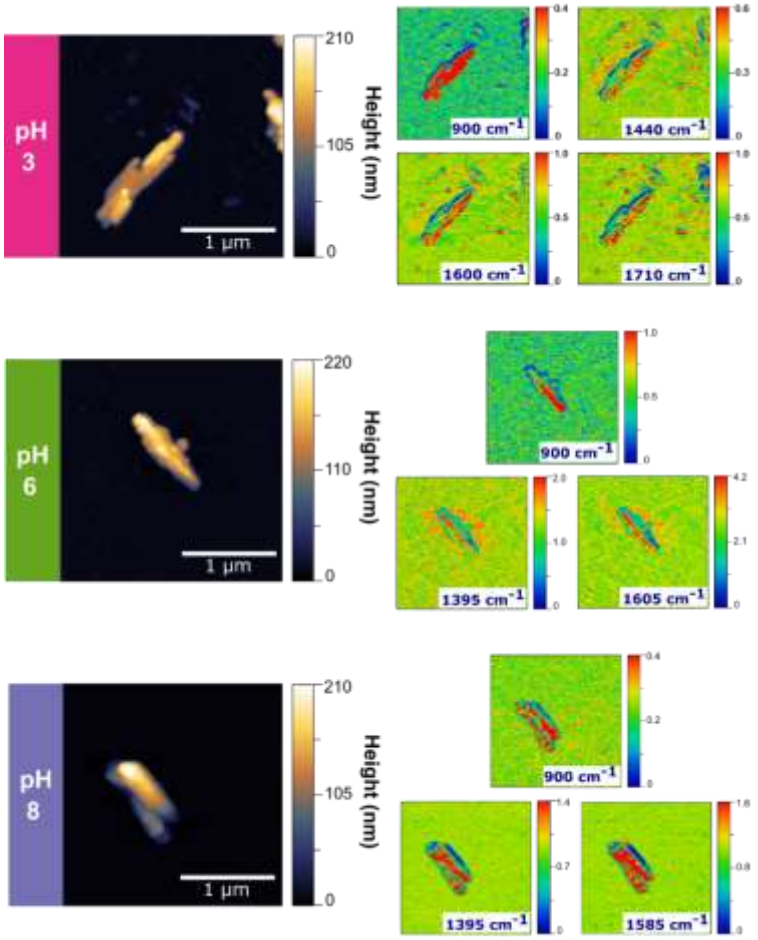

Figure 3.9 AFM-IR height image and corresponding point spectra of single and small clusters of SRFA-coated α-FeOOH particles prepared from solutions of pH (a) 3, (b) 6, (c) 8.

While the intensities of the maps, shown on the right side of Figure 3.9 are relative, they provide insights into the distribution of SRFA. Specifically, each of the maps provides specific functional groups of interest: the O-H bending modes of α-FeOOH, the asymmetric and symmetric carboxylic acid groups, and the protonated carboxylic group for pH 3. As can be seen

by each of the maps, the nanoparticles are partially and not fully coated by SRFA. In addition, there are randomly dispersed "hot" spots shown in red along the image. These spots are not rod-like, suggesting the presence of small aggregates of SRFA. The microspectroscopic capability this technique allows for full confirmation of the presence or absence of α-FeOOH in these images.[23,34,35] While single particle maps indicate heterogeneity on the nanoscale level, there are further efforts needed to understand the spatial distribution and phase segregation of SRFA as a function of pH and other environmental conditions of salinity and temperature. Further development of microspectroscopic techniques on the single particle level can provide scientific insights on spatial heterogeneity that hitherto were unattainable.

3.5 Conclusions

In this study, we utilized two spectroscopic probes – ATR-FTIR spectroscopy and AFM-IR spectroscopy – to better understand SRFA and its interaction with α–FeOOH. These complementary techniques show the importance of pH in the adsorption process and identifies functional groups within the complex sample. The spatially resolved information provided by microspectroscopic analysis allows for the heterogeneity within these samples of thin films of SRFA, thin films of SRFA with α–FeOOH and individual particles or small aggregates of α-FeOOH interacting with SRFA. In each case, there were spatially resolved heterogeneities observed including regions rich of different compounds present within SRFA, segregation of mineral and organic phases, and different coverages of SRFA on the surface of a-FeOOH within single particles. Overall, the findings in this study provide insights into these complex samples on

nanoscale and microscale dimensions that can only be uncovered using micro-spectroscopic probes such as AFM-IR spectroscopy.

3.6 Acknowledgements

Chapter 3, in full, is a reprint of the material published by ACS Earth & Space Chemistry in: Kim, D.; Grassian, V. H. Attenuated Total Reflection-Fourier Transform Infrared and Atomic Force Microscopy-Infrared Spectroscopic Investigation of Suwannee River Fulvic Acid and Its Interactions with α-FeOOH. *ACS Earth Space Chem* **2022**, *6* (1), 81–89.

The research reported here was funded in whole or in part by the Army Research Office/Army Research Laboratory *via* grant #W911NF-19-1-0078 to the University of California, San Diego. Any errors and opinions are not those of the Army Research Office or Department of Defense and are attributable solely to the authors.

3.7 Bibliography

(1) Islam, M. A.; Morton, D. W.; Johnson, B. B.; Angove, M. J. Adsorption of Humic and Fulvic Acids onto a Range of Adsorbents in Aqueous Systems, and Their Effect on the Adsorption of Other Species: A Review. *Sep. Purif. Technol.* **2020**, *247*, 1-19.

(2) Weng, L.; van Riemsdijk, W. H.; Koopal, L. K.; Hiemstra, T. Adsorption of Humic Substances on Goethite: Comparison between Humic Acids and Fulvic Acids. *Environ. Sci. Technol.* **2006**, *40*, 7494–7500.

(3) Jayalath, S.; Larsen, S. C.; Grassian, V. H. Surface Adsorption of Nordic Aquatic Fulvic Acid on Amine-Functionalized and Non-Functionalized Mesoporous Silica Nanoparticles. *Environ. Sci. Nano* **2018**, *5*, 2162–2171.

(4) Yoon, T. H.; Johnson, S. B.; Gordon, E. B. Adsorption of Suwannee River Fulvic Acid on Aluminum Oxyhydroxide Surfaces: An *in situ* ATR-FTIR Study. *Langmuir* **2004**, *20*, 5655–5658.

(5) Gu, B.; Schmitt, J.; Chen, Z.; Liang, L.; McCarthy, J. F. Adsorption and Desorption of Natural Organic Matter on Iron Oxide: Mechanisms and Models. *Environ. Sci. Technol.* **1994**, *28*, 38–46.

(6) Yang, K.; Xing, B. Interactions of Humic Acid with Nanosized Inorganic Oxides. *Environ. Pollut.* **2009**, *157*, 1095–1100.

(7) von Wandruszka, R. Humic Acids: Their Detergent Qualities and Potential Uses in Pollution Remediation. *Geochem. Trans.* **2000**, *1*, 10–15.

(8) Wijenayaka, L. A.; Rubasinghege, G.; Baltrusaitis, J.; Grassian, V. H. Surface Chemistry of α-FeOOH Nanorods and Microrods with Gas-Phase Nitric Acid and Water Vapor: Insights into the Role of Particle Size, Surface Structure, and Surface Hydroxyl Groups in the Adsorption and Reactivity of α-FeOOH with Atmospheric Gases. *J. Phys. Chem. C* **2012**, *116*, 12566–12577.

(9) Rubasinghege, G.; Lentz, R. W.; Scherer, M. M.; Grassian, V. H. Simulated Atmospheric Processing of Iron Oxyhydroxide Minerals at Low PH: Roles of Particle Size and Acid Anion in Iron Dissolution. *Proc. Natl. Acad. Sci. U.S.A.* **2010**, *107*, 6628–6633.

(10) Wang, L.; Putnis, C. V.; Ruiz-Agudo, E.; Hövelmann, J.; Putnis, A. *In Situ* Imaging of Interfacial Precipitation of Phosphate on Goethite. *Environ. Sci. Technol.* **2015**, *49*, 4184–4192.

(11) Saito, T.; Koopal, L. K.; Van Riemsdijk, W. H.; Nagasaki, S.; Tanaka, S. Adsorption of Humic Acid on Goethite: Isotherms, Charge Adjustments, and Potential Profiles. *Langmuir* **2004**, *20*, 689–700.

(12) Filius, J. D.; Lumsdon, D. G.; Meeussen, J. C. L.; Hiemstra, T.; Van Riemsdijk, W. H. Adsorption of Fulvic Acid on Goethite. *Geochim. Cosmochim. Acta* **2000**, *64*, 51–60.

(13) Lehmann, J.; Solomon, D.; Kinyangi, J.; Dathe, L.; Wirick, S.; Jacobsen, C. Spatial Complexity of Soil Organic Matter Forms at Nanometre Scales. *Nat. Geosci.* **2008**, *1*, 238–242.

(14) Sit, I.; Wu, H.; Grassian, Vicki, H. Environmental Aspects of Oxide Nanoparticles: Probing Oxide Nanoparticle Surface Processes Under Different Environmental Conditions. *Annu. Rev. Anal. Chem.* **2021**, 14, 489-514.

(15) Dazzi, A.; Prater, C. B. AFM-IR: Technology and Applications in Nanoscale Infrared Spectroscopy and Chemical Imaging. *Chemical Reviews*. 2017, *117*, 5146-5173.

(16) Mudunkotuwa, I. A.; Minshid, A. Al; Grassian, V. H. ATR-FTIR Spectroscopy as a Tool to Probe Surface Adsorption on Nanoparticles at the Liquid-Solid Interface in Environmentally and Biologically Relevant Media. *Analyst* **2014**, *139*, 870–881.

(17) Dazzi, A.; Glotin, F.; Carminati, R. Theory of Infrared Nanospectroscopy by Photothermal Induced Resonance. *J. Appl. Phys* **2010**, *107*, 1-8.

(18) Dazzi, A.; Prater, C. B.; Hu, Q.; Bruce, D.; Rabolt, J. F.; Marcott, C. Focal Point Review AFM-IR: Combining Atomic Force Microscopy and Infrared Spectroscopy for Nanoscale Chemical Characterization. *Appl Spectrosc.* **2012**, *66*, 1365–1384.

(19) Dinar, E.; Mentel, T. F.; Rudich, Y. The Density of Humic Acids and Humic like Substances (HULIS) from Fresh and Aged Wood Burning and Pollution Aerosol Particles. *Atmos. Chem. Phys.* **2006**, *6*, 5213–5224.

(20) Yoon, T. H.; Johnson, S. B.; Brown, G. E. Adsorption of Organic Matter at Mineral/Water Interfaces. IV. Adsorption of Humic Substances at Boehmite/Water Interfaces and Impact on Boehmite Dissolution. *Langmuir* **2005**, *21*, 5002–5012.

(21) Trueblood, J. V.; Alves, M. R.; Power, D.; Santander, M. V.; Cochran, R. E.; Prather, K. A.; Grassian, V. H. Shedding Light on Photosensitized Reactions within Marine-Relevant Organic Thin Films. *ACS Earth Sp. Chem.* **2019**, *3*, 1614–1623.

(22) Fu, H.; Quan, X. Complexes of Fulvic Acid on the Surface of Hematite, Goethite, and Akaganeite: FTIR Observation. *Chemosphere* **2006**, *63*, 403–410.

(23) Cwiertny, D. M.; Hunter, G. J.; Pettibone, J. M.; Scherer, M. M.; Grassian, V. H. Surface Chemistry and Dissolution of & alpha-FeOOH Nanorods and Microrods: Environmental Implications of Size-Dependent Interactions with Oxalate. *J. Phys. Chem. C*, **2009**, *113*, 2175–2186.

(24) Assemi, S.; Hartley, P. G.; Scales, P. J.; Beckett, R. Investigation of Adsorbed Humic Substances Using Atomic Force Microscopy. *Colloids Surfaces A Physicochem. Eng. Asp.* **2004**, *248*, 17–23.

(25) Namjesnik-Dejanovic, K.; Maurice, P. A. Atomic Force Microscopy of Soil and Stream Fulvic Acids. *Colloids Surfaces A Physicochem. Eng. Asp.* **1997**, *120*, 77–86.

(26) Alvarez-puebla, R. A.; Garrido, J. J.; Aroca, R. F. Surface-Enhanced Vibrational Microspectroscopy of Fulvic Acid Micelles. **2004**, *76*, 7118–7125.

(27) Kang, S.; Xing, B. Humic Acid Fractionation upon Sequential Adsorption onto Goethite. *Langmuir* **2008**, *24*, 2525–2531.

(28) Persson, P.; Axe, K. Adsorption of Oxalate and Malonate at the Water-Goethite Interface: Molecular Surface Speciation from IR Spectroscopy. *Geochim. Cosmochim. Acta* **2005**, *69*, 541–552.

(29) Boily, J. F.; Persson, P.; Sjöberg, S. Benzenecarboxylate Surface Complexation at the Goethite (α-FeOOH)/Water Interface: II. Linking IR Spectroscopic Observations to Mechanistic Surface Complexation Models for Phthalate, Trimellitate, and Pyromellitate. *Geochim. Cosmochim. Acta.* **2000**, *64*, 3453–3470.

(30) Yates J. T. Jr.;Madey, T. *Vibrational Spectroscopy of Molecules on Surfaces*; Plenum Press., **1987**.

(31) Kleber, M.; Sollins, P.; Sutton, R. A Conceptual Model of Organo-Mineral Interactions in Soils: Self-Assembly of Organic Molecular Fragments into Zonal Structures on Mineral Surfaces. *Biogeochemistry* **2007**, *85*, 9–24.

(32) Possinger, A. R.; Zachman, M. J.; Enders, A.; Levin, B. D. A.; Muller, D. A.; Kourkoutis, L. F.; Lehmann, J. Organo–Organic and Organo–Mineral Interfaces in Soil at the Nanometer Scale. *Nat. Commun.* **2020**, *11*, 1–11.

(33) Johannes Lehmann; Dawit Solomon. Organic Carbon Chemistry in Soils Observed by Synchrotron-Based Spectroscopy. In *Developments in Soil Science* **2010**, 289–312.

(34) Rubasinghege, G.; Kyei, P. K.; Scherer, M. M.; Grassian, V. H. Proton-Promoted Dissolution of α-FeOOH Nanorods and Microrods: Size Dependence, Anion Effects (Carbonate and Phosphate), Aggregation and Surface Adsorption. *J. Colloid Interface Sci.* **2012**, *385*, 15–23.

(35) Sharan, C.; Khandelwal, P.; Poddar, P. The Mechanistic Insight into the Biomilling of Goethite (α-FeO(OH)) Nanorods Using the Yeast Saccharomyces Cerevisiae. *RSC Adv.* **2015**, *5*, 91785–91794.

CHAPTER 4
ANALYSIS OF MICRO- AND NANOSCALE HETEROGENEITIES WITH ENVIRONMENTALLY RELEVANT THIN FILMS CONTAINING BIOLOGICAL COMPONENTS, OXYANIONS, AND MINERALS USING AFM-IR SPECTROSCOPY

4.1 Abstract

Minerals in groundwater interact with various chemical and biological species including organic matter, proteins, and prevalent oxyanions, resulting in surface coatings and thin films of these different components. Surface interactions and the surface adsorption of these components on both oxide and oxyhydroxide iron surfaces have been widely investigated using a variety of spectroscopic methods. Despite these numerous studies, there still remains uncertainty with respect to interactions between these individual components, as well as heterogeneities and phase segregations within these thin films. In this study, we investigate mixtures containing Fe-containing minerals, proteins, and oxyanions to better understand surface interactions and phase segregation using Atomic Force Microscopy Infrared (AFM-IR) spectroscopy. The results of this study show that AFM-IR spectroscopy can identify both nano- and microscale heterogeneities present within these thin films that are difficult to discern with other more conventional techniques such as ATR-FTIR spectroscopy due to phase segregation and mineral surface interactions. Overall, AFM-IR spectroscopy provides insights into multi-component environmental films that are difficult to uncover using other methodologies. This method has the potential to differentiate between bound and unbound toxic species as well as biological components, including environmental DNA, which can be used to assess the fate and transport of these species in the environment.

4.2 Introduction

Groundwater contains a myriad of different biological and chemical species – both natural and anthropogenic – including organic matter, proteins, oxyanions, and chemical contaminants. Over the past few decades, the interactions of each of these components have been examined in laboratory studies with commonly found minerals in the environment.[1–4] These studies provide great insight into molecular level interactions at geochemical surfaces.[5,6] Several factors that impact these mineral interactions including the nature of the mineral, specific mineral surface planes, adsorbed water and solution pH and ionic strength. All of these factors alter the dynamics of the surface adsorption process for mineral surfaces.[7] However, few studies have probed multi-component systems. as competitive interactions between different species can drive the surface chemistry of mineral surfaces.[8–13]

In the environment, biological components represent an important fraction of these different species and range from free amino acids to proteins, to environmental DNA (eDNA) and to entire organisms such as bacteria.[10] Bovine Serum Albumin (BSA) has been chosen in several studies as a representative model protein due to its stability in the environment as well as its natural state at circumneutral pH.[14] BSA has a molar mass of 66 kDa and an isoelectric point of 4.5 to 5.0, which is within the range of many other proteins extracted from groundwater.[15,16]

Besides biological components, the interaction of oxyanions, including phosphate, sulfate and carbonate, and mineral surfaces have been widely investigated.[17–20] The protonation states of these anions change as a function of solution pH and can impact the coordination to the surface, whether outer versus inner sphere and mono- or bi-dentate. Sulfate speciation on oxide surfaces has, in particular, been widely studied by vibrational spectroscopy due to its affinity to adsorb onto mineral surfaces.[21] Changes in the vibrational modes upon adsorption provide insights into the

decrease in symmetry, change in protonation state and nature of the coordination mode. Past studies have reported sulfate speciation to be highly sensitive to factors such as pH, dehydration, and ionic strength, which has resulted in many proposed mechanisms of sulfate coordination onto iron-containing surfaces, such as goethite.[22–28] Sulfate can also block sites for surface adsorption of other species present, which can affect the availability of trace metals in the environment.[15] Additionally, interactions between biological species like BSA, and phosphate, another commonly studied oxyanion, have been investigated, but BSA interactions with sulfate have yet been explored.[29] These different interactions can result in the formation of different complexes that have vibrationally distinct spectral features.[30]

In this study, we investigate thin films of BSA protein, sodium sulfate, and goethite to determine the degree of heterogeneity in these films. Dried, thin films on the order of several hundred nanometers thick have been prepared by forming suspensions of different environmentally-relevant components at a circumneutral pH. While more typical vibrational techniques like ATR-FTIR spectroscopy can provide spectral characterization of the average surface interactions occurring within these films, further insights into the micro- and nanoscale heterogeneities are explored with AFM-IR spectroscopy. In particular, phase segregation and different mineral interactions are probed through localized point spectra and larger area chemical mapping. These results provide information on spatial scales that have not been previously explored and suggest insights can be gained concerning phase segregation, mineral interactions, bioavailability, and transport of different biological and chemical species in the environment. Given that this method has the potential to differentiate between bound and unbound species, it can potentially be used to assess not only the fate but also the transport of such species in the environment.

4.3 Experimental Methods

Sample preparation and source of materials. In these studies, samples for both AFM-IR spectroscopy and complementary ATR-FTIR spectroscopy were prepared for analysis for both techniques. Stock solutions were made for each component at a concentration of 1 mg/mL for BSA (Sigma Aldrich) and sodium sulfate (Fisher Scientific) and 0.3 mg/mL for goethite (Alfa Aesar) in milli-Q water. Single component thin films were prepared by drop-casting 1 mL aliquots of each solution onto an AMTIR (Amorphous Material Transmitting Infrared Radiation) crystal for ATR-FTIR analysis and 5 µL onto a cleaned silica wafer for AFM-IR analysis.

For AFM-IR and ATR-FTIR analysis, solutions were allowed to dry for 5 hours and 3 hours, respectively; the differences in the drying times were dependent on the differences in the volume of solution as well as the surface area coverage of each substrate. For the multi-component thin films, mixtures containing a 1:1 volume ratios, or 1:1:1 volume ratios for two- and three-component systems, respectively, were prepared with the components of interest from the initial stock solutions. For goethite containing samples, the suspension was probe-sonicated for 15 seconds, inverted, and then repeated once more to facilitate the mixing of goethite particles with the solution. Post sonication, the solution turned into an opaque, yellow color, indicating proper mixing of the nanoparticles. Once the mixtures were prepared, the same procedure for drop-casting and drying was applied for thin film formation, as adapted in previous studies, ensuring comparable film deposition between both substrates. All of the data collected and presented here have been selected as the most representative from a triplicate set of measurements that have been taken from at least three different samples and regions. In addition, there are no high safety hazards that were encountered during the course of this sample preparation.

Atomic Force Microscopy-Infrared (AFM-IR) spectroscopy. AFM-IR spectroscopy is a microspectroscopic technique that utilizes a sharp AFM probe tip which is typically on the order of tens of nanometers in diameter, that is usually at the end of a cantilever. For infrared measurements, this technique is based on the principle of photothermal induced resonance, where the IR absorption signal is transduced from the cantilever oscillation upon photothermal expansion of the sample in a nondestructive and nonperturbative manner.[31,32] Using a nanoIR2 microscopy system (Bruker, Anasys – Santa Barbara, CA) equipped with a mid-IR tunable quantum cascade laser (QCL), samples were analyzed after drying onto a silica wafer. Images, PTIR spectra, and spectral maps were collected in primarily contact mode using gold-coated silicon nitride probes, with tip radii of ~30 nm, a resonant frequency of 75 kHz and a spring constant of 1 to 7 N/m. PTIR spectra were collected at a resolution of 5 cm^{-1}. For point spectra, the data is plotted as absorbance, which is proportional to the change in the photodiode as a result of the cantilever deflection, as a function of wavenumber. Absorbances in these PTIR spectra are related to the deflection of the cantilever upon sample absorption of IR light. For imaging and chemical mapping, the scan rate was set to 0.2 Hz. AFM images and IR maps were prepared using the Gwyddion software and the spectra presented were co-averaged from 5 spectra and were filtered using a 10-point, 3rd order polynomial, Savitzky-Golay algorithm.

Attenuated Total Reflectance Fourier Transform Infrared (ATR-FTIR) spectroscopy. ATR-FTIR spectroscopy is based upon the principle of total internal reflection between an optically dense and an optically rare medium.[8] For these experiments, an AMTIR crystal, an internal reflecting element, that is housed in a horizontal, Teflon-coated flow cell (Pike Technologies) configured for multiple reflections, is used. Specifically, an AMTIR crystal was chosen for its high effective path

length, resulting in high spectral sensitivity. It should be noted that while the flow cell can hold 500 µL when capped, when open, it can hold up to a solution volume of 1 mL. Dried, thin films were prepared as described previously and after drying was complete, infrared spectra were averaging over 100 scans at a resolution of 4 cm^{-1} over a spectral range from 725 to 4000 cm^{-1}.

4.4 Results and Discussion

Comparison of AFM-IR spectra of single component BSA, sulfate, and goethite thin films. AFM-IR of thin films of BSA, sulfate and goethite are shown in Figure 4.1.

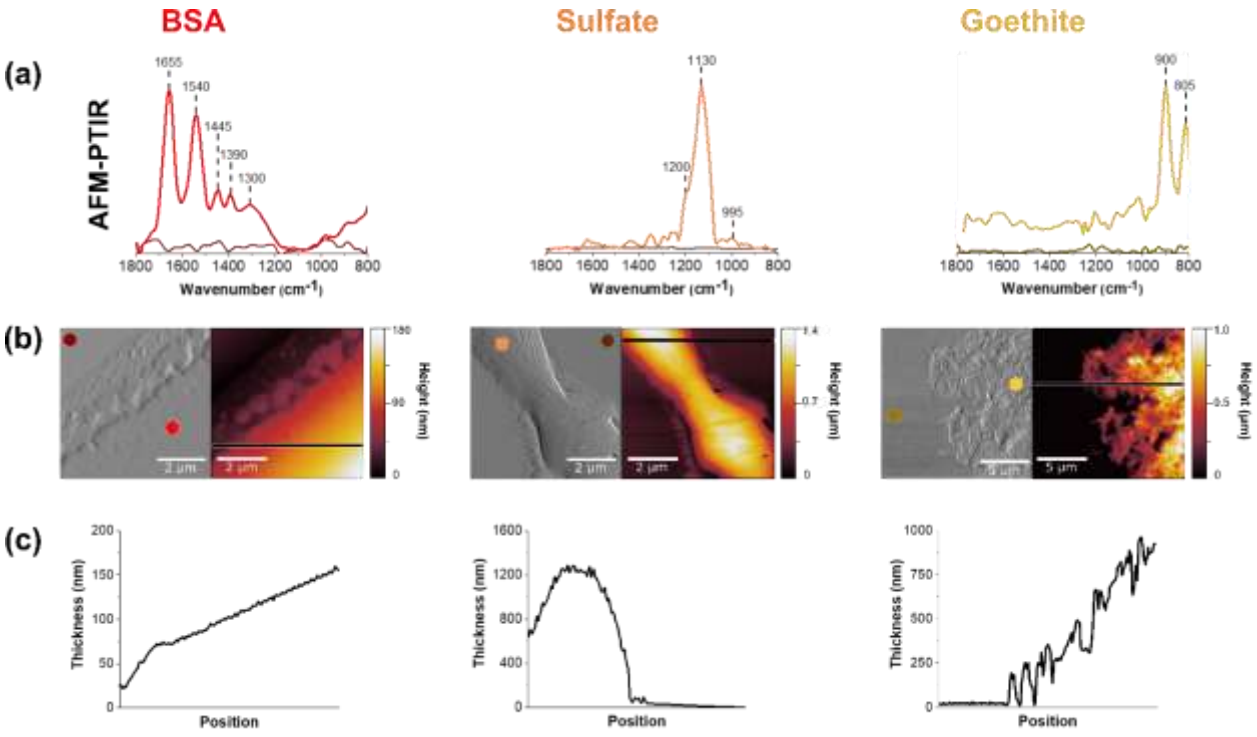

Figure 4.1. (a) AFM-IR spectra of dried, thin films of BSA, sodium sulfate, and goethite on a silica wafer substrate, respectively. (b) AFM images are shown in both height (left) and deflection (right) modes. The PTIR spectra on and off of each of these thin films are shown. (c) The black line marked on each AFM height image indicates where the height profile was taken.

The amide I and II vibrational modes, representative of proteins, are observed at ca. 1655 cm^{-1} and 1540 cm^{-1}, respectively, in the AFM-IR spectra.[33,34] It is seen in the sulfate spectrum that there is a strong absorption band at 1132 cm^{-1}, which corresponds to the υ_3 asymmetric sulfate stretching vibration. Sulfate speciation and symmetry are influenced by environmental factors such as phase and hydration state. In its aqueous form, sulfate oxyanions are tetrahedral in geometry, belonging to the T_d symmetry. Within these oxyanions, there is a nondegenerate, symmetric vibration, υ_1, and a triply degenerate, asymmetric vibration, υ_3, in the spectral region from ca. 975 cm^{-1} to 1100 cm^{-1}. Here, the υ_1 band is IR active at 994 cm^{-1}, whereas the υ_3 band is IR active at 1132 cm^{-1}.[23,27,35,36]

The peak positions shown in Figure 4.1 are attributed to a dehydrated film. In particular, Figure 4.1a shows a broad, asymmetric peak at 1132 cm^{-1} with a shoulder at 1168 cm^{-1} and a sharp peak at 994 cm^{-1}. These changes are related to the distortion of the tetrahedral geometry as well as the shift to 994 cm^{-1}, for the nondegenerate υ_1 band, as sodium sulfate becomes more crystalline.[23,35,36] For the goethite thin film, the ATR-FTIR spectrum shows two sharp peaks present at 805 cm^{-1} and 900 cm^{-1}.[37] These bands are attributed to the in/out-of-plane bending modes of the bulk surface hydroxyls within the iron oxyhydroxide. The AFM-IR spectrum shows peaks at the same wavenumbers, but the full peak at 805 cm^{-1} cannot be seen due to the limited range of the laser being used, starting at 800 cm^{-1}. The vibrational peak assignments of these spectra are summarized in Table 4.1.

Table 4.1 Select vibrational peak assignments for AFM-IR and ATR-FTIR spectra of BSA, sodium sulfate, and goethite.[14,15,23,26,36,37]

	Wavenumber (cm^{-1})	Vibrational peak assignment
BSA	1654 to 1656	Amide I
	1534 to 1540	Amide II
Sulfate	1132 to 1140	Asymmetric sulfate stretch (υ_3)
	994 to 995	Symmetric sulfate stretch (υ_1)
Goethite	805	In-plane O-H bend
	900	Out-of-plane O-H bend

Further chemical analysis using AFM-IR spectroscopy of these single component thin films are shown in Figure 4.1B. There is overall agreement with these single component, nanoscale point spectra and ATR-FTIR spectra collected but it should be noted that they are not identical, as shown in Figure 4.2, below.

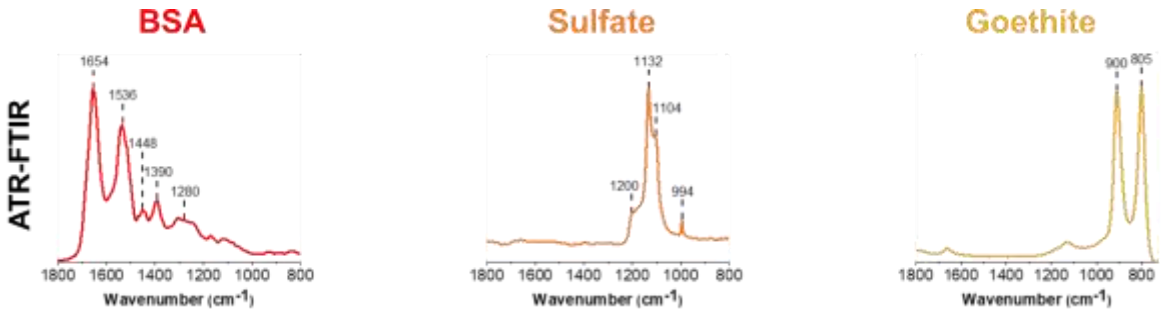

Figure 4.2 Normalized ATR-FTIR spectra of thin films of BSA, sulfate, and goethite on an AMTIR crystal.

For example, in the BSA spectra, differences in the 1655/1540 cm^{-1} peak ratio, i.e., the ratio in intensity of the Amide I/Amide II band can be observed. Since AFM-IR point spectra probes the "local" environment, it can give slightly different spectral measurements compared to the bulk ATR-FTIR spectra. The two techniques also operate under different principles, one being a photothermal technique and the other, an optical absorption technique. This can result in peaks

that differ in intensity and frequency. However, it is important to recognize that they are in good agreement with each other.

In addition to point spectra, AFM-IR spectroscopy offers physical insight into these films as shown in Figure 4.1c, and 1d. As can be seen by the height images in Figure 4.1c, these films range in thickness from several hundreds to thousands of nanometers. Images are shown in both height and deflection mode, and two-point spectra were taken on each 5x5 μm image- one spectrum on the film and the other on the substrate. In addition, the morphologies of each of the thin films are seen to be distinct from each other. While the BSA film is smooth and has a monotonic increase in height, the sodium sulfate film is over a smaller region and is thicker on the order of 1.4 mm at the highest point. The BSA film has a root mean square roughness of 240 nm and can also be qualitatively examined by the smoothness of the line scan across the region. It should also be made clear that the BSA height profile begins at 25 nm in the film. The height profile increases steadily in thickness and the line is straight, contrasted to that of the sulfate film where there are significantly tall features with a more jagged profile. This suggests that aggregates in the sulfate image are a result of sodium sulfate crystallization as the film dried out from an initial, aqueous solution.[38] For the goethite thin film, individual rods can be resolved in the goethite thin film, consistent with the known morphology of goethite particles.[37,39] One consistent behavior between all three films is the gradual increase in film thickness from the edge of the film towards the center due to the drop-cast and drying methods was used to prepare these films.

Figure 4.3 shows an analysis of a BSA thin film as a function of thickness across the region of interest. Although the BSA thin film appears smooth and homogenous, a larger image size was specifically chosen to measure point spectra with increasing film thickness across the film. Figure 4.3b shows a compilation of 15 point spectra taken across the 30x30 μm film, as a function of

wavenumber, absorbance, and thickness. The limit of detection as well as detection saturation can be determined to be ~50 nm and ~400 nm, respectively. This was determined by comparing the signal-to-noise ratios (SNR) of groups of spectra. For example, the limit of detection for this particular film was determined by a significant decrease in the SNR, whereas the detection saturation was determined by a significant increase in SNR.[40,41] Furthermore, these estimates can be quantified by plots that show the relationship between increasing signal and BSA film thickness. Figure 4.3c shows how these plots are nonlinear. Instead of the signal increasing linearly with increasing thickness, the signal increases monotonically with film thickness initially and then saturates.[42] The dashed lines in these plots represent linear fits for film thicknesses below 400 nm, prior to the plateau observed for film thicknesses above ca. 400 nm. The differences in the slopes of each line directly correlates with the relative intensity of each of the vibrational modes analyzed.

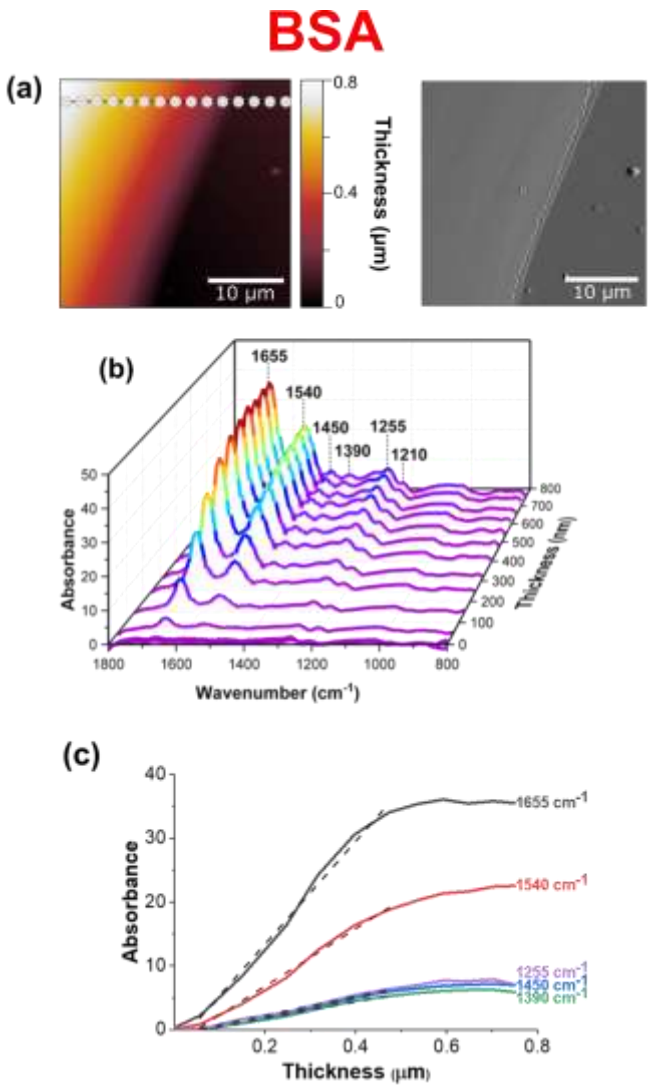

Figure 4.3 Analysis of a thin film of 1 mg/mL BSA. The 2D height and corresponding deflection images are shown in (a). The AFM image is taken at the edge of the film in order to show the clear contrast between on and off the film. (b) is a compilation of 15 AFM-IR spectra plotted as a function of absorbance, wavenumber, and film thickness. The relationship between the absorbance intensity of the different vibrational bands found in BSA is shown as a function of thickness in (c). The darker, dotted lines represent a linear fit to the portion of the spectra below 400 nm as the signal saturates at ca. 400 nm. The signal-to-noise ratio falls below 3 at a thickness of 50 nm.

ATR-FTIR spectroscopy of multi-component thin films. For multi-component thin films, mixtures were prepared in solution and then dried to form thin films containing different components (see Experimental Methods for more detail on sample preparation). The ATR-FTIR spectra of these

different films are shown in Figure 4.4. Spectral signatures of each of the components are clearly identified, as confirmed by the peak assignments presented in Table 4.1.

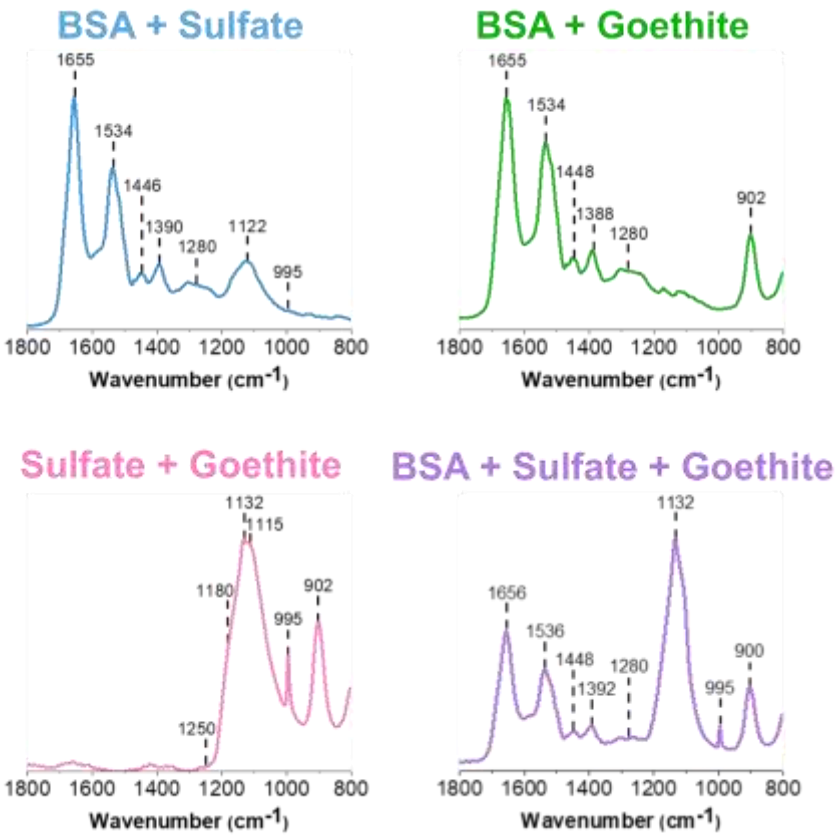

Figure 4.4 Normalized ATR-FTIR spectra of two and three-component thin films of BSA, sodium sulfate, and goethite.

First, it is important to establish any similarities and differences between the single component spectra and these two and three component spectra. The BSA and sulfate spectrum (blue) presented in Figure 4.4 contains the characteristic features of its two components. BSA, as indicated by the 1655 cm^{-1} and 1534 cm^{-1} bands, and sulfate, as indicated by the 1122 cm^{-1} band. Compared to the reference single component BSA and sodium sulfate spectra presented in Figure 4.2, the major difference is in the shift and broadening of the sulfate band, which shifts from 1132 cm^{-1} to 1122 cm^{-1} and the relatively weak presence of the 995 cm^{-1} band. Given the IR spectrum

shown in Figure 4.4, it is difficult to support the presence of the same, sharp 995 cm^{-1} band. However, its inconsistent presence in sulfate-containing systems suggests that it is most likely related to changes in the symmetry of the anion, protonation state and intermolecular interactions. While the interaction of BSA and sodium sulfate has not been studied extensively, spectrally, the speciation of sodium sulfate, such as its crystallization, appears to be affected by the presence of the protein. Furthermore, the broadening suggests there may be some interaction between the negatively charged sulfate anion with positively charged lysine and arginine residues on the outer surface of the protein. Hydrogen bonding and other non-ionic interactions most likely comprise these interactions.[43–45]

Comparing the BSA and goethite spectrum (light green) in Figure 4.4 to that of BSA and goethite alone (Figure 4.2), there are no differences in the relative peak intensities and ratio of Amide I/Amide II in the BSA region. The presence of goethite is indicated by the 900 cm^{-1} peak and the ca. 800 cm^{-1} peak shifts below the region of the laser used for these measurements. Overall, this assessment aligns with what has been proposed by Schmidt *et al.*, where it was suggested that a deconvolution of the Amide I and Amide II peaks has indicated BSA adsorption onto goethite as a result of conformational changes, that cannot be distinguished within the broad band.[15] Furthermore, past studies have also shown BSA adsorption onto iron-containing mineral oxide surfaces from conformational changes, mainly *via* electrostatic interactions.[46–48]

For the sodium sulfate and goethite spectrum (pink), there are some notable changes in the sulfate region compared to the BSA/sodium sulfate spectrum discussed above. For example, there is clear evidence for a disruption in the sodium sulfate symmetry, as seen by the sharp feature at 995 cm^{-1}. Another change is the relative enhancement of the intensity of the sulfate peak at 1132 cm^{-1}, along with broadening of the peak compared to the reference sulfate spectrum presented in

Figure 4.2. This broadening serves as evidence of coordinated sulfate to goethite nanoparticles, as the band is more symmetric than asymmetric. Previous studies have associated sulfate adsorption onto goethite with monodentate or bidentate bridging mechanisms, which is accompanied by the splitting of the major v_3 symmetric stretch. While these bands are not clearly resolved, there is an emergence of shoulders in the spectra at 1115 cm^{-1} and 1180 cm^{-1} along with a major 1132 cm^{-1} band which suggests a combination of sulfate crystallization as well as inner-sphere bridging occurring at the surface.[23,36]

Observing an inner-sphere binding mechanism at a circumneutral pH may appear to be inconsistent with past studies which have concluded that sodium sulfate adsorption in aqueous conditions follows an inner-sphere binding mechanism in acidic environments, and an outer-sphere binding mechanism as pH increases. However, the reported findings here are from dried, thin films of sulfate and goethite at a circumneutral pH, which is a non-acidic environment. For dried films such as those that are presented in this manuscript, the effect of dehydration on potential interactions must be considered.[23] Paul *et al.* has reported that hydrated mineral surfaces can become more acidic as a function of drying, indicating that the dehydration can result in a potential acidification of the goethite thin film. It was proposed that this is a result of the dissociation of water adsorption on polarizable metal cation sites, which, in this case, would be Fe.[24,49] Therefore, this subsequent proton accumulation is likely responsible for creating a slightly more acidic environment, allowing for such binding to occur. The differences between coordinated and non-coordinated sulfate can be clearly identified from differences in broadness and presence of shoulders between the ATR-FTIR spectra of sodium sulfate and sodium sulfate/goethite in Figures 4.2 and 4.4 respectively. However, within the sodium sulfate/goethite thin film, there could also exist free, “uncoordinated sulfate” (used as a general term here to distinguish from surface

coordinated and crystalline sulfate) within different microenvironments present in the film. This serves as evidence as to why utilizing microspectroscopic tools such as AFM-IR spectroscopy is crucial to further exploring these heterogeneities.

The three component ATR-FTIR spectrum (purple) shown in Figure 4.4, clearly shows each of the three components as evident by distinct absorption bands: BSA at 1656 cm^{-1}, sulfate at 1132 cm^{-1}, and goethite at 900 cm^{-1}. The most prominent difference between this multicomponent spectrum compared to both of its single and two component systems is again the clear enhancement of the sulfate peak indicating interactions with goethite as noted above as well as crystallization of sodium sulfate, as discussed for the two-component spectrum of sulfate and goethite. The shape and intensity of the sulfate region centered at 1132 cm^{-1} does not appear to resemble exactly the two component systems but instead appears to be a close combination of the different spectra, suggesting that specific interactions may be occurring in these films. The ATR-FTIR technique can provide important chemical information on the macroscopic adsorbate-mineral interactions, including the type of coordination occurring on the surface of goethite. However, this technique is limited in detecting the heterogeneities present across the system, which are features that can only be exploited *via* micro-spectroscopic probes such as AFM-IR spectroscopy, increasing the level of chemical complexity that can be achieved.

AFM-IR spectroscopy of a BSA and sodium sulfate thin film. In Figure 4.5, data collected for a thin film of BSA and sodium sulfate with AFM-IR spectroscopy are shown. The height and deflection image in Figure 4.5a show an interesting tee-shaped aggregate that has arranged itself onto a smoother and thinner underlying film. This aggregate is the main contributor to the tallest feature of this image, with a thickness of 525 nm. This appears to be crystalline with jagged edges, of

varying sizes and shapes, that resemble those previously observed from the sodium sulfate thin film. In this 5x5 µm image, a total of 4 point spectra were taken – 3 on the film itself and one on the substrate.

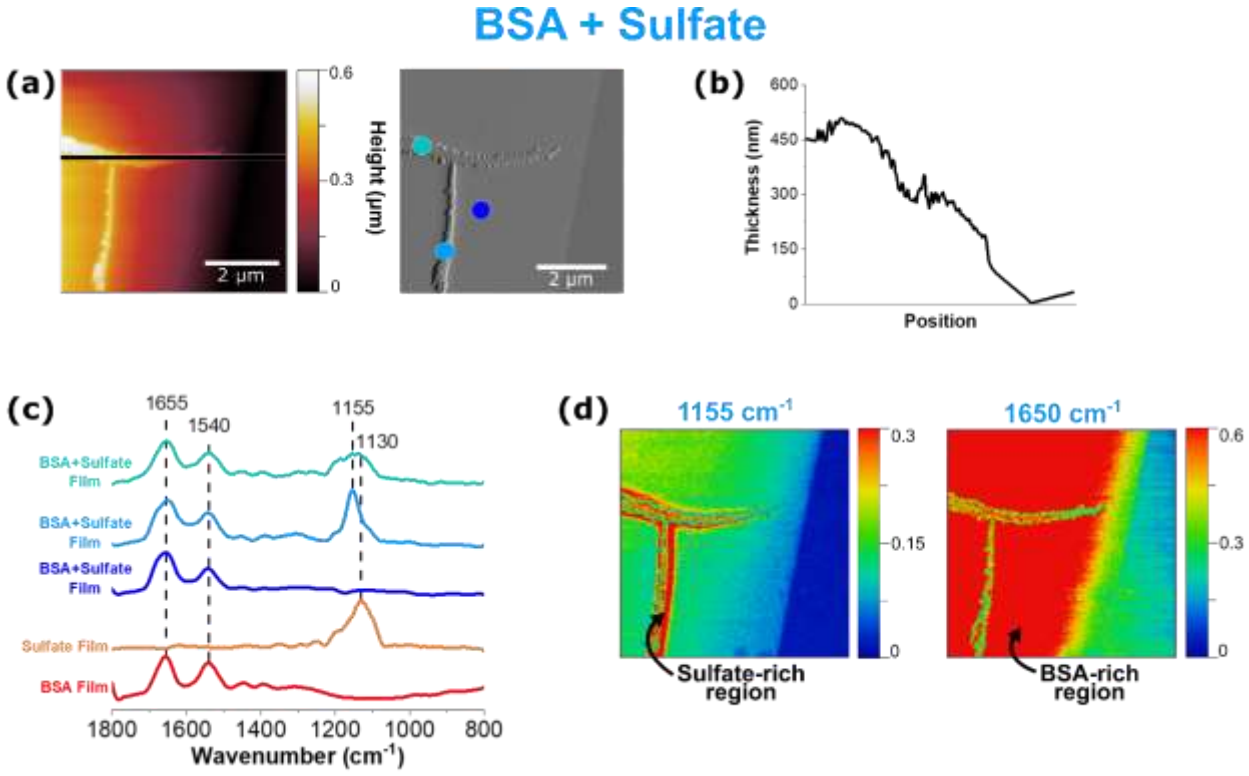

Figure 4.5. AFM-IR images, point spectra and spectral maps of a BSA and sodium sulfate thin film. (a) shows the height and deflection image of the 5x5 µm region and (b) represents the height profile across the region. (c) shows point spectra taken across the surface, where the colors of the dots on the deflection image correspond to line colors of the corresponding PTIR spectra. In particular, Film 1, Film 2 and Film 3 seem to suggest different films. Spectral heat maps are seen in (d), at representative wavenumbers of sulfate at 1155 cm^{-1} and BSA at 1650 cm^{-1}.

In Figure 4.5, each PTIR spectrum shows various combinations of BSA and sodium sulfate spectral features. However, the point spectra shown in Figure 4.4c show much more variation in not only the intensity of the peaks but also the shape and ratio between these two components. For spectral mapping, 1155 cm^{-1} was selected because it was the common band present in all of the

sulfate-attributed spectra, that also included the 1130 cm^{-1}, which has been shown to be representative of both crystalline and non-coordinated sulfate. Maps at representative wavenumbers confirm that the T-shaped aggregate is indeed sulfate while the smoother areas of the film are BSA.

Each of the point spectra taken on in the film provides unique information. The dark blue point spectrum indicates a region that is only BSA, which is consistent as the red "hot" spot on the 1650 cm^{-1} map as well as the position on the smooth film as visualized by the deflection image. However, the remaining two spectra (light blue and teal) are taken on different parts of the sulfate aggregate. While the light blue spectrum shows a singular, sharp peak at 1155 cm^{-1}, the teal spectrum shows a very broad double peak. The differences in relative peak intensity, peak shift, and peak shape in the sulfate band suggest changes in sulfate speciation and interaction in the presence of and with BSA, respectively. AFM-IR spectroscopy allows for infrared mapping by tuning and fixing the laser at a particular wavenumber of interest as it scans across a particular region. While the regions color-coded in red indicate high relative absorbance, the regions color-coded in blue indicate low to no absorbance at the particular wavenumber of interest. Using this information, a heat map is generated.

From this information, we can deduce the presence of an interaction between these two components, as discussed previously from similar observations made from sulfate peak broadening and lack of variability in the reference sulfate spectra, as seen in ATR-FTIR spectra presented in Figure 4.1. The physical, crystalline features on this film suggest the presence of sodium sulfate crystallinity. However, the absence of a strong, sharp 995 cm^{-1} peak, which has been used to identify sodium sulfate crystallinity, is clear. While this result appears to be contradictory to previous statements, the absence of this peak can be attributed to three potential reasons: 1) there

are weaker interactions present, that do not alter the morphological features of the sodium sulfate crystals or that preserves the phase; 2) AFM-IR spectroscopy is unable to detect detailed physical differences between crystalline sulfate and uncoordinated sulfate and; 3) sulfate crystallinity is much more complex than is currently known, and should not absolutely be defined only from a chemical perspective, such as the presence of the 995 cm^{-1} peak, but rather as shifts in the peak location and shape, as a whole. Moreover, it is important to highlight this heterogeneity that is detected *via* AFM-IR spectra, differing vastly from what could be discerned from the ATR-FTIR spectrum in Figure 4.4. There is also spectral evidence of BSA in each of those points, which suggests two possible modes of microphase segregation: 1) sodium sulfate crystals have arranged themselves on top of the BSA film and 2) there are smaller aggregates of BSA embedded in the larger, sodium sulfate crystals.

AFM-IR spectroscopy of a BSA and goethite thin film. The ability to take localized, point spectra on nanometer length scales allows the investigation of heterogeneity of mineral-containing thin films. BSA and goethite films are shown in Figure 4.6. The images and line scan in 5a and 5b show the presence of goethite as well as an increase in the height image from 200 nm to 600 nm, respectively. This increase in thickness can be attributed directly to the presence and aggregation of rod-like goethite nanoparticles, which can be resolved in the corresponding deflection image and offers more contrast of the region of interest. It can be seen that the goethite nanoparticles cluster in different regions including on the edge of the thin film, giving insight into some of the nanoscale phase segregation occurring in these thin films.

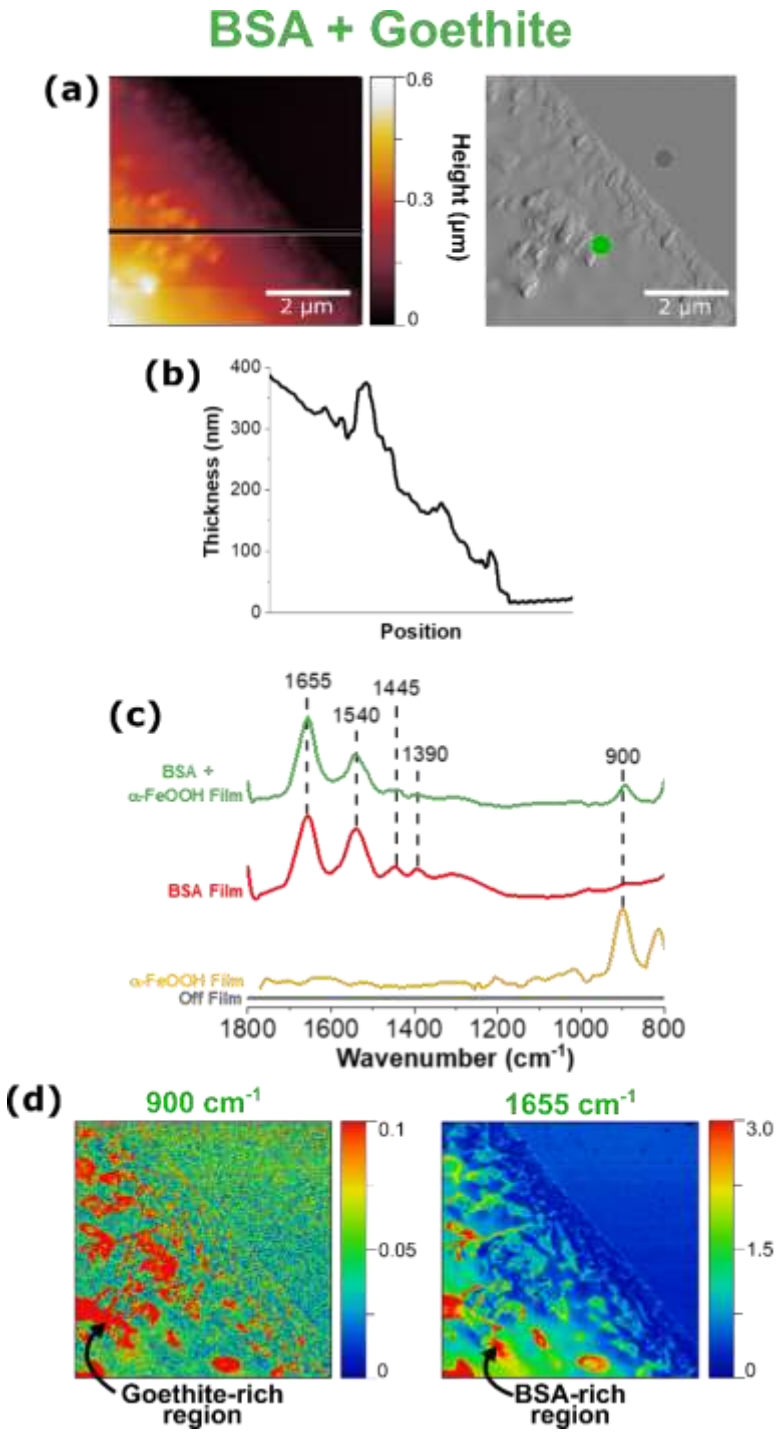

Figure 4.6 AFM-IR images, point spectra and spectral maps of a BSA and goethite thin film. (a) shows the height and deflection image of the 5x5 µm region as well as the height profile in (b). (c) represents the point spectra taken both on and off the film. The colors of the dots present on the deflection image correspond to the location in which the point spectra were taken. Additional spectra presented are reference PTIR spectra. AFM-IR maps are shown in (d), at representative wavenumbers of goethite at 900 cm^{-1} and BSA at and 1640 cm^{-1}. Examples of protein-rich and mineral-rich regions are also shown in (d).

Figure 4.6c shows point spectra both on and off the film; the presence of the bands from 1390 cm^{-1} to 1655 cm^{-1} and at 900 cm^{-1} indicates BSA and goethite, respectively. Using the peak positions identified in each spectrum, infrared maps of the same 5x5 μm region were generated, as shown in Figure 4.6d. Here, we are able to confirm that the taller features on the film are attributed to goethite aggregation, as indicated by the red "hot" spots from the 900 cm^{-1} map. The 1650 cm^{-1} map represents BSA, and we see how BSA appears to concentrate specifically in regions where goethite aggregation is present, but not homogenously across the entire surface. In comparison with the BSA FTIR spectrum, the light green AFM-IR spectrum shows no qualitative difference in the peak shape, peak shift, or Amide I/Amide II ratio but allows for us to conclude that this adsorption process is heterogenous, with specific areas present that are richer in BSA.

AFM-IR spectroscopy of a sodium sulfate and goethite thin film. It is evident from ATR-FTIR spectroscopy that sulfate coordination and crystallization can occur in multicomponent microenvironments. In order to further probe the heterogenous nature of this interaction, AFM-IR spectroscopy was employed as shown in Figure 4.7.

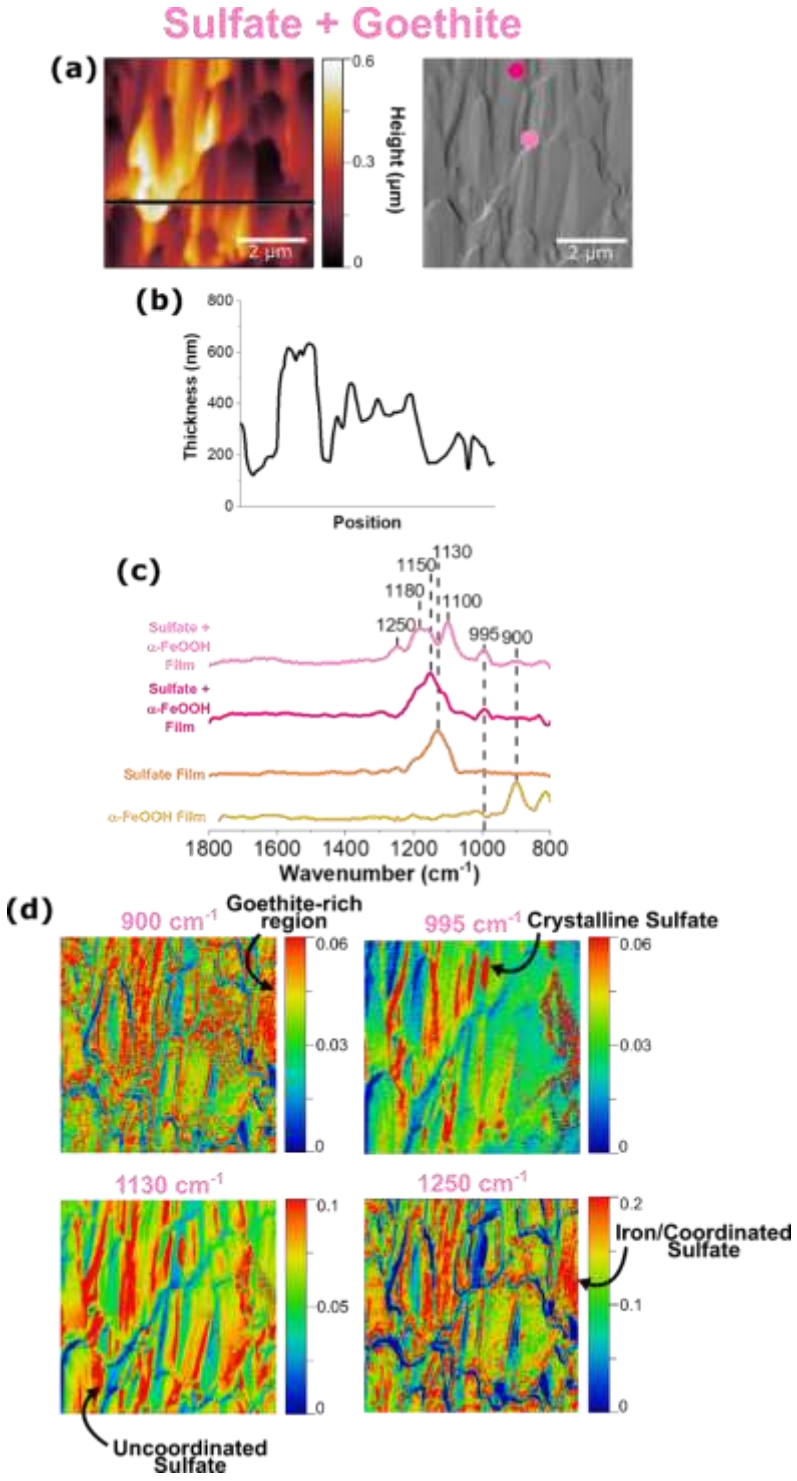

Figure 4.7 AFM-IR images, point spectra and spectral maps of a sodium sulfate and goethite thin film. (a) shows the height and deflection image of the 5x5 μm region and the height profile in (b). Point spectra taken across the film are seen (c), where the colors of the dots on the deflection image correspond to spectra. PTIR spectral maps are shown in (d), at representative wavenumbers of goethite at 900 cm^{-1}, crystalline sulfate at 995 cm^{-1}, uncoordinated sulfate at 1130 cm^{-1} and iron-coordinated sulfate at 1250 cm^{-1}.

The height and deflection image in Figure 4.7a show random aggregations, that appear to resemble a combination of sodium sulfate crystals due to its jagged edges, as well as goethite nanoparticles due to the rod-like shape. It should be noted that the height profile does not start at 0 nm because this image was collected in the center of a sulfate-goethite thin film, rather than the edge, where the bare substrate is simultaneously exposed. For this thin film, point spectra were taken at 2 different regions, as denoted by the light and dark pink dots on the deflection image. Similar to what has been observed (*vide supra*), each point spectrum represents sulfate in different environments. While the light pink spectrum represents uncoordinated sulfate, the dark pink spectrum provides evidence for adsorbed sulfate with inner-sphere coordination to goethite nanoparticles. This evidence is crucial in understanding the heterogenous existence of both forms of sulfate within a thin film, confirming the presence of both micro- and nano-environments in these films.

It is important to note how the distribution of surface-coordinated sulfate at 1250 cm^{-1} and uncoordinated sulfate at 1130 cm^{-1} differ. The prevalence of the 1130 cm^{-1} free sulfate map across the entire region indicates the presence of free sulfate evenly distributed across the surface. The distribution of coordinated sulfate as indicated by the 1250 cm^{-1} spectral map aligns with the distribution of goethite nanoparticles, confirming a physical interaction between the two species. In addition, a chemical interaction between the two is evidenced by discussions reported by previous studies, of strong electrostatic interactions between sulfate and iron oxide surfaces.[17,22,24] Therefore, it is important to examine the sodium sulfate and goethite ATR-FTIR spectra in Figure 4.4 and compare them to the AFM-IR spectra shown above.

The spectrum shown in light pink has a singular peak that is well in agreement with what is known as non-coordinated sulfate. It should be noted that there is a slight upward shift in the

wavenumber, compared to the AFM-IR spectrum for a reference sodium sulfate thin film as shown in Figure 4.1a. This shift can suggest outer-sphere mechanisms or other, non-coordinating interactions that are causing slights shifts to the molecular symmetry of the free sulfate molecules. The ATR-FTIR spectrum shown in Figure 4.4 is an average of many spectra taken across the bulk, thin film surface, which serves as an explanation for any differences between that and the localized PTIR spectra seen in Figure 4.7. The differences in each of the localized PTIR spectra taken across this region is shown to highlight the heterogeneity of the interactions of sulfate within the sample.

Previous studies have utilized the relationship between molecular vibrational modes and molecular symmetry to specify the potential inner-sphere binding mechanisms that can occur in these systems. Upon coordination to Fe, the number of bands the υ_3 asymmetric band splits into can help determine whether or not monodentate bridging or bidentate bridging can occur.[23] Looking closely at the spectrum shown in dark pink, there are well-resolved shoulders 1100 cm^{-1}, 1180 cm^{-1}, and 1250 cm^{-1}, which is representative of the υ_3 band splitting into three indicating bidentate binuclear bridging, where the two Fe ions are each coordinated to an oxygen atom in the sulfate molecule.[23,25] In addition, the strong IR activity of the nondegenerate υ_1 band at 995 cm^{-1} lines also suggest the presence of crystalline sulfate, which can be deduced as the large, jagged features seen in the AFM image.[36] However, the various peaks shown in dark pink is slightly more complex, as it can correspond to a few different binding mechanisms. For example, there exists a peak at 1180 cm^{-1}, which has also been suggested by Peak *et al.* to be the result of a hydrogen bond between a sulfate and a monodentate sulfate.[23] In addition, the PTIR spectrum also shows a 1250 cm^{-1} peak, which has been hypothesized as a change in sulfate speciation, from mono or bidentate bridging sulfate to mono or bidentate bridging bisulfate.[22,24,27,50] While AFM-IR spectroscopy has proven to be a unique and valuable technique in identifying the presence of multiple sulfate-

goethite interactions, it is important to note that further investigation is needed to explicitly identify every type of sulfate-goethite interaction. Although the overlapping peaks are difficult to delineate from one another, changes in point spectra at differing locations in the film confirm the presence of heterogenous sulfate behavior. A summary of these sulfate interactions is shown in Table 4.2.

Table 4.2. Summary of vibrational peak assignments for AFM-IR and ATR-FTIR of sodium sulfate interactions.[14,15,23,26,37]

Wavenumber (cm^{-1})		**Type of Sulfate**	**Figure Reference**
AFM-IR	ATR-FTIR		
995,1130	994,1132	Crystalline Sulfate	Figure 4.1, 4.2, 4.4, 4.7, 4.8
1130-1155	1122, 1130	Free, uncoordinated sulfate; outer-sphere sulfate;	Figure 4.1, 4.2, 4.4, 4.7, 4.8
1100-1180, 1250	1115-1180, 1250	Inner-sphere sulfate	Figure 4.1, 4.2, 4.4, 4.7, 4.8

AFM-IR spectroscopy of a BSA, sodium sulfate, and goethite thin film. Data collected for a multi-component thin film in which all three components are present are shown in Figure 4.8. As can be seen by the height profiles presented in Figure 4.8b, this multi-component film contains features that are smooth with randomly dispersed rougher aggregates.

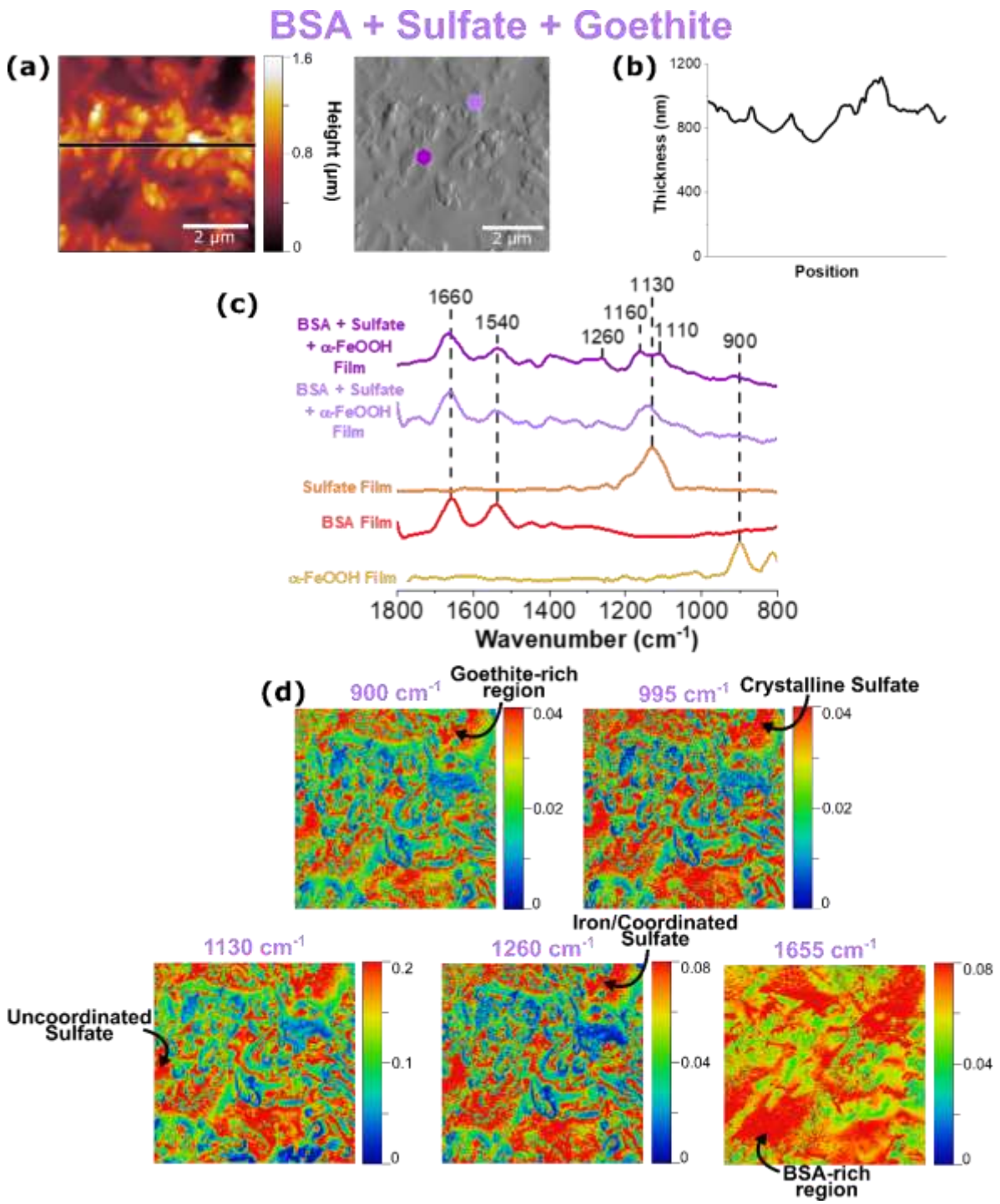

Figure 4.8 AFM-IR images, point spectra and spectral maps of a BSA, sodium sulfate and goethite thin film. (a) shows the height and deflection image of the 5x5 μm region and the height profile in (b). Point spectra taken across the film are seen in (c), where the colors of the dots on the deflection image correspond to the line color for each of the spectra. AFM-IR maps are shown in (d), at representative wavenumbers of goethite at 900 cm^{-1}, crystalline sulfate at 995 cm^{-1}, non-coordinated sulfate at 1130 cm^{-1}, coordinated sulfate at 1260 cm^{-1}, and BSA at 1655 cm^{-1}.

Similar to the two-component systems shown previously, heterogeneity in the AFM-IR spectra can be seen by the differences in the shape and frequencies observed in the sulfate region, as seen by the light and dark purple spectra. The purple ATR-FTIR spectrum of the multi-component system presented in Figure 4.4 shows a very broad and intense sulfate spectrum, compared to what is observed in Figure 4.8b. The variation between the intensity ratios of these bands across this region not only indicates heterogeneity, but also emphasizes the importance of spatially, well-resolved techniques such as AFM-IR spectroscopy in providing data to detect these differences occurring on the micro- and nanoscale level.

In order to further probe the sulfate region, three different spectral regions were selected to map this 5x5 μm region. Consistent with the previous maps, crystalline sulfate arising from sulfate symmetry distortion was represented at 995 cm^{-1}, non-coordinated sulfate at 1130 cm^{-1}, and coordinated sulfate at 1260 cm^{-1}. On the microscale level, all three maps appear to look very similar; however, it is important to focus on the nanoscale features of these maps. There are significantly more red-colored spots on the top region of this image for the 995 cm^{-1} spectral map, indicating localization of crystalline sulfate. This differs from the 1130 cm^{-1} map, representative of uncoordinated sulfate, which is more present in the bottom half of the region. We can also see the similarities between the 900 cm^{-1} and 1260 cm^{-1} map, which is consistent with what is expected since the latter map represents coordinated sulfate onto iron nanoparticles, as indicated by the former. From the prominent 1260 cm^{-1} peak in the AFM-IR spectra as well as these maps matching up to goethite-rich areas, it can be concluded that sodium sulfate interacts with goethite *via* bidentate binuclear bridging.[22] Furthermore, the red, hot spots in the BSA map at 1655 cm^{-1} are consistent with regions rich in BSA that form smooth domains within these films.

4.5 Conclusions

In this study, environmentally relevant thin films containing biological components, oxyanions, and minerals were analyzed *via* a novel approach utilizing microspectroscopic probes. While vibrational spectroscopic techniques such as ATR-FTIR spectroscopy provide hints of these different interactions, it is important to recognize the added value provided by micro- and nanoscale techniques. This study shows AFM-IR spectroscopy to be a useful measurement tool in the distribution of interactions occurring along mineral surfaces in the environment, through examinations of micro-structural heterogeneities. This study has depicted that by using AFM-IR spectroscopy complemented with ATR-FTIR spectroscopy, the complex nature of the chemistry occurring in these systems can be unraveled one at a time, to better understand the various environmental processes these species undergo in the environment. However, limitations in delineating overlapping spectral peaks, has indicated the need for further experimental development and utilization of other analytical tools to accurately determine the exact mechanisms and phase transitions occurring along these interfaces. With more information on the chemistry occurring at the micro- and nanoscale level, a greater understanding of environmental processes can be achieved.

4.6 Acknowledgements

Chapter 4, in full, is a reprint of the material published by ACS Earth & Space Chemistry in: Kim, D.; Grassian, V. H. Analysis of Micro- and Nanoscale Heterogeneities within Environmentally Relevant Thin Films Containing Biological Components, Oxyanions and Minerals Using AFM-PTIR Spectroscopy. *Environ. Sci. Process Impacts*, **2023**, *25* (3), 484-495.

The research reported here was funded in whole or in part by the Army Research Office/Army Research Laboratory *via* grant #W911NF-19-1-0078 to the University of California, San Diego. Any errors and opinions are not those of the Army Research Office or Department of Defense and are attributable solely to the authors.

4.7 Bibliography

(1) Coward, E. K.; Ohno, T.; Sparks, D. L. Direct Evidence for Temporal Molecular Fractionation of Dissolved Organic Matter at the Iron Oxyhydroxide Interface. *Environ. Sci. Technol.* **2019**, *53*, 642–650.

(2) Bhattacharyya, A.; Schmidt, M. P.; Stavitski, E.; Martínez, C. E. Iron Speciation in Peats: Chemical and Spectroscopic Evidence for the Co-Occurrence of Ferric and Ferrous Iron in Organic Complexes and Mineral Precipitates. *Org. Geochem.* **2018**, *115*, 124–137.

(3) Jun, Y. S.; Lee, B.; Waychunas, G. A. *In Situ* Observations of Nanoparticle Early Development Kinetics at Mineral-Water Interfaces. *Environ. Sci. Technol.* **2010**, *44*, 8182–8189.

(4) Kim, D.; Grassian, V. H. Attenuated Total Reflection-Fourier Transform Infrared and Atomic Force Microscopy-Infrared Spectroscopic Investigation of Suwannee River Fulvic Acid and Its Interactions with α-FeOOH. *ACS Earth Sp. Chem.* **2022**, *6*, 81–89.

(5) Brown, G. E.; Foster, A. L.; Ostergren, J. D. Mineral Surfaces and Bioavailability of Heavy Metals: A Molecular-Scale Perspective. *Proc. Natl. Acad. Sci. U.S.A.* **1999**, *96*, 3388–3395.

(6) Brown, G. E.; Henrich, V. E.; Casey, W. H.; Clark, D. L.; Eggleston, C.; Felmy, A.; Goodman, D. W.; Gratzel, M.; Maciel, G.; McCarthy, M. I.; Nealson, K. H.; Sverjensky, D. A.; Toney, M. F.; Zachara, J. M. Metal Oxide Surfaces and Their Interactions with Aqueous Solutions and Microbial Organisms. *Chem. Rev.* **1999**, *99*, 71-174.

(7) Kubicki, J. D.; Schroeter, L. M.; Itoh, M. J.; Nguyen, B. N.; Apitz, S. E. Attenuated Total Reflectance Fourier-Transform Infrared Spectroscopy of Carboxylic Acids Adsorbed onto Mineral Surfaces. *Geochim. Cosmochim. Acta.* **1999**, *63*, 2709–2725.

(8) Mudunkotuwa, I. A.; Minshid, A. Al; Grassian, V. H. ATR-FTIR Spectroscopy as a Tool to Probe Surface Adsorption on Nanoparticles at the Liquid-Solid Interface in Environmentally and Biologically Relevant Media. *Analyst* **2014**, *139*, 870–881.

(9) Mudunkotuwa, I. A.; Grassian, V. H. Biological and Environmental Media Control Oxide Nanoparticle Surface Composition: The Roles of Biological Components (Proteins and Amino Acids), Inorganic Oxyanions and Humic Acid. *Environ. Sci. Nano.* **2015**, *2*, 429–439.

(10) Sit, I.; Wu, H.; Grassian, Vicki, H. Environmental Aspects of Oxide Nanoparticles: Probing Oxide Nanoparticle Surface Processes Under Different Environmental Conditions. *Ann. Rev. Anal. Chem.* **2021**, *14*, 489-514.

(11) Wu, H.; Huang, L.; Rose, A.; Grassian, V. H. Impact of Surface Adsorbed Biologically and Environmentally Relevant Coatings on TiO_2 Nanoparticle Reactivity. *Environ. Sci. Nano.* **2020**, *7*, 3783–3793.

(12) Wu, H.; Gonzalez-Pech, N. I.; Grassian, V. H. Displacement Reactions between Environmentally and Biologically Relevant Ligands on TiO_2 Nanoparticles: Insights into the Aging of Nanoparticles in the Environment. *Environ. Sci. Nano.* **2019**, *6*, 489–504.

(13) Lin, X.; Wei, G.; Liang, X.; Liu, J.; Ma, L.; Zhu, J. The Competitive Adsorption of Chromate and Sulfate on Ni-Substituted Magnetite Surfaces: An ATR-FTIR Study. *Minerals* **2021**, *11*, 1–17.

(14) Givens, B. E.; Xu, Z.; Fiegel, J.; Grassian, V. H. Bovine Serum Albumin Adsorption on SiO_2 and TiO_2 Nanoparticle Surfaces at Circumneutral and Acidic pH: A Tale of Two Nano-Bio Surface Interactions. *J. Coll. Int. Sci.* **2017**, *493*, 334–341.

(15) Schmidt, M. P.; Martínez, C. E. Supramolecular Association Impacts Biomolecule Adsorption onto Goethite. *Environ. Sci. Technol.* **2018**, *52* (7), 4079–4089.

(16) Schulze, W. X. Protein Analysis in Dissolved Organic Matter: What Proteins from Organic Debris, Soil Leachate and Surface Water Can Tell Us - A Perspective. *Biogeosciences* **2005**, *2*, 75–86.

(17) Kubicki, J. D.; Kwon, K. D.; Paul, K. W.; Sparks, D. L. Surface Complex Structures Modelled with Quantum Chemical Calculations: Carbonate, Phosphate, Sulphate, Arsenate and Arsenite. *Eur. J. Soil. Sci.* **2007**, *58*, 932–944.

(18) Kwon, K. D.; Kubicki, J. D. Molecular Orbital Theory Study on Surface Complex Structures of Phosphates to Iron Hydroxides: Calculation of Vibrational Frequencies and Adsorption Energies. *Lang.* **2004**, *20*, 9249–9254.

(19) Kubicki, J. D.; Paul, K. W.; Kabalan, L.; Zhu, Q.; Mrozik, M. K.; Aryanpour, M.; Pierre-Louis, A. M.; Strongin, D. R. ATR-FTIR and Density Functional Theory Study of the Structures, Energetics, and Vibrational Spectra of Phosphate Adsorbed onto Goethite. *Langmuir* **2012**, *28*, 14573–14587.

(20) Elzinga, E. J.; Sparks, D. L. Phosphate Adsorption onto Hematite: An *In Situ* ATR-FTIR Investigation of the Effects of PH and Loading Level on the Mode of Phosphate Surface Complexation. *J. Coll. Int. Sci.* **2007**, *308*, 53–70.

(21) Eggleston, C. M.; Hug, S.; Stumm, W.; Sulzberger, B.; Afonso, M. D. S. Surface Complexation of Sulfate by Hematite Surfaces: FTIR and STM Observations. *Geochim. Cosmochim. Acta.* **1998**, *62*, 585–593.

(22) Hug, S. J. *In Situ* Fourier Transform Infrared Measurements of Sulfate Adsorption on Hematite in Aqueous Solutions. *J. Coll. Int. Sci.* **1997**, *188*, 415–422.

(23) Peak, D.; Ford, R. G.; Sparks, D. L. An *In Situ* ATR-FTIR Investigation of Sulfate Bonding Mechanisms on Goethite. *J. Coll. Int. Sci.* **1999**, *218* (1), 289–299.

(24) Paul, K. W.; Borda, M. J.; Kubicki, J. D.; Sparks, D. L. Effect of Dehydration on Sulfate Coordination and Speciation at the Fe-(Hydr)Oxide-Water Interface: A Molecular Orbital/Density Functional Theory and Fourier Transform Infrared Spectroscopic Investigation. *Langmuir* **2005**, *21*, 11071–11078.

(25) Wijnja, H.; Schulthess, C. P. Vibrational Spectroscopy Study of Selenate and Sulfate Adsorption Mechanisms on Fe and Al (Hydr)Oxide Surfaces. *J. Coll. Int. Sci.* **2000**, *229*, 286–297.

(26) Wang, X.; Wang, Z.; Peak, D.; Tang, Y.; Feng, X.; Zhu, M. Quantification of Coexisting Inner- and Outer-Sphere Complexation of Sulfate on Hematite Surfaces. *ACS Earth Sp. Chem.* **2018**, *2*, 387–398.

(27) Parfitt, R. L.; Smart, R. St. C. The Mechanism of Sulfate Adsorption on Iron Oxides. *Soil Sci. Soc. Am. Jour.* **1978**, *42*, 48–50.

(28) Martinez, C. E.; Kleinschmidt, A. W.; Tabatabai, M. A. Sulfate Adsorption by Variable Charge Soils: Effect of Low-Molecular-Weight Organic Acids. *Biol. Fertil. Soils.* **1998**, *26*, 157–163.

(29) Xu, Z.; Grassian, V. H. Bovine Serum Albumin Adsorption on TiO_2 Nanoparticle Surfaces: Effects of pH and Coadsorption of Phosphate on Protein−Surface Interactions and Protein Structure. *J. Phys. Chem. C* **2017**, *121*, 21763–21771.

(30) Han, J.; Kim, M.; Ro, H. M. Factors Modifying the Structural Configuration of Oxyanions and Organic Acids Adsorbed on Iron (Hydr)Oxides in Soils. A Review. *Environ. Chem. Lett*. **2020**, *18*, 631-662.

(31) Dazzi, A.; Prater, C. B. AFM-IR: Technology and Applications in Nanoscale Infrared Spectroscopy and Chemical Imaging. *Chem. Rev*. **2017**, *117*, 5146-5173.

(32) Dazzi, A.; Prater, C. B.; Hu, Q.; Bruce, D.; Rabolt, J. F.; Marcott, C. Focal Point Review AFM-IR: Combining Atomic Force Microscopy and Infrared Spectroscopy for Nanoscale Chemical Characterization. *Appl. Spectrosc.* **2012**, *66*, 1365–1384.

(33) Grdadolnik, J.; Maréchal, Y. Bovine Serum Albumin Observed by Infrared Spectrometry. II. Hydration Mechanisms and Interaction Configurations of Embedded H_2O Molecules. *Biopolym. – Biospec. Sect.* **2001**, *62*, 54–67.

(34) Schmidt, M. P.; Martínez, C. E. Supramolecular Association Impacts Biomolecule Adsorption onto Goethite. *Environ. Sci. Technol.* **2018**, *52*, 4079–4089.

(35) Parfitt, R. L. Variations in Infrared Spectra, Molecular Symmetry and Site Symmetry of Sulfate Minerals. *Am. Min.* **1965**, *50*, 132–147.

(36) Feng, X. N.; Chen, H. N.; Luan, Y. M.; Tan, S. H.; Pang, S. F.; Zhang, Y. H. In-Situ FTIR-ATR Spectroscopic Observation on the Dynamic Efflorescence/Deliquescence Processes of Na_2SO_4 and Mixed Na_2SO_4/Glycerol Droplets. *Chem. Phys.* **2014**, *430*, 78–83.

(37) Cwiertny, D. M.; Hunter, G. J.; Pettibone, J. M.; Scherer, M. M.; Grassian, V. H. Surface Chemistry and Dissolution of α-FeOOH Nanorods and Microrods: Environmental Implications of Size-Dependent Interactions with Oxalate. *J. Phys. Chem. C.* **2009**, *113*, 2175–2186.

(38) Rodriguez-Navarro, C.; Doehne, E.; Sebastian, E. How Does Sodium Sulfate Crystallize? Implications for the Decay and Testing of Building Materials. *Chem. Concr. Res.* **2000**, *30*, 1527–1534.

(39) Rubasinghege, G.; Kyei, P. K.; Scherer, M. M.; Grassian, V. H. Proton-Promoted Dissolution of α-FeOOH Nanorods and Microrods: Size Dependence, Anion Effects (Carbonate and Phosphate), Aggregation and Surface Adsorption. *J. Coll. Int. Sci.* **2012**, *385*, 15–23.

(40) Kenkel, S.; Mittal, A.; Mittal, S.; Bhargava, R. Probe − Sample Interaction-Independent Atomic Force Microscopy − Infrared Spectroscopy: Toward Robust Nanoscale Compositional Mapping. **2018**, *90*, 8845-8855.

(41) Ramer, G.; Aksyuk, V. A.; Centrone, A.; Nanocenter, M. Quantitative Chemical Analysis at the Nanoscale Using the Photothermal Induced Resonance Technique. *Anal. Chem.* **2017**, *89*, 13524–13531.

(42) Morsch, S.; Lyon, S.; Edmondson, S.; Gibbon, S. Reflectance in AFM-IR: Implications for Interpretation and Remote Analysis of the Buried Interface. *Anal. Chem.* **2020**, *92*, 8117–8124.

(43) Thompson, L. D.; Pantoliano, M. W.; Springer, B. A. Energetic Characterization of the Basic Fibroblast Growth Factor-Heparin Interaction: Identification of the Heparin Binding Domain. *Biochemistry* **1994**, *33*, 3831–3840.

(44) Yu, M.; Zhang, T.; Zhang, W.; Sun, Q.; Li, H.; Li, J. P. Elucidating the Interactions Between Heparin/Heparan Sulfate and SARS-CoV-2-Related Proteins—An Important Strategy for Developing Novel Therapeutics for the COVID-19 Pandemic. *Fr. Mol. Biosci.* **2021**, *7*, 1–13.

(45) Ustunol, I. B.; Coward, E. K.; Quirk, E.; Grassian, V. H. Interaction of Beta-Lactoglobulin and Bovine Serum Albumin with Iron Oxide (α-Fe_2O_3) Nanoparticles in the Presence and Absence of Pre-Adsorbed Phosphate. *Environ. Sci. Nano.* **2021**, *8*, 2811–2823.

(46) Servagent-Noinville, S.; Revault, M.; Quiquampoix, H.; Baron, M. H. Conformational Changes of Bovine Serum Albumin Induced by Adsorption on Different Clay Surfaces: FTIR Analysis. *J. Coll. Int. Sci.* **2000**, *221*, 273–283.

(47) Barreto, M. S. C.; Elzinga, E. J.; Alleoni, L. R. F. The Molecular Insights into Protein Adsorption on Hematite Surface Disclosed by In-Situ ATR-FTIR/2D-COS Study. *Sci. Rep.* **2020**, *10*, 1–13.

(48) Liu, F.; Li, X.; Sheng, A.; Shang, J.; Wang, Z.; Liu, J. Kinetics and Mechanisms of Protein Adsorption and Conformational Change on Hematite Particles. *Environ. Sci. Technol.* **2019**, *53*, 10157–10165.

(49) Mortland, M. M.; Raman, K. V. Surface Acidity of Smectites in Relation to Hydration, Exchangeable Cation, and Structure. *Clays Clay Miner* **1968**, *16*, 393–398.

(50) Parfitt, R. L. Infrared Spectra from Binuclear Bridging Complexes of Sulphate Adsorbed, *J. Chem. Soc. Faraday Trans.* **1976**, 796–802.

CHAPTER 5
VIBRATIONAL SPECTROSCOPY AS A PROBE OF GEOCHEMICAL THIN FILMS AND SINGLE PARTICLE ON MACRO, MICRO, AND NANOSCALES

5.1 Abstract

Minerals play a critical role in the chemistry occurring along the interface of different environmental systems, including the atmosphere/geosphere and hydrosphere/geosphere. In the past few decades, vibrational spectroscopy has been used as a probe for studying interfacial geochemistry. Most recently, the emergence of micro-spectroscopic probes has offered new insights into heterogeneities within geochemical thin films and particles. Here, we compare four different vibrational techniques for probing physical and chemical features across different mineral samples and length scales, from the macroscale to nanoscale. These methods include Attenuated Total Reflection – Fourier Transform Infrared (ATR-FTIR), Optical Photothermal Infrared (O-PTIR), Atomic Force Microscopy-Infrared (AFM-IR) and micro-Raman spectroscopy. By comparing and integrating data across these measurement techniques, new insights into sample differences and heterogeneities can be gained. Interrogation of the various mineral samples at smaller length scales is shown to be particularly informative in highlighting unique "chemical environments" for chemically complex, multicomponent samples as well as single component samples.

5.2 Introduction

Minerals play a critical role along the interface of different environmental systems. Interfacial geochemistry, which occurs at the intersection of the atmosphere/geosphere and hydrosphere/geosphere, plays an important role in air quality, water quality, elemental cycling, climate, soil contamination, food production and possibly the fate of environmental DNA.[1–4] Minerals in contact with groundwater and other water systems play a major role in the transport of contaminants in the environment. The complexity prevalent in environmental samples and interfaces, in particular, is largely due to the myriad of compounds and chemical species found as well as the heterogeneity in these samples. For geochemical interfaces, whether mineral dust aerosols that are transported in the atmosphere or minerals that are in contact with groundwater, the mineralogy-specific, surface facet-dependent chemistry is important to unravel.[5,6]

The prevalence of mineral dust aerosol drives a great deal of interfacial geochemistry in the atmosphere, although volcanic eruptions and volcanic ash also play a role. Mineral dust aerosol is highly complex and are composed of a myriad of different mineral oxides and oxyhydroxides, as some of the most well-studied components.[7–11] Iron oxides and oxyhydroxides, such as hematite and goethite in particular, are some of the most prevalent due to the great natural abundance of iron on Earth.[12–14] The prevalence of iron-containing minerals is important as iron plays an important role in different biogeochemical cycles.[14–16] Carbonate minerals, including calcite, are also relevant to such systems, as they are naturally present in minerals but also in industrial buildings as well as in the ocean as coral.[7,11] Clays, such as kaolinite and montmorillonite, also represent an important class of compounds in mineral dust aerosol.[17] Zeolites, crystalline aluminosilicates, with porous structures are found naturally in aquatic systems but also have been used in environmental remediation.[2]

Furthermore, mineral dust aerosols undergo heterogenous reactions in the atmosphere that can result in the formation of sulfate or nitrate coatings that drive different atmospheric processes.[9,18,19] Representative compounds include ammonium sulfate, sodium sulfate, and sodium nitrate. These species on the surface of mineral dust particles can impact the subsequent properties of dust.[18,20] They can also directly participate as cloud condensation nuclei or be a potential source for HONO production in the atmosphere in the case of nitrate coatings.[21–23] In addition, these species can also act as common adsorbates and can compete for sites on mineral surfaces.[24,25]

Vibrational spectroscopy probes the different vibrational modes and unique chemical signatures from different functional groups. This allows for the identification of different chemical species and phases present as well as some of the unique "local environments" due to hydration, complexation, different phases, and other chemical and physical heterogeneities within environmental systems.[26,27] By monitoring the peak position, shape, and intensity of vibrational bands, insights can be gained at the molecular scale. While a great deal of the current literature has used different vibrational methods with limited spatial resolution, the recent development of micro-spectroscopic probes has been found to be able to provide information on much smaller length scales.[24,28–35] Besides local chemical environments, differences in spectra due to heterogeneities of film thickness and crystal orientation with respect to laser polarization will also give rise to differences in the vibrational spectra.

Providing more details of geochemical interfaces and thin films on micro and nanoscales can be particularly insightful when trying to understand the complexity within these interfaces. Here we have used four different spectroscopic probes from three instruments that can provide insights on multiple length scales, i.e., macroscale, microscale, and nanoscale, for different geochemical thin films that vary in their complexity and heterogeneity. The different vibrational

methods used have different modes of operation and, in some cases, different selection rules. These different modes of operation range from light absorption (attenuated total reflectance Fourier transform infrared, ATR-FTIR, spectroscopy), light scattering (micro-Raman spectroscopy), and photothermal response (optical-photothermal infrared, O-PTIR, spectroscopy and atomic force microscopy coupled to infrared, AFM-IR, spectroscopy). We present here an analysis using these different methods of several oxides/oxyhydroxides, carbonates, nitrates, sulfates, and aluminosilicate samples as well as a complex, multi-component sample such as Arizona Test Dust (AZTD). Furthermore, these spectra can be used as a library of information for the analysis and characterization of mineralogy within different environmental samples.

5.3 Experimental Methods

Sample preparation and sources of materials. Thin films of different minerals were prepared for analysis. Each thin film prepared for ATR-FTIR, AFM-IR, O-PTIR, and micro-Raman spectroscopic data collection and analysis originated from the same sample in order to minimize any additional variables that could affect these samples and their vibrational spectra. Oxide solids were suspended into milli-Q water at a concentration of 5 mg/mL and then sonicated for two minutes to de-aggregate the sample. For carbonate, sulfate, and nitrate samples, the concentration of the stock solutions was 0.1 M. All compounds were purchased commercially, and a compiled list of the sources of these materials can be found in Table 5.1.

Table 5.1 Summary of classes of minerals, minerals, CAS numbers and sources used.

Classes of Minerals	Minerals	CAS #	Source
Oxides	α-FeOOH (Goethite)	20344-49-4	Alfa Aesar
	α-Al_2O_3 (Corundum)	1344-28-1	Alfa Aesar
	TiO_2 (Anatase)	13463-67-7	Nanostructured & Amorphous Materials Inc.
	SiO_2 (Amorphous)	7631-86-9	Aldrich Chemistry
Carbonates, Sulfates, and Nitrates	$NaNO_3$	7631-99-4	Sigma Aldrich
	$CaCO_3$ (Calcite)	471-34-1	Alfa Aesar
	Na_2SO_4	7757-82-6	Fisher Chemical
	$(NH_4)_2SO_4$	7783-20-2	Fisher Scientific
Clays and Aluminosilicates	Kaolinite	1318-74-7	Sigma-Aldrich
	Montmorillonite	SWy-2 *	The Clay Minerals Society
	Zeolite (Type 13X)	1318-02-1	Sigma Aldrich
Complex Multi-component Samples	Arizona Test Dust	ISO 12103-1*	Powder Technology Inc.

*CAS # is not provided, so specific sample type is provided instead.

A fixed volume of each solution was drop-cast onto a designated substrate and dried. This produced a thin, geochemical film. For ATR-FTIR spectroscopic measurements, a 1 mL aliquot of the stock solution was deposited onto a cleaned, Amorphous Material Transmitting Infrared Radiation (AMTIR) crystal and allowed to air-dry for at least 5 hours. For AFM-IR and O-PTIR spectroscopic measurements, a 5 µL aliquot of the stock solution was drop-casted onto a cleaned silica wafer and calcium fluoride (CaF_2) substrate, respectively, and allowed to air-dry for at least 3 hours. Both substrates were chosen specifically for each respective technique due to the absence of spectral interference. For single particle AFM images, the same procedure discussed in the text above was repeated but with a stock solution that was diluted 5-fold to make thinner films are to reduce the presence of aggregates.

ATR-FTIR spectroscopy: Nicolet iS10 FTIR spectrometer: ATR-FTIR spectroscopy is a macroscopic measurement technique that is based upon the principles of total internal reflection.

An incoming broadband infrared light source is reflected internally at the interface between an optically dense medium, the ATR crystal, and an optically rare medium, the sample, where the angle of incidence exceeds the critical angle. A peak is detected when the wavelength of light is in resonance with a vibrational mode, similar to transmission absorption infrared spectroscopy.[36–38] The depth of penetration, d_p, of this IR beam into the sample can be expressed by Equation 5.1[36]:

$$d_p = \frac{\lambda_1}{2\pi\sqrt{sin^2\theta - {n_{21}}^2}} \quad \text{(Eq. 5.1)}$$

Here, λ_1 refers to the wavelength of light divided by the refractive index of the ATR crystal and θ represents the angle of incidence of the IR beam. n_{21} is representative of the ratio of the refractive indices of an optically dense medium (ATR crystal) to the optically rare medium (sample).[36,39] The absorbance, A, can be written as a modified Beer's Law as shown in Equation 5.2,[40]

$$A = \varepsilon N d_p c \quad \text{(Eq. 5.2)}$$

where ε refers to the molar absorption coefficient, which is a function of wavenumber, and N refers to the number of internal reflections at the interface of the ATR crystal and sample and c is the concentration.

For ATR-FTIR spectroscopic measurements, a 500 µL Teflon-coated horizontal flow cell, housing an AMTIR crystal (Pike Technologies) was used. While the capped flow cell can hold 500 µL in liquid volume, when open, the trough of the cell can hold up to 1 mL in liquid volume. Once the thin films were prepared and dried, infrared (IR), each spectrum was recorded at a

resolution of 4 cm^{-1} and were averaged over 100 scans in the spectral range from 725 to 4000 cm^{-1}. For these measurements, a commercial instrument, a Nicolet iS10 FTIR spectrometer (Thermo Fischer Scientific), equipped with an MCT-A detector is used. The AMTIR crystal has a refractive index of 2.5, with an angle of incidence at 45º. Each spectrum was processed using the OMNIC software and plotted with Origin. There were no corrections applied to the ATR data to account for the wavelength dependent probe depth and anomalous dispersion of the refractive index which can cause band shifts of ca. 2 to 10 cm^{-1}.

O-PTIR and micro-Raman spectroscopy: mIRage-Raman. O-PTIR and micro-Raman spectroscopic data were collected using a mIRage infrared + Raman microscope system (Photothermal Spectroscopy Corp., Santa Barbara, CA) with a continuous wave, 532 nm laser. O-PTIR spectroscopy is a technique based upon a photothermal response caused by infrared absorption of a sample. Unlike traditional transmission IR spectroscopy, this is an indirect method, whereby the signal acquired from the instrument is a result of a change in the refractive index of the sample upon absorption of light and simple heating. By using a visible light source that is collinear to the IR laser beam as the probe, an O-PTIR signal is generated as a response to the absorption of an infrared photon that is resonant with a specific vibrational mode. This is followed by warming of the sample which produces a thermal response that is detected by the change in the refractive index. The modulated probe beam is reflected back to the detector and can be expressed as ΔP_{pr}, since it is a change in the refractive index of the probe. This change is representative of the O-PTIR signal, which is linearly proportional to the IR absorbance of the sample, as shown in Equation 5.3[41]:

$$\Delta P_{pr} \propto \frac{\sigma N \alpha}{\kappa C_p} P_{pr} P_{IR} \quad \text{(Eq. 5.3)}$$

The first few terms in Equation 5.3 describe the physical property of the sample, where σ is the absorption cross-section which is a function of wavenumber, N is the number density, κ is the heat conductivity, C_p is the heat capacity and α is the thermo-optic coefficient. The probe and infrared laser powers are represented by P_{pr} and P_{IR}, respectively.[41–44] In addition, the Raman scattering signal is generated simultaneously, as the scattered photons from this modulated signal are then diverted to a Raman spectrometer[42] consisting of a monochromator and CCD detector. These measurements (O-PTIR and Raman) are simultaneously collected and can provide complementary spectroscopic features that are useful for mineral identification. Most importantly, this instrument has a spatial resolution that is determined by its visible light probe, which is on the order of 0.6 μm.[45,46]

For the O-PTIR spectroscopic data collection, optical images of samples are first collected with two objectives: a 10x, low magnification, visible objective lens and a 40x, high magnification reflective Cassegrain objective lens. It should be noted that the O-PTIR spectra are collected with the 40x reflective Cassegrain objective, while the 10x visible objective is used to provide a lower resolution optical image of the sample. The system is also equipped with two mid-IR tunable lasers: a quantum cascade laser (QCL) and an optical parametric oscillator (OPO) laser. In these experiments, s-polarized light is used. The spectral range for the QCL laser is 755 to 1855 cm^{-1} and the spectral range for the OPO laser is 2600 to 3600 cm^{-1}. In addition to the IR lasers, the mIRage system also yields Raman data in the spectral range of 400 to 4000 cm^{-1}. Once samples are prepared onto CaF_2 substrates, they are placed in the sample compartment of the instrument for analysis. Settings for probe and IR laser power are determined by optimizing the photothermal

signal. The probe power ranges anywhere from 0.5% to 19% while the IR laser power ranges from 20% to 100%. For micro-Raman spectral measurements, the most optimal probe power and integration time are determined by the settings that give the highest signal-to-noise ratio. The probe power for Raman ranges from 0.2% to 19% while the integration time ranged from 1 to 10 seconds. All spectra are collected at a resolution of 1 cm^{-1}. After data collection, spectra are baseline corrected using the Photothermal PTIR Studio software and plotted *via* Origin.

Micro-Raman spectroscopy measures the amount of scattered light from a sample and is often used for mineral differentiation and identification.[47,48] While IR spectra can be obtained when the changes in the molecular vibrations result in a change in dipole, Raman spectra can be obtained when these vibrations result in a change in polarizability, which leads to an induced dipole, as shown in Equation 5.4.[49,50]

$$\mu_{ind} = \alpha\varepsilon \qquad \text{(Eq. 5.4)}$$

ε refers to the electric field that is driven by light and the resulting induced dipole moment, μ_{ind}.

AFM-IR spectroscopy: NanoIR2. AFM-IR spectroscopy is a hybrid technique that combines the nanoscale spatial resolution of AFM with the chemical analysis capability of IR spectroscopy by using the cantilever tip as the detector for IR absorbance. High spatial resolution on the scale of the tip diameter can be achieved. Like O-PTIR spectroscopy, AFM-IR spectroscopy is also a photothermal response to absorption of infrared light.[51] This localized thermal expansion is known as photothermal induced resonance (PTIR), where the sample expansion is detected mechanically

through a device that is sensitive to changes in force and displacement, such as an AFM cantilever tip, which provides nanoscale spatial resolution. Thus, AFM-IR spectroscopy to be used for chemical characterization of samples as it proportionally relates the thermal expansion to the cantilever deflection. This transduced signal can be represented by Equation 5.5[51]:

$$S_n(\omega_n, \sigma) = H_m H_{AFM} H_{opt} H_{th} \sigma \kappa(\sigma) \quad \text{(Eq. 5.5)}$$

H_m refers to the mechanical contribution from the sample, H_{AFM} accounts for the cantilever contribution from the deflection, H_{opt} is the optical contribution and H_{th} is the thermal contribution. This equation represents the PTIR response as a function of frequency, ω_n, and wavelength, σ, where the changes in the detected signal are largely dependent on the response of the sample to the wavelength of light illuminated onto the sample.[51–55]

For AFM-IR images and spectra, a nanoIR2 microscopy system (Bruker, Anasys – Santa Barbara, CA) is used. Similar to the mIRage-Raman, the system is equipped with a QCL laser, with a spectral range from 800 to 1800 cm^{-1}. It should be noted that the system is also equipped with a pulsed, tunable optical parametric oscillator (OPO) laser that has a spectral range of 850 to 2000 cm^{-1} and 2235 to 3600 cm^{-1}. While this laser offers a range that can provide chemical information regarding the C-H, N-H, and O-H region, it was not used for this study because the spectra can only be collected in contact mode, which, due to the roughness of these thin films, was extremely difficult for image collection. Therefore, tapping mode had to be used in order to collect clear AFM height images that corresponded with the PTIR spectra. Regardless, the QCL region provides high quality spectra in the fingerprint region. Once samples are prepared and dried onto the silica wafer, PTIR spectra and images are collected primarily in Tapping AFM-IR mode, using

a gold-coated silicon nitride probe (Bruker), with tip radii of ~30 nm, a resonant frequency of 75 ± 15 kHz and a spring constant of 1 to 7 N/m. The scan rate for imaging and mapping varies depending on the roughness of each thin film but within the range of 0.1 to 0.8 Hz. All images are collected at a resolution of 512 pixels and all spectra are collected at a resolution of 2 cm^{-1} with s-polarized light. After data collection, AFM images and PTIR maps are processed using the Gwyddion software and plotted in Origin.

5.4 Results and Discussion

Vibrational spectroscopy of oxides and oxyhydroxides. Goethite, α-FeOOH, an iron-containing oxyhydroxide, was chosen as a representative mineral due to its chemical signatures and prevalence in geochemical interfaces. Figure 5.1 compares the four different vibrational spectroscopic probes used to analyze goethite thin films over three different length scales.

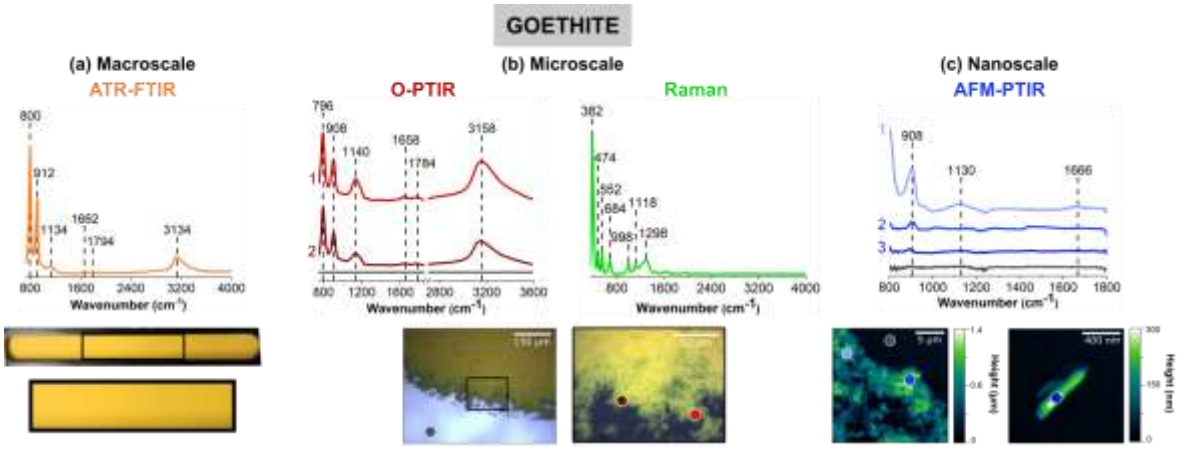

Figure 5.1 Comparison of (a) macroscale, (b) microscale, and (c) nanoscale spectral analysis for goethite (α-FeOOH), collected with ATR-FTIR spectroscopy, O-PTIR + Raman spectroscopy and AFM-IR spectroscopy, respectively. Point spectra collected using O-PTIR, Raman, and AFM-IR spectroscopy are shown. In (a), a picture of the thin film on the ATR crystal is shown and the portion in a black box is expanded further. Optical images of a goethite thin film are presented in (b) at low magnification (10x) and high magnification (40x) of the region specified by the black box. AFM 2D-height images of the goethite thin film as well as a single cluster of goethite nanoparticles are shown in (c). For microscale and nanoscale analysis, the colored point spectra correspond to the colored dots on the image. The colored dot with the green outline indicates the region in which the Raman spectrum was taken. Spectra taken on the substrate, for both O-PTIR and AFM-IR spectroscopy, are shown by the dark gray dot and the gray spectrum.

Thin films prepared for each of the instruments are shown below the different spectra collected and on the different length scales. Figure 5.1a shows a macroscopic image of a goethite thin film, where the film appears to be, by visual inspection, homogenous and yellowish in color. The images taken with the mIRage-Raman system on the edge of the film show smaller clusters and particles that can be seen on the micrometer length scale. While the film appears to be somewhat homogenous toward the center of the film in the 10x optical image, the 40x optical image shows greater variability with thicker and thinner regions. For the nanoIR2 system, individual goethite clusters can be resolved, and the highest spatial resolution image shown gives a more detailed image of single particles. This progression of images from macroscale, microscale, and nanoscale imaging is combined with spectral analysis as discussed below.

The spectral range for each instrument is slightly different due to the different detectors and/or light sources as already noted in the Materials and Methods section. For ATR-FTIR, O-PTIR, Raman, and AFM-IR spectroscopies, the spectra regions correspond to 725 to 4000 cm^{-1}, 755 to 3600 cm^{-1}, 400 to 4000 cm^{-1}, and 800 to 1800 cm^{-1}, respectively. When the infrared peak positions of ATR-FTIR, O-PTIR, and AFM-IR spectra are compared with one another, the peak positions and relative ratios of the peaks are typically within 10 cm^{-1} for sharper peaks and can increase up to 40 cm^{-1} for much broader peaks. Goethite has two distinct peaks below 1000 cm^{-1}, one near 795 cm^{-1} and the other near 910 cm^{-1}. Both of these peaks can be observed in the spectra for each of the three different measurement modes. These two peaks are assigned to the in-plane and out-of-plane bending modes of the OH groups, respectively.[12,13] The presence of the peak near 795 cm^{-1} in the AFM-IR data are not clear because of the nanoIR2 system cutoff at 800 cm^{-1}. The broad O-H stretching mode is detected with ATR-FTIR and O-PTIR spectroscopy, as indicated by the broad band with a peak maximum between 3135 and 3160 cm^{-1}.[12,13]

Spectral shifts are observed when comparing spectra between instruments, and this can be attributed to potential effects from specular reflectance that come from the different substrates used.[56] Differences in spectral intensity with the same technique but for different spots on the same sample attributed to variation in the sample thickness. For the two laser-based methods, O-PTIR and AFM-IR, the orientation of the particles within the thin film will be a factor.[97,98] Since polarized light is being used, single particles of different orientation can give rise to different spectra, the exact differences depend on crystal symmetry. This typically manifests in different spectral shifts and/or intensity differences.

Table 5.2 Vibrational mode assignments for goethite, sodium nitrate and kaolinite and frequencies measured from ATR-FTIR, O-PTIR, AFM-IR and micro-Raman spectroscopies.

Sample	Wavenumber (cm^{-1})			Assignment	Wavenumber (cm^{-1})	Assignment
	ATR-FTIR	O-PTIR	AFM-IR		Raman	
Goethite [10,11,51,52,55,56]	800	796	--	In-plane O-H bend	382	Fe-O-Fe, O-H symmetric stretch
	912	908	908	Out-of-plane O-H bend	474, 552	Fe-OH asymmetric stretch
	1134	1140	1130	O-H bend	684	Fe-O symmetric stretch
	1662	1658	1666	H-O-H bend	--	--
	1794	1784	--	Goethite overtone bend	--	--
	3134	3158	--	O-H stretch	--	--
Sodium Nitrate [57–59]	834	834	834	υ_2, out-of- plane deformation	720	υ_4, in-plane bend
	1348, 1440	1350, 1390, 1444	1342, 1352, 1374, 1396	υ_3, asymmetric stretch	1070	υ_1, symmetric stretch
	--	--	--	--	1384	υ_3, asymmetric stretch
Kaolinite [60–64]	796, 916, 1026, 1114	798, 924, 1018, 1118	920, 998, 1034, 1056, 1080, 1120	Al-OH stretch, O-H bend	3624, 3700	O-H stretch
	1026	924, 1018, 1118	998, 1034, 1056, 1080, 1120	In-plane Si-O stretch		
	3618, 3651, 3670, 3696	--	--	O-H stretch	--	--

The novelty of micro-spectroscopic studies lies in the ability to probe smaller length scales since the spatial resolution is no longer determined by the wavelength of light used, which in the infrared is on the order of a several microns. With the mIRage-Raman, as shown in Figure 5.1b, point spectra can be resolved on the order of sub-microns. The simultaneous acquisition of micro-Raman spectra provides information about Raman active modes are used for mineral chemical identification, especially for more complex samples. Figure 1b shows a micro-Raman spectrum of

goethite with several identified at 382 cm^{-1}, 474 cm^{-1} and 552 cm^{-1}, and 684 cm^{-1}, which are assigned to Fe-O-Fe stretching modes, Fe-OH asymmetric stretching modes, and Fe-O symmetric stretching modes, respectively.[57,58] Peak positions and assignments for the micro-Raman spectrum of goethite are also given in Table 1. Most importantly, micro-Raman spectra provide low frequency vibrations below 700 cm^{-1} that are particularly useful for mineral identification. There is more variation in the intensity of the AFM-IR spectra. Point spectra can be obtained on particles or clusters as shown in Figure 1c, that are below the of the mIRage-Raman system. In addition, a single goethite nanocluster can be spatially resolved. One point that should be highlighted is that each spectrum collected is for a 30 nm spot in the lateral plane.

Measurements were also made on several oxide samples. Spectra for corundum (α-Al_2O_3), anatase (TiO_2) and amorphous silicon dioxide (SiO_2) are shown in Figure 5.2. The differences within the O-PTIR spectra can be attributed to a few factors. These thin films, which are crystalline powders by nature, are composed of single particles which can be oriented differently with respect to the polarization of the infrared beam. Combined with the local thickness variations within these films, small spectral shifts and differences and intensities are observed as already noted for AFM-IR data.[97-99]

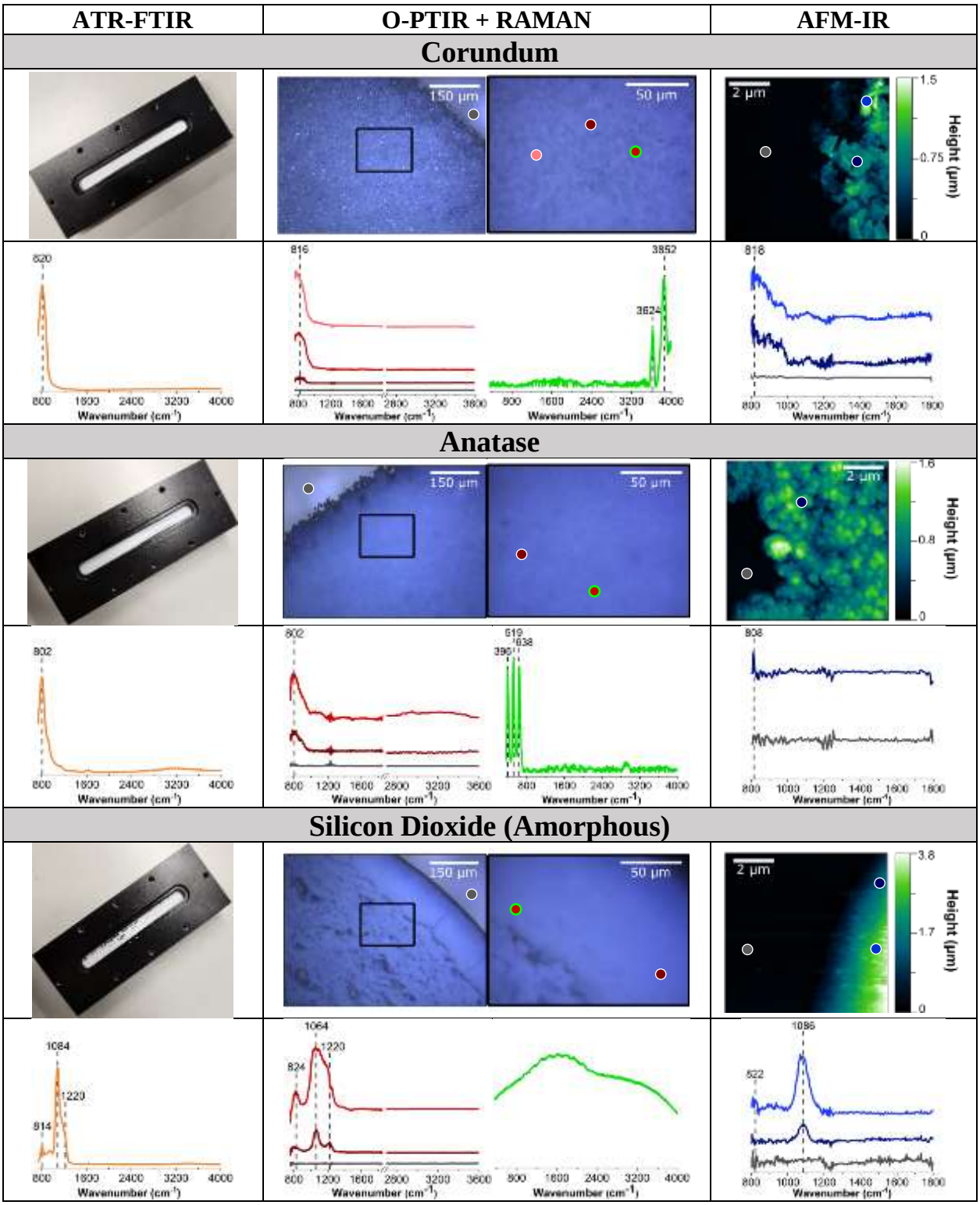

Figure 5.2 Images and spectra recorded for different oxide minerals – corundum, anatase and silicon dioxide (amorphous) utilizing ATR-FTIR spectroscopy, O-PTIR and Raman spectroscopy and AFM-IR spectroscopy.

This is clearly seen for the O-PTIR spectra of corundum, where the progression from dark red, red, to pink spectra indicates higher intensity of the 816 cm^{-1} band. The different mineral films have different degrees of roughness as some thin films dry more uniformly than others. For example, titanium dioxide is very densely packed, as can be seen by the low magnification image in Figure 5.2, unlike silicon dioxide which has a dense ring on the outside and a less uniform center portion. For mineral oxides like aluminum and silicon oxides, the AFM images were difficult to collect due to differences in height along the film. However, the titanium dioxide sample consisted of anatase nanoparticles, which were resolved very clearly with the nanoIR2. For samples like titanium dioxide, the micro-Raman spectrum can be extremely helpful in identifying which phase is present as different phases of titanium dioxide – rutile, anatase and brookite – all have different low frequency modes.[59,60] In the case of amorphous SiO_2, there was considerable fluorescence observed from the sample (see Figure 5.2).

Table 5.3 Vibrational mode assignments of different mineral oxides from infrared spectroscopy utilizing ATR-FTIR, O-PTIR, and AFM-IR spectroscopy.

Sample	**Wavenumber (cm^{-1})**			**Assignment**
	ATR-FTIR	*O-PTIR*	*AFM-IR*	
Corundum (α-Al_2O_3)[1]	820	816	818	Al-O stretch
Anatase (TiO_2) [2]	802	802	808	Ti-O stretch
Amorphous SiO_2[3,4]	814	824	822	Si-O stretch
	1084, 1220	1064, 1220	1086	Si-O-Si stretch

Specific IR and Raman peak assignments for these compounds are listed in Table 5.3 and Table 5.4, respectively.

Table 5.4 Vibrational mode assignments of different mineral oxides from micro-Raman spectroscopy.

Sample	Wavenumber (cm^{-1})	Assignment
	Raman	
Corundum (α-Al_2O_3)[5]	3624	O-H stretch
	3852	
Anatase (TiO_2) [6–8]	396	O-Ti-O bend
	519	Ti-O stretch
	638	Ti-O bend
Amorphous SiO_2	Fluorescence signal observed	–

Vibrational spectroscopy of Nitrates, Carbonates, and Sulfates. Figure 5.3 shows vibrational spectra collected of sodium nitrate thin films and individual particles. Sodium nitrate has distinct vibrational peaks due to the symmetric and asymmetric stretching and bending modes of nitrate anion. For infrared modes, ATR-FTIR, O-PTIR, and AFM-IR spectroscopy show the most intense bands associated with the asymmetric stretch of the nitrate anion in the region between 1342 to 1444 cm^{-1} (*vide infra*).[61]

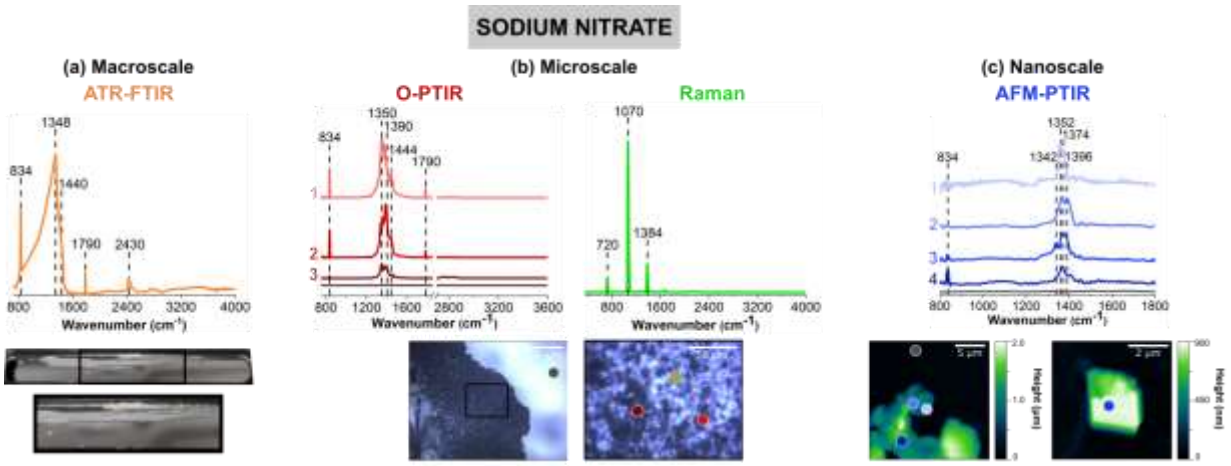

Figure 5.3 Comparison of (a) macroscale, (b) microscale, and (c) nanoscale spectral analysis for sodium nitrate thin films, collected with ATR-FTIR spectroscopy, O-PTIR + Raman spectroscopy and AFM-IR spectroscopy, respectively. Point spectra collected using O-PTIR, Raman, and AFM-IR spectroscopy are shown. In (a), a picture of the thin film on the ATR crystal is shown and the portion in a black box is expanded further. Optical images of a sodium nitrate thin film are presented in (b) at low magnification (10x) and high magnification (40x) of the region specified by the black box. AFM 2D-height images of the sodium nitrate thin film as well as a sodium nitrate cluster are shown in (c). For microscale and nanoscale analysis, the colored point spectra correspond to the colored dots on the image. The colored dot with the green outline indicates the region in which the Raman spectrum was taken. Spectra taken on the substrate, for both O-PTIR and AFM-IR spectroscopy, are shown by the dark gray dot and the gray spectrum.

The image of a sodium nitrate thin film on the ATR crystal (Figure 5.3a) shows that sodium nitrate does not dry evenly on the ATR crystal as it aggregates into irregular-shaped clumps along the ATR crystal. The 40x optical image shows patches of sodium nitrates clusters, as seen by the different reflective regions within the thin film. Utilizing AFM, Figure 5.3c offers a closer look at the edge of a sodium nitrate thin film as well as individual particles. The AFM 2D height images show that these sodium nitrate particles are irregular-shaped with varying heights. The 20 μm x 20 μm image of the thin film shows that the thin film is oriented in a way where the nitrate clusters are packed together to form taller, 2 μm films. However, from the 5 μm x 5 μm image shown on the right side, the nanoscale features indicate the variance in height within a single particle. Each

of these features do not appear to be nano-sized, but with the nanoIR2 system, the heterogeneity within these clusters can be probed effectively.

For sodium nitrate, there are two important variations that should be noted when comparing the macroscopic nitrate spectra across s scales and with different techniques. Most notable are the differences in the spectral region from 1340 to 1445 cm^{-1}, which can be clearly observed in terms of peak frequency, peak shape, and relative intensity. The nitrate anion has a D_{3h} symmetry and has four vibrational modes – υ_1, υ_2, υ_3, and υ_4 – which represent the symmetric stretch, out-of-plane deformation, asymmetric stretch and in-plane bend, respectively. The υ_3 nitrate asymmetric stretching mode is the most prominent peak and it is also doubly degenerate, and its vibrational mode frequency shifts the most in different local environment and changes in symmetry due to hydration state, crystallinity and coordinating cations. The loss of symmetry is evident by the υ_3 nitrate asymmetric stretching mode splits into two modes: a broad band from 1342 cm^{-1} to 1444 cm^{-1} and a sharper band at 834 cm^{-1}. This splitting is highly dependent on the reduction in symmetry and distortion of the nitrate anion away from D_{3h} symmetry, which depends on the hydration, crystallinity, and coordination environments. For example, even in the hydration sphere of bulk aqueous systems, the υ_1 mode, albeit quite weak, becomes infrared active.[62–65] In addition, the spectra of highly crystalline compounds of high symmetry will depend on light polarization.[97] The effect of polarized light on infrared spectra of crystalline nitrates showed the changes in nitrate absorptions using different light polarizations. [100] Additional for crystalline anisotropic materials variations and their interactions with polarize light from microspectroscopic probes have showed variations in spectral intensities and peak positions.[101] Microspectroscopic techniques, therefore, may provide insights into the local microenvironment as well as heterogeneities of the sodium nitrate thin film.

For the ATR-FTIR spectrum in Figure 5.3a, it can be seen that there is a very broad peak centered around 1384 cm^{-1}, increased spatial resolution can contribute in deconvoluting a broad spectrum to spectra with more defined peaks. In addition, to the asymmetric stretch, there is sharper band at 834 cm^{-1} due to the out-of-plane nitrate bend. O-PTIR spectroscopy can offer more insight into differences in the local nitrate environment. For example, there are differences in the peak maximum observed for different parts of the film, in the spectrum labeled as 1 (pink) in Figure 5.3b the peak maximum observed at 1350 cm^{-1} whereas the spectrum labeled 2 (red) the peak maximum is shifted to higher frequencies 1390 cm^{-1}. Additionally, the spectrum labeled 3 (dark red) shows to have a doublet within the same region. For these three spectra, there is also a small shoulder ca. 1445 cm^{-1}. The AFM-IR spectra also shows variability. In particular, spectrum 1 (light periwinkle) has a major peak at 1396 cm^{-1} and spectrum 2 (periwinkle) exhibits a doublet at 1368 cm^{-1} and 1396 cm^{-1}. The differences in peak intensity can also be observed, with Spectrum 3 (blue) in Figure 5.3b and Spectrum 4 (dark blue) in Figure 5.3c, having the lowest peak intensity. While the differences in intensity or minor peak shifts can be attributed to changes in substrates and sample thickness, the major differences in the peak positions are more likely due to changes that occur in the nitrate symmetry – due to differences in crystallinity and the presence of small amounts of water due to incomplete drying.

Although differences in the infrared spectra were evident of different nitrate local environments, the micro-Raman spectra were consistent across all spectra, and a single spectrum is shown in Figure 5.3b. There are three distinct Raman peaks at 720 cm^{-1}, 1070 cm^{-1}, and 1384 cm^{-1} which are representative of the NO_3^- υ_4, in-plane bend, υ_1, the symmetric stretch, and υ_3, the asymmetric stretch, respectively.

Other minerals investigated include calcite, sodium sulfate, and ammonium sulfate. Calcite has distinct peaks at 874 cm^{-1}, 1400 to 1514 cm^{-1}, and 1796 cm^{-1} (Table 5.5).

Table 5.5 Vibrational mode assignments of different carbonates and sulfates from infrared spectroscopy utilizing ATR-FTIR, O-PTIR, and AFM-IR spectroscopy.

Compound	**Wavenumber (cm^{-1})**			**Assignment**
	ATR-FTIR	*O-PTIR*	*AFM-IR*	
Calcite ($CaCO_3$) [9–11]	874	874	874	υ_2, Out-of-plane bend
	1432	1400, 1444, 1514	1424, 1458, 1504	υ_3, Asymmetric stretch
	1796	1796	--	Combination bands ($\upsilon_1 + \upsilon_4$)
Sodium Sulfate[12,13]	997	992	990	υ_1, SO_4^{2-} stretch
	1125, 1184	1130, 1171, 1188	1104, 1128, 1188	υ_3, SO_4^{2-} stretch
Ammonium Sulfate[14,15]	1082, 1164	1090, 1170	1080, 1110, 1130, 1160	υ_3, SO_4^{2-} stretch
	1412	1420	1416	υ_4, NH_4^+ stretch
	3040, 3208	3206	--	υ_3, NH_4^+ stretch

These bands represent the out-of-plane bending, asymmetric stretching mode, and a combination band, of the carbonate ion, respectively.[66–68] The variation in the intensity and small spectral shifts for calcium carbonate can be attributed to the differences in thickness. These features are representative for different carbonate phases but with slightly different frequencies. In addition, nanoscale features for calcium carbonate clusters can be resolved. These clusters are small and are seen aggregating when cast into a thin film. The micro-Raman spectrum of calcite shows a combination of bending and stretching modes of carbonate at 714 cm^{-1}, 1090 cm^{-1} and 1440 cm^{-1}, respectively. The 1758 cm^{-1} peak in the Raman spectrum is most likely attributed to a combination band.[69] The Raman peaks are summarized and assigned in Table 5.6.

Table 5.6 Vibrational mode assignments of different carbonate and sulfates from micro-Raman spectroscopy.

Compound	Wavenumber (cm^{-1})	Assignment
	Raman	
Calcite ($CaCO_3$)[16]	714	υ_4, in-plane bend
	1090	υ_1, symmetric stretch
	1440	υ_3, asymmetric stretch
	1758	Combination bands ($\upsilon_1 + \upsilon_4$)
Sodium Sulfate[17,18]	456	υ_2, SO_4^{2-} stretch
	630	υ_4, SO_4^{2-} stretch
	990	υ_1, SO_4^{2-} stretch
	1126	υ_3, SO_4^{2-} stretch
Ammonium Sulfate[14,17–20]	446	υ_2, SO_4^{2-} stretch
	618	υ_4, SO_4^{2-} stretch
	973	υ_1, SO_4^{2-} stretch
	3143	N-H stretch

Like nitrates, sulfates are ubiquitous oxyanions in the environment. The vibrational frequencies for the sulfate anion also depend on hydration state as well as the local environment. For the unperturbed anion, sulfate is of tetrahedral symmetry.[70–72] These shifts for both sodium and ammonium sulfate that are observed in the spectra are listed in Table 5.5. There are also some major differences in intensity and the presence of different bands. For example, the spectrum shown in pink for sodium sulfate has a stronger 992 cm^{-1} than the others. This is observed in the spectrum shown in dark red for ammonium sulfate, where the 866 cm^{-1} is more prevalent than in the red spectrum. For ammonium sulfate, similarities between the υ_3 SO_4^{2-} stretching mode in the 1080 to 1170 cm^{-1} region and the υ_4, NH_4^+ stretching mode in the 1412 to 1420 cm^{-1} region are seen between different scales.[70,72–74] However, there are notable differences in the intensity seen in the point spectra. For example, for the AFM-IR spectra in Figure 5.4 for the three different regions.

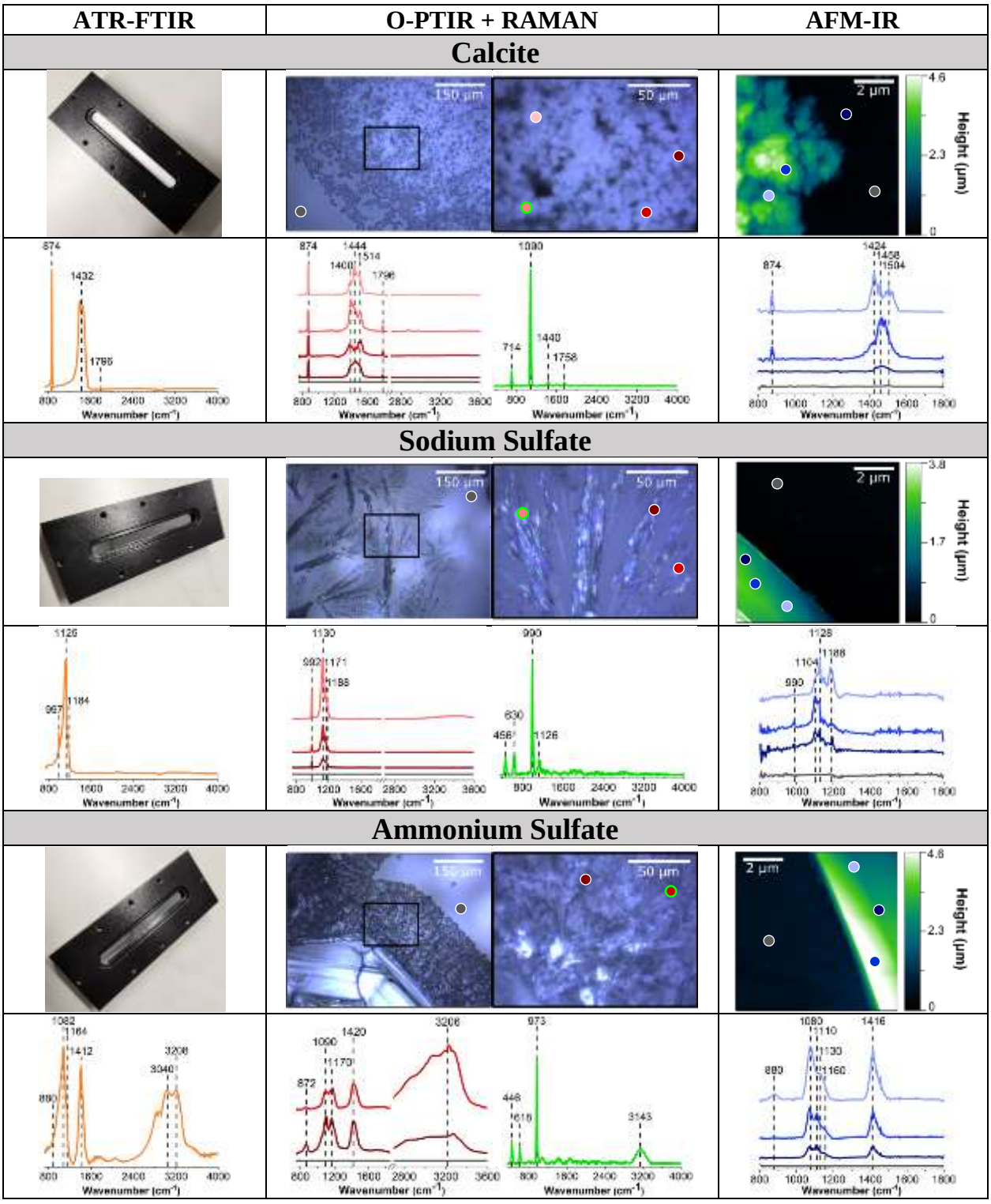

Figure 5.4 Images and spectra recorded for different carbonate and sulfate minerals – calcite, sodium sulfate and ammonium sulfate utilizing ATR-FTIR spectroscopy, O-PTIR and Raman spectroscopy and AFM-IR spectroscopy.

For these two compounds, the optical images from the mIRage-Raman display their crystalline nature most accurately, compared to the 20 μm x 20 μm images collected with the nanoIR2 system. The crystalline nature of these compounds results in a thin film that is extremely rough, with jagged edges that are extremely difficult to image with AFM. The micro-Raman spectra of sodium and ammonium sulfate overlap in three regions: (1) at 446 to 456 cm^{-1}, representing the υ_2 SO_4^{2-} stretching mode, (2) at 618 to 630 cm^{-1}, representing the υ_4, SO_4^{2-} stretching mode, and (3) at 973 to 990 cm^{-1}, representing the υ_1, SO_4^{2-} stretching mode.[75–78] In addition to these peaks, sodium sulfate has a small band at 1126 cm^{-1} which has been assigned to the υ_3 SO_4^{2-} stretching mode.[76] Consequently, ammonium sulfate has a relatively broad peak at 3143 cm^{-1} due to the N-H stretching modes that are specific to this compound.[75,77,78] Specific IR and Raman peak assignments for these minerals are listed in Table 5.5 and Table 5.6, respectively.

Vibrational spectroscopic analysis of aluminosilicates: clays and zeolites. Figure 5.5 shows vibrational data for kaolinite, a clay mineral, which is known to contain different stoichiometric ratios of alumina and silica derivatives.[79] Figure 5.5a shows a very lightly colored beige film that uniformly adheres to the ATR crystal. Upon closer inspection of the film with the mIRage-Raman, small features that vary in size and reflectivity are seen in the low magnification, 10x image. The AFM height image shows that this film is thick, at 5 μm in height. Unlike goethite and sodium nitrate, for kaolinite there were not obvious single particles but instead particles were associated with the film.

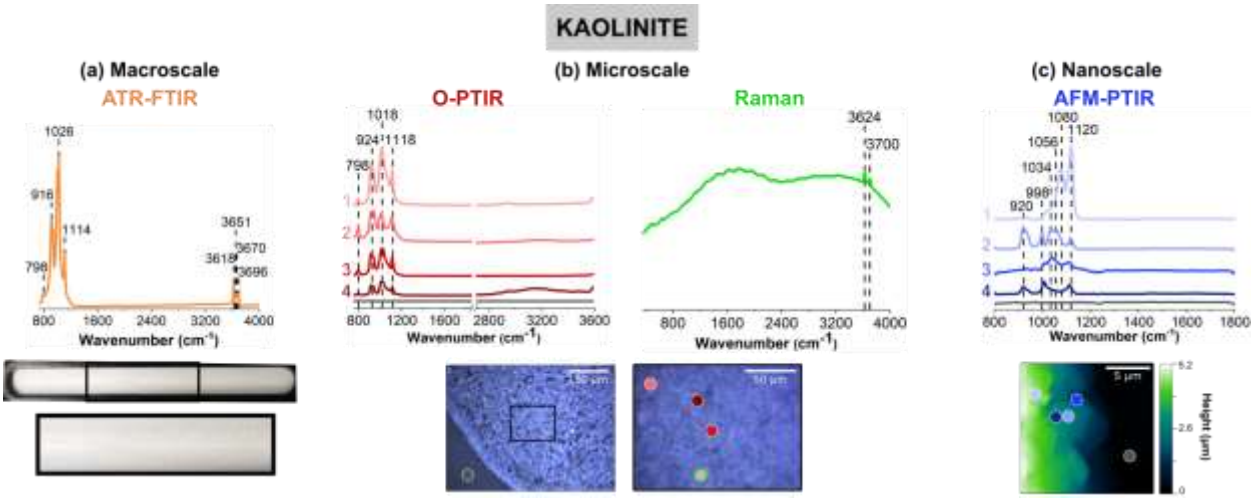

Figure 5.5 Comparison of (a) macroscale, (b) microscale, and (c) nanoscale spectral analysis for kaolinite thin films, collected with ATR-FTIR spectroscopy, O-PTIR + Raman spectroscopy and AFM-IR spectroscopy, respectively. Point spectra collected using O-PTIR, Raman, and AFM-IR spectroscopy are shown. In (a), a picture of the thin film on the ATR crystal is shown and the portion in a black box is expanded further. Optical images of a zeolite thin film are presented in (b) at low magnification (10x) and high magnification (40x) of the region specified by the black box. AFM 2D-height images of the kaolinite thin film are shown in (c). For microscale and nanoscale analysis, the colored point spectra correspond to the colored dots on the image. The colored dot with the green outline indicates the region in which the Raman spectrum was taken. Spectra taken on the substrate, for both O-PTIR and AFM-IR spectroscopy, are shown by the dark gray dot and the gray spectrum.

An ATR-FTIR spectrum of kaolinite is shown in orange in Figure 3a. The spectrum shows an intense triplet at 916 cm^{-1}, 1026 cm^{-1}, and 1114 cm^{-1}, as well as peaks in the O-H stretching regions from 3620 to 3700 cm^{-1}. This region is indicative of aluminosilicate derivatives in clays as well as zeolite or mineral oxides such as aluminum oxide and silicon dioxide, as shown in Table 5.3.[79–82] It should be noted that the relative intensities of the three peaks is that the 1026 cm^{-1} is highest in intensity, followed by the 916 cm^{-1} peak, and then the 1114 cm^{-1} peak.

The heterogeneity of the kaolinite sample is evident with the data collected with the mIRage-Raman system, where the ratio of the three main peaks differs within each spectrum in the O-PTIR spectra. For example, in Figure 5.5b, the spectra labeled as 1 (light pink), 3 (red) and (dark red), show ratios of the three peaks resembles that of the ATR-FTIR spectrum in Figure 5.5a

qualitatively but quantitatively are different. In addition, the peak at 1018 cm^{-1} is broader in 3 (red) than 1 (light pink) whereas the peak at 924 cm^{-1} is sharpest for 1 (light pink). Furthermore, the spectrum labeled 2 (pink), has a different ratio, where the 924 cm^{-1} band is the strongest, followed by the 1018 cm^{-1} and 1118 cm^{-1}. Lastly, for Spectrum 2, there is a more intense 798 cm^{-1} peak, which may be indicative of the Al-O bending mode.[83] This peak is also as a minor contribution in the ATR-FTIR spectrum in Figure 5.5a. From this microscale spectral analysis, evidence for heterogeneity is uncovered by the differences in intensity of the point spectra as well as differences in the ratios.

With AFM-IR spectroscopy, greater insights into local heterogeneities can be explored. Four spectra collected on different locations of the 20 μm x 20 μm region is shown in Figure 5.5c. Significant differences in these spectra are important to note. Figure 5.5c, the spectrum labeled 1 (light periwinkle), has a prominent doublet at 1080 cm^{-1} and a more intense 1120 cm^{-1}. Unlike that shown for 2 (periwinkle) and 4 (dark blue), where the 920 cm^{-1} peak is absent, suggesting an absence of alumina derivatives in that region. In Figure 5.5c, the spectrum labeled 2 (periwinkle) is also particularly interesting, as it has a strong 920 cm^{-1} bending mode, along with sharper peaks at 998 cm^{-1} and 1120 cm^{-1} but a broad peak centered at ca. 1070 cm^{-1}. This may suggest a strong presence of silica derivatives coupled to alumina and potentially other phases. Lastly, the spectrum labeled 3 (blue) is low in spectral intensity and has a broad peak from ca. 1000 cm^{-1} to 1120 cm^{-1}. This region most likely is comprised of several silica derivatives, as it appears to be more poorly resolved compared to the other spectra. Overall, the nanoscale spectra provide the greatest amount of information about heterogeneity. The varying stoichiometric ratios of silica and alumina derivatives are expected, as clay minerals such as kaolinite are made up of tetrahedral and octahedral sheets of such compounds.

The micro-Raman spectrum of kaolinite shows high background signal indicative of fluorescence from the sample and two distinct features on top of that attributed to the inner and outer hydroxyl groups, at 3624 cm^{-1} and 3700 cm^{-1}, respectively, as seen in the ATR-FTIR spectrum. The positions of these hydroxyl groups refer to where they are situated along the inner and outer planes of a kaolinite unit cell. Kaolinite is known to have two other outer hydroxyl groups that are not clearly resolved by the Raman spectrum shown, which may be due to the presence of other aluminosilicates that are present.[84,85] The fluorescence observed in the micro-Raman spectrum of kaolinite resembles the spectra of Arizona Test Dust and montmorillonite, as can be seen in Figure 5.6 and 5.7, respectively.

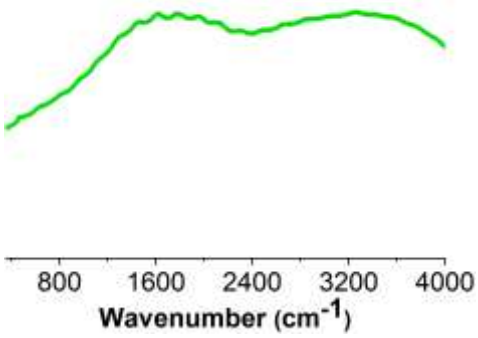

Figure 5.6. Raman spectrum for Arizona Test Dust (AZTD). As can be seen, fluorescence signal is observed.

Although fluorescence is commonly observed in such samples, the reasons for this vary. Ritz *et al.* suggests that fluorescence could occur due: (1) presence of organic matter, (2) presence of iron embedded into the clay mineral structure, and (3) even settings for Raman spectral data collection.[86–89] Kaolinite is not known to contain high levels of cations such as iron or organic matter. However, both Ritz *et al*. and Frost *et al.* both suggest that fluorescence for clay minerals can be heavily dependent on its sources as well as the wavelength of light used for analysis.[79,86,89] For example, it appears that the 1064 nm laser is preferred over the 532 nm laser for SWy-2 type

of montmorillonite, which exhibits fluorescence, consistent with what is seen in Figure 5.7. This information suggests that the fluorescence observed in this study is due to the presence of cations embedded in the mineral structure.

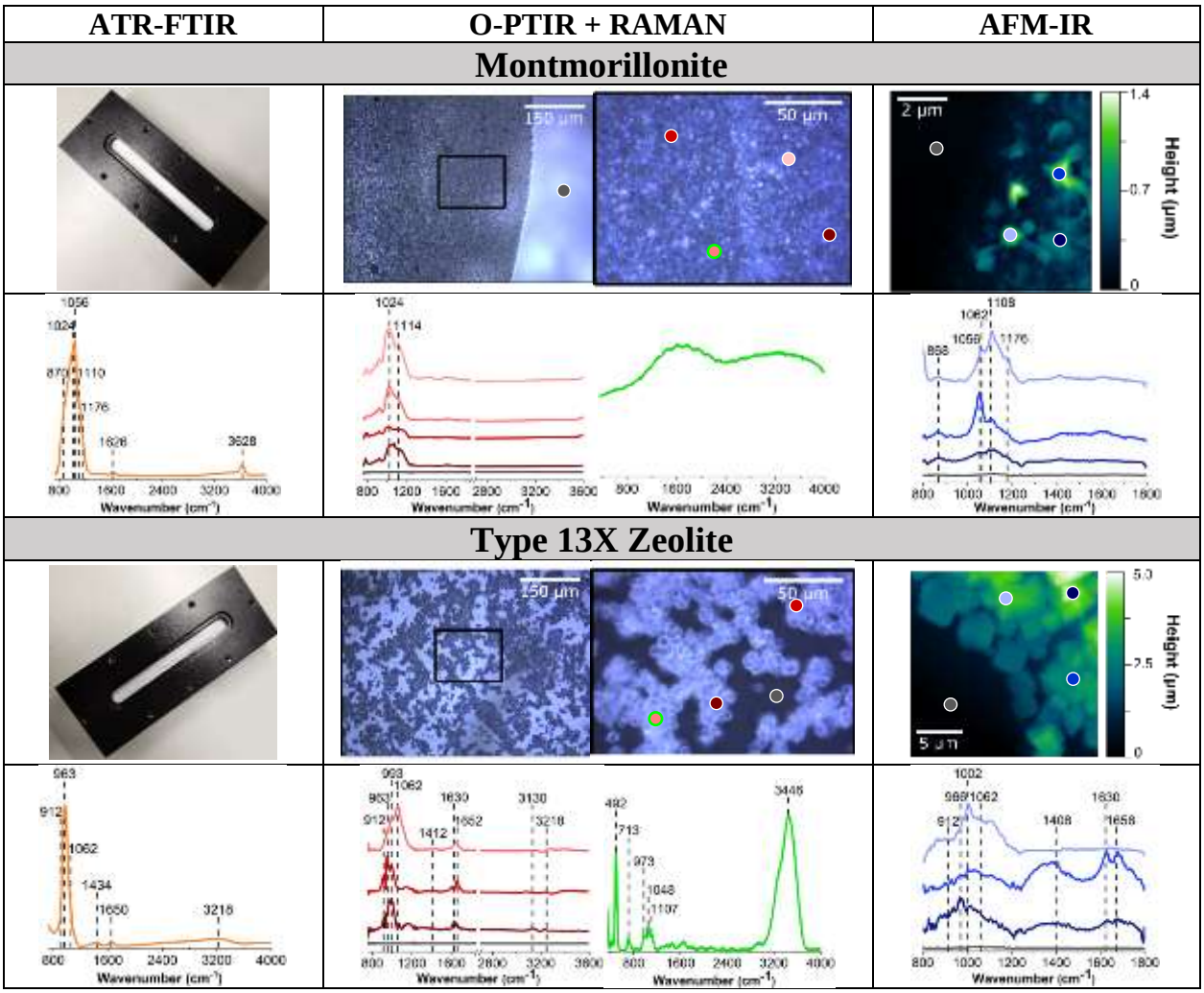

Figure 5.7 Images and spectra recorded for different aluminosilicates – montmorillonite and zeolite utilizing ATR-FTIR spectroscopy, O-PTIR and Raman spectroscopy and AFM-IR spectroscopy.

The physical and chemical behavior exhibited by kaolinite is similar to some of the other aluminosilicate clays, zeolites, and complex multi-component samples. Optical and AFM images as well as chemical spectra of montmorillonite and zeolite are presented in Figure 5.7. A consistent

observation seen between all three types of spectra collected is that these compounds all show broad ATR-FTIR spectrum. When probed on the microscale, small differences in the spectra can be resolved, whether it be in intensity differences, as clearly shown by the zeolite O-PTIR spectra, or in peak-to-peak ratio shifts, as shown in the montmorillonite O-PTIR spectra. This is summarized in Table 5.7.

Table 5.7 Vibrational mode assignments of different aluminosilicates from infrared spectroscopy utilizing ATR-FTIR, O-PTIR, and AFM-IR spectroscopy.

Compound	**Wavenumber (cm^{-1})**			**Assignment**
	ATR-FTIR	*O-PTIR*	*AFM-IR*	
Montmorillonite[21]	870	874	868	Al-Fe-OH bend
	1024, 1056, 1110, 1176	1024, 1114	1056, 1062, 1108, 1176	Si-O stretch
	1626	--	--	O-H bend
	3628	--	--	O-H stretch
Zeolite[22]	912, 963, 1062	912, 963, 983, 1062	912, 966, 1002, 1062	Al-O or Si-O asymmetric stretch
	1434	1412	1408	AlO_4 tetrahedra
	1650	1630, 1650	1630, 1656	O-H bend
	3218	3130, 3218	--	O-H bend

The zeolite sample is the only sample that showed a high quality micro-Raman spectrum. The vibrational mode assignments for the micro-Raman spectrum are given in Table 5.8. These micro and nanoscale differences most likely are contributed to in part to different chemical environments since compounds in this class of minerals are more heterogenous and complex by nature than the other minerals discussed above although crystal orientation and anisotropic crystal materials can result in intensity variations and peaks present.[97-101]

Table 5.8 Vibrational mode assignments and observation of fluorescence for different aluminosilicates and for AZTD

Compound	Wavenumber (cm^{-1})	Assignment
	Raman	
Montmorillonite	Fluorescence signal observed	–
Zeolite[22–25]	492	Al-O-Al or Si-O-Si stretch
	713	Si-O bend
	973	Al-O-Al stretch, SiO_4 stretch
	1048	Al-O bend, Si-O bend
	1107	Si-O stretch
	3446	O-H stretch
Arizona Test Dust (AZTD)	Fluorescence signal observed	–

Vibrational spectroscopic analysis of complex, multi-component sample: Arizona Test Dust. Mineral aerosols play an important role in the chemistry that occurs in the atmosphere, as they not only are transported great distances but they also contribute significantly to the global budget of such other aerosols and gases.[32,90,91] Arizona Test Dust has been used as a proxy for natural dust samples as it is easily accessible and well characterized in composition.[92] Much of these aerosols originate from desert dust sources, and AZTD is a great model system to study as it contains a myriad of different elements, such as aluminosilicates, iron oxides, calcium carbonate, and potassium nitrate.[32,91,93] In Figure 5.8, the spectral heterogeneity of AZTD, a complex, multi-component sample, is compared using three different vibrational spectroscopic probes at macroscale, microscale, and nanoscale resolution.

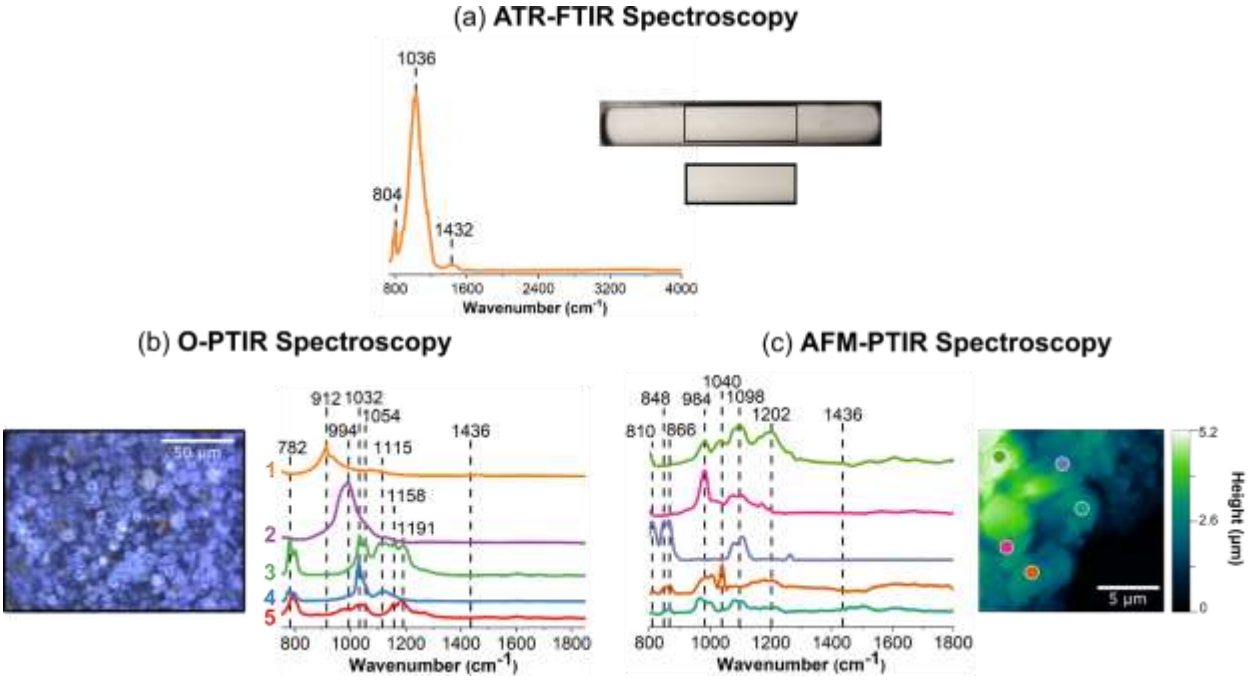

Figure 5.8 Comparison of infrared spectra collected for Arizona Test Dust (AZTD) from the three different instruments used in this study (a) Nicolet iS10 spectrometer (ATR-FTIR spectroscopy), (b) nanoIR2 (AFM-IR spectroscopy), and (c) mIRage-Raman (O-PTIR spectroscopy). A high magnification (40x) image of an AZTD thin film is shown in (b) while an AFM 2D height image is shown in (c). Selected point spectra are shown. Colored dots on the regions of the corresponding images match each of the colored spectra.

Consistent with what has been observed for the aluminosilicates, AZTD shows similar features in the ATR-FTIR spectrum from 725 cm^{-1} to 1300 cm^{-1}, as shown in Figure 5.8a. The ATR-FTIR spectrum also indicates a peak at 1432 cm^{-1} which is attributed to the presence of carbonates, as seen in Table 5.5. O-PTIR spectra show variation in intensity and peak position. The high magnification optical image of AZTD depicts a highly heterogenous samples, with features that are more spherical or trapezoidal that vary in height, size, color, and shape, layered on top of one another. The nanoscale perspective by the AFM image provides quantitative information about the roughness of these samples, indicating that the height of the film can reach as high as 5µm.

When comparing the spectra obtained between the mIRage-Raman and nanoIR2, there are clear variations observed in the 980 cm^{-1} to 1200 cm^{-1} region. In Figure 5.8b, the spectra labeled 1 (orange) and 2 (purple) exhibit broad peaks at 912 cm^{-1} and 994 cm^{-1}, respectively. These two regions suggest the presence of aluminosilicate derivatives. For example, spectra labeled 3 (green), 4 (blue), and 5 (red) all have a band ca. 780 cm^{-1}, which is indicative of alumina as well as iron.[94] Among these spectra, there is more variation in the ca. 1000 cm^{-1} to ca. 1200 cm^{-1} region, which suggests the varying stoichiometric ratios of alumina and silica, as well as the presence of some sulfates, which are known to be a component of AZTD.[93,94] Broader spectral features for the O-PTIR spectra are attributed to the difference in spatial resolution, being able to distinguish between various minerals and components that make up this complex sample.

Figure 5.8c provides additional evidence of the different species that compose AZTD. The five spectra in Figure 4c are distinct from one another. The spectra labeled 3 (purple), 4 (orange), and 5 (teal) show bands below 866 cm^{-1}. In this region, we can expect alumina derivatives as well as carbonate derivates, as indicated by aluminum oxide and calcium carbonate in Table 5.3 and 5.5, respectively. On the other hand, the spectra labeled 1 (green) and 2 (pink) are absent of these peaks but are much richer in silica and sulfate derivatives. The data collected here can be used to better understand the composition of these complex mineral samples, along with other complementary to other techniques. For example, Cwiertny *et al.* has characterized AZTD using XRD and SEM-EDX and found that this sample contained quartz and aluminosilicates with interlayer cations such as iron.[95] The presence of iron can be the reason for the observed fluorescence of AZTD that is observed in the Raman spectrum shown in Table 5.8, consistent with the previous discussion on the source of for fluorescence in clay minerals.[86,88]

Chemical maps provide additional insights into the heterogeneity in these sample, by spatially resolving the distribution of the absorption bands that are present within a selected region. In order to generate chemical maps, the QCL laser is tuned to specific wavelengths resonant with peaks in the spectra. Chemical maps that were collected on the microscale and nanoscale using O-PTIR and AFM-IR spectroscopies are shown in Figure 5.9. The images and spectral maps collected with O-PTIR spectroscopy are 125 µm x 165 µm whereas for AFM-IR spectroscopy, they are 15 µm x 15 µm. as the specific wavenumbers chosen for these spectral heat maps are based on the spectra that were obtained in Figure 4. With AZTD, there are two main regions that are distinct – a sharp peak below 868 cm^{-1}, representing in-plane bending modes of carbonates, and a more complex region around 910 to 1265 cm^{-1}, representing aluminosilicate derivatives.[66,96]

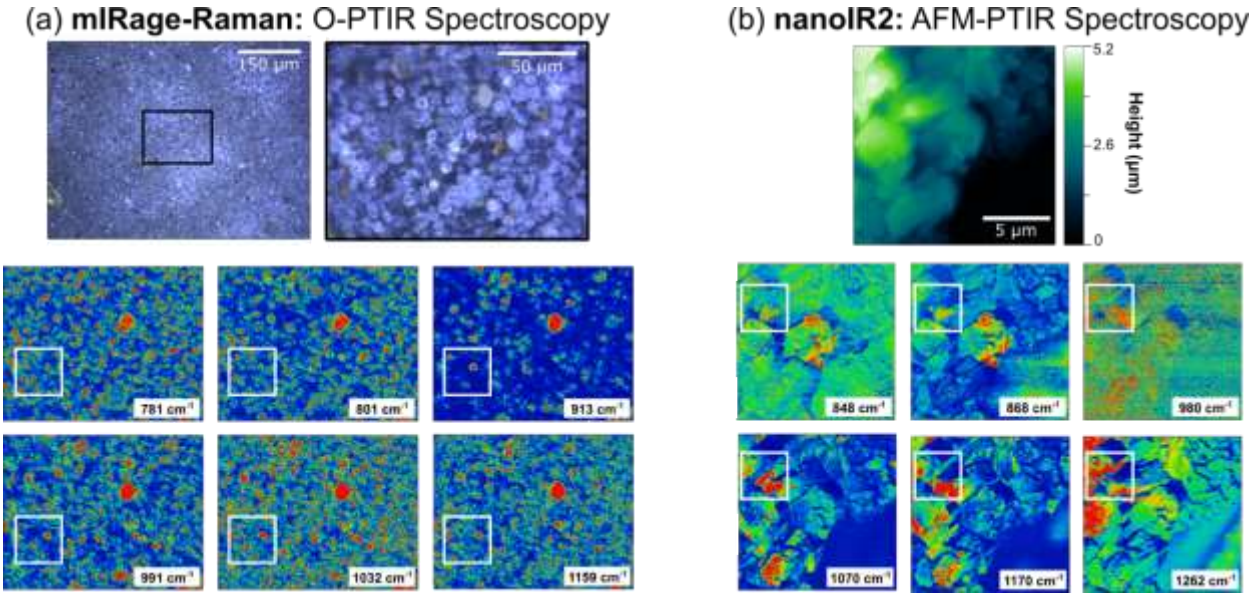

Figure 5.9 Comparison of spatial heterogeneity detected in Arizona Test Dust (AZTD) on micro- and nanoscales: (a) mIRage-Raman (O-PTIR spectroscopy) and (b) nanoIR2 (AFM-IR spectroscopy), respectively. The optical images are shown at both 10x and 40x magnification as identified by the black box region in the 10x image. The chemical map images are at 10x magnification of a 125 µm x 165 µm region. The AFM 2D height image of an AZTD thin film with spectral maps are shown for a 15 µm x 15 µm region. The boxed areas in white highlight specific regions in which spatial heterogeneities are observed on both the microscale and nanoscale level.

Figure 5.9a shows six chemical maps at different wavenumbers collected for a specific region of an AZTD thin film with the mIRage-Raman. At a glance, the O-PTIR maps look very similar; however, the microscopic differences present in the white boxes provide different information. The 781 cm^{-1} and 801 cm^{-1} O-PTIR maps differ from the rest of the chemical maps, which show a highly IR active circular particle near the center of the white boxes. This suggests that the particle contains components that are IR active at 913 cm^{-1}, 991 cm^{-1}, 1032 cm^{-1}, and 1159 cm^{-1}, which can be assigned to aluminosilicates, consistent with the O-PTIR spectra shown in Figure 5.9. Moreover, the red-colored hot spots that are specific to the 781 cm^{-1} and 801 cm^{-1} suggest regions in which iron or aluminum oxide could be enriched, as these are close to the frequencies reported in Table 5.3. Figure 5.9b shows AFM-IR chemical maps, where the white boxes highlight nanoscale heterogeneity. The 848 cm^{-1} and 868 cm^{-1} maps exhibit similar features that are significantly distinct from the maps at 980 cm^{-1}, 1070 $cm^{-1,}$ 1100 cm^{-1}, and 1170 cm^{-1}. However, these maps show differences as well within different regions of the sample, providing insights into the different ratios of species present. Using Figures 5.3, 5.5, and 5.7, the 980 cm^{-1} and 1070 cm^{-1} maps show where pockets of either pure aluminum oxide or silicon dioxide, as well as aluminosilicates such as montmorillonite or zeolite, exist. In addition, the maps at 1100 cm^{-1} and 1170 cm^{-1} show where other components, such as sodium sulfate, are potentially present as well. These spectral maps of the different features provide detailed evidence of the heterogeneity of this sample due to the different components present within it and are complementary to the heterogeneity of the spectra collected in Figure 5.9. By combining both microscopy and spectroscopy together, the heterogeneity of complex materials and the thin films that they form become evident.

5.5 Conclusion

We have investigated the use of several different vibrational spectroscopic methods to probe geochemical thin films and particles across different length scales from the macro- to the micro- to the nanoscale. Several important conclusions come from this comparison: (1) the intensities and frequencies for single component mineral thin films differ between the different vibrational methods used because of different modes of operation and selection rules; (2) heterogeneities can be seen in the intensities across films measured on micro and nanoscales; (3) for these thin films, *both* single component films and more chemically complex, AZTD sample, spectra collected on the micro and nanoscale spectra show variability. These variabilities can be due to local chemical environments – including coordination mode, impurities and structural heterogenies as well as different chemical components for AZTD. In addition, in some cases polarization effects due to crystalline particle orientation can contribute to variation in spectra for these laser-based microspectroscopic probes.[97-100] Amongst the three methods, AFM-IR spectroscopy requires the greatest amount of time for spectral and image data collection but can provide the most detailed information about local environments for thin films and single particles. Overall, this study provides an overview of these different vibrational methods for physical and chemical characterization of different minerals and geochemical thin films that play a critical role in interfacial geochemistry occurring at the interface of the atmosphere/geosphere and hydrosphere/geosphere.

5.6 Acknowledgements

Chapter 5, contains unpublished material coauthored with Townsley, S. and Grassian, V. H. The dissertation author was the primary investigator and author of this paper. The authors would like to thank Dr. Carolina Molina for her contribution in helpful discussions surrounding preliminary data collection for the minerals investigated in this manuscript.

5.7 Bibliography

(1) Sit, I.; Wu, H.; Grassian, V. H. Environmental Aspects of Oxide Nanoparticles: Probing Oxide Nanoparticle Surface Processes Under Different Environmental Conditions. *Ann. Rev. Anal. Chem.* **2021**, *14*, 489-514.

(2) Song, W.; Li, G.; Grassian, V. H.; Larsen, S. C. Development of Improved Materials for Environmental Applications: Nanocrystalline NaY Zeolites. *Environ. Sci. Technol.* **2005**, *39* (5), 1214–1220.

(3) Gao, J.; Mikutta, R.; Jansen, B.; Guggenberger, G.; Vogel, C.; Kalbitz, K. The Multilayer Model of Soil Mineral–Organic Interfaces—a Review. *J. Plant Nutr. Soil Sci*. **2020**, *183* (1), 27–41.

(4) Kok, J. F.; Storelvemo, T.; Kaydis, V. A.; Adebiyi, A. A.; Mahowald, N. M.; Evan, A. T.; He, C.; Leung, D. M. Mineral Dust Aerosol Impacts on Global Climate and Climate Change. *Nat. Rev. Earth Environ.* **2023**, *4*, 71–86.

(5) Brown, G. E.; Henrich, V. E.; Casey, W. H.; Clark, D. L.; Eggleston, C.; Felmy, A.; Goodman, D. W.; Grätzel, M.; Maciel, G.; McCarthy, M. I.; Nealson, K. H.; Sverjensky, A.; Toney, M. F.; Zachara, J. M. Metal Oxide Surfaces and Their Interactions with Aqueous Solutions and Microbial Organisms. *Chem. Rev.* **1999**, *99*, 77-174.

(6) Banuelos, J.; Borguet, E.; Brown, G.; Cygan, R.; De Yoreo, J.; Dove, P.; Gaigeot, M.-P.; Geiger, F.; Gibbs, J.; Grassian, V.; Ilgen, A.; Jun, Y.-S.; Kabengi, N.; Katz, L.; Kubicki, J.; Lutzenkirchen, J.; Putnis, C.; Remsing, R.; Rosso, K.; Rother, G.; Sulpizi, M.; Villalobos, M.; Zhang, H. Oxide- and Silicate-Water Interfaces and Their Roles in Technology and the Environment. *Chem. Rev.* **2023**.

(7) Usher, C. R.; Michel, A. E.; Grassian, V. H. Reactions on Mineral Dust. *Chem. Rev.* **2003**, *103* (12), 4883–4939.

(8) Goodman, A. L.; Underwood, G. M.; Grassian, V. H. Heterogeneous Reaction of NO_2: Characterization of Gas-Phase and Adsorbed Products from the Reaction, $2NO_2(g) + H_2O(a) \rightarrow HONO(g) + HNO_3$ (a) on Hydrated Silica Particles. *J. Phys. Chem. A* **1999**, *103* (36), 7217–7223.

(9) Goodman, A. L.; Li, P.; Usher, C. R.; Grassian, V. H. Heterogeneous Uptake of Sulfur Dioxide on Aluminum and Magnesium Oxide Particles. *J. Phys. Chem. A* **2001**, *105* (25), 6109–6120.

(10) Yu, Z.; Jang, M.; Park, J. Modeling Atmospheric Mineral Aerosol Chemistry to Predict Heterogeneous Photooxidation of SO_2. *Atmos. Chem. Phys.* **2017**, *17* (16), 10001–10017.

(11) Sobanska, S.; Hwang, H.; Choël, M.; Jung, H. J.; Eom, H. J.; Kim, H.; Barbillat, J.; Ro, C. U. Investigation of the Chemical Mixing State of Individual Asian Dust Particles by the Combined Use of Electron Probe X-Ray Microanalysis and Raman Microspectrometry. *Anal. Chem.* **2012**, *84* (7), 3145–3154.

(12) Cwiertny, D. M.; Hunter, G. J.; Pettibone, J. M.; Scherer, M. M.; Grassian, V. H. Surface Chemistry and Dissolution of α-FeOOH Nanorods and Microrods: Environmental Implications of Size-Dependent Interactions with Oxalate. *J. Phys. Chem. C* **2009**, *113* (6), 2175–2186.

(13) Cwiertny, D. M.; Handler, R. M.; Schaefer, M. V.; Grassian, V. H.; Scherer, M. M. Interpreting Nanoscale Size-Effects in Aggregated Fe-Oxide Suspensions: Reaction of Fe (II) with Goethite. *Geochim. Cosmochim. Acta* **2008**, *72* (5), 1365–1380.

(14) Waychunas, G. A.; Kim, C. S.; Banfield, J. F. Nanoparticulate Iron Oxide Minerals in Soils and Sediments: Unique Properties and Contaminant Scavenging Mechanisms. In *J. Nano. Res.* **2005**, *7*, 409–433.

(15) Bhattacharyya, A.; Schmidt, M. P.; Stavitski, E.; Martínez, C. E. Iron Speciation in Peats: Chemical and Spectroscopic Evidence for the Co-Occurrence of Ferric and Ferrous Iron in Organic Complexes and Mineral Precipitates. *Org. Geochem.* **2018**, *115*, 124–137.

(16) Garg, S.; Xing, G.; Waite, T. D. Influence of pH on the Kinetics and Mechanism of Photoreductive Dissolution of Amorphous Iron Oxyhydroxide in the Presence of Natural Organic Matter: Implications to Iron Bioavailability in Surface Waters. *Environ. Sci. Technol.* **2020**, *54* (11), 6771–6780.

(17) Tang, M.; Cziczo, D. J.; Grassian, V. H. Interactions of Water with Mineral Dust Aerosol: Water Adsorption, Hygroscopicity, Cloud Condensation, and Ice Nucleation. *Chem. Rev.* **2016**, *116* (7), 4205–4259.

(18) Xu, C.; Deng, K. ying; Li, J.; Xu, R. Impact of Environmental Conditions on Aggregation Kinetics of Hematite and Goethite Nanoparticles. *J. Nanopart. Res.* **2015**, *17* (10), 1-13.

(19) Hoffman, R. C.; Laskin, A.; Finlayson-Pitts, B. J. Sodium Nitrate Particles: Physical and Chemical Properties during Hydration and Dehydration, and Implications for Aged Sea Salt Aerosols. *J. Aerosol Sci.* **2004**, *35* (7), 869–887.

(20) Ye, B.; Ji, X.; Yang, H.; Yao, X.; Chan, C. K.; Cadle, S. H.; Chan, T.; Mulawa, P. A. Concentration and Chemical Composition of PM 2.5 in Shanghai for a 1-Year Period; **2003**, *37* (4), 499-510.

(21) Mora Garcia, S. L.; Pandit, S.; Navea, J. G.; Grassian, V. H. Nitrous Acid (HONO) Formation from the Irradiation of Aqueous Nitrate Solutions in the Presence of Marine Chromophoric Dissolved Organic Matter: Comparison to Other Organic Photosensitizers. *ACS Earth Sp. Chem.* **2021**, *5* (11), 3056–3064.

(22) Hatch, C. D.; Gierlus, K. M.; Schuttlefield, J. D.; Grassian, V. H. Water Adsorption and Cloud Condensation Nuclei Activity of Calcite and Calcite Coated with Model Humic and Fulvic Acids. *Atmos. Environ.* **2008**, *42* (22), 5672–5684.

(23) Gibson, E. R.; Gierlus, K. M.; Hudson, P. K.; Grassian, V. H. Generation of Internally Mixed Insoluble and Soluble Aerosol Particles to Investigate the Impact of Atmospheric Aging and Heterogeneous Processing on the CCN Activity of Mineral Dust Aerosol. *Aerosol Sci. Tech.* **2007**, *41* (10), 914–924.

(24) Kim, D.; Grassian, V. H. Analysis of Micro- and Nanoscale Heterogeneities within Environmentally Relevant Thin Films Containing Biological Components, Oxyanions and Minerals Using AFM-PTIR Spectroscopy. *Environ. Sci. Process Impacts* **2023**, *25* (3), 484-495.

(25) Violante, A. Elucidating Mechanisms of Competitive Sorption at the Mineral/Water Interface. *Adv. in Agro.* **2013**, *118*, 111–176.

(26) Lee, A. K. Y.; Chan, C. K. Single Particle Raman Spectroscopy for Investigating Atmospheric Heterogeneous Reactions of Organic Aerosols. *Atmos. Environ.* **2007**, *41* (22), 4611–4621.

(27) Mirrielees, J. A.; Kirpes, R. M.; Haas, S. M.; Rauschenberg, C. D.; Matrai, P. A.; Remenapp, A.; Boschi, V. L.; Grannas, A. M.; Pratt, K. A.; Ault, A. P. Probing Individual Particles Generated at the Freshwater-Seawater Interface through Combined Raman, Photothermal Infrared, and X-Ray Spectroscopic Characterization. *ACS Meas. Sci. Au* **2022**, *2* (6), 605–619.

(28) Kim, D.; Grassian, V. H. Attenuated Total Reflection-Fourier Transform Infrared and Atomic Force Microscopy-Infrared Spectroscopic Investigation of Suwannee River Fulvic Acid and Its Interactions with α-FeOOH. *ACS Earth Sp. Chem.* **2022**, *6* (1), 81–89.

(29) Ro, C. U.; Hwang, H.; Kim, H.; Chun, Y.; Van Grieken, R. Single-Particle Characterization of Four "Asian Dust" Samples Collected in Korea, Using Low-Z Particle Electron Probe X-Ray Microanalysis. *Environ. Sci. Technol.* **2005**, *39* (6), 1409–1419.

(30) Li, W.; Shao, L.; Zhang, D.; Ro, C. U.; Hu, M.; Bi, X.; Geng, H.; Matsuki, A.; Niu, H.; Chen, J. A Review of Single Aerosol Particle Studies in the Atmosphere of East Asia: Morphology, Mixing State, Source, and Heterogeneous Reactions. *J. Cleaner Prod.*, **2016**, *112*, 1330–1349.

(31) Hwang, H. J.; Ro, C. U. Direct Observation of Nitrate and Sulfate Formations from Mineral Dust and Sea-Salts Using Low-Z Particle Electron Probe X-Ray Microanalysis. *Atmos. Environ.* **2006**, *40* (21), 3869–3880.

(32) Ro, C.-U.; Oh, K.-Y.; Kim, H.; Chun, Y.; Osán, J.; de Hoog, J.; Grieken, V. Chemical Speciation of Individual Atmospheric Particles Using Low-Z Electron Probe X-Ray Microanalysis: Characterizing "Asian Dust" Deposited with Rainwater in Seoul, Korea. *Atmos. Environ.* **2001**, *35* (29), 4995-5005.

(33) Song, X.; Boily, J. F. Water Vapor Adsorption on Goethite. *Environ. Sci. Technol.* **2013**, *47* (13), 7171–7177.

(34) Song, X.; Boily, J. F. Structural Controls on OH Site Availability and Reactivity at Iron Oxyhydroxide Particle Surfaces. *Phys. Chem. Chemic. Physics* **2012**, *14* (8), 2579–2586.

(35) Boily, J. F.; Persson, P.; Sjöberg, S. Benzenecarboxylate Surface Complexation at the Goethite (α-FeOOH)/Water Interface: II. Linking IR Spectroscopic Observations to Mechanistic Surface Complexation Models for Phthalate, Trimellitate, and Pyromellitate. *Geochim. Cosmochim. Acta* **2000**, *64* (20), 3453–3470.

(36) Mudunkotuwa, I. A.; Minshid, A. Al; Grassian, V. H. ATR-FTIR Spectroscopy as a Tool to Probe Surface Adsorption on Nanoparticles at the Liquid-Solid Interface in Environmentally and Biologically Relevant Media. *Analyst* **2014**, *139* (5), 870–881.

(37) Hase, M.; Scheffelmaier, R.; Hayden, S.; Rivera, D. Quantitative *in situ* Attenuated Total Internal Reflection Fourier Transform Infrared Study of the Isotherms of Poly(Sodium 4-Styrene Sulfonate) Adsorption to a TiO_2 Surface over a Range of Cetylpyridinium Bromide Monohydrate Concentration. *Langmuir* **2010**, *26* (8), 5534–5543.

(38) Sit, I.; Quirk, E.; Hettiarachchi, E.; Grassian, V. H. Differential Surface Interactions and Surface Templating of Nucleotides (dGMP, dCMP, dAMP, and dTMP) on Oxide Particle Surfaces. *Lang.* **2022**, *38* (49), 15038–15049.

(39) Hug, S. J.; Sulzberger, B. *In Situ* Fourier Transform Infrared Spectroscopic Evidence for the Formation of Several Different Surface Complexes of Oxalate on TiO2 in the Aqueous Phase. *Lang.* **1994**, *10* (10), 3587–3597.

(40) Mudunkotuwa, I. A.; Grassian, V. H. Biological and Environmental Media Control Oxide Nanoparticle Surface Composition: The Roles of Biological Components (Proteins and Amino Acids), Inorganic Oxyanions and Humic Acid. *Environ. Sci. Nano.* **2015**, *2* (5), 429–439.

(41) Zhang, D.; Li, C.; Zhang, C.; Slipchenko, M. N.; Eakins, G.; Cheng, J. X. Depth-Resolved Mid-Infrared Photothermal Imaging of Living Cells and Organisms with Submicrometer Spatial Resolution. *Sci. Adv.* **2016**, *2* (9), 1-7.

(42) Li, X.; Zhang, D.; Bai, Y.; Wang, W.; Liang, J.; Cheng, J. X. Fingerprinting a Living Cell by Raman Integrated Mid-Infrared Photothermal Microscopy. *Anal. Chem.* **2019**, *91* (16), 10750-10756.

(43) Bai, Y.; Zhang, D.; Lan, L.; Huang, Y.; Maize, K.; Shakouri, A.; Cheng, J. X. Ultrafast Chemical Imaging by Widefield Photothermal Sensing of Infrared Absorption. *Sci. Adv.* **2019**, *5* (7), 1-8.

(44) Olson, N. E.; Xiao, Y.; Lei, Z.; Ault, A. P. Simultaneous Optical Photothermal Infrared (O-PTIR) and Raman Spectroscopy of Submicrometer Atmospheric Particles. *Anal. Chem.* **2020**, *92* (14), 9932–9939.

(45) Li, Z.; Aleshire, K.; Kuno, M.; Hartland, G. V. Super-Resolution Far-Field Infrared Imaging by Photothermal Heterodyne Imaging. *J. Phys. Chem. B* **2017**, *91*(16), 10750-10756.

(46) Marcott, C.; Kansiz, M.; Dillon, E.; Cook, D.; Mang, M. N.; Noda, I. Two-Dimensional Correlation Analysis of Highly Spatially Resolved Simultaneous IR and Raman Spectral Imaging of Bioplastics Composite Using Optical Photothermal Infrared and Raman Spectroscopy. *J. Mol. Struct.* **2020**, *1210*, 1-6.

(47) de Faria, D. L. A.; Lopes, F. N. Heated Goethite and Natural Hematite: Can Raman Spectroscopy Be Used to Differentiate Them? *Vib. Spectrosc.* **2007**, *45* (2), 117–121.

(48) Dele-Duboisl, M. L.; Dhamelincourtl, P.; Poirotz, J. P.; Schubnel, H. J. Differentiation between gems and synthetic minerals by laser Raman microspectroscopy. *J. Mol. Struc.* **1986**, *143* (1), 135-138.

(49) Skoog, D. A.; Holler, F. J.; Crouch, S. R. *Principles of Instrumental Analysis*, Sixth.; Brooks Cole: Belmont, **2007**.

(50) Smith, Ewen.; Dent, Geoffrey. Modern Raman Spectroscopy: A Practical Approach. *J. Wiley*, **2005**.

(51) Dazzi, A.; Prater, C. B.; Hu, Q.; Bruce, D.; Rabolt, J. F.; Marcott, C. Focal Point Review AFM-IR: Combining Atomic Force Microscopy and Infrared Spectroscopy for Nanoscale Chemical Characterization. *Appl. Spectrosc.* **2012**, *66* (12), 1365–1384.

(52) Dazzi, A.; Prater, C. B. AFM-IR: Technology and Applications in Nanoscale Infrared Spectroscopy and Chemical Imaging. *Chem. Rev.* **2016**, *117* (7), 5146–5173.

(53) Dazzi, A.; Glotin, F.; Carminati, R. Theory of Infrared Nanospectroscopy by Photothermal Induced Resonance. *J. Appl. Phys.* **2010**, *107* (123519), 1-8.

(54) Ramer, G.; Aksyuk, V. A.; Centrone, A.; Nanocenter, M. Quantitative Chemical Analysis at the Nanoscale Using the Photothermal Induced Resonance Technique. *Anal. Chem.* **2017**, *89* (24), 13524–13531.

(55) Voigtländer, B. *Atomic Force Microscopy*, 2nd ed.; Springer International Publishing, **2019**.

(56) Morsch, S.; Lyon, S.; Edmondson, S.; Gibbon, S. Reflectance in AFM-IR: Implications for Interpretation and Remote Analysis of the Buried Interface. *Anal. Chem.* **2020**, *92* (12), 8117–8124.

(57) Weckler, B.; Lutz, H. D. Lattice vibration spectra. Part XCV. Infrared spectroscopic studies on the iron oxide hydroxides goethite, akageneite, lepidocrocite, and feroxyhite. *Euro. J. Solid State and Inorg. Chem.* **1998**, *35* (8), 531-544.

(58) Legodi, M. A.; de Waal, D. The Preparation of Magnetite, Goethite, Hematite and Maghemite of Pigment Quality from Mill Scale Iron Waste. *Dyes and Pigments* **2007**, *74* (1), 161–168.

(59) Frank, O.; Zukalova, M.; Laskova, B.; Kürti, J.; Koltai, J.; Kavan, L. Raman Spectra of Titanium Dioxide (Anatase, Rutile) with Identified Oxygen Isotopes (16, 17, 18). *Phys. Chem. Chemic. Physics* **2012**, *14* (42), 14567–14572.

(60) Hu, Y.; Tsai, H.-L.; Huang, C.-L. Effect of Brookite Phase on the Anatase-Rutile Transition in Titania Nanoparticles. *J. Euro. Ceramic Soc.*, **2003**, *23*, 691-696.

(61) Trivedi, M. K.; Dahryn Trivedi, A. B. Spectroscopic Characterization of Disodium Hydrogen Orthophosphate and Sodium Nitrate after Biofield Treatment. *J. Chromatogr. Sep. Tech.* **2015**, *6* (5), 1-5.

(62) Liu, J. H.; Zhang, Y. H.; Wang, L. Y.; Wei, Z. F. Drawing out the Structural Information of the First Layer of Hydrated Ions: ATR-FTIR Spectroscopic Studies on Aqueous NH_4NO_3, $NaNO_3$, and $Mg(NO_3)_2$ Solutions. *Spectrochim. Acta A Mol. Biomol. Spectrosc.* **2005**, *61* (5), 893–899.

(63) Wang, P.; Wang, N.; Pang, S. F.; Zhang, Y. H. Hygroscopicity of Internally Mixed Particles Glycine/$NaNO_3$ Studied by FTIR-ATR Technique. *J. Aerosol Sci.* **2018**, *116*, 25–33.

(64) Ahlijah, G. E. B. Y.; Mooney, E. F. The Attenuated Total Reflection Spectra of Polyatomic Inorganic Anions – II. The Nitrogen Containing Anions. *Spectrochim. Acta* **1968**, *25*, 619-627.

(65) Zhang, Q. N.; Zhang, Y.; Cai, C.; Guo, Y. C.; Reid, J. P.; Zhang, Y. H. *In Situ* Observation on the Dynamic Process of Evaporation and Crystallization of Sodium Nitrate Droplets on a ZnSe Substrate by FTIR-ATR. *J. Phys. Chem. A* **2014**, *118* (15), 2728–2737.

(66) Al-Hosney, H. A.; Grassian, V. H. Water, Sulfur Dioxide and Nitric Acid Adsorption on Calcium Carbonate: A Transmission and ATR-FTIR Study. *Phys. Chem. Chemic. Physics* **2005**, *7* (6), 1266–1276.

(67) Andersen, F. A; Brečević, L. Infrared Spectra of Amorphous and Crystalline Calcium Carbonate. *Acta Chem. Scand.* **1991**, *45*, 1018-1024.

(68) Al-Abadleh, H. A.; Al-Hosney, H. A.; Grassian, V. H. Oxide and Carbonate Surfaces as Environmental Interfaces: The Importance of Water in Surface Composition and Surface Reactivity. *J. Mol. Cat. A: Chem.* **2005**, *228*, 47–54.

(69) Gunasekaran, S.; Anbalagan, G.; Pandi, S. Raman and Infrared Spectra of Carbonates of Calcite Structure. *J. Raman Spec.* **2006**, *37* (9), 892–899.

(70) Peak, D.; Ford, R. G.; Sparks, D. L. An *in situ* ATR-FTIR Investigation of Sulfate Bonding Mechanisms on Goethite. *J. Coll. Int. Sci.* **1999**, *218* (1), 289–299.

(71) Paul, K. W.; Borda, M. J.; Kubicki, J. D.; Sparks, D. L. Effect of Dehydration on Sulfate Coordination and Speciation at the Fe-(Hydr)Oxide-Water Interface: A Molecular Orbital/Density Functional Theory and Fourier Transform Infrared Spectroscopic Investigation. *Lang.* **2005**, *21* (24), 11071–11078.

(72) Wang, X.; Wang, Z.; Peak, D.; Tang, Y.; Feng, X.; Zhu, M. Quantification of Coexisting Inner- and Outer-Sphere Complexation of Sulfate on Hematite Surfaces. *ACS Earth Sp. Chem.* **2018**, *2* (4), 387–398.

(73) Bondy, A. L.; Kirpes, R. M.; Merzel, R. L.; Pratt, K. A.; Banaszak Holl, M. M.; Ault, A. P. Atomic Force Microscopy-Infrared Spectroscopy of Individual Atmospheric Aerosol Particles: Subdiffraction Limit Vibrational Spectroscopy and Morphological Analysis. *Anal. Chem.* **2017**, *89* (17), 8594–8598.

(74) Yeung, M. C.; Lee, A. K. Y.; Chan, C. K. Phase Transition and Hygroscopic Properties of Internally Mixed Ammonium Sulfate and Adipic Acid (AS-AA) Particles by Optical Microscopic Imaging and Raman Spectroscopy. *Aero. Sci. Tech.* **2009**, *43* (5), 387–399.

(75) Jariwala, M.; Crawford, J.; LeCaptain, D. J. *In Situ* Raman Spectroscopic Analysis of the Regeneration of Ammonium Hydrogen Sulfate from Ammonium Sulfate. *Ind. Eng. Chem. Res.* **2007**, *46* (14), 4900–4905.

(76) Qiu, J.; Li, X.; Qi, X. Raman Spectroscopic Investigation of Sulfates Using Mosaic Grating Spatial Heterodyne Raman Spectrometer. *J. IEEE Photonics* **2019**, *11* (5), 1-13.

(77) Rindelaub, J. D.; Craig, R. L.; Nandy, L.; Bondy, A. L.; Dutcher, C. S.; Shepson, P. B.; Ault, A. P. Direct Measurement of pH in Individual Particles *via* Raman Microspectroscopy and Variation in Acidity with Relative Humidity. *J. Phys. Chem. A* **2016**, *120* (6), 911–917.

(78) Chan, M. N.; Lee, A. K. Y.; Chan, C. K. Responses of Ammonium Sulfate Particles Coated with Glutaric Acid to Cyclic Changes in Relative Humidity: Hygroscopicity and Raman Characterization. *Environ. Sci. Technol.* **2006**, *40* (22), 6983–6989.

(79) Frost, R. L. The Structure of the Kaolinite Minerals — a FT-Raman Study. *Clay Miner* **1997**, *32* (1), 65–77.

(80) Chen, H.; Koopal, L. K.; Xiong, J.; Avena, M.; Tan, W. Mechanisms of Soil Humic Acid Adsorption onto Montmorillonite and Kaolinite. *J. Coll. Int. Sci.* **2017**, *504*, 457–467.

(81) Madejová, J. FTIR Techniques in Clay Mineral Studies. *Vib Spectrosc* **2003**, *31* (1), 1–10.

(82) Zhang, R.; Yan, W.; Jing, C. Mechanistic Study of PFOS Adsorption on Kaolinite and Montmorillonite. *Coll. Surf. A Physicochem. Eng. Asp.* **2014**, *462*, 252–258.

(83) Ludwig, B.; Burke, T. T. Infrared Spectroscopy Studies of Aluminum Oxide and Metallic Aluminum Powders, Part I: Thermal Dehydration and Decomposition. *Powders* **2022**, *1* (1), 47–61.

(84) Frost, R. L. The Structure of the Kaolinite Minerals — a FT-Raman Study. *Clay Min.* **1997**, *32* (1), 65–77.

(85) Farmer, V. C. Differing Effects of Particle Size and Shape in the Infrared and Raman Spectra of Kaolinite. *Clay Min.* **1998**, *33* (4), 601–604.

(86) Ritz, M.; Vaculíková, L.; Kupková, J.; Plevová, E.; Bartoňová, L. Different Level of Fluorescence in Raman Spectra of Montmorillonites. *Vib. Spec.* **2016**, *84*, 7–15.

(87) Alia, J. M.; Edwards, H. G. M.; Garcia-Navarro, F. J.; Parras-Armenteros, J.; Sanchez-Jimenez, C. J. Application of FT-Raman Spectroscopy to Quality Control in Brick Clays Firing Process. *Talanta* **1999**, *50* (2), 291-298.

(88) Košařová, V.; Hradil, D.; Němec, I.; Bezdička, P.; Kanický, V. Microanalysis of Clay-Based Pigments in Painted Artworks by the Means of Raman Spectroscopy. *J. Raman Spec.* **2013**, *44* (11), 1570–1577.

(89) Frost, R. L. Fourier Transform Raman Spectroscopy of Kaolinite, Dickite and Halloysite. *Clays and Clay Min.* **1995**, *43*, 191-195.

(90) Bian, H.; Zender, C. S. Mineral Dust and Global Tropospheric Chemistry: Relative Roles of Photolysis and Heterogeneous Uptake. *J. Geophys. Research: Atmos.* **2003**, *108* (21), 1-14.

(91) Ramaswamy, V.; Boucher, O.; Haigh, J.; Hauglustaine, D.; Haywood, J.; Myhre, G.; Nakajima, T.; Shi, G.; Solomon Contributing Authors Betts, S. R.; Charlson, R.; Chuang, C.; Daniel, J.; Del Genio, A.; van Dorland, R.; Feichter, J.; Fuglestvedt, J.; de Forster, P. F.; Ghan, S.; Jones, A.; Kiehl, J.; Koch, D.; Land, C.; Lean, J.; Lohmann, U.; Minschwaner, K.; Penner, J.; Roberts, D.; Rodhe, H.; Roelofs, G.; Rotstayn, L.; Schneider, T.; Schumann, U.; Schwartz, S.; Shine, K.; Smith, S.; Stevenson, D.; Stordal, F.; Tegen, I.; Zhang, Y.; Srinivasan, J.; Joos, F. Radiative Forcing of Climate Change. *IPCC Third Assessment Rep.* **2001**.

(92) Perkins, R. J.; Gillette, S. M.; Hill, T. C. J.; Demott, P. J. The Labile Nature of Ice Nucleation by Arizona Test Dust. *ACS Earth Sp. Chem.* **2020**, *4* (1), 133–141.

(93) Vlasenko, A.; Sjögren, S.; Weingartner, E.; Gäggeler, H. W.; Ammann, M. Generation of Submicron Arizona Test Dust Aerosol: Chemical and Hygroscopic Properties. *Aero. Sci. Tech.* **2005**, *39* (5), 452–460.

(94) Navea, J. G.; Chen, H.; Huang, M.; Carmichel, G. R.; Grassian, V. H. A Comparative Evaluation of Water Uptake on Several Mineral Dust Sources. *Environ. Chem*. *7* (2), **2010**, 162–170.

(95) Cwiertny, D. M.; Baltrusaitis, J.; Hunter, G. J.; Laskin, A.; Scherer, M. M.; Grassian, V. H. Characterization and Acid-Mobilization Study of Iron-Containing Mineral Dust Source Materials. *J. Geophys. Research Atmos.* **2008**, *113* (5), 1-18.

(96) Laskina, O.; Young, M. A.; Kleiber, P. D.; Grassian, V. H. Infrared Extinction Spectroscopy and Micro-Raman Spectroscopy of Select Components of Mineral Dust Mixed with Organic Compounds. *J. Geophys. Research Atmos.* **2013**, *118* (12), 6593–6606.

(97) Ramer, G.; Aksyuk, V. A.; Centrone, A. Quantitative Chemical Analysis at the Nanoscale Using the Photothermal Induced Resonance Technique. *Anal. Chem.* **2017**, *89* (24) 13524–13531

(98) Schwartz, J. J.; Jakob, D. S.; Centrone, A. A guide to nanoscale IR spectroscopy: resonance enhanced transduction in contact and tapping mode AFM-IR. *Chem. Soc. Rev.*, **2022**, *51* (13), 5248–5267.

(99) Kurouski, D.; Dazzi, A.; Zenobi, R.; Centrone, A. Infrared and Raman chemical imaging and spectroscopy at the nanoscale. *Chem. Soc. Rev.*, **2020**, *49* (11), 3315–3347.

(100) Newman, R.; Halford, R. S. Motions of Molecules in Condensed Systems. VII. The Infra-

Red Spectra for Single Crystals of Ammonium Nitrate and Thallous Nitrate in Polarized Radiation. *J. Chem. Phys.*, **1950**, *18* (9), 1276–1290.

(101) Hinrichs, K.; Shaykhutdinov, T. Polarization-Dependent Atomic Force Microscopy–Infrared Spectroscopy (AFM-IR): Infrared Nanopolarimetric Analysis of Structure and Anisotropy of Thin Films and Surfaces. *Appl. Spectrosc.*, **2018**, *72* (6), 817–832.

CHAPTER 6
APPLICATIONS OF MICRO-SPECTROSCOPY IN PROBING OTHER ENVIRONMENTAL SYSTEMS

In this dissertation thus far, it is shown how micro-spectroscopic probes can be used as a tool to study the heterogenous interactions occurring along geochemical interfaces. However, these probes can also be used to probe the physical and chemical properties of substrate deposited aerosol particles relevant to both indoor and outdoor settings. This chapter discusses collaborative efforts using these tools to investigate the deposition of atmospheric aerosols on surfaces both purposefully, through particle deposition for the collection of sea spray aerosols, and unintentionally, through particle deposition on surfaces occurring in indoor environments due to different human activities and environmental scenarios. More specifically, the application of atomic force microscopy-photothermal infrared (AFM-IR) spectroscopy on indoor surfaces in the presence of common household events such as cooking and wildfire smoke intrusion as well as on outdoor environments such as substrate-deposited sea spray aerosol (SSA) are explored.

6.1 Introduction

The first part of this chapter focuses on collaborations using AFM-IR spectroscopy of single particles involving sea spray aerosols. Sea spray aerosols (SSA) are aerosols that are generated from the bursting of air bubbles when they are released from the wave breaking motion of the ocean.[1–4] Like other atmospherically relevant aerosols, SSA can directly influence the radiative budget of Earth both directly and indirectly, by scattering solar radiation or acting as

cloud condensation nuclei.[1,5–9] They are also highly complex in composition, and contain a mixture of organic, inorganic, and biological species that originate from the seawater directly or transferred from the sea surface microlayer.[1,2,6,10,11] This results in SSA that are highly diverse and different in size, morphology, and origin, allowing for these particles to participate in many types of surface chemistry that influence the biogeochemical cycling in the atmosphere.[2,3,5,12] When SSA are released and transported through the atmosphere, they can undergo atmospheric aging due to transformations from physical variables such as relative humidity, or from chemical variables such as reactions with oxidants, via OH radicals and ozone.[5,13–16] While the physicochemical properties of particulate SSA have been studied previously and are complex, due to the size-dependent chemical composition to date, there have not been many studies that investigate the effects of SSA as a result of SSA formation on variables such as windspeed and aging on a single particle level. (REF). With a microspectroscopic technique such as AFM-IR spectroscopy, this complexity can be probed to better understand how SSA behaves in the atmosphere.

The second campaign involved this chapter on collaborations using AFM-IR spectroscopy of single particles involves deposition of biomass burning particles on to surfaces present in indoor environments. Since 2020, there has been a notably increasing number of wildfires around the world, especially in California. While these wildfires have had disastrous impacts on forests and buildings, they have also begun to affect indoor environments as the smoke permeates into homes and spaces in which humans spend the majority of their time inside.[17] The introduction of smoke to these environments is a point of concern, as biomass burning aerosols that get into homes are known to contain many primary and secondary air pollutants that are extremely harmful for human health.[18,19] Therefore, in order to create cleaner and safer indoor environments that have been affected by wildfire smoke, it is important to understand the types of particles that are being

deposited onto indoor surfaces.[20] Through microspectroscopic techniques like AFM-IR spectroscopy, we can start to identify the different types of macromolecules these smoke particles are composed of, to eventually understand how it transforms on indoor surfaces and in the indoor we breathe.

The third application discussed in this chapter explores the potential of shale as a sink for hydrogen storage by investigating how high pressures of hydrogen interact with shale as determined by AFM-IR and O-PTIR spectroscopy. Shale is a type of sedimentary that is often formed from hydraulically fractured wells used for oil and gas recovery.[21–23] Shale can be characterized and categorized in a variety of different ways, due to its complex nature. It can be categorized by region or by its physicochemical properties such as permeability, pore size, composition, etc. Shale can be found in 28 major basins across the US, each of which vary in size and composition.[21–23] Eagle Ford shale, the shale used in these studies, comes from the Western Gulf Basin, which encompasses the southeastern Texas region and is comprised of carbonates, quartz, clays, and other minerals.[22–25]

Shale has been of particular interest in the past few decades due to its potential as a method to provide affordable energy and reduce greenhouse gases. Thus, research has focused on how shale interacts with energy relevant gases such as carbon dioxide and hydrogen. CO_2 can be used to increase shale production, enhance hydrocarbon recovery, or as a fracturing agent.[21,24] The reactivity of shale with hydrogen gas has recently been of interest due to its potential as a possible sink for subsurface dissolved hydrogen.[26–28] Thus far, hydrogen gas has been shown to significantly alter the mineral composition via mineral dissolution or precipitation.[26,29] However, the lack of experimental evidence in regard to how these reactions impact shale structure and the

reactions that occur with the different mineral components such as oxides, clays and carbonates is one of the barriers to moving forward with this development.[26,29]

6.2 Micro-spectroscopic Analysis of the Effects of Aging and Wind Speed on Substrate-Deposited Marine Sea Spray Aerosol

Aerosol generation and AFM-IR data collection and analysis of marine SSA. Samples used for both studies were prepared for two different campaigns organized by the NSF Center for Aerosol Impacts on Chemistry of the Environment (CAICE), that involved a wave-simulation channel facility, containing filtered seawater from La Jolla, California. Two different collaborative studies were held across two campaigns. The first study, that investigated the effects of aging on marine SSA, was held in 2019 through a campaign called Sea Spray Chemistry and Particle Evolution (SeaSCAPE) using the wave flume in the hydraulics laboratory down at Scripps Institution of Oceanography. The second study, which explored the effects of wind speed on marine SSA, was held in 2022 using a newly constructed ocean-atmosphere facility. This campaign was called Characterizing Atmospheric-Oceanic parameters of SOARS (CHAOS). SOARS stands for the Scripps Ocean Atmosphere Research Simulator.

For the SeaSCAPE study, nascent SSA (nSSA) were generated from a phytoplankton bloom contained in a large wave flume, filled with seawater. A micro-orifice uniform deposit impactor (MOUDI; MSP, Inc., model 110), was utilized to deposit nSSA particles released from the wave-breaking motion from the channel, at a flow rate of 30 L/min. These aerosol particles were deposited onto silica wafers (Ted Pella) that were hydrophobically coated with Rain-X after cleaning to make them hydrophobic. Aged SSA were generated by exposing nSSA to OH radicals

in efforts to mimic approximately 4-5 days of aging in the atmosphere. This protocol was adapted by Kaluarachchi et al, 2022.[5]

For the CHAOS study, a newly constructed ocean-atmosphere simulator filled with seawater was used to generate marine SSA. For aerosol deposition, the MOUDI was utilized and set to the same flow rate of 30 L/min. In this large scale experiment, rather than exposing the collected SSA to OH radicals for aging, the generated aerosols were collected at different wind speeds of 850 RPM and 1600 RPM. The particles were deposited onto cleaned silica wafers (Ted Pella).

The data sets for each of the SSA campaigns were organized by particle size. However, because the types of SSA particles vary in size and shape, it would not be accurate to simply assume they are all spherical and measure its diameter. Therefore, a volume-equivalent diameter was utilized for these studies in order to take into account the particle volume, which can be generated through the AFM processing software, Gwyddion. Mathematically, the volume-equivalent diameter is shown below, in Equation 7.1.

$$dV = \sqrt[3]{\frac{6dV}{\pi}}$$

(Eq. 6.1)

Here, dV represents the volume-equivalent diameter, and V refers to the volume of a single particle, which is automatically calculated and retrieved from the AFM software.

For both studies, AFM-IR spectroscopy was used to obtain vibrational spectra of individual particles. These spectra data complemented other measurements including AFM images alone of

substrate deposited particles collected by the Tivanski group at the University of Iowa. For these measurements, such as the AFM-IR measurements, a commercial nanoIR2 system (Bruker) equipped with a mid-IR quantum cascade laser (QCL) was used. Data collection took place under ambient temperature and pressure. AFM-IR analysis was conducted in Tapping AFM-IR mode, using gold-coated silicon nitride probes with tip radii of ~30 nm, a resonant frequency of 75 ± 15 kHz and a spring constant of 1 to 7 N/m. PTIR spectra were collected at a resolution of 4 cm^{-1}. The scan rate in which the AFM images were collected ranged from 0.5 to 0.8 Hz, depending on the sample. AFM-IR spectra presented were co-averaged from 5 spectra and taken at the center of each rounded particle and at the respective core and shell regions of each core-shell particle. AFM images were processed using the Gwyddion software. AFM-IR spectra were filtered using a 5-point, 3rd order polynomial, Savitzky-Golay algorithm and plotted in Origin. AFM-IR data was processed jointly by the dissertation author and Dr. Carolina Molina for the wind speed study.

Effects of aging on marine SSA. There are five different classes of aerosols identified by morphologies seen in AFM images from the 2019 SeaSCAPE campaign. The five categories are: (1) prism-like, (2) core-shell, (3) rounded, (4) rod-shell, and (5) aggregate.[1,5] Many research groups studying the physical properties of sea spray aerosols have classified them both quantitatively and qualitatively.[30–36] Quantitatively, two factors that can be used to describe an aerosol's physical properties: (1) aspect ratio, and (2) sphericity factor.

Aspect ratio refers to the spreading of a particle onto a surface upon impact. This measurement can be calculated using the diameter and height of a particle, as shown in Equation 7.2, below.[32,33]

$$AR = \frac{d_{max}}{d_{perp}}$$

(Eq. 6.2)

Here, the aspect ratio, denoted by AR, can be calculated by taking the ratio of d_{max}, which refers to the maximum diameter of the selected particle, and d_{perp}, which refers to the diameter perpendicular to the maximum diameter.[32,33] Aspect ratios have also been used as a way to distinguish various phase states that aerosols can possess from each other. For example, an aerosol can be more solid, liquid, or semi-solid, and the values of aspect ratios have been one method in which these particles were categorized.[30–33] In most cases, aspect ratios that are greater than 1 indicate that they are not elongated or distorted in any direction, suggesting a more solid-like composition. Conversely, particles with aspect ratios less than 1 are more likely to be liquid-like, or flatter.[30–33]

Sphericity, on the other hand, is a factor that measures how round a particle is. A sphericity factor of 1 indicates a particle that is perfectly spherical. Thus, any particle that has a sphericity factor vastly different than 1 is considered to be aspherical, or more oblong in shape.[32,33] The equation for sphericity is given in Equation 6.3 below.[32,33]

$$C = 4\pi \frac{A}{p^2}$$

(Eq. 6.3)

C , stands for circularity, which is another way sphericity is represented. In the equation, A refers to the area of the particle, p refers to the perimeter of the particle. Particle sphericity is an important

measurement for aerosols, as it can control properties of an aerosol such as particle mobility, as it travels through the atmosphere, participating in a wide range of atmospheric chemical reactions.[34]

Qualitatively, these aerosols were SSA were classified qualitatively by the Tivanski group, based on the particle height and phase images collected via AFM.[1,5] As reported by Kaluarachchi, the majority of nSSA is dominated by the rounded particles, whereas aged SSA is composed mainly of core-shell particles, suggesting that a chemical reaction with the exposure of OH radicals to the nSSA is eliciting a physical transformation. In addition, after the aging process, it appears that the nascent rod particles become absent. Instead, there is a significant presence of rod-shell particles that appear after the aging process. The increased formation of species containing shells post-aging is evidence of further chemical reactions that need to be explored.

While these different nSSA morphologies were compared to that of aged SSA using AFM, the quantitative features were compared using AFM-IR spectroscopy was used for different chemical identification. Figure 6.1 shows the average AFM-IR spectra collected on both nascent and aged rounded SSA particles. Spectra were recorded in the center of each particle for a total of 8 particles – 4 for nascent SSA and 4 for aged SSA.

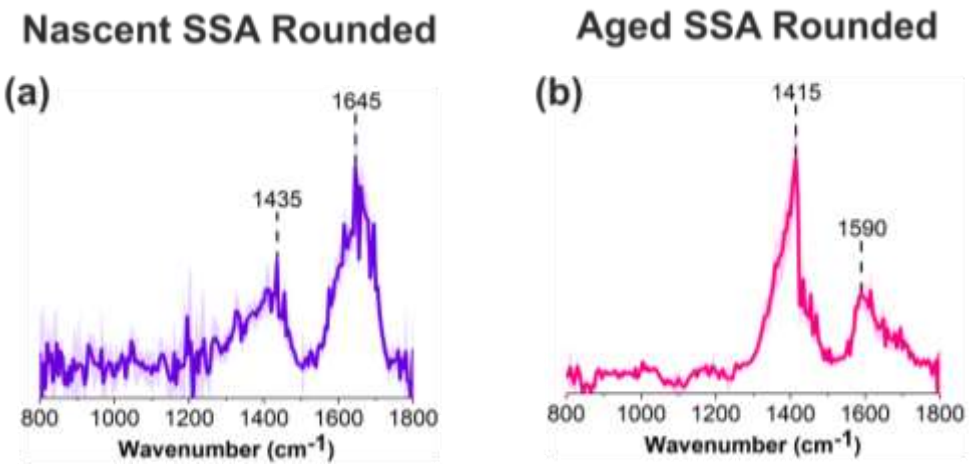

Figure 6.1 PTIR spectra (top) and AFM images (bottom) for (a) nascent and (b) aged rounded SSA within the volume-equivalent diameter range from 0.10 to 0.60 μm. For rounded SSA, spectra were taken at the center. Solid lines show the average spectra of 4 nascent particles as shown in (a) and 4 aged particles as shown in (b). The shaded lines represent the standard deviation from the average spectrum.

Most notably, there are two significant peaks centered around 1415 to 1435 cm^{-1} and another between 1590 to 1650 cm^{-1} which are most likely indicative of CH_2 and CH_3 aliphatic chains and COO^-, C=O, C=C stretching modes, respectively. The aged SSA rounded particles show a narrow peak at 1590 cm^{-1} in comparison to the broader peak at 1645 cm^{-1} in nSSA rounded particles. The broad mode is indicative of many overlapping peaks with contributions from both oxygenated and non-oxygenated species such as C=O and C=C stretching modes, as well as the bending mode of water.[5,37,38] While the different relative intensities of each of these two main modes can potentially explain variability in functional groups, it is more likely that similar functional groups are present for both types of aerosols.

Figures 6.2 and 6.3 show the individual point spectra taken on single nascent and aged, rounded SSA particles, respectively.

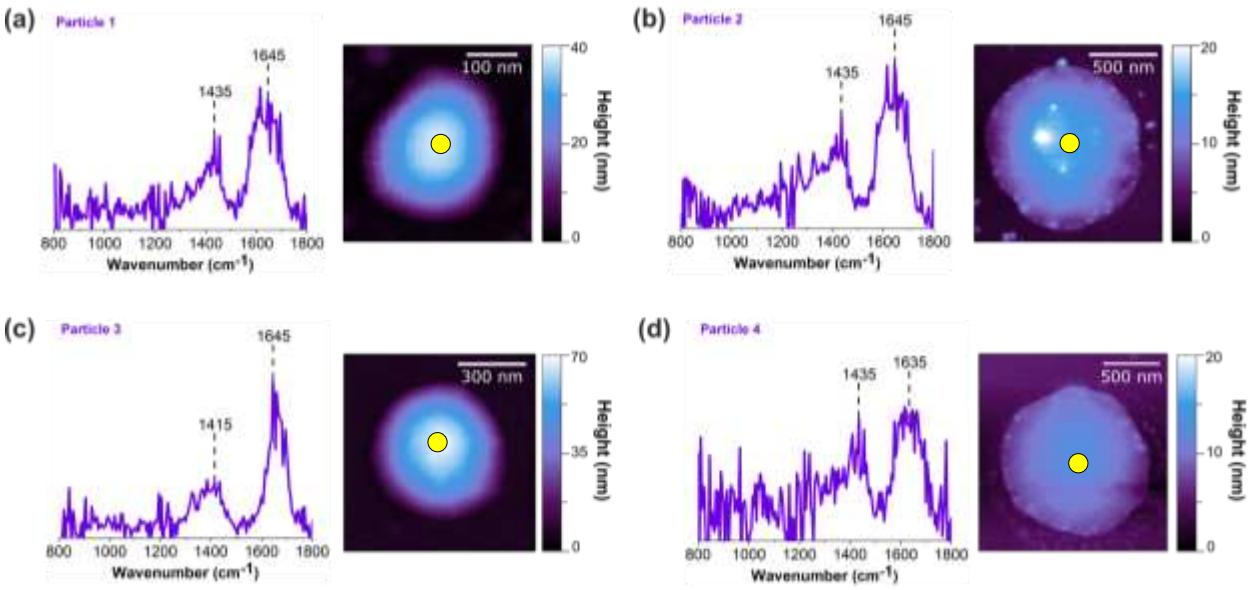

Figure 6.2 AFM-IR spectra and images for nascent rounded SSA. The AFM-IR spectra are shown on the left side, in blue, and the AFM 2D-height images are shown on the right side. AFM-IR spectra shown in (a) through (d) are averaged together to make up the solid spectrum in Figure 6.1. The yellow dots on the image are indicative of the location in which spectra were taken.

In Figure 6.2, four different nascent rounded SSA particles are shown. These spectra show that each of the individual are similar with main bands centered at 1435 cm^{-1} and 1645 cm^{-1}. However, each of the nanoscale point spectra differ slightly. For example, the 1645 cm^{-1} peak is slightly more intense than the 1435 cm^{-1} peak whereas in Figure 6.2d, they are of equal intensity. Conversely, between the two major bands in Figure 6.2a and 6.2b are similar to each other, whereas in Figure the 1645 cm^{-1} peak is significantly stronger in intensity in Figure 6.2c, indicating varying ratios of functional groups present in these SSA particles. These differences are also observed physically, where the physical features of the rounded particles slightly differ from each other. Particle 1 and Particle 3, shown in Figure 6.2a and 6.2c respectively, are similar in that they both are rounder, exhibit a uniform a spherical particle, with a taller center and a shorter outer rim. However, Particle 3 is more circular in shape and has a sphericity parameter of 1 whereas Particle 1 is more oval-like with a sphericity parameter of < 1. In contrast, Particle 2, and Particle 4, shown

in Figures 6.2b and 6.2d respectively, are flatter in height and more of a pancake shape. Hence, these particles have a low aspect ratio, and would most likely exhibit properties that make them more semi-solid or liquid-like than solid. Taking both the chemical and physical similarities and differences into consideration, it is clear that these SSA particles are complex since the particles that look the same do not necessarily exhibit the same spectral characteristics.

Additionally, Figure 6.3 shows a compilation of aged SSA rounded particles and their AFM images and PTIR spectra.

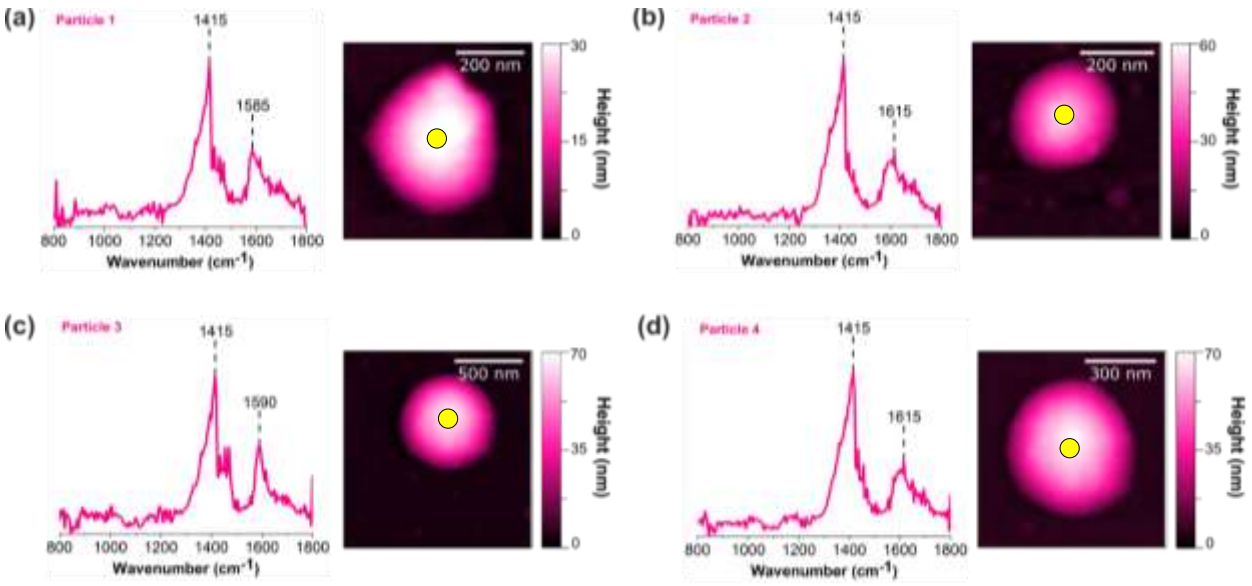

Figure 6.3 A comprehensive breakdown of AFM-IR spectra and images for aged rounded SSA. The AFM-IR spectra are shown on the left side, in pink, and the AFM 2D-height images are shown on the right side. AFM-IR spectra shown in (a) through (d) are averaged together to make up the solid spectrum in Figure 7.1. The yellow dots on the image are indicative of the location in which spectra were taken.

There is not a significant amount of spectral variability shown in the AFM-IR spectra for the four aged rounded SSA. However, one small difference that should be noted is the Particle 3 shown in Figure 6.3c, that has a prominent right shoulder near the major 1415 cm^{-1} band, and a sharper 1590 cm^{-1} peak compared to the others. More intensity of the 1415 cm^{-1} rather than the

1590 cm^{-1} peak can suggest the presence of more aliphatic carbon chain derivatives. From the morphologies, the rounded particles exhibit similar properties but are much more variable in size, as shown by the differences in the scale bars for each AFM 2D-height image. While Particles 2, 3, and 4 are more spherical in shape, Particle 1 is slightly more irregular and oblong in shape with an asphericity factor of < 1.

Overall, it should be noted that the large chemical variance within SSA is expected, due to the complexity of such aerosols.[5] Therefore, while some particular functional groups have been detected with AFM-IR spectroscopy, the results presented in this figure are not representative of every species present in these particles.

Effects of wind speed on marine SSA. In Figure 6.4, the average AFM-IR spectra obtained on select core-shell and rounded SSA particles generated at 7 m/s and 14 m/s wind speed is shown. The average spectrum shown in Figure 6.4a, 6.4b, 6.4c, and 6.4d, are averages of 4, 6, 2, and 3 SSA particles, respectively.

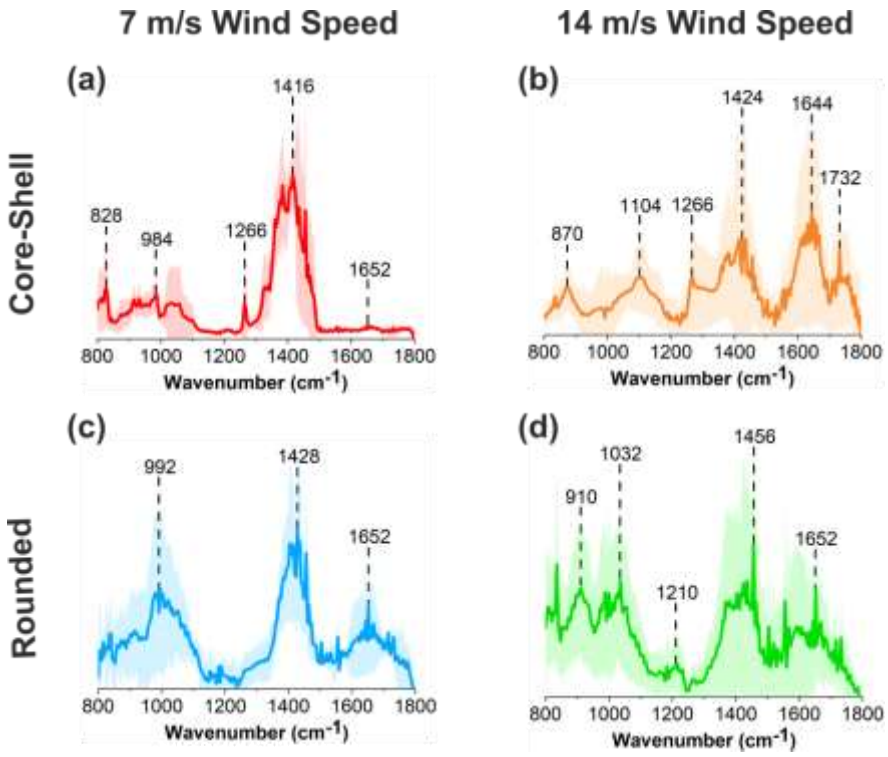

Figure 6.4 PTIR spectra for (a) core-shell particles from 7 m/s (b) core-shell particles from 14 m/s, (c) rounded particles from 7 m/s, (d) rounded particles from 14 m/s within the volume-equivalent diameter range of 0.18–0.56 μm. Spectra were taken at shell regions for core-shell particles and solid lines show the averaged spectra and shaded lines represent the standard deviation.

The spectra collected for these aerosols are consistent with what has been observed in past field studies.[4,5,39,40] The peaks in the 800 to 1000 cm^{-1} region are attributed to the C-C or C-H deformation stretching modes, while the vibrational modes in the 1000 to 1250 cm^{-1} region are attributed to phenolic compounds that contain C-O-C, C-O or C-C stretching modes. [5,41,42] Methyl and methylene bending modes are observed in the 1350 to 1470 cm^{-1} region, and in the 1550 to 1750 cm^{-1} region, C=C, C=O and COO^- stretching modes are observed.[5,41,42] The particles that are presented in this manuscript are SSA with a volume-equivalent diameter ranging from 0.18 to 0.56 μm.

For this study, a total of 10 core-shell SSA particles are analyzed and presented below. Figure 6.5 shows a breakdown of all 4 core-shell SSA at 7 m/s wind speed whereas Figure 6.6

shows a breakdown of all 6 core-shell SSA at 14 m/s wind speed. For core-shell SSA presented in this study, only the AFM-IR spectra for the shell regions are shown in Figure 6.5 and 6.6 since the core either exhibited no IR activity or displayed similar spectral characteristics as the shell. At 7 m/s wind speed, there is a distinct peak at 1415 cm^{-1}, which is attributed to the methyl and methylene, aliphatic-rich compounds, which is supported by the presence of smaller peaks in the 800 to 1000 cm^{-1} region, indicative of C-H wagging modes.

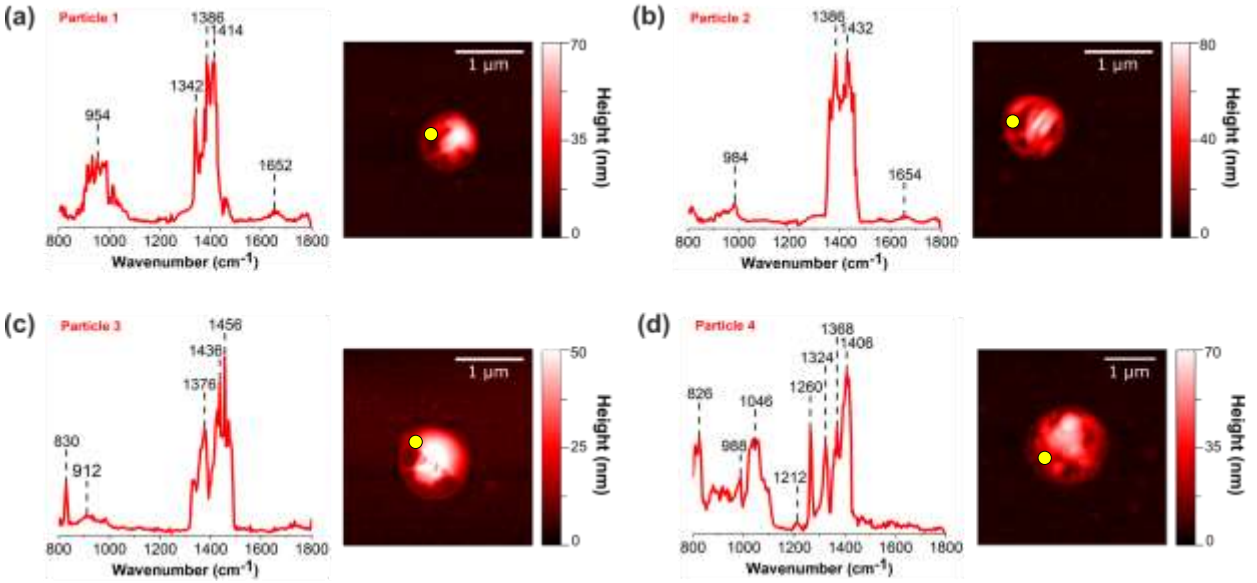

Figure 6.5 AFM-IR spectra and images for core-shell SSA at 7 m/s wind speed. The AFM-IR spectra are shown on the left side, in red, and the AFM 2D-height images are shown on the right side. AFM-IR spectra shown in (a) through (d) are averaged together to make up the solid spectrum in Figure 6.4. The yellow dots on the image are indicative of the location in which spectra were taken.

The reason for the large standard deviations shown Figure 6.4 is shown in Figures 6.5, 6.6, 6.7, and 6.8 in that the PTIR spectra are all distinct from each other, indicating heterogeneity between particles. Figure 6.5 shows four different core-shell SSA particles that show two absorptions, one weaker one around in the 800-1000 cm^{-1} region and one more intense, broader one centered around 1400 cm^{-1}. These features are exhibited by Particle 1, 2, and 3, as shown by Figure 6.5a, 6.5b, and

6.5c. However, within these point spectra, there are still major differences. Particle 1 has a strong, broad peak at 954 cm^{-1}. However, Particle 2 has a small peak at 984 cm^{-1} whereas Particle 3 has a sharp peak at 830 cm^{-1}. Slight shifts and broadness in the bands in this region indicate varying ratios of C-C or C-H deformation stretching modes.[5,41,42] However, compared to first three particles, Particle 4 is the most distinct in its spectrum, as it exhibits a strong peak at 1046 cm^{-1}, which can be indicative of C-O groups such as alcohols.[43] When comparing the AFM images of the particles, it is clear that there are distinct nanoscale features present. While Figures 6.5a and 6.5d show particles with the tallest, aggregated features on the side of the particle, Figure 6.5c has a "core" that is more centralized within the particle. Conversely, Particle 2, as shown by Figure 6.5b, possesses evenly distributed smaller features, with a rod-like core in the center of the SSA particle.

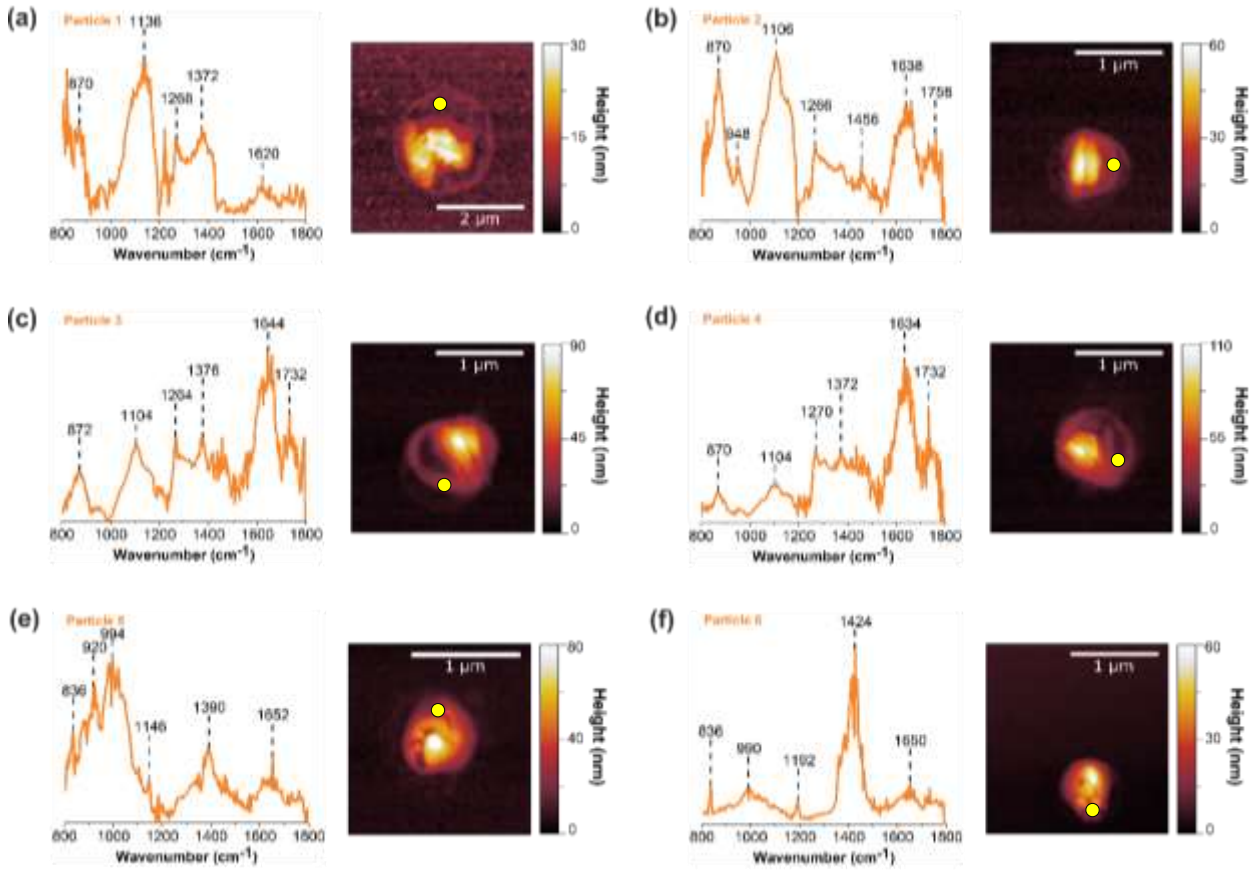

Figure 6.6 AFM-IR spectra and images for core-shell SSA at 14 m/s wind speed. The AFM-IR spectra are shown on the left side, in orange, and the AFM 2D-height images are shown on the right side. AFM-IR spectra shown in (a) through (f) are averaged together to make up the solid spectrum in Figure 6.4. The yellow dots on the image are indicative of the location in which spectra were taken.

At 14 m/s, there is a great amount of heterogeneity in the nanoscale point spectra that has been measured for core-shell SSA particles. As shown in Figure 6.6, six different core-shell particles are shown above, all of which are spectrally distinct. To start, Particle 6, shown in Figure 6.6f, is the closest to resembling the PTIR spectra of the core-shell SSA particles at 7 m/s wind speed. This suggests that although wind speed can change the chemistry of sea spray aerosol, However, the remainder of the core-shell particles at 14 m/s appear to be composed of the same compounds as those seen at 7 m/s, but with the addition of more functional groups in the 1640-1730 cm^{-1} region, which suggests a mixture of carboxylic acids, esters, or carboxylates.[5,41,42] The

presence of each of these functional groups can be attributed to a variety of macromolecules, such as humic and fulvic acids, or even biological components such as protein and bacteria.

Some of the differences between the two wind speeds for core-shell SSA are thought to be attributed to variations in (1) water composition and (2) particle formation mechanisms. Lower wind speeds often result in calmer oceanic conditions, which often results in are formation of a thicker, surface microlayer (SML) that is rich with aliphatic compounds.[16,44] When there is an increase in wind speed and higher oceanic activity from higher wind speeds, mixing is expected to occur, resulting in a more homogenous water column that contains a wider array of species, such as water-soluble compounds.[16] This will, in turn, increase the water composition of SSA since there is no SML creating a boundary between different species.

According to Wang et al., the mechanism of SSA formation is another factor that is influenced by wind speed.[45] This study reports that film drop mechanisms, which exhibit a higher fraction of aliphatic species, are more prevalent at 7 m/s. On the other hand, jet drop mechanisms are more commonly found at 14 m/s for SSA compounds and have been found to contain a higher fraction of oxygenated species.[45] Often times, core-shell SSA are extremely complex since they are often formed as a result of a chemical and physical transformation. It has been reported that these particles are products of heterogenous reactions or gas condensation of inorganic materials as they interact with various species in the atmosphere. [46] This complexity of SSA production can explain its variable composition and morphology at different wind speeds, as observed in this dissertation chapter.

In addition to core-shell SSA particles, rounded SSA particles exposed to various wind speeds were also studied. Figure 6.7 shows a breakdown of 2 rounded SSA at 7 m/s wind speed whereas Figure 6.7 shows a breakdown of all 3 core-shell SSA at 14 m/s wind speed.

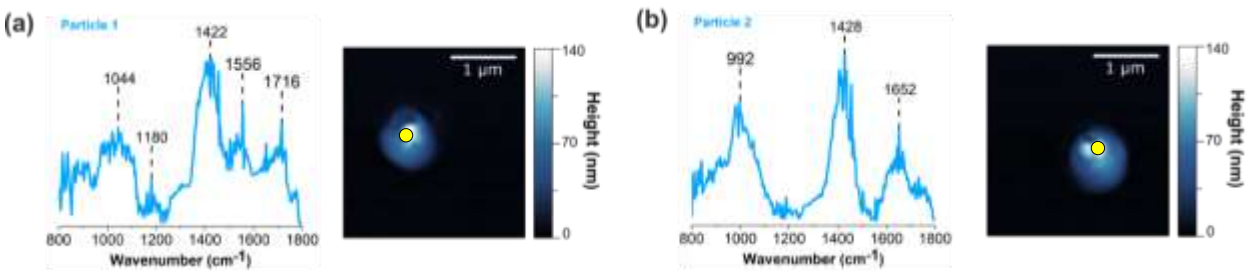

Figure 6.7 AFM-IR spectra and images for rounded SSA at 7 m/s wind speed. The AFM-IR spectra are shown on the left side, in blue, and the AFM 2D-height images are shown on the right side. AFM-IR spectra shown in (a) through (d) are averaged together to make up the solid spectrum in Figure 6.4. The yellow dots on the image are indicative of the location in which spectra were taken.

For rounded SSA, there appeared to be no major changes between the two wind speeds. The major peaks are present in the 950 to 1050 cm^{-1}, 1350 to 1450 cm^{-1}, and 1650 cm^{-1} regions, which correspond to C-O stretching, CH_2 and CH_3 bending, and C=O stretching, respectively.[5,41,42] Similarities in the AFM-IR spectra for both wind speeds suggest that there are not major chemical transformations that occur for rounded SSA when exposed to higher wind speeds. At 7 m/s the rounded particles appear to have a significant band at 1650 cm^{-1}, which are comparable to the core-shell particles at the same wind speed. This band is most likely representative of C=O stretching modes. This can be seen in Figure 6.7, where both rounded SSA particles exhibit a strong presence in this region. Although there is some spectral variance observed, the physical features of the rounded SSA particles at 7 m/s wind speed appear to be very similar in size, height, and shape.

In addition, the peaks in the 1350 to 1450 cm^{-1} and 950 to 1050 cm^{-1} regions are indicative of CH_2 and CH_3 bending modes as well as C-O and C-C stretching modes, respectively.[5,41,42] The presence of this band is only present in core-shell particles at 14 m/s, suggesting that rounded SSA naturally contains more oxidized chemical species compared to core-shell SSA. This feature is seen in Figure 6.8, where there is clearer distinction in each of these regions rather than being a

singular, broad band, as shown in Figure 6.7. Similar to what was observed for core-shell particles at 14 m/s wind speed, the rounded SSA particles at 14 m/s wind speed are significantly more functionalized and complex, chemically, compared to at 7 m/s wind speed. There also appears to be more differences in the nanoscale physical features of the SSA particles. While Particle 1 and Particle 2 are more uniform on the surface, there is a small but tall feature present in the center of Particle 3, making it higher in sphericity than Particles 1 and 2.

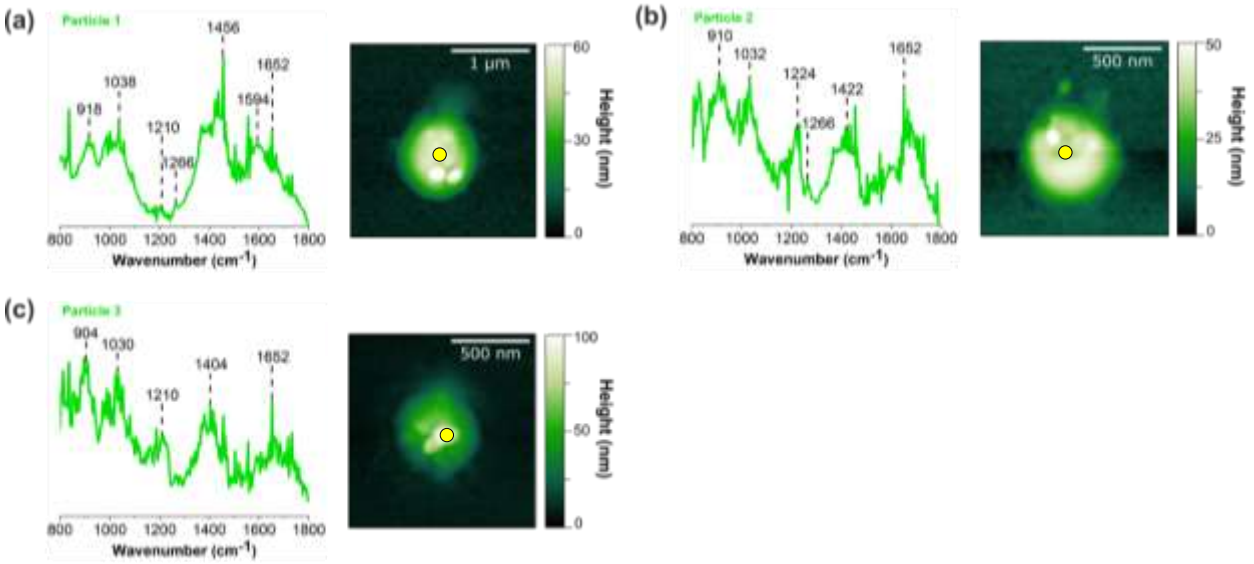

Figure 6.8 AFM-IR spectra and images for rounded SSA at 14 m/s wind speed. The AFM-IR spectra are shown on the left side, in green, and the AFM 2D-height images are shown on the right side. AFM-IR spectra shown in (a) through (d) are averaged together to make up the solid spectrum in Figure 6.4. The yellow dots on the image are indicative of the location in which spectra were taken.

Overall, the AFM-IR results from this study have demonstrated the complexity of marine SSA that are released from the ocean. Single-particle methods for studies like this are found to be extremely complementary to bulk approaches. However, a more comprehensive analysis of the effect of wind speed on SML, surface tensions, and formation mechanisms much be done to fully understand the chemistry occurring along the marine boundary layer.

6.3 Micro-spectroscopic Analysis of the Effects of Wildfire Smoke Events on Indoor Surfaces

Sample preparation and AFM-IR data collection and analysis of particle deposition on indoor surfaces. Samples analyzed for this study was collected a campaign named, Chemical Assessment of Surfaces and Air (CASA), which took place at the National Institute of Standards and Technology (NIST) Net-Zero Energy Research Test Facility (NZERTF) in Gaithersburg, Maryland in 2022. The CASA campaign focused on observing the chemical transformations occurring in the gas, particle, and surface phases in an indoor air environment. CASA focused on a various number of events such as cooking, cleaning, but, mainly, wildfire smoke.

For the wildfire smoke study, fresh smoke was directly injected into the NIST test house for 10 minutes. Aged smoke was indirectly injected into the house by first being injected into a Teflon chamber that contained fresh smoke and then oxidized with ozone. These injections were made for 60 minutes. A cocktail smoker (Breville, BSM600SILUSC) was used to produce fresh smoke from ponderosa pine woodchips. For each direct injection of fresh smoke, about 0.25 to 0.5 grams of woodchips were measured out and burned.[47] The procedure for window glass placement from HOMEChem was repeated for this CASA experiment.[48] For the CASA study, the glass slides were placed vertically and horizontally near the kitchen and living room area, for 24 hours on the day in which the fresh smoke was injected into the house. After smoke deposition, the samples were collected, sealed in petri dishes, and shipped to UCSD at the end of the campaign for analysis. Upon arrival at UCSD, the samples were stored in the dark in ambient conditions to minimize any variables that could potentially change on the surface of the glass.

This study used both the AFM and PTIR components of the nanoIR2 system. For these AFM-IR studies, 30 μm x 30 μm images were collected at a scan rate of 0.2 Hz and a resolution

of 512 pixels. a gold-coated silicon nitride cantilever, with a tip radius of ~ 30 nm, spring constant of 1 to 7 N/m, and a resonant frequency of 60 to 90 kHz was used. The AFM-IR spectra presented were co-averaged from 7 spectra and operated at a 100% power in tapping mode. AFM images were processed using the Gwyddion software and AFM-IR spectra were plotted in Origin.

Deposition of particles from wildfire smoke on indoor glass surfaces. After the introduction of smoke, the glass samples that were exposed to the indoor air were collected for both physical and chemical analysis via AFM-IR spectroscopy. Figure 6.9 shows two different types of particles that were identified on exposed glass surfaces: (1) aggregate-like and (2) rounded.

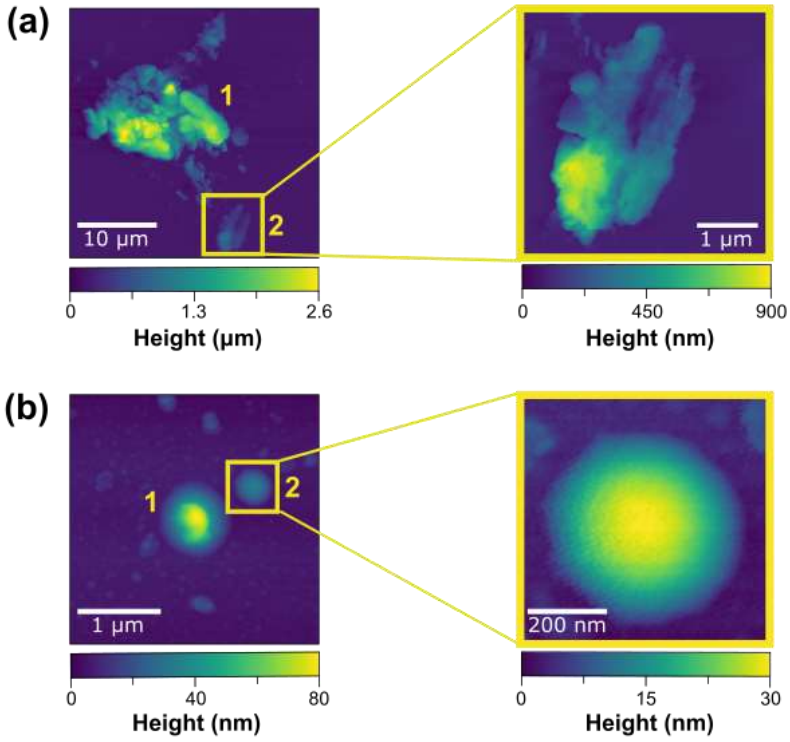

Figure 6.9 AFM 2D height images of smoke particle deposition on lass in two different regions on the surface with two different particles labelled 1 (a) and 2 (b). The left side is a larger region, and the right side is a zoomed-in perspective of the particle labeled 2.

In both Figures 6.9a and 6.9b, there are colored insets that are drawn over smaller features. Those features are shown on a bigger scale as seen on the left side of the images, and a smaller, more zoomed-in perspective on the right side. The features shown in the aggregate-type particle are more jagged with different patches of heights and, overall, irregular in shape. However, the rounded particles are much more spherical. While thin films of smoke were also expected on bare glass surfaces, they were unable to be detected with these set of samples. This result could be due to two reasons: (1) Smoke thin films slowly evaporated prior to AFM-IR analysis or during the time in which the sample was packed away and shipped off for analysis from Maryland to California (2) Smoke thin films are much thinner than the large, bulky particles deposited on the bare glass surfaces and thus, went easily undetected.

In addition to differences in shape between the two types of smoke-deposited particles, quantitative differences are observed in the heights of these features. The particles in Figures 6.9a are significantly larger, taller, and rougher compared to those shown in Figures 6.9b. This is shown by a tall height as high as 2.6 μm, as presented in Figure 6.10. In Figure 7.10c, the height profiles of two aggregate-type smoke particles are presented and the rough and jagged profiles can be seen. These profiles can be quantified with RMS values that are shown in green. Particle 1 and Particle 2 possess RMS values of 645 nm and 170 nm, respectively.

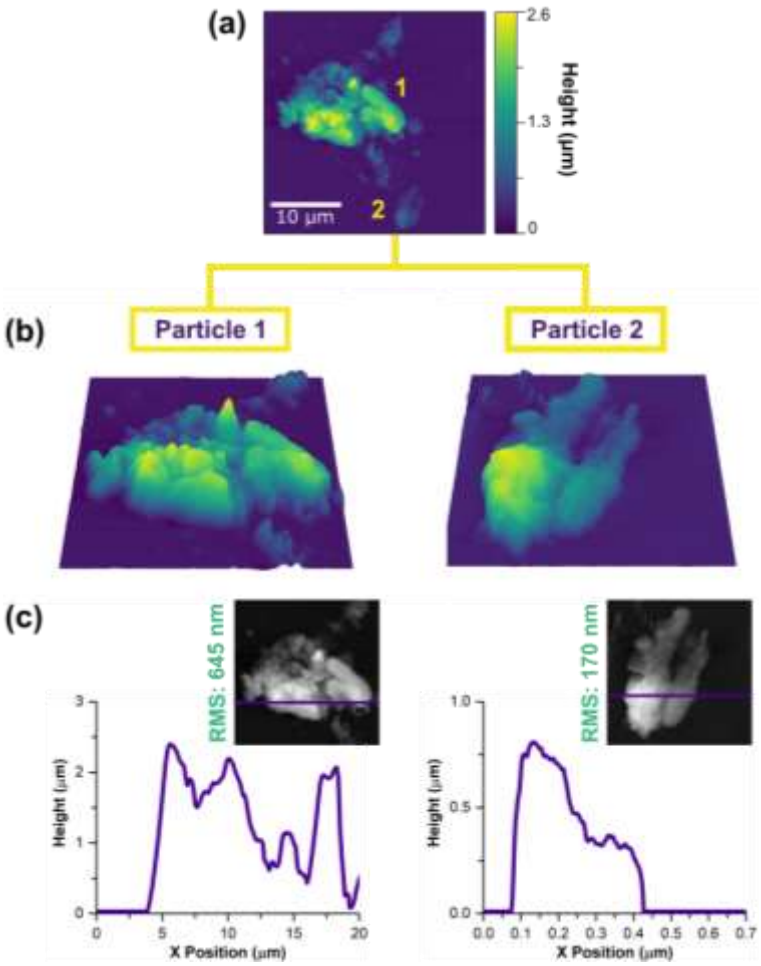

Figure 6.10 (a) AFM 2D height image of aggregate-type smoke with two specific particle regions labeled as "1" and "2" in yellow. (b) AFM 3D height image of Particle 1 and Particle 2. (c) Height profiles of Particle 1 and Particle 2 on the left and right, respectively. The location of the height profile is shown in the horizontal purple line shown on the upper right corner. Root mean square, RMS, roughness values are also indicated in green.

Figure 6.11 shows a comprehensive height analysis of rounded-type smoke particles – Particle 1 and Particle 2. As can be seen by the 3D height images, shown in Figure 6.11b, the rounded particles are much smoother and less jagged than what was observed in Figure 6.10b. This is confirmed by the smoother height profiles presented in Figure 6.11c, with significantly lower RMS values of 20 nm and 8 nm, for Particle 1 and 2, respectively.

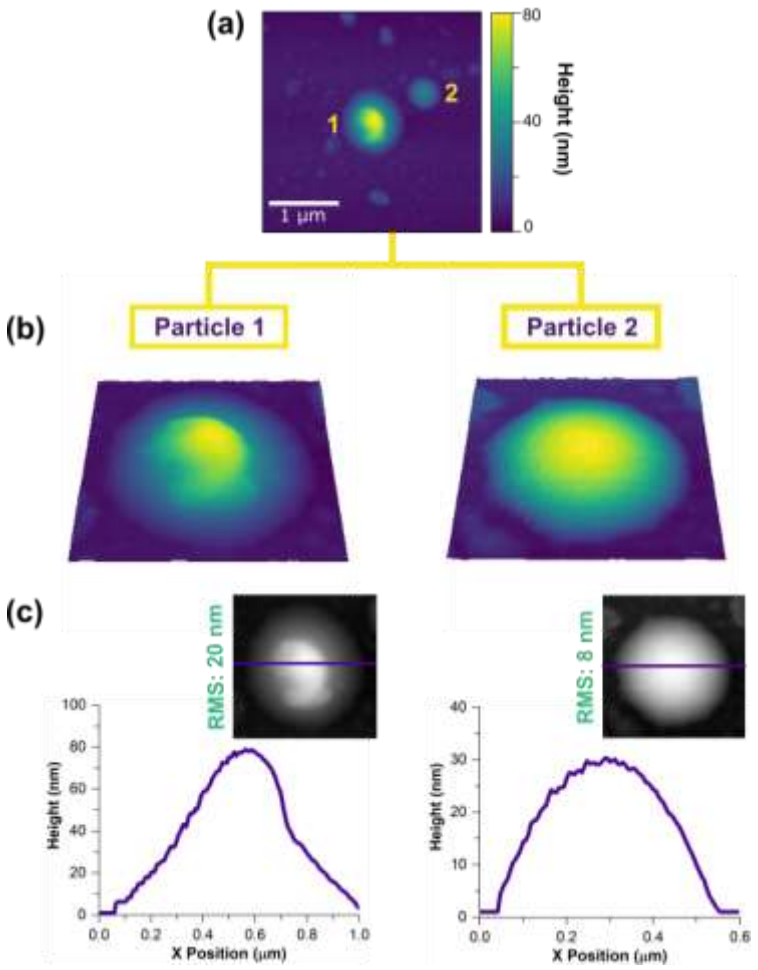

Figure 6.11 (a) AFM 2D height image of rounded-type smoke with two specific particle regions labeled as "1" and "2" in yellow. (b) AFM 3D height image of Particle 1 and Particle 2. (c) Height profiles of Particle 1 and Particle 2 on the left and right, respectively. The location of the height profile is shown in the horizontal purple line shown on the upper right corner. Root mean square, RMS, roughness values are also indicated in green.

While AFM-IR spectroscopy provided valuable information, spectral data would allow for chemical characterization of these smoke-deposited particles.

Figure 6.12 shows a spectral analysis of a selected, aggregate-type and rounded-type smoke particles that have been deposited onto a glass substrate. Specifically, Figure 6.12b shows the point spectra taken across an aggregate of smoke particles, where each spectrum is seen to be distinct from one another. For example, the orange and blue spectra are similar, with both having broad

peaks around 1166 cm^{-1}, which can be associated with C-O stretching found in esters, C-O-C stretching, or potentially sulfate derivatives.[43] However, the blue spectrum also has an additional peak at 1420 cm^{-1} which corresponds to the peak shown in the green spectrum. This band is likely indicative of aliphatic carbon chains that make up some of the sugars. The orange spectrum has a small, distinctive peak at 1784 cm^{-1}, which suggests C=O stretching from esters which are known contaminants in indoor environments.[49–51] Compared to the other spectra, the green spectrum appears to be highly functionalized, with the greatest number of oxidized and non-oxidized functional groups. The differences from each of the three spectra on a single aggregate clearly depict the complexity of these samples and provide evidence of how they are composed of many different functional groups.

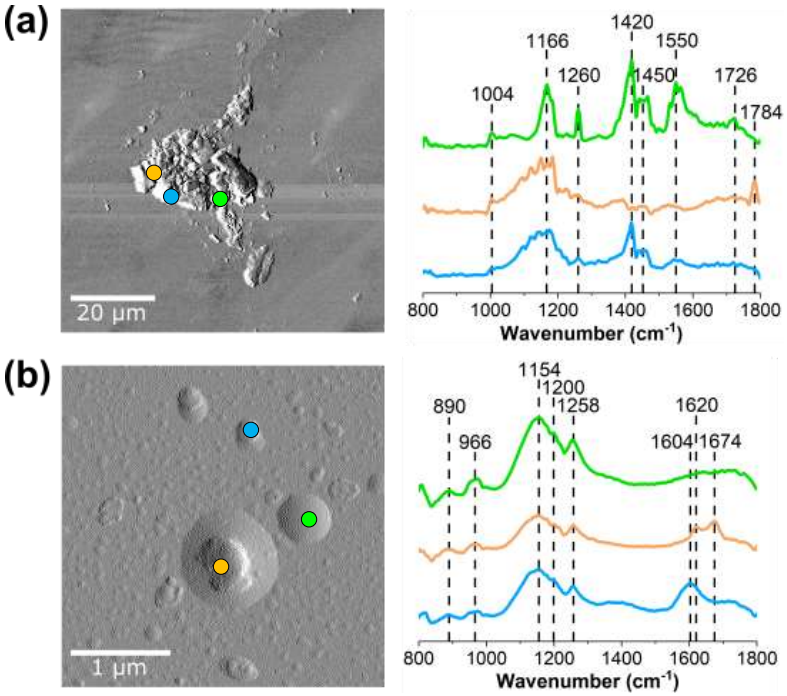

Figure 6.12 AFM deflection image of aggregate-type smoke and select, PTIR point spectra of (a) aggregate-type and (b) rounded-type smoke particles. The color of the point spectra corresponds to the color of the dots on the image. AFM-IR chemical maps (c) for three select wavenumbers are shown below.

Compared to the spectra shown in the aggregate-type region, the spectra of the rounded smoke particles exhibit broad bands ranging from 1000 cm^{-1} to 1300 cm^{-1}. This suggests a large mix of C=C, C-C, and phenolic functional groups which are commonly present in aerosols generated from biomass burning activities such as levoglucosan or catechol.[52,53] In addition, the rounded-type smoke particles have defined peaks at 1604 cm^{-1}, 1620 cm^{-1} and 1674 cm^{-1}, as shown by the orange and blue spectra, suggesting the presence of aromatic C=C or aldehyde functional groups, respectively.[43,53–55] Compared to the aggregate-type smoke spectra, the rounded-type spectra do not appear to possess significant bands in the 1500 cm^{-1} region, which is indicative of nitrogen-containing compounds.[43] Although more analysis is necessary to fully characterize composition of these smoke-deposited aerosols, this analysis provides evidence for the deposition of smoke particles on window glass surfaces that are not varying in size and morphology, but also in composition.

6.4 Interaction of Hydrogen with Shale: Potential Implications for Subsurface Hydrogen Storage

Sample acquisition, preparation, and AFM-IR and O-PTIR data collection of Eagle Ford shale. Eagle Ford shale (ES-1) was originally purchased from Kocurek Industries. ES-1 Eagle Ford shale contains a significant concentration of carbonates (~66 wt.% calcite) and quartz (~26 wt.%). In addition to these components, trace amounts of clay, pyrite and dolomite minerals have also been detected. The acquired Eagle Ford shale sample was initially polished down to 2 mm in height so that it can physically fit inside the instruments used for analysis. After polishing at the National Energy Technology Laboratory (NETL), the sample was sent to UC San Diego for analysis with

AFM-IR and O-PTIR spectroscopy. This initial analysis of the shale sample is referred to as a "Pre-Reaction". After this initial analysis, the shale sample was sent back to NETL. At NETL, the sample was placed in a 500 mL polytetrafluoroethylene (PTFE) lined containers, which were then placed in the autoclave. The autoclave was heated to 40 °C and pressurized to 10.3 MPa with dry H_2 for a duration of 6 weeks. These conditions were specifically chosen in efforts to mimic those acceptable for geologic subsurface hydrogen storage. Then, the autoclave was depressurized slowly over 5 to 6 hours in order to maintain sample integrity. After being removed from the autoclave, the reacted Eagle Ford shale sample was initially characterized by scanning electron microscopy (SEM) and SEM-EDX and then sent back to UC San Diego. These samples were then analyzed again with AFM-IR and O-PTIR spectroscopy. Analysis conducted at this state of the shale sample is referred to as "Post-Reaction".

As already discussed in detail. Atomic Force Microscopy-Infrared (AFM-IR) spectroscopy is a hybrid technique that combines the nanoscale spatial resolution of AFM with the chemical analysis capability of IR spectroscopy. This technique implements the phenomenon of Photothermal Induced Resonance (PTIR), which is when a sample locally expands upon absorption of infrared light at a given frequency. By utilizing a sharp but flexible nanometer tip of a cantilever as the detector, this physical expansion is measured through the position on a photodiode and then translated into a proportional IR signal, which results in a PTIR spectrum.[56–58]

The Eagle Ford shale sample was adhered onto a stainless steel disc that was magnetically secured onto the sample holder that fit into the instrument. The sample was analyzed with the nanoIR2 microscopy system (Bruker, Anasys – Santa Barbara, CA) that is equipped with a mid-IR tunable quantum cascade laser (QCL). AFM images were collected at a scan rate of 0.1 – 0.6

Hz, depending on the roughness of the sample, both pre and post-reaction. Both images and PTIR spectra were collected using gold-coated silicon nitride probes, with tip radii of ~30 nm. Tapping mode probes were purchased from Bruker and had a spring constant of 1 to 7 N/m, and a resonant frequency of 75 kHz. PTIR spectra were collected at a resolution of 2 cm^{-1}. Due to roughness of the sample post-reaction, it was not possible for images for both pre and post reaction to be collected in the same location. It should be noted that any AFM images shown in this study are representative of regions that we were able to image and measure and may not be representative of the entire sample.

As discussed in this thesis, Optical Photothermal Infrared (O-PTIR) spectroscopy is another submicron hybrid technique that measures a proportional infrared absorption signal based on the changes in the refractive index from a co-linear visible light source. O-PTIR spectroscopy operates similar to AFM-IR spectroscopy in that they are both based on a response to photothermal expansion. However, with O-PTIR spectroscopy, the detector measures a change in the intensity of the refractive index which is the basis of the extracted IR signal.[41,59–61]

For the O-PTIR spectroscopic data collection, optical images of the Eagle Ford sample were first collected with two objective lenses: a 10x, low magnification lens and a 40x, high magnification reflective Cassegrain lens. All O-PTIR spectra are collected with the 40x reflective Cassegrain objective, while the 10x visible objective is used to provide a lower resolution optical image of the sample. Specifically, the 10x provides a helpful macroscopic view of the sample, which is useful for targeting specific regions of interest. The mIRage-Raman system is also equipped with two mid-IR tunable lasers: a quantum cascade laser (QCL) and an optical parametric oscillator (OPO) laser. These two lasers are used for O-PTIR spectroscopic measurements. The spectral range for the QCL laser is 755 to 1855 cm^{-1} while that of the OPO laser is 2600 to 3600

cm^{-1}. The Raman attachment, discussed previously in this thesis, provides spectra in the 400 to 4000 cm^{-1} range.

The Eagle Ford shale sample analyzed by AFM-IR spectroscopy was then secured onto the magnetic piece on a microscope slide that was placed into the sample compartment of the O-PTIR + Raman instrument for analysis. Settings for probe and IR laser power were determined by optimizing the photothermal signal and ranged anywhere from 0.5% to 20% for the probe power and 30% to 100% for the IR laser power. For micro-Raman spectral measurements, the most optimal probe power and integration time are typically determined by the settings that give the highest signal-to-noise ratio. However, due to fluorescence for these shale samples, the probe power and integration time were not adjusted separately. Both O-PTIR and Raman spectra are collected at a resolution of 1 cm^{-1}. The same regions of analysis were achieved by using macroscopic and then microscopic markers. For example, several photos were taken before H_2 reaction to ensure proper orientation of the shale sample in the sample compartment. Afterwards, fine-tuning of the specific region was achieved by using the 10x objective lens and comparing optical images before reaction. After data collection, spectra are processed using the Photothermal PTIR Studio software and plotted *via* Origin.

Reaction of Eagle Ford shale with H_2 gas. After reaction with hydrogen gas at high pressure, physical comparisons of the same region on the same Eagle Ford shale sample were initially made to provide insights into the nanoscale features of the shale sample. However, upon reaction with hydrogen, the shale sample was no longer suitable for imaging with due to significant changes and a large increase in roughness of the sample. Nevertheless, one feature that is unique to AFM-IR spectroscopy is its ability to provide high resolution topographic images, that quantify the height

of the sample. Figure 6.13 displays some of these AFM images and compares them both qualitatively and quantitatively.

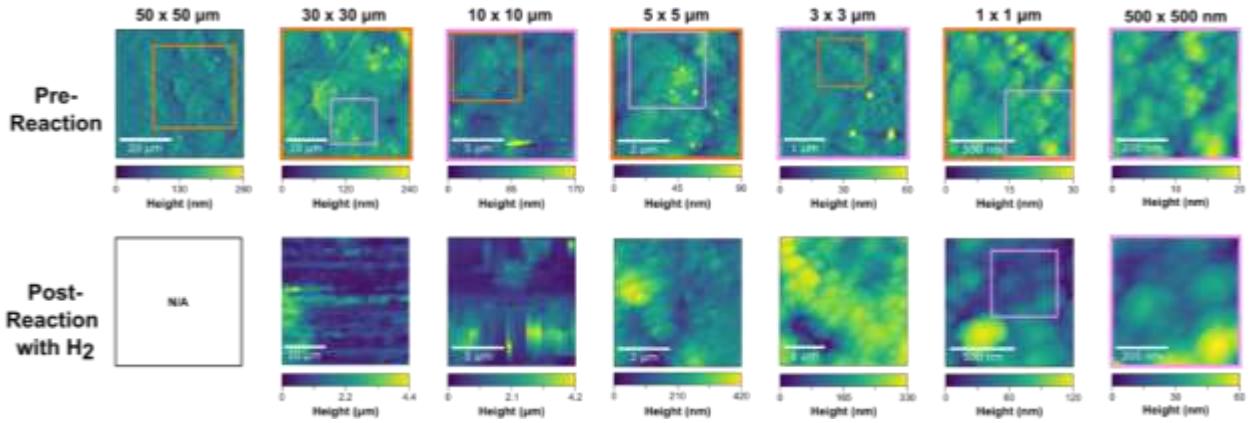

Figure 6.13 AFM height images about a shale rock sample, both pre and post hydrogen gas reaction.

In Figure 6.13, the pre-reaction AFM images of Eagle Ford shale are shown at different levels of imaging size, 50 µm x 50 µm to 500 nm x 500 nm. The 50 µm x 50 µm appears to be fairly flat, with no major, tall features being present, and being only 260 nm tall in height. However, taller features are revealed in the smaller size range as shown by the bright yellow features presented by the 5 µm x 5 µm image. Moving to the submicron level imaging, rounded aggregates that are tightly packed together are observed. It should be highlighted that this region is extremely flat, only about 20 nm in height. After reaction with hydrogen gas, there is a significant change in the larger-scale images. As shown in the post-reaction images in Figure 6.17, the 30 µm x 30 µm and 10 µm x 10 µm images contain many streaks suggesting probe displacement from deepened fractals and fissures within the shale sample. Additionally, one major difference that should be noted is the difference in heights. While the images for the 30 µm x 30 µm and 10 µm x 10 µm regions may not be helpful, the heights are reported to be on the order of

4 micron, which is significantly taller than the equivalent areas before reaction with H_2. This significant height difference is consistent in the submicron regions, where the heights on the color bars are about 3 to 4 times greater in the post-reaction images than the pre-reaction images. For the largest image, 50 µm x 50 µm region, the roughness was too large for imaging. Overall, the collected AFM images indicate that reaction with hydrogen gas resulted in a significant increase in the surface roughness, most likely with deeper and more frequent fractals along the surface.

Unlike the nanoIR2 system, the mIRage-Raman operates on a non-contact mode. Although it may not provide insights along the nanoscale level, O-PTIR spectroscopy is extremely unique in its ability to allow for a direct comparison of the same region on the Eagle Ford shale sample at the microscale level, before and after reaction with H_2 gas. First, significant physical differences in the pre-reaction and post-reaction Eagle Ford shale are shown in the optical images presented in Figure 6.14.

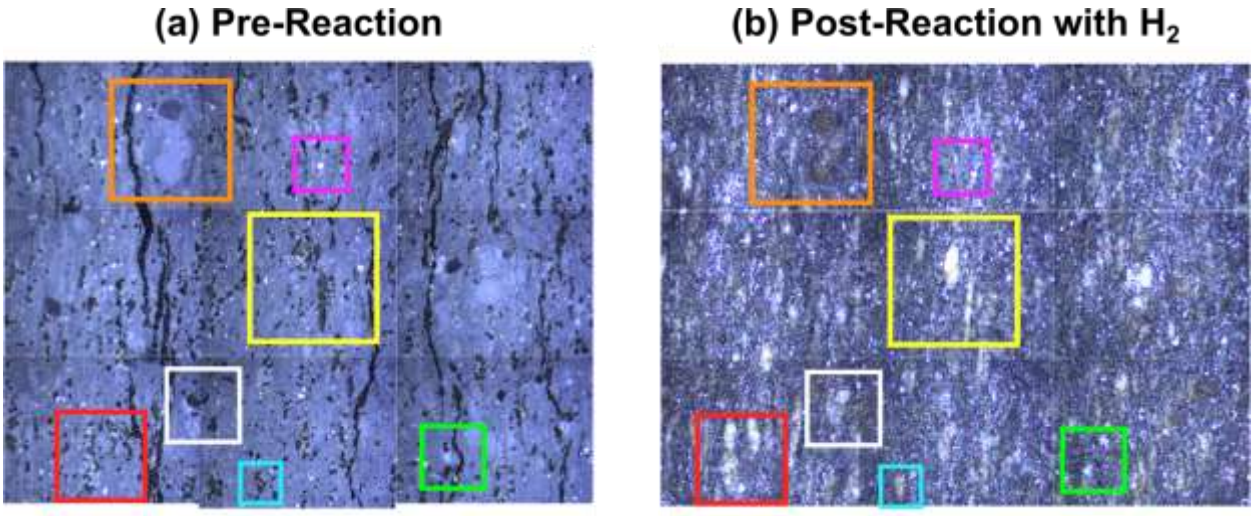

Figure 6.14 O-PTIR optical images from (a) before reaction and (b) after reaction with hydrogen gas. The colored boxes highlight some of the regions with distinct physical features underwent changes in surface morphology.

The optical image shown is a mosaic of a total of 9 images (3 on top, middle and bottom), each at size of 470 µm x 630 µm. By creating a mosaic at this large scale, it was possible to analyze a significantly large sample area at the same time. In addition, it provided insight into the macroscopic features and orientation of the sample. In Figure 6.14, there are colored boxes across the optical image. Each of these boxes highlight significant differences between the pre-reaction image, shown in Figure 6.14a, and the post-reaction image, shown in Figure 6.14b. One notable difference between the two images is the absence of fractals in the post-reaction optical image. This is highlighted by yellow and orange boxes, where the black lines running through the boxed regions in Figure 6.14a are no longer present in Figure 6.14b. This suggests a decrease in porosity on a microscale level, from the formation of precipitated calcium sulfate, or gypsum, upon reaction with hydrogen.[62,63]

The mIRage-Raman also provides valuable chemical information, as shown in Figure 6.16. Here, O-PTIR spectra collected on two different regions for both pre-reaction and post-reaction shale are plotted. These two regions are micro-regions in the first mosaic square, shown in Figure 6.14, where the orange box is located. When comparing the blue dotted box on the left, as shown in Figure 6.16a to the blue solid box on the right, as shown in Figure 6.16b, the most notable physical change is the increase in reflectivity of that region, indicated by the lighter colored feature. This suggests the presence of pyrrhotite, a reduced form of pyrite, that is prevalent in Eagle Ford shale. Pyrrhotite, FeS, is the reduced form of pyrite, FeS_2, in the presence of hydrogen.[63–65] The full reduction mechanism is presented in Equation 6.5. Below the optical images are O-PTIR point spectra taken at these same location, roughly in the center of each boxed region. In particular, corresponding to the boxes, the dotted spectra represent the pre-reaction spectra, whereas the solid spectra represent the post-reaction spectra, as shown in both Figure 6.15c and 6.15d.

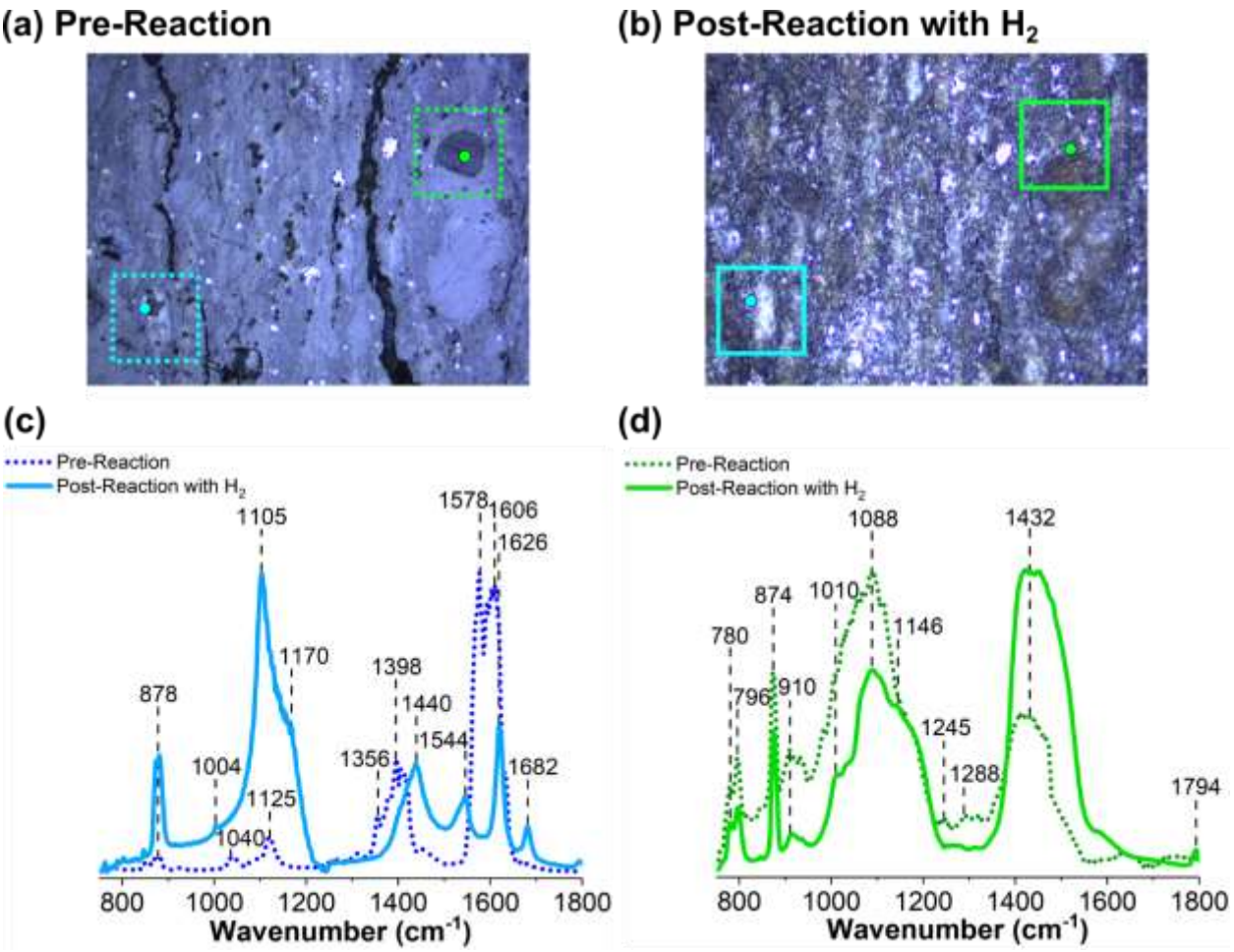

Figure 6.15 Optical images of Eagle Ford shale (a) before reaction and (b) after reaction. The blue and green colored boxes highlight two regions of interest. O-PTIR point spectra are shown below, with dotted and solid spectra representing pre and post-reaction. Point spectra in (c) blue and (d) green correspond to the colored boxes above.

The comparison of the O-PTIR spectra is valuable in that a direct, chemical transformation can be detected. Compared to the green spectra, the blue spectra show significant differences in the major bands present. In the pre-reaction spectrum, as shown by the dotted, dark blue spectrum in Figure 6.15c, there is a noticeable presence of carbonates, as indicated by the υ_2, out-of-plane bending, and υ_3, asymmetric stretching modes at 878 cm^{-1} and 1398 cm^{-1} peak, respectively.[21,62,63] However, there is a significant contribution around 1600 cm^{-1}, which may be indicative of C=C

stretching modes for unsaturated hydrocarbons.[22,23] However, after reaction with H_2 gas, the solid blue spectrum in Figure 6.15c exhibits a different chemical profile. There appears to a relatively lower ratio of carbonates, coupled by a significant, broad band centered at 1105 cm^{-1}, which shows evidence of Si-O stretching modes, from an increase in quartz or aluminosilicate derivates, or an increase in sulfate derivatives.[21,62,63,66–68] This decrease in carbonate is potentially evident of carbonate dissolution, which is currently hypothesized to occur via to two mechanisms: The first, a reductive dissolution of calcium carbonate through a direct reaction with aqueous H_2, as shown in Equation 6.4 below:[69]

$$CaCO_3 + 4H_2 \rightarrow Ca^{2+} + CH_4 + H_2O + 2OH^-$$

(Eq. 6.4)

The second proposed mechanism is more indirect, starting with the reduction of pyrite, which is commonly found in Eagle Ford shale, upon interaction with hydrogen. The reduction of pyrite is given in Equation 6.5:[65,69,70]

$$FeS_2 + H_2 \rightarrow FeS + H_2S$$

(Eq. 6.5)

In solution, H_2S can break down into H^+ and HS^-, as shown in Equation 6.6.[70]

$$H_2S \rightarrow H^+ + HS^-$$

(Eq. 6.6)

This can, in turn, decrease the pH of the local environment, resulting in carbonate dissolution as can be seen in Equation 6.7:[69]

$$CaCO_3 + 4H_2 \rightarrow Ca^{2+} + CH_4 + H_2O + 2OH^-$$

(Eq. 6.7)

Ultimately, the free Ca^{2+} released from both carbonate dissolution mechanisms can react with sulfur that is extracted from Eagle Ford shale, to produce calcium sulfate, as shown in Equation 6.8:[62,63]

$$CaCO_3 + H_2SO_4 \rightarrow Ca^{2+} + CaSO_4 + CO_2 + H_2O$$

(Eq. 6.8)

Previous studies conducted by Goodman et al. have noted that precipitation of $CaSO_4$ results in the formation of gypsum, which ultimately can reduce the porosity on the microscale level.[62] Although more complementary analysis is necessary to confirm these proposed mechanisms, Equations 6.4 and 6.8 can provide potential mechanistic explanations for the significant increase and broadening of the 1105 cm^{-1} region. Lastly, there is the emergence of a 1682 cm^{-1} peak, which was not initially present in the pre-reaction shale spectrum. This peak may be evident of potential organics, such as ketones, from organic matter that have surfaced from the physical breakdown of mineral networks.[71]

The pre-reaction and post-reaction spectra, shown in the dotted and solid green lines, respectively, in Figure 6.15d look more similar than what was observed in the region of the sample highlighted by the blue box. While there are not significant changes in the profiles, one significant difference is in the relationship between the 1088 cm^{-1} and the 1432 cm^{-1} peaks, which represent Si-O stretching modes from aluminosilicates as well as quartz and carbonates, respectively.[21,62,63] Unlike what was seen in the pre-reaction spectra in the blue region, where the peaks due to the aluminosilicates are more intense than for carbonates. These relative intensities switch upon reaction with H_2 gas when the carbonate peaks become more intense relative to the aluminum silicate peak. This may be indicative of a decrease in sulfate derivatives such as calcium sulfate; further analysis with other microspectroscopic methods such as TEM/EDX can provide corroborative evidence for these different mechanisms.

Overall, in collaboration with the National Energy Technology Laboratory, this shale study utilizes both O-PTIR and AFM-IR spectroscopy in a complementary way to gather information about the physical and chemical transformations occurring on the microscale and nanoscale level. More specifically, AFM analysis has detected a significant increase in surface roughness on the nanoscale level. Concurrently, decreased porosity from gypsum formations as well as increased reflectivity from pyrite reduction have been observed on the microscale level with the mIRage-Raman. It should be noted that an increase in surface roughness does not always translate to an increase in porosity. This is because AFM operates on the nanoscale level; therefore, surface roughness can be defined as features that are taller than a few microns, whereas porosity is on a microscale, since it refers to a mineral's ability to hold liquid in open space. However, it should be highlighted that because both techniques probe different types of environments, any differences that arise can also be attributed to the perspective in which the system is being observed. Using O-

PTIR spectroscopy, the presence of hydrogen is proposed to result in the dissolution of calcium carbonate and the reduction of pyrite. When these chemical reactions are coupled together, it is deduced that calcium sulfate, which can precipitate into gypsum, is formed. While valuable information has been gathered via AFM and O-PTIR spectroscopy, other micro-spectroscopic methods such as SEM-EDX is currently planned to be used to better support the proposed mechanisms presented in this study. Overall, a clear understanding of this system will help understanding the potential of shale as a source for H_2 gas storage.

6.5 Conclusions

The emergence of micro-spectroscopic probes has resulted in a rising number of applications to various environmental systems. For the SeaSCAPE and CHAOS studies, AFM-IR spectroscopy has allowed us to target and probe individual particles to understand the changes in composition, phase, and heterogeneity, which has been a significant improvement than analyzing them only on the bulk scale. By observing these size-dependent and morphology-dependent changes, we can gather more specific information about the chemistry occurring on the nanoscale level. The single-particle measurements show how atmospheric aging results in higher functionalization and oxidation compared to nascent SSA. In addition, it suggests that an increase in wind speed leads to a higher emission of primary organic aerosols. Insights into how wind speed is related to the SSA formation mechanism can be used to predict SSA behavior. For the indoor CASA campaign, AFM-IR spectroscopy has shown that events that influence the indoor environment, like wildfire smoke, have significant effects on particle deposition on common indoor surfaces such as window glass. While the specific reaction chemistry that is occurring on

these deposited surfaces can be further understood when complemented with other techniques, characterizing the particles deposited on the surface is a promising first step. In just 24 hours of smoke exposure, two notably different types of particles are observed. Lastly, the Eagle Ford shale study has proven the unique information provided by micro-spectroscopic probes. The complementary nature of AFM-IR and O-PTIR spectroscopy is shown when limitations are met by the former technique and mitigated by the latter. With AFM-IR spectroscopy, physical characteristics about nanoscale features and pore size are observed. However, the challenges faced with locating the same region was mitigated through O-PTIR spectroscopy, which allowed for the before and after H_2 gas reaction comparison, on a more macroscopic level. In addition, the spectra collected from both technique reveal the presence of micro and nano environments within the sample.

The studies presented in this dissertation chapter show the importance of probing these various environmental systems on the nanoscale level. There are important changes in phase, heterogeneity, and chemistry that are critical for understanding the complex chemistry that occurs in the atmosphere. These studies not only provide evidence for the usefulness of micro-spectroscopic techniques, but also their potential as a complementary tool for studies of complex environmental systems.

6.6 Acknowledgements

Chapter 6, in part, contains materials that have been published or are currently being prepared for submission. The study investigating the effect of aging on marine sea spray aerosol has been published by ACS Earth & Space Chemistry in: Kaluarachchi, C. P., **Kim, D.**; Grassian,

V. H. Effects of Atmospheric Aging Processes on Nascent Sea Spray Aerosol Physicochemical Properties. *ACS Earth & Space Chemistry.* **2022**, 6 (11), 2732-2744. The research reported here was funded by the National Science Foundation (NSF) through the NSF Center for Aerosol Impacts on Chemistry of the Environment (CAICE) under grant no. CHE-1801971. We would like to specially acknowledge Dr. Chathuri Kaluarachchi for her AFM morphological data collection and helpful discussion preceding spectroscopic data collection, which was conducted by the author of this dissertation.

The research reported here was funded by the National Science Foundation (NSF) through the NSF Center for Aerosol Impacts on Chemistry of the Environment (CAICE). We would like to acknowledge Dr. Carolina Molina and Lincoln Mehndiratta for their collection of the samples analyzed for this study. In particular, the author of this dissertation would like to specially thank Dr. Carolina Molina's hard work in processing and analyzing the data collected for this study. We would also like to acknowledge Chamika K. Madawala for her collection of AFM morphological samples as well as helpful discussion preceding spectroscopic data collection, which was conducted by the author of this dissertation.

The research reported here was funded by the Alfred P. Sloan Foundation grant #G-2020-12365 and #G-2020-12675. The author of this dissertation would like to thank the entire CASA science team, specifically Dr. Delphine Farmer and Dr. Marina Vance, for their leadership and invaluable contributions in successfully completing this field study. We would also like to thank Dr. Shubhrangshu Pandit for assisting with the collection of the smoke-deposited samples during this campaign.

The manuscript for the Eagle Ford shale study is currently being prepared for submission. The author of this dissertation would like to thank Samantha Townsley for her assistance in O-

PTIR data collection and processing. In addition, we would also like to thank and acknowledge Dr. Angela Goodman and Dr. Barbara Kutchko from the National Energy Technology Laboratory (NETL) for their valuable and helpful discussions regarding this study as well as their support during the entirety of this collaboration.

6.7 Bibliography

(1) Kaluarachchi, C. P.; Or, V. W.; Lan, Y.; Madawala, C. K.; Hasenecz, E. S.; Crocker, D. R.; Morris, C. K.; Lee, H. D.; Mayer, K. J.; Sauer, J. S.; Lee, C.; Dorce, G.; Malfatti, F.; Stone, E. A.; Cappa, C. D.; Grassian, V. H.; Prather, K. A.; Tivanski, A. V. Size-Dependent Morphology, Composition, Phase State, and Water Uptake of Nascent Submicrometer Sea Spray Aerosols during a Phytoplankton Bloom. *ACS Earth Sp. Chem.* **2022**, *6* (1), 116–130.

(2) Cochran, R. E.; Laskina, O.; Trueblood, J. V.; Estillore, A. D.; Morris, H. S.; Jayarathne, T.; Sultana, C. M.; Lee, C.; Lin, P.; Laskin, J.; Laskin, A.; Dowling, J. A.; Qin, Z.; Cappa, C. D.; Bertram, T. H.; Tivanski, A. V.; Stone, E. A.; Prather, K. A.; Grassian, V. H. Molecular Diversity of Sea Spray Aerosol Particles: Impact of Ocean Biology on Particle Composition and Hygroscopicity. *Chem.* **2017**, *2* (5), 655–667.

(3) Cochran, R. E.; Ryder, O. S.; Grassian, V. H.; Prather, K. A. Sea Spray Aerosol: The Chemical Link between the Oceans, Atmosphere, and Climate. *Acc. of Chem. Res*. **2017**, *50* (3), 599–604.

(4) Sauer, J. S.; Mayer, K. J.; Lee, C.; Alves, M. R.; Amiri, S.; Bahaveolos, C. J.; Franklin, E. B.; Crocker, D. R.; Dang, D.; Dinasquet, J.; Garofalo, L. A.; Kaluarachchi, C. P.; Kilgour, D. B.; Mael, L. E.; Mitts, B. A.; Moon, D. R.; Moore, A. N.; Morris, C. K.; Mullenmeister, C. A.; Ni, C. M.; Pendergraft, M. A.; Petras, D.; Simpson, R. M. C.; Smith, S.; Tumminello, P. R.; Walker, J. L.; Demott, P. J.; Farmer, D. K.; Goldstein, A. H.; Grassian, V. H.; Jaffe, J. S.; Malfatti, F.; Martz, T. R.; Slade, J. H.; Tivanski, A. V.; Bertram, T. H.; Cappa, C. D.; Prather, K. A. The Sea Spray Chemistry and Particle Evolution Study (SeaSCAPE): Overview and Experimental Methods. *Env. Sci.: Proc. and Imp.*, **2022**, *2*, 290–315.

(5) Kaluarachchi, C. P.; Or, V. W.; Lan, Y.; Hasenecz, E. S.; Kim, D.; Madawala, C. K.; Dorcé, G. P.; Mayer, K. J.; Sauer, J. S.; Lee, C.; Cappa, C. D.; Bertram, T. H.; Stone, E. A.; Prather, K. A.; Grassian, V. H.; Tivanski, A. V. Effects of Atmospheric Aging Processes on Nascent Sea Spray Aerosol Physicochemical Properties. *ACS Earth Sp. Chem.* **2022**, *6* (11), 2732–2744.

(6) Collins, D. B.; Zhao, D. F.; Ruppel, M. J.; Laskina, O.; Grandquist, J. R.; Modini, R. L.; Stokes, M. D.; Russell, L. M.; Bertram, T. H.; Grassian, V. H.; Deane, G. B.; Prather, K. A.

Direct Aerosol Chemical Composition Measurements to Evaluate the Physicochemical Differences between Controlled Sea Spray Aerosol Generation Schemes. *Atmos. Meas. Tech.* **2014**, *7* (11), 3667–3683.

(7) Prather, K. A.; Bertram, T. H.; Grassian, V. H.; Deane, G. B.; Stokes, M. D.; DeMott, P. J.; Aluwihare, L. I.; Palenik, B. P.; Azam, F.; Seinfeld, J. H.; Moffet, R. C.; Molina, M. J.; Cappa, C. D.; Geiger, F. M.; Roberts, G. C.; Russell, L. M.; Ault, A. P.; Baltrusaitis, J.; Collins, D. B.; Corrigan, C. E.; Cuadra-Rodriguez, L. A.; Ebben, C. J.; Forestieri, S. D.; Guasco, T. L.; Hersey, S. P.; Kim, M. J.; Lambert, W. F.; Modini, R. L.; Mui, W.; Pedler, B. E.; Ruppel, M. J.; Ryder, O. S.; Schoepp, N. G.; Sullivan, R. C.; Zhao, D. Bringing the Ocean into the Laboratory to Probe the Chemical Complexity of Sea Spray Aerosol. *PNAS* **2013**, *110* (19), 7550–7555.

(8) Quinn, P. K.; Collins, D. B.; Grassian, V. H.; Prather, K. A.; Bates, T. S. Chemistry and Related Properties of Freshly Emitted Sea Spray Aerosol. *Chem. Rev*. **2015**, *115* (10), 4383–4399.

(9) Mitts, B. A.; Wang, X.; Lucero, D. D.; Beall, C. M.; Deane, G. B.; DeMott, P. J.; Prather, K. A. Importance of Supermicron Ice Nucleating Particles in Nascent Sea Spray. *Geophys. Res. Lett*. **2021**, 1-10.

(10) Crocker, D. R.; Hernandez, R. E.; Huang, H. D.; Pendergraft, M. A.; Cao, R.; Dai, J.; Morris, C. K.; Deane, G. B.; Prather, K. A.; Thiemens, M. H. Biological Influence on 13C and Organic Composition of Nascent Sea Spray Aerosol. *ACS Earth Sp. Chem.* **2020**, *4* (9), 1686–1699.

(11) Hasenecz, E. S.; Jayarathne, T.; Pendergraft, M. A.; Santander, M. V.; Mayer, K. J.; Sauer, J.; Lee, C.; Gibson, W. S.; Kruse, S. M.; Malfatti, F.; Prather, K. A.; Stone, E. A. Marine Bacteria Affect Saccharide Enrichment in Sea Spray Aerosol during a Phytoplankton Bloom. *ACS Earth Sp. Chem.* **2020**, *4* (9), 1638–1649.

(12) Alpert, P. A.; Kilthau, W. P.; Bothe, D. W.; Radway, J. A. C.; Aller, J. Y.; Knopf, D. A. The Influence of Marine Microbial Activities on Aerosol Production: A Laboratory Mesocosm Study. *J. Geophys. Res.* **2015**, *120* (17), 8841–8860.

(13) Lim, C. Y.; Browne, E. C.; Sugrue, R. A.; Kroll, J. H. Rapid Heterogeneous Oxidation of Organic Coatings on Submicron Aerosols. *Geophys. Res. Lett.* **2017**, *44* (6), 2949–2957.

(14) Lim, Y. Bin; Ziemann, P. J. Products and Mechanism of Secondary Organic Aerosol Formation from Reactions of N-Alkanes with OH Radicals in the Presence of NO x. *Environ. Sci. Technol.* **2005**, *39* (23), 9229–9236.

(15) Slade, J. H.; Thalman, R.; Wang, J.; Knopf, D. A. Chemical Aging of Single and Multicomponent Biomass Burning Aerosol Surrogate Particles by OH: Implications for Cloud Condensation Nucleus Activity. *Atmos. Chem. Phys.* **2015**, *15* (17), 10183–10201.

(16) Gantt, B.; Meskhidze, N.; Facchini, M. C.; Rinaldi, M.; Ceburnis, D.; O'Dowd, C. D. Wind Speed Dependent Size-Resolved Parameterization for the Organic Mass Fraction of Sea Spray Aerosol. *Atmos. Chem. Phys.* **2011**, *11* (16), 8777–8790.

(17) Radeloff, V. C.; Helmers, D. P.; Anu Kramer, H.; Mockrin, M. H.; Alexandre, P. M.; Bar-Massada, A.; Butsic, V.; Hawbaker, T. J.; Martinuzzi, S.; Syphard, A. D.; Stewart, S. I. Rapid Growth of the US Wildland-Urban Interface Raises Wildfire Risk. *PNAS* **2018**, *115* (13), 3314–3319.

(18) Aguilera, R.; Corringham, T.; Gershunov, A.; Benmarhnia, T. Wildfire Smoke Impacts Respiratory Health More than Fine Particles from Other Sources: Observational Evidence from Southern California. *Nat. Commun.* **2021**, *12* (1), 1-8.

(19) Reid, C. E.; Brauer, M.; Johnston, F. H.; Jerrett, M.; Balmes, J. R.; Elliott, C. T. Critical Review of Health Impacts of Wildfire Smoke Exposure. *Env. Health Perspec.* **2016**, *124* (9), 1334–1343.

(20) Davison, G.; Barkjohn, K. K.; Hagler, G. S. W.; Holder, A. L.; Coefield, S.; Noonan, C.; Hassett-Sipple, B. Creating Clean Air Spaces During Wildland Fire Smoke Episodes: Web Summit Summary. *Front Pub. Health* **2021**, *9*, 1-9.

(21) Goodman, A.; Kutchko, B.; Sanguinito, S.; Natesakhawat, S.; Cvetic, P.; Haljasmaa, I.; Spaulding, R.; Crandall, D.; Moore, J.; Burrows, L. C. Reactivity of CO2with Utica, Marcellus, Barnett, and Eagle Ford Shales and Impact on Permeability. *En. and Fuels* **2021**, *35* (19), 15894–15917.

(22) Jubb, A. M.; Birdwell, J. E.; Hackley, P. C.; Hatcherian, J. J.; Qu, J. Nanoscale Molecular Composition of Solid Bitumen from the Eagle Ford Group across a Natural Thermal Maturity Gradient. *En. and Fuels* **2020**, *34* (7), 8167–8177.

(23) Wang, K.; Ma, L.; Taylor, K. G. Nanoscale Geochemical Heterogeneity of Organic Matter in Thermally-Mature Shales: An AFM-IR Study. *Fuel* **2022**, *310* (122278), 1-16.

(24) Loucks, R. G.; Reed, R. M.; Ruppel, S. C.; Hammes, U. Spectrum of Pore Types and Networks in Mudrocks and a Descriptive Classification for Matrix-Related Mudrock Pores. *Am. Assoc. Pet. Geol. Bull.* **2012**, *96* (6), 1071–1098.

(25) Harrison, A. L.; Jew, A. D.; Dustin, M. K.; Thomas, D. L.; Joe-Wong, C. M.; Bargar, J. R.; Johnson, N.; Brown, G. E.; Maher, K. Element Release and Reaction-Induced Porosity Alteration during Shale-Hydraulic Fracturing Fluid Interactions. *App. Geochem.* **2017**, *82*, 47–62.

(26) Goodman, A.; Kutchko, B.; Lackey, G.; Gulliver, D.; Strazisar, B.; Tinker, K.; Wright, R.; Haeri, F.; Huerta, N.; Baek, S.; Bagwell, C.; De, J.; Camargo, T.; Freeman, G.; Kuang, W.; Torgeson, J. *Choose an Item. Subsurface Hydrogen and Natural Gas Storage: State of Knowledge and Research Recommendations Report SHASTA: Subsurface Hydrogen Assessment, Storage, and Technology Acceleration Project*; **2022**.

(27) Ozarslan, A. Large-Scale Hydrogen Energy Storage in Salt Caverns. *Int. J. Hyd. En.* **2012**, *37* (19), 14265–14277.

(28) Zhang, F.; Zhao, P.; Niu, M.; Maddy, J. The Survey of Key Technologies in Hydrogen Energy Storage. *Int. J. Hyd. En*. **2016**, 14535–14552.

(29) van Gessel, S.; Fernandez Yuste, C.; Fournier, C.; Kumar, R. *Hydrogen TCP-Task 42 UNDERGROUND HYDROGEN STORAGE*. **2023**.

(30) Ray, K. K.; Lee, H. D.; Gutierrez, M. A.; Chang, F. J.; Tivanski, A. V. Correlating 3D Morphology, Phase State, and Viscoelastic Properties of Individual Substrate-Deposited Particles. *Anal. Chem.* **2019**, *91* (12), 7621–7630.

(31) Lee, H. D.; Tivanski, A. V. Atomic Force Microscopy: An Emerging Tool in Measuring the Phase State and Surface Tension of Individual Aerosol Particles. *Annu. Rev. Phys. Chem.* **2021**, *72*, 235-252.

(32) Ault, A. P.; Peters, T. M.; Sawvel, E. J.; Casuccio, G. S.; Willis, R. D.; Norris, G. A.; Grassian, V. H. Single-Particle SEM-EDX Analysis of Iron-Containing Coarse Particulate Matter in an Urban Environment: Sources and Distribution of Iron within Cleveland, Ohio. *Environ. Sci. Technol.* **2012**, *46* (8), 4331–4339.

(33) Ault, A. P.; Moffet, R. C.; Baltrusaitis, J.; Collins, D. B.; Ruppel, M. J.; Cuadra-Rodriguez, L. A.; Zhao, D.; Guasco, T. L.; Ebben, C. J.; Geiger, F. M.; Bertram, T. H.; Prather, K. A.; Grassian, V. H. Size-Dependent Changes in Sea Spray Aerosol Composition and Properties with Different Seawater Conditions. *Environ. Sci. Technol.* **2013**, *47* (11), 5603–5612.

(34) Nakagawa, M.; Nakayama, T.; Sasago, H.; Kuruma, Y.; Yai, H.; Ogawa, S.; Deng, Y.; Mochida, M.; Matsumi, Y. Assessment of the Sphericity of Submicrometer Particles Using a Single-Particle Polar Nephelometer at an Urban Site in Japan. *Aerosol Air Qual. Res.* **2020**, *20* (11), 2474–2484.

(35) Dommer, A. C.; Wauer, N. A.; Angle, K. J.; Davasam, A.; Rubio, P.; Luo, M.; Morris, C. K.; Prather, K. A.; Grassian, V. H.; Amaro, R. E. Revealing the Impacts of Chemical Complexity on Submicrometer Sea Spray Aerosol Morphology. *ACS Cent. Sci.* **2023**. *9* (6), 1088-1103.

(36) Barkley, A. E.; Olson, N. E.; Prospero, J. M.; Gatineau, A.; Panechou, K.; Maynard, N. G.; Blackwelder, P.; China, S.; Ault, A. P.; Gaston, C. J. Atmospheric Transport of North African Dust-Bearing Supermicron Freshwater Diatoms to South America: Implications for Iron Transport to the Equatorial North Atlantic Ocean. *Geophys. Res. Lett.* **2021**, *48* (5), 1-12.

(37) Or, V. W.; Estillore, A. D.; Tivanski, A. V.; Grassian, V. H. Lab on a Tip: Atomic Force Microscopy-Photothermal Infrared Spectroscopy of Atmospherically Relevant Organic/Inorganic Aerosol Particles in the Nanometer to Micrometer Size Range. *Analyst* **2018**, *143* (12), 2765–2774.

(38) Maria, S. F.; Russell, L. M.; Turpin, B. J.; Porcja, R. J. FTIR Measurements of Functional Groups and Organic Mass in Aerosol Samples over the Caribbean. *Atmos. Env.* **2002**, 36 (33), 5185-5196.

(39) Trueblood, J. V.; Wang, X.; Or, V. W.; Alves, M. R.; Santander, M. V.; Prather, K. A.; Grassian, V. H. The Old and the New: Aging of Sea Spray Aerosol and Formation of Secondary Marine Aerosol through OH Oxidation Reactions. *ACS Earth Sp. Chem.* **2019**, *3* (10), 2307–2314.

(40) Estillore, A. D.; Morris, H. S.; Or, V. W.; Lee, H. D.; Alves, M. R.; Marciano, M. A.; Laskina, O.; Qin, Z.; Tivanski, A. V.; Grassian, V. H. Linking Hygroscopicity and the Surface Microstructure of Model Inorganic Salts, Simple and Complex Carbohydrates, and Authentic Sea Spray Aerosol Particles. *Phys. Chem. Chem. Phys.* **2017**, *19* (31), 21101–21111.

(41) Olson, N. E.; Xiao, Y.; Lei, Z.; Ault, A. P. Simultaneous Optical Photothermal Infrared (O-PTIR) and Raman Spectroscopy of Submicrometer Atmospheric Particles. *Anal. Chem.* **2020**, *92* (14), 9932–9939.

(42) Mirrielees, J. A.; Kirpes, R. M.; Haas, S. M.; Rauschenberg, C. D.; Matrai, P. A.; Remenapp, A.; Boschi, V. L.; Grannas, A. M.; Pratt, K. A.; Ault, A. P. Probing Individual Particles Generated at the Freshwater-Seawater Interface through Combined Raman, Photothermal Infrared, and X-Ray Spectroscopic Characterization. *ACS Meas. Sci. Au* **2022**, *2* (6), 605–619.

(43) Popovicheva, O.; Ivanov, A.; Vojtisek, M. Functional Factors of Biomass Burning Contribution to Spring Aerosol Composition in a Megacity: Combined FTIR-PCA Analyses. *Atmos.* **2020**, *11* (319), 1-20.

(44) Penezić, A.; Drozdowska, V.; Novak, T.; Gašparović, B. Distribution and Characterization of Organic Matter within the Sea Surface Microlayer in the Gulf of Gdańsk. *Oceano.* **2022**, *64* (4), 631–650.

(45) Wang, X.; Deane, G. B.; Moore, K. A.; Ryder, O. S.; Stokes, M. D.; Beall, C. M.; Collins, D. B.; Santander, M. V.; Burrows, S. M.; Sultana, C. M.; Prather, K. A. The Role of Jet and Film Drops in Controlling the Mixing State of Submicron Sea Spray Aerosol Particles. *PNAS* **2017**, *114* (27), 6978–6983.

(46) Unga, F.; Choël, M. Microscopic Observations of Core-Shell Particle Structure and Implications for Atmospheric Aerosol Remote Sensing. *J. Geophys. Res.* **2018**, *123* (24), 944–962.

(47) Li, J.; Link, M. F.; Pandit, S.; Webb, M. H.; Mayer, K. J.; Garofalo, L. A.; Rediger, K. L.; Poppendieck, D. G.; Zimmerman, S. M.; Vance, M. E.; Grassian, V. H.; Morrison, G. C.; Turpin, B. J.; Farmer, D. K. The Persistence of Smoke VOCs Indoors: Partitioning, Surface Cleaning, and Air Cleaning in a Smoke-Contaminated House. *Sci Adv.* In Prep.

(48) Farmer, D. K.; Vance, M. E.; Abbatt, J. P. D.; Abeleira, A.; Alves, M. R.; Arata, C.; Boedicker, E.; Bourne, S.; Cardoso-Saldaña, F.; Corsi, R.; Decarlo, P. F.; Goldstein, A. H.; Grassian, V. H.; Hildebrandt Ruiz, L.; Jimenez, J. L.; Kahan, T. F.; Katz, E. F.; Mattila, J. M.; Nazaroff, W. W.; Novoselac, A.; O'Brien, R. E.; Or, V. W.; Patel, S.; Sankhyan, S.; Stevens, P. S.; Tian, Y.; Wade, M.; Wang, C.; Zhou, S.; Zhou, Y. Overview of HOMEChem: House

Observations of Microbial and Environmental Chemistry. *Env. Sci.: Proc. and Imp*. **2019**, 1280–1300.

(49) Fang, Y.; Lakey, P. S. J.; Riahi, S.; McDonald, A. T.; Shrestha, M.; Tobias, D. J.; Shiraiwa, M.; Grassian, V. H. A Molecular Picture of Surface Interactions of Organic Compounds on Prevalent Indoor Surfaces: Limonene Adsorption on SiO_2. *Chem Sci.* **2019**, *10* (10), 2906–2914.

(50) Potapova, E.; Carabante, I.; Grahn, M.; Holmgren, A.; Hedlund, J. Studies of Collector Adsorption on Iron Oxides by in Situ ATR-FTIR Spectroscopy. *Ind. Eng. Chem. Res.* **2010**, *49* (4), 1493–1502.

(51) Van Den Brand, J.; Blajiev, O.; Beentjes, P. C. J.; Terryn, H.; De Wit, J. H. W. Interaction of Ester Functional Groups with Aluminum Oxide Surfaces Studied Using Infrared Reflection Absorption Spectroscopy. *Lang.* **2004**, *20* (15), 6318–6326.

(52) Simoneit, B. R. T.; Schauer, J. J.; Nolte, C. G.; Oros, D. R.; Elias, V. O.; Fraser, M. P.; Rogge, W. F.; Cass, G. R. Levoglucosan, a Tracer for Cellulose in Biomass Burning and Atmospheric Particles. *Atmos. Env.* **1999**, *33*, 173-182.

(53) Finewax, Z.; De Gouw, J. A.; Ziemann, P. J. Identification and Quantification of 4-Nitrocatechol Formed from OH and NO3 Radical-Initiated Reactions of Catechol in Air in the Presence fof NOx: Implications for Secondary Organic Aerosol Formation from Biomass Burning. *Environ. Sci. Technol.*, **2018**, *52* (4), 1981–1989.

(54) Lindenmaier, R.; Williams, S. D.; Sams, R. L.; Johnson, T. J. Quantitative Infrared Absorption Spectra and Vibrational Assignments of Crotonaldehyde and Methyl Vinyl Ketone Using Gas-Phase Mid-Infrared, Far-Infrared, and Liquid Raman Spectra: S-Cis vs s-Trans Composition Confirmed via Temperature Studies and Ab Initio Methods. *Journal of Phys. Chem. A* **2017**, *121* (6), 1195–1212.

(55) Johnson, T. J.; Sams, R. L.; Profeta, L. T. M.; Akagi, S. K.; Burling, I. R.; Yokelson, R. J.; Williams, S. D. Quantitative IR Spectrum and Vibrational Assignments for Glycolaldehyde Vapor: Glycolaldehyde Measurements in Biomass Burning Plumes. *JPC A* **2013**, *117* (20), 4096–4107.

(56) Dazzi, A.; Prater, C. B. AFM-IR: Technology and Applications in Nanoscale Infrared Spectroscopy and Chemical Imaging. *Chem. Rev.* **2017**, *117* (7), 5146–5173.

(57) Dazzi, A.; Prater, C. B.; Hu, Q.; Bruce, D.; Rabolt, J. F.; Marcott, C. Focal Point Review AFM-IR: Combining Atomic Force Microscopy and Infrared Spectroscopy for Nanoscale Chemical Characterization. *Appl. Spectrosc.* **2012**, *66* (12), 1365–1384.

(58) Dazzi, A.; Prater, C. B.; Hu, Q.; Chase, D. B.; Rabolt, J. F.; Marcott, C. AFM-IR: Combining Atomic Force Microscopy and Infrared Spectroscopy for Nanoscale Chemical Characterization. *Appl. Spectrosc.* **2012**, *66* (12), 1365–1384.

(59) Klementieva, O.; Sandt, C.; Martinsson, I.; Kansiz, M.; Gouras, G. K.; Borondics, F. Super-Resolution Infrared Imaging of Polymorphic Amyloid Aggregates Directly in Neurons. *Advanced Science* **2020**, *7* (6), 1-9.

(60) Marcott, C.; Kansiz, M.; Dillon, E.; Cook, D.; Mang, M. N.; Noda, I. Two-Dimensional Correlation Analysis of Highly Spatially Resolved Simultaneous IR and Raman Spectral Imaging of Bioplastics Composite Using Optical Photothermal Infrared and Raman Spectroscopy. *J. Mol. Struct.* **2020**, *1210*, 128045.

(61) Kansiz, M.; Prater, C.; Dillon, E.; Lo, M.; Anderson, J.; Marcott, C.; Demissie, A.; Chen, Y.; Kunkel, G. Optical Photothermal Infrared Microspectroscopy with Simultaneous Raman – A New Non-Contact Failure Analysis Technique for Identification of <10 Mm Organic Contamination in the Hard Drive and Other Electronics Industries. *Micros. Today* **2020**, *28* (3), 26–36.

(62) Goodman, A.; Sanguinito, S.; Tkach, M.; Natesakhawat, S.; Kutchko, B.; Fazio, J.; Cvetic, P. Investigating the Role of Water on CO2-Utica Shale Interactions for Carbon Storage and Shale Gas Extraction Activities – Evidence for Pore Scale Alterations. *Fuel* **2019**, *242*, 744–755.

(63) Sanguinito, S.; Cvetic, P.; Goodman, A.; Kutchko, B.; Natesakhawat, S. Characterizing Pore-Scale Geochemical Alterations in Eagle Ford and Barnett Shale from Exposure to Hydraulic Fracturing Fluid and CO2/H2O. *Energy and Fuels* **2021**, *35* (1), 583–598.

(64) Goodman, A. L.; Li, P.; Usher, C. R.; Grassian, V. H. Heterogeneous Uptake of Sulfur Dioxide on Aluminum and Magnesium Oxide Particles. *J. Phys. Chem. A* **2001**, *105* (25), 6109–6120.

(65) Safari, A.; Zeng, L.; Nguele, R.; Sugai, Y.; Sarmadivaleh, M. Review on Using the Depleted Gas Reservoirs for the Underground H2 Storage: A Case Study in Niigata Prefecture, Japan. *Int. J. of Hydr. En*. **2023**, 10579–10602.

(66) Peak, D.; Ford, R. G.; Sparks, D. L. An in Situ ATR-FTIR Investigation of Sulfate Bonding Mechanisms on Goethite. *J. Colloid Int. Sci.* **1999**, *218* (1), 289–299.

(67) Wang, X.; Wang, Z.; Peak, D.; Tang, Y.; Feng, X.; Zhu, M. Quantification of Coexisting Inner- and Outer-Sphere Complexation of Sulfate on Hematite Surfaces. *ACS Earth Sp. Chem.* **2018**, *2* (4), 387–398.

(68) Paul, K. W.; Borda, M. J.; Kubicki, J. D.; Sparks, D. L. Effect of Dehydration on Sulfate Coordination and Speciation at the Fe-(Hydr)Oxide-Water Interface: A Molecular Orbital/Density Functional Theory and Fourier Transform Infrared Spectroscopic Investigation. *Lang.* **2005**, *21* (24), 11071–11078.

(69) Zeng, L.; Vialle, S.; Ennis-King, J.; Esteban, L.; Sarmadivaleh, M.; Sarout, J.; Dautriat, J.; Giwelli, A.; Xie, Q. Role of Geochemical Reactions on Caprock Integrity during Underground Hydrogen Storage. *J. Energy Storage* **2023**, *65*, 107414.

(70) Truche, L.; Berger, G.; Destrigneville, C.; Guillaume, D.; Giffaut, E. Kinetics of Pyrite to Pyrrhotite Reduction by Hydrogen in Calcite Buffered Solutions between 90 and 180°C: Implications for Nuclear Waste Disposal. *Geochim. Cosmochim. Acta.* **2010**, *74* (10), 2894–2914.

(71) Yesiltas, M.; Kebukawa, Y. Associations of Organic Matter with Minerals in Tagish Lake Meteorite via High Spatial Resolution Synchrotron-Based FTIR Microspectroscopy. *Meteorit. Planet Sci.* **2016**, *51* (3), 584–595.

CHAPTER 7
CONCLUSIONS AND FUTURE DIRECTIONS

The research presented herein focuses on the development and application of microscale and nanoscale spectroscopic techniques for analyses of relevant surface for environmental systems present in both indoor and outdoor environments. Traditional IR spectroscopy has been utilized for decades as a powerful technique that can provide valuable chemical information about unknown samples and the complex chemistry they undergo. The growth of micro-spectroscopic techniques has proven to successfully open up new ways in which these systems can be analyzed. However, in the field of environmental chemistry, the applications of these submicron infrared micro-spectroscopic probes have been limited in some cases to the new research area of microplastics. In this dissertation, various studies have shown that these probes can be developed to study complex interfaces occurring for either outdoor surfaces such as geochemical interfaces or indoor surfaces.

Chapter 3 shows the first application of AFM-IR spectroscopy to a well-studied, complex system: the adsorption of organic matter onto iron oxide surfaces. In this study, the reaction between Suwannee River Fulvic Acid (SRFA), and α-FeOOH, goethite, is investigated. Due to its complexity, large number of different molecular species and high molar mass, the chemistry of SRFA is considered to be highly complex, especially in an environment with many variables of solution pH, ionic strength, and sorption. However, the presence of functional groups that readily bind to the surface of different geochemical interfaces has made it a system of great interest. In this study, we gathered new insights into this adsorption process by utilizing the high spatial resolution provided uniquely by AFM-IR spectroscopy. Upon closer investigation, this technique

revealed both physical and chemical heterogeneities on the micro and nanoscale level occurring along this interaction. We not only observed heterogeneities within SRFA itself, but also on the single particle level when chemical maps of goethite nanoparticles with adsorbed SRFA were shown not to homogenously coated the particle. In addition, SRFA adsorption onto goethite is highly dependent on pH, and the pH-dependence observed using more traditional methods such as ATR-FTIR spectroscopy were also observed with AFM-IR spectroscopy.

Moving forward, Chapter 4 was built upon the findings that were presented in Chapter 3. As already noted, the adsorption and interaction of organic matter with goethite was explored in Chapter 3, which was shown to be highly complex due to the highly heterogeneous nature of SRFA. However, in environmental systems there are other ionic and molecular species, including biomacromolecules. Both oxyanions and biological components are important factors in many environmental systems. Therefore, in efforts to build complexity, a bottom-up approach was initiated with sodium sulfate, as a representative oxyanion, and BSA, as a model protein. The interactions between goethite, sodium sulfate, and BSA were introduced at the start of a 2-component study since goethite alone had already been investigated preliminarily. From here, various combinations were studied, such as BSA and sulfate, and then, a 3-component system with BSA, sulfate, and goethite, altogether in a single thin film. Upon investigation with AFM-IR spectroscopy, different phase states as well as micro and nano-environments were detected in these 2 and 3-component systems. More specifically, we observed aggregates of goethite and sulfate whereas BSA homogenously coated the majority of the film.

Future studies for both Chapter 3 and Chapter 4 are related to developing micro-spectroscopic tools to study environmental systems by building complexity, one at a time. bottom up approach by increasing complexity. This can be broken down into two main categories: (1) by

adding more components that are likely to be present in these environments, or (2) by exposing these systems to various environmental factors. One way to increase complexity is by adding relevant chemical contaminants such as perfluorooctanoic acids, otherwise known as PFAS. PFAS are commonly found in household products that has not only been detected in drinking water but also found to be extremely toxic over time. By mixing PFAS into an aqueous system containing oxyanions, biological components, organic matter, and mineral oxides, we can gather more information about how its chemistry is altered in the presence of other environmentally-relevant adsorbates. For example, the aggregation behavior of PFAS can be probed with micro-spectroscopic tool to see if it exhibits any preferential binding to one species over another in the presence of other environmentally relevant adsorbates. The surface chemistry that occurs along geochemical interfaces has been known to be heavily influenced by environmental factors, which also can be explored for future studies. In Chapter 3, the effect of pH is shown to alter the protonation state of SRFA. The complexity of environmental systems can be increased by seeing how these components respond to changes in acidic or basic conditions, salinity, or even light. In addition, the process of dehydration has also been found to alter the phase states of some crystalline species, such as sodium sulfate and sodium nitrate. This effect can be further explored via experimentation involving wet-dry-cycling. By increasing complexity in both ways, we can better mimic an aqueous environmental system, in efforts to understand how bigger macromolecules travel and transform through these systems over time.

Chapter 5 introduces a new micro-spectroscopic technique that not only combines imaging and IR spectroscopy, but also incorporates Raman spectroscopy. The instrument, called the mIRage-Raman, is a sub-micron resolution IR spectroscopy and imaging system with Raman capabilities that operates under the phenomenon of Optical Photothermal InfraRed (O-PTIR)

spectroscopy. While O-PTIR spectroscopy operates similarly to AFM-IR spectroscopy in that they both are based off of the principle of photothermal expansion, it is extremely complementary to the nanoIR2 system. This chapter of the dissertation compares O-PTIR spectroscopy to Raman, ATR-FTIR and AFM-IR spectroscopy. Together, a comprehensive spectral library has been built that can be used as a reference for future studies involving mineral compounds. In efforts to encapsulate the various classes of minerals, a total of 14 different compounds were analyzed and each fall into one of the four classes: (1) mineral oxides, (2) carbonates, sulfates, and nitrates, (3) clays and aluminosilicates, (4) complex dust samples. As discussed previously, there has yet to be an extensive number of studies centered in environmental surface chemistry in AFM-IR and O-PTIR research. Therefore, building a spectral library as a sources is important and can provide references for future studies in this field. Future studies can also include adding to the current list of compounds with minerals that are also studied such as hematite, calcium sulfate, and gypsum. In addition, these libraries can be built for other environmental systems such as sea spray aerosol, fatty acids and lipids are prevalent. Biological components can also be an area of interest, as they can encompass anywhere from nucleotides or amino acids to protein, and even some commonly found bacteria in aquatic systems.

Chapter 6 is a compilation of four different studies in which AFM-IR and O-PTIR spectroscopy are used in different applications as part of several collaborative efforts. Three of the four studies were part of different field campaigns: SeaSCAPE, CHAOS, and CASA and the last study was in collaboration with the Department of Energy National Energy Technology Laboratory (NETL), with shale rock samples. This chapter highlights how using micro-spectroscopic probes as a complementary method to better understand complex field samples can be extremely powerful. The ability to spatially resolve the probe on the nanoscale level allows for

imaging of single particles and aerosols, as shown by the data collected from CASA and SeaSCAPE/CHAOS, respectively. For the shale study, it has allowed for detection of carbonate dissolution in micro and nano-environments, with increased porosity and thus permeability, upon reaction with H_2 gas.

Over the past 5 years, there has been a clear, growing interest in the use of both AFM-IR and O-PTIR spectroscopy, suggesting that there are a number of new possibilities for the different applications of these techniques as well as future collaborative o. Some preliminary studies have used these instruments to profile homogeneity or heterogeneity within synthesized, inorganic materials or taking spectra of nanoscale environments present in biological samples such as biofilms. In addition, the non-contact method of the mIRage-Raman eliminates the need for extensive sample preparation, widening the fields in which these techniques can be applied. On the other hand, if small, nanoscale features need to be probed within a sample, the nanoIR2 would be able to achieve images and spectra on that nanoscale level. For shale, future studies could include reacting to the same Eagle Ford shale sample with CO_2 gas after reaction with H_2 gas could be very interesting, as it could result in the formation of the calcite that was dissolved out in the initial reaction. In addition, shale rock samples vary in composition and are categorized based on the location they are from. Therefore, these experiments can be conducted in the future for other shale samples such as Wolfgang or Marcellus shale to better understand the variability.

In conclusion, the goal of this dissertation was to provide new insights that are offered by micro-spectroscopic tools into the composition and chemistry occurring on indoor and outdoor surfaces. While these tools are highly innovative and can provide a comprehensive analysis on their own, when complemented with other analytical tools, they can enhance the level of understanding of complex samples in unique ways.